Stellingen behorende bij het proefschrift

HIGH–PURITY SILICON
SOFT X–RAY SENSOR ARRAYS

van

Sarah Anne Steigerwald Audet

1   The high–purity silicon sensor arrays presented in this thesis can
    ideally be used in the imaging of soft X–radiation with energies between
    $8 - 20$ keV.

2   Long term ionization effects can occur in semiconductor soft X–ray
    sensors due to the build up of trapped charge in the insulator
    layers. Because of this, devices which employ functional oxide layers are
    more sensitive to radiation damage than their junction counterparts,
    Sect. 2.2.6.

3   The realization of large (7.6×7.6 cm^2) high–purity silicon soft X–ray
    sensor arrays of small elements ($20 \times 20 \; \mu$m^2) based on the double–layer
    metalization design detailed in this thesis is feasible. An array with these
    specifications would have a spatial resolution of 6 μm in both the
    x– and the y–dimensions and would be large enough to use in
    experimental systems, Sect. 3.2.

4   Although a number of incompatibilities exist in the co–integration of
    radiation sensors and electronics on the same high–purity silicon
    substrate, the benefits such a system would provide, e.g. minimum
    parasitic capacitances, minimum total power, size and wiring costs and
    maximum signal–to–noise ratios, justify future research into this area,
    Sect. 5.4.

5   The function of a radiation detector is inherently coupled to
    its own destruction and thus only has a limited lifetime, Sect. 2.2.6.

6   The stress associated with deposited–diaphragm films realized through
    silicon micromachining techniques limits the sensitivity and the size of
    deposited–diaphragm silicon capacitive pressure sensors. These
    problems can be avoided through the use of bulk–diaphragm structures.

7   Only those universities with their own material science and integrated—circuit processing facilities can significantly contribute to the field of information technology.

8   In order to decrease medical costs and patient trauma and increase the success rate of surgical operations, traditional surgical therapy should be replaced by minimal invasive therapy based on endoscopic procedures.

9   Thorough consideration of the anatomical structure of the human body and the physical effects of meat consumption leads to the conclusion that the human body is better suited to a vegetarian diet than one that includes meat. Of the twenty—two amino acids, all but eight can be synthesized by the human body itself, and these eight "essential amino acids" exist in abundance in nonmeat foods.

10   The stifling of an individual's creativity, physical and mental growth or self—development at any stage of life is one of the greatest human tragedies.

11   The increasing evidence of political scandals in the United States at all levels of government increases the feeling of helplessness and powerlessness of the American people, who have come to feel their individual vote is uninfluential.

12   The requirement that every resident in the Netherlands must have medical insurance justly insures the physical and mental care of the entire population, which results in one of the lowest rates of child mortality at birth in the world and eliminates discrimination in the receival of care based on income.

13   An emancipated workforce can only be created if society is willing to guarantee that equal opportunities exist in all occupations for both sexes and instills in their children that this is a worthwhile effort.
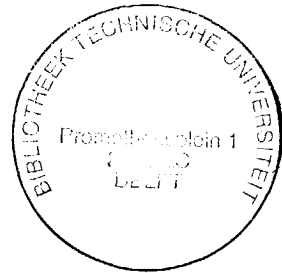
HIGH–PURITY SILICON
SOFT X–RAY SENSOR ARRAYS

HIGH–PURITY SILICON
SOFT X–RAY SENSOR ARRAYS

PROEFSCHRIFT

ter verkrijging van de graad van doctor
aan de Technische Universiteit Delft,
op gezag van de Rector Magnificus,
prof.drs. P.A. Schenck,
in het openbaar te verdedigen
ten overstaan van een commissie
aangewezen door het College van Dekanen
op donderdag 7 juni 1990, te 14.00 uur

door

Sarah Anne Steigerwald Audet

Master of Science in Electrical Engineering,
geboren te Syracuse, New York, U.S.A.

Dit proefschrift is goedgekeurd door de
promotor prof.dr.ir. S. Middelhoek

This work is dedicated to

Jack and Teresa Audet,
Frank and Patsy Steigerwald,
Amy, Jake, Mary Beth, Matt, Joe, Luke and Mark Steigerwald

and Emily, wherever we may find her.

CONTENTS

1

INTRODUCTION

1.1 SENSORS IN ELECTRONIC MEASUREMENT AND CONTROL SYSTEMS

Electronic measurement and control systems, e.g. multimeters, oscilloscopes, computers, etc., can be depicted in a functional block diagram consisting of three units: an input transducer, an electronic modifier and an output transducer [1.1].
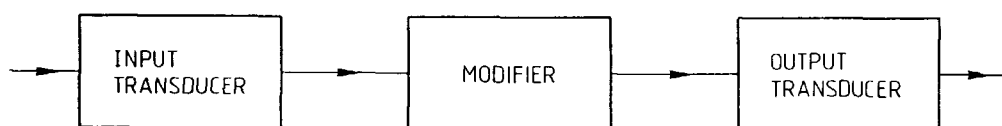
Fig. 1.1 *Functional block diagram of an electronic measurement and control system* [1.1].

A physical or chemical quantity to be measured, such as light intensity, gas flow, temperature, magnetic–field intensity or pH, is converted in the input transducer into an electrical signal. A transducer converts a measurand from one signal domain into another. Signal conversion in transducers is always based on energy conversion. Therefore, six signal domains can conveniently be

distinguished: radiant, mechanical, thermal, electrical, magnetic and chemical [1.1]. Electrical energy is currently the preferred energy signal form at the output of the first unit, the input transducer. These specialized transducers are often called sensors.

The electrical signal is modified in the second unit. The signal modification can take many forms, e.g. signal amplification, signal comparison or signal storage. However, the energy form of the signal is not altered in the modification unit.

In the output transducer, the electrical signal is converted into an alternate signal form, so that it can be perceived by one of our senses. One common conversion occurs in a display, where an electrical signal is converted into a radiant signal. Electrical signals are also commonly converted into mechanical signals, e.g. in acoustic devices. When the electrical signal is converted into a signal that gives rise to an active operation, the output transducer is called an actuator.

The development of advanced, inexpensive electronic measurement and control systems for a wide range of fields has been stimulated by the availability of superior microelectronics. The first silicon (Si) bipolar transistor was introduced in 1959 and since then developments in the field of microelectronics have been continual. Remarkable advancements have been made in the fabrication of silicon integrated circuits using silicon planar–processing technologies. The cost of producing silicon integrated circuits has dramatically decreased, while the level of device sophistication has significantly increased. As a result, there has been a continual improvement in the performance/price ratios of microelectronic devices.

However, most of the research has been focused on electronic modifiers, e.g. microprocessors and static and dynamic RAMs. A great challenge is currently being presented to researchers working in the area of sensors and actuators, as these two units of the functional block diagram, Fig. 1.1, i.e. the input and output transducers, are presently the weak links in electronic measurement and control systems. High performance, low cost sensors and actuators are in high demand for the transduction of many physical and chemical effects and for interfacing electronic modifiers to the outside world. The performance capabilities of scientific (robotic, automotive and air–transport), medical (medical imaging and automated infusion) and entertainment–oriented (home video) control systems can be greatly updated by the availability of sophisticated, inexpensive sensors and actuators.

Many technologies existed, and still exist, for the fabrication of sensors, including those based on piezoelectric materials, polymers, metal oxides, thin and thick films and optical–glass fibers, as well as those based on semiconductor technologies [1.1]. However, only silicon–based sensor technologies have uniquely been able to progress directly by reaping the benefits of the expertise and the skill gained in the development of the silicon integrated circuit and its fabrication technology.

Through the use of the diverse, sophisticated silicon planar technologies available, silicon sensors can be batch–fabricated in a wide variety of geometrical dimensions, together with signal–processing electronics on the same chip. The signal–processing electronics can be dedicated to on–chip signal amplification (thereby reducing the noise and disturbances associated with the connections to discrete units), to signal comparison (i.e. to a reference standard), to signal standardization (providing TTL or other compatible output voltage levels), to

analog–to–digital or to digital–to–frequency conversion. On–chip signal–processing electronics can also be designed for the elimination or compensation of offset or nonlinearities (i.e. cross–sensitivities or temperature effects). A standard signal with high accuracy and reliability can therefore be obtained at the sensor output, thus improving the sensor's specifications and applicability.

In addition to the well–developed technology available for processing silicon sensors, silicon displays many other characteristics desirable for sensor fabrication. Silicon exhibits many physical and chemical effects, which may be used for sensing purposes [1.1]. These include self–generating as well as modulating effects.

No auxiliary energy sources are necessary to produce a self–generating effect. Examples of self–generating effects in silicon include the photovoltaic effect used in radiant–signal sensors, the Seebeck effect used in thermal–signal sensors and the Galvano–electric effect used in chemical–signal sensors [1.1]. Silicon also displays numerous effects that require the presence of additional energy sources in order to obtain a signal output. These effects are called modulating effects. Examples in silicon include the photoelectric effect used in radiant–energy sensing, the piezoresistive effect used in mechanical–signal sensing and the Hall effect employed in magnetic sensors for the measurement of magnetic–field strengths [1.1].

Tandem transduction occurs when an intermediary signal is used in the conversion process. An example of such a process can be depicted by an infrared radiation sensor based on a silicon thermopile, which converts incident infrared radiation into an electrical output signal [1.1]. A material layer deposited on the silicon sensor next to one end of the silicon thermopile absorbs the incident radiation. This absorption causes a local increase in the temperature of the sensor. The absorbing material thus converts the incident radiation into a local increase in temperature. A temperature difference, then existing between the two ends of the silicon thermopile, creates a measurable output voltage across the terminals of the thermopile. A temperature difference is thereby converted into an electrical signal [1.1].

Silicon also displays desirable mechanical properties. The elasticity limit in silicon is higher than that in steel and silicon does not display hysteresis when subjected to repeated stress. Moreover, the micromachining of many highly sensitive three–dimensional mechanical sensors has proven very successful [1.2]. However, the magnetic permeability and piezoelectric coefficients of silicon are negligible. In order to compensate for this, magnetic and piezoelectric thin–film deposition techniques have been developed, which are compatible with silicon integrated–circuit technology [1.1].

Although there have been many successful silicon–based sensor designs manufactured with standard bipolar, NMOS or CMOS processing sequences, the fabrication of silicon–based sensors usually follows, in some form or other, nonstandard processes [1.1]. A combination of the bipolar and the NMOS processes will sometimes satisfy the fabrication requirements of a given silicon sensor, while in other designs, the standard processing steps remain the same, but the time, temperature, impurity level, dose or energy may need to be altered. Additional processing steps must often be added during the fabrication of many sensor designs, e.g. the deposition of piezoelectric or magnetic thin or thick films [1.3]. Other silicon–based sensors require special materials [1.4], e.g. nuclear–radiation sensors and millimeter–wave devices are typically processed on

high–ohmic silicon wafers [1.5–1.6]. The extra equipment and materials necessary are often expensive and the technologies are not as well known. Batch fabrication is often impossible when a particular step or sequence of steps can only be performed on a few wafers at a time. The bonding and encapsulation of silicon pressure and chemical sensors still remain great problems and impeding obstacles to further development [1.7]. All these nonstandard procedures cause the turnaround time to increase and the yield to decrease. In addition, silicon has a limited temperature range of operation, −50 to 150 °C.

Although the development of silicon sensors has remarkably progressed from the knowledge acquired from the sophistication of silicon microelectronic circuits, their integration into electronic measurement and control systems is still very narrow. Intensive research in the area of silicon integrated sensors and actuators aims at providing solutions to these numerous challenges in order to allow their rapid infiltration into many scientific, medical and entertainment–oriented systems. However, of all the existing sensor technologies, silicon and other semiconductor–based sensor technologies are of particular importance, because they offer the possibility of integrating the sensor and the signal–processing circuits on the same chip in the construction of a smart sensor [1.8].

Silicon is not the optimum semiconductor in every respect. The electron and hole drift mobilities at 300 K in pure, defect free germanium (Ge) (3900 and 1900 cm^2/Vs, respectively) and gallium arsenide (GaAs) (8500 and 450 cm^2/Vs, respectively) are equal to or higher than those values in pure, defect free silicon (1350 and 480 cm^2/Vs, respectively) [1.9]. This permits the fabrication of Ge and GaAs semiconductor devices with higher frequency responses. Germanium has a higher atomic number (32) than silicon (14), which leads to its higher efficiency in the detection of high–energy electromagnetic radiation. Gallium arsenide is a direct bandgap semiconducting material, permitting the fabrication of many electro–optical devices that cannot be made with silicon technology [1.8].

However, due to the relatively narrow bandgap of germanium (0.67 eV), devices fabricated in Ge display high junction–leakage currents and therefore must be operated at low temperatures. As gallium arsenide is a compound semiconductor, GaAs purification and growth technologies are more complicated than those of Si. In addition, the thermal oxide of silicon (SiO_2) is unparalleled in its dielectric and interfacial properties, and silicon, as well as its thermal oxide, are inert in many hostile environments. Silicon is therefore the principle material used in the fabrication of most semiconductor integrated circuits, devices and sensors [1.10].

1.2 RADIANT–SIGNAL DOMAIN

1.2.1 Introduction

The radiant–signal domain has always attracted and maintained considerable interest in the sensor field. Radiant sensors are based on the most fundamental and well–known principles of physics and have been thoroughly characterized [1.1, 1.4, 1.9]. Semiconductor–radiation sensors are considered to be the first

semiconductor sensors developed. However, the radiant–sensor field is not by any means considered to be a static or dying field, as can be seen by the continual advancements and new developments in solid–state imaging devices, in high–speed photodetectors for the ultraviolet and infrared regions and in sensors for nuclear radiation [1.1, 1.4].

The radiant–signal domain is concerned with electromagnetic radiation of all frequencies, as well as nuclear–particle radiation.

1.2.2 Electromagnetic radiation

Electromagnetic radiation includes, among others, microwaves, far and near infrared light, visible light, ultraviolet light, soft X–rays, X–rays and gamma photons. Figure 1.2 displays the entire electromagnetic spectrum and the names associated with the various frequency ranges, while the light spectrum is expanded and shown in Fig. 1.3. The visible–light spectrum, i.e. that region of the electromagnetic spectrum to which the human eye is sensitive, lies within the light spectrum spanning the region of approximately 0.4 to 0.7 μm.

Differences between the various types of radiation lie in their characteristic frequencies and in their origins [1.9]. The extensions of the regions named above tend to overlap with their bordering spectral regions, as photons of a given energy can emanate from different origins. Light photons are emitted when an electrical discharge is passed through heated solids or gases. X–rays result from transitions between states of the orbital electrons or may be produced by the deceleration of an electron beam. Gamma photons are produced in nuclear processes originating from a nucleus or from a fundamental particle [1.11].
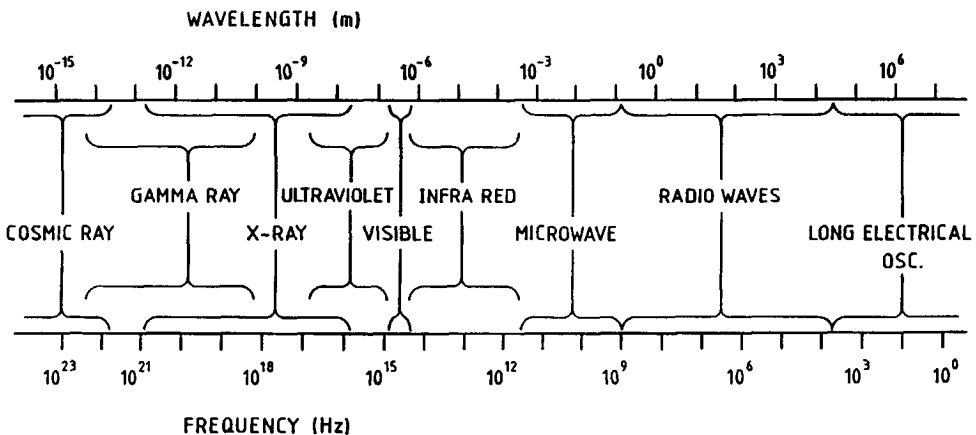
Fig. 1.2 *The electromagnetic spectrum* [1.9].

Important experimental work performed with vacuum tubes by several scientists: Herz, Hallwachs and Lenard, in the late 1800s provided evidence of the corpuscular properties of electromagnetic radiation and laid the ground work for modern quantum theory [1.12]. In 1900 Planck derived an empirical formula, which was a modified version of an accepted classical function, to characterize the spectral distribution of blackbody radiation on the assumption of discrete–energy quantization. Einstein applied these ideas to the photoelectric effect and demonstrated in 1905 that electromagnetic energy is not distributed continuously in space but quantized in small bundles called photons. The energy of a photon E_p is directly related to its frequency and inversely proportional to its wavelength [1.11]

$$E_p = h\nu = hc/\lambda \tag{1.1}$$

where $h = 4.136 \times 10^{-15}$ eVs is Planck's constant, ν is the frequency of the electromagnetic radiation in Hz, $c = 2.998 \times 10^8$ m/s is the speed of light in vacuum and λ is the wavelength of the electromagnetic radiation in m.
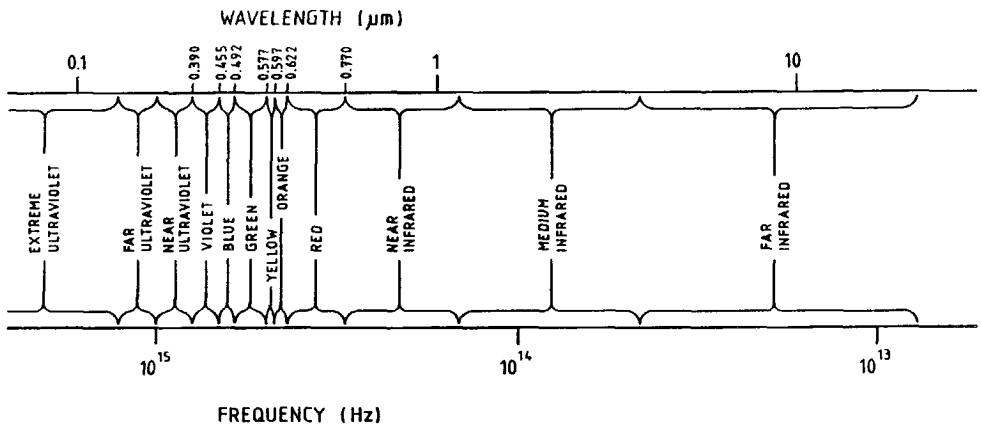
Fig. 1.3 *The light spectrum* [1.9].

1.2.3 Nuclear–particle radiation

Nuclear–particle radiation includes, among others, alpha particles, beta particles and neutrons. Alpha particles were shown by Rutherford to be the charged nuclei of ^{4}He atoms [1.13]. They are emitted when heavy elements undergo natural radioactivity or from the bombardment of a target with nuclear radiation. Alpha particles belong to a class of charged particles called

heavy–charged particles, which includes all charged nuclei from protons and deuterons to the heaviest fission fragments. The particles in this class may carry any charge from q to Zq, where q is the electronic charge and Z is the atomic number [1.13].

Beta particles are fast electrons, which may be emitted through natural or induced radioactivity, or may be produced by the acceleration of electrons in an electric field. They have the mass of an electron and are negatively charged. Beta particles belong to a separate class of charged particles, sometimes referred to as light–charged particles, which also includes particles called positrons. Positrons are produced by natural or induced radioactive decay. They have the same mass and charge magnitude as those of electrons, but their charge is positive [1.13].

The neutron is a neutral particle, with a mass slightly greater than that of a proton. It belongs to a class of particles called uncharged particles. Lacking charge, particles in this class cannot cause ionization and therefore cannot be detected by electromagnetic interactions. The detection of uncharged particles requires the transfer of its energy to a charged particle, which can subsequently be detected. Polyethylene or other layers are often deposited onto a radiation detector, so as to create charged particles when uncharged particles interact within the layer [1.13].

Although sensors used for the detection of nuclear particles are very similar to those used for the detection of electromagnetic radiation, it is the purpose of this thesis to discuss sensors for high–energy electromagnetic (specifically soft X–ray) radiation. In view of this, nuclear–particle radiation will not be discussed further. The term radiant is now dealt with only in the context of electromagnetic radiation.

1.2.4 Sensors for radiant signals

Early devices used for the detection of electromagnetic radiation within the light spectrum, Fig. 1.3, included detectors based on thermal transduction principles, i.e. thermopiles and pyrodetectors, as well as vacuum photodetectors [1.14]. Conventional methods of detecting higher energy electromagnetic radiation, i.e. (soft and hard) X–rays and gamma photons, were originally, and are still, based on the use of photographic films, gas–ionization chambers and scintillating crystals [1.13]. Sensors for detecting (soft and hard) X–ray and gamma radiation will be simultaneously discussed at this point, as their frequency spectrums overlap and the sensors employed for their detection are often the same. Sensors for soft X–ray detection are more thoroughly discussed in Sect. 1.3.

1.2.4.1 Photographic film

Photographic film is the oldest detector of X–rays. The advantages of film include its ability to record a complete spectrum simultaneously from pulsed

sources, its excellent two–dimensional spatial resolution (on the order of 10 μm in both the x– and the y–dimensions) and a range of photon energy response of $3 - 4$ orders of magnitude. One disadvantage of film involves the difficulty in quantitatively relating the film density to the incident photon energy or intensity [1.15–1.16]. When one photon interacts with an X–ray film composed of silver bromide (AgBr), one silver grain (Ag) is formed after development of the film. This leads to an exposure saturation effect, as one AgBr particle develops into an Ag grain only once. Moreover, film does not provide an instant response. The instantaneous response provided by solid–state detectors often gives them a distinctive edge over photographic films. In addition, the sensitivity and dynamic range of certain solid–state sensor arrays have been found to be two to three orders of magnitude higher than those values associated with photographic films [1.17–1.18].

1.2.4.2 Gas–ionization chambers

The detection of X–rays and gamma photons in gas–ionization chambers is based on the creation of electron–hole pairs upon the absorption of incident electromagnetic radiation in an inert gas and on the subsequent collection of this charge at boundary electrodes (when the detector is under the presence of an electric field). The charge carriers drift toward the bounding electrodes. The drift velocity and the charge–collection efficiency are dependent on the electric field and the nature, the temperature and the pressure of the gas. Inert gases are most often used, as they do not capture electrons. For simple gas–ionization chambers, the amount of charge carriers collected at the contacts is given by the formula

$$Q = qh\nu/\epsilon \tag{1.2}$$

where q is the charge of an electron, $h\nu$ is the energy of the incident radiation and ϵ is the ionization energy, i.e. the energy required to create one electron–hole pair, Sect. 2.1.3. In most gases, ϵ is on the order of 30 eV. If the voltage placed across the electrodes is increased, as is the case in proportional–multiwire detectors and in Geiger counters, charge–carrier multiplication will occur and Eqn. (1.2) will no longer hold. A multiplication factor must be included, which is exponentially proportional to the applied voltage. One great advantage associated with these devices is that large area gaseous detectors can be fabricated relatively easily.

Gaseous detectors are modulating sensors, as an external voltage supply is necessary to create the electric field, which is required to efficiently collect the total charge created by the incident radiation. Both one– and two–dimensional position–sensitive gaseous detectors have been fabricated [1.15–1.16].

1.2.4.3 Scintillation detectors

A scintillation detector is a tandem transducer. The incident high–energy electromagnetic radiation is first converted by a scintillating (fluorescent) crystal with an activator into light quanta. The absorption of incident radiation brings the crystal atoms into an excited state. Energy is transferred to the activator within 0.3 nsec. Photons, with energies lower than that of the original radiation, are emitted upon a return of the atoms to the ground state. The light emission occurs within 230 nsec. These photons are subsequently (conventionally) transduced into electrical energy by a photomultiplier tube (PMT). The primary scintillator detector systems of choice for applications in nuclear medicine, nuclear fuel science, geophysical and environmental science, space science and high–energy physics employ NaI(Tl) crystals. BGO and $CdWO_4$ crystals are often used for X–ray spectroscopic studies [1.19].

Rapid advancements in nuclear–medical instrumentation were achieved in the 1960s due to NaI(Tl) scintillator technology. Nuclear–medical studies require the efficient imaging of gamma photons emitted from functional organs within the body, where they have been concentrated. NaI(Tl) scintillator gamma cameras, i.e. Anger cameras, are still the standard instruments used in nuclear medicine. An Anger camera is composed of a large scintillator plate, which is optically coupled to an arrangement of numerous PMTs and a pulse arithmetic unit. An estimate of the x–y coordinates and the energy of each detected event is recorded. Other detectors have been built from a matrix of small scintillator blocks, each optically coupled to its own PMT.

An advantage of NaI(Tl) scintillator detectors is that NaI(Tl) crystals can be made very large in order to image whole organ systems. In addition, scintillator crystals are usually fabricated from heavy materials with high atomic numbers and therefore have better absorption efficiencies than those detectors fabricated from silicon or germanium. However, inefficient processes are involved in the conversion of high–energy electromagnetic radiation into light quanta by the scintillator and light quanta into electrons by the photomultiplier tubes. These inefficiencies limit the detector's spatial and energy resolutions. Scintillator detectors also suffer from afterglow, which occurs up to 150 msec after the light emission, low scatter rejection, low contrast ratios, low clarity of boundary definitions and low uniformity [1.15–1.16, 1.19].

1.2.4.4 Semiconductor–radiation sensors

While television served as the prime stimulus for the replacement of vacuum tubes by semiconductor detectors in light applications, the lower ionization energy of semiconductor materials (approximately 3 eV) proved to be the motivating factor involved in the introduction of semiconductor detectors into applications for the detection of high–energy electromagnetic radiation [1.15–1.16]. The same radiation will generate approximately an order of magnitude more charge in a semiconductor detector than in a gaseous detector, Eqn. (1.2). This leads to a significant improvement in the energy resolution of the

detection system. Moreover, the probability of absorption of incident radiation is directly related to the density of the detecting material, Sect. 2.1.2. Semiconductor detectors, having higher densities than gaseous detectors, can be fabricated much thinner than their gas counterparts.

Other advantages of a semiconductor detector include an excellent bandwidth and count–rate performance, a linearity of performance over a large range, a good stability and a low noise. Furthermore, a wide variety of semiconductor detector geometries are obtainable due to the advanced processing technologies developed for the fabrication of semiconductor devices.

As in reverse–biased gaseous detectors, the detection of X–rays and gamma photons in reverse–biased semiconductor detectors is also based on the absorption of incident electromagnetic radiation, the ensuing creation of electron–hole pairs and the subsequent collection of this charge at boundary electrodes. The number of charge carriers ideally collected at the contacts is also given by Eqn. (1.2).

A number of parameters are important when comparing the usefulness of different semiconductor materials for the detection of high–energy electromagnetic radiation. These include the net concentration of dopant atoms, the bandgap, the ionization energy, the drift and diffusion lengths and the atomic number(s) of the semiconductor substrate material [1.20].

Given that the magnitude of the reverse–bias voltage placed across a semiconductor detector is sufficiently high to deplete the entire substrate thickness, the detector's sensitive volume will equal that volume existing between the boundary electrodes. Fully depleting the substrate creates a relatively high electric field in a thick sensitive volume, which ensures the fast and complete collection of the charge generated within the detector. The expression for the depletion width of a one–sided abrupt p^+–n junction, appropriate for $N_a \gg N_d$ is [1.9]

$$x_n = \left[\frac{2\epsilon_0 \epsilon_{si} V_t}{q N_d} \right]^{1/2} \tag{1.3}$$

where ϵ_0 and ϵ_{si} are the permittivity of free space and the dielectric constant of silicon, respectively, V_t is the sum of the built–in and the reverse–bias voltages and N_d is the donor impurity concentration. Since the breakdown phenomenon limits the reverse–bias voltage that can be applied, the only way to achieve large depletion layers is through the use of high–purity (or compensated) silicon material, Sect. 4.2. Large ingots of high–purity monocrystalline silicon and germanium readily fulfill the demand for a low net concentration of dopant atoms [1.20–1.22].

The thermal generation of carriers decreases as the bandgap increases. Therefore, to reduce the background current, one would like to maximize E_g. With respect to this demand, silicon is superior to germanium, due to its larger bandgap. Negligible values for the junction–leakage current of Ge detectors can only by obtained by operating the device at liquid nitrogen temperatures.

However, as the bandgap increases, the ionization energy, ϵ, also increases. As ϵ increases, the total number of electron–hole pairs generated by a given radiation source, N_0, decreases, as $N_0 = h\nu/\epsilon$. The energy resolution, which is directly

proportional to N_o, Sect. 2.2.3, will also decrease.

In order to be collected, the charge–carrier drift and diffusion lengths must be larger than the distance the carriers have to migrate in the depletion layer or in the undepleted layers, respectively, before reaching a contact (or the depletion layer in the latter case). If these lengths are long, the signal becomes independent of the incident photon's point of absorption within the detector's sensitive volume. The drift and diffusion lengths for electrons and holes are given respectively by

$$L_{dr\text{-}e,\text{-}h} = \mu_{e,h} \tau_{e,h} \mathscr{E} \tag{1.4a}$$

$$L_{e,h} = \left[D_{e,h} \tau_{e,h} \right]^{1/2} \tag{1.4b}$$

where $\mu_{e,h}$ represents the charge–carrier mobility for electrons or holes, $\tau_{e,h}$ represents the charge–carrier lifetime for electrons or holes, $\mathscr{E}$ represents the electric–field strength and $D_{e,h}$ represents the diffusion constant for electrons or holes [1.20].

Relatively high charge–carrier mobilities and long charge–carrier lifetimes can be obtained in Si and Ge substrates due to the remarkable achievements in their crystal growth and purification technologies [1.21–1.22]. These values in compound semiconductors such as cadmium telluride (CdTe), mercuric iodide (HgI_2) and GaAs are from one to one hundred thousand times lower, due to the difficulty in fabricating high–purity material [1.20].

The efficiency for the photoelectric absorption of incident radiation is proportional to the atomic number of the semiconductor material to the power 5, Sect. 2.1.2. With respect to this demand, compound semiconductors such as CdTe, HgI_2 and GaAs have a definite advantage over Si and Ge.

Values for the net concentrations of dopant atoms in the purest materials available, the bandgaps, the ionization energies, the mean electron and hole mobilities, the mean electron and hole lifetimes and the atomic numbers of various semiconductor materials are found in Table 1.1 [1.20–1.21].

Research on CdTe and HgI_2 began in the mid–1960s and in the early 1970s, respectively, in an effort to find semiconductor materials with higher atomic numbers for use in the detection of high–energy photons [1.23–1.24]. Due to their higher atomic numbers (48 and 52 for CdTe and 53 and 80 for HgI_2), the efficiencies for X– and gamma–radiation detection are significantly higher than those values associated with Si and Ge, Sect. 2.1.2. The bandgaps of CdTe and HgI_2 (1.56 eV and 2.13 eV, respectively) are large enough to allow the fabrication of detectors for use in room temperature X–ray and gamma photon spectrometry with excellent energy resolutions. CdTe and HgI_2 have also been used in the fabrication of miniature probes for diagnostic purposes, which can be operated at body temperature with good energy resolutions [1.20, 1.23–1.24].

There are however disadvantages associated with the use of these semiconductor materials. As is true of all crystal growing methods, especially those associated with the production of compound semiconductors, it is difficult to grow large volume crystals that are highly uniform in purity, stoichiometry

and charge–collection properties. There are currently three methods available for the fabrication of CdTe crystals: the zone melting method, the travelling heater method and the Bridgmann method. High–quality crystals can be produced using the zone–melting method, but the resistivities are low. High–resistivity crystals can be produced using the other two methods, but they tend to have severe problems with polarization, i.e. with time dependent changes in the depleted thicknesses or in the charge–collection properties [1.23].

Table 1.1   *Parameter values for various materials used in fabricating semiconductor–radiation sensors* [1.20–1.21].

Material	$\|N_d - N_a\|$	E_g	ϵ	μ_e	μ_h	τ_e	τ_h	Z
	[cm^{-3}]	[eV]	[eV]	$\left[\dfrac{cm^2}{V\,s}\right]$	$\left[\dfrac{cm^2}{V\,s}\right]$	[s]	[s]	
Si	3×10^{10}	1.12	3.61	1350	480	5×10^{-3}	5×10^{-3}	14
Ge	$>5\times10^{9}$	0.67	2.98	3900	1900	2×10^{-5}	2×10^{-5}	32
CdTe	10^{12}–10^{13}	1.56	4.43	1050	100	1×10^{-6}	1×10^{-6}	48, 52
HgI$_2$	Semi–insulator	2.13	4.2	100	–	1×10^{-6}	2×10^{-6}	53, 80
GaAs	10^{12}–10^{13}	1.42	4.7	8500	450	5×10^{-8}	5×10^{-8}	31, 33

Single HgI$_2$ crystals can be grown from the vapor phase or by solution regrowth. However, the fabrication of HgI$_2$ detectors is even more difficult than that of CdTe due to the softness of the material, its agressivity against many materials (e.g. aluminum (Al) and gold (Au)), its small thermal resistance, its solubility in most solvents and its toxicity. In addition, HgI$_2$ is unstable at temperatures above 70 ºC and it is nearly impossible to apply metal contacts to the semiconductor, as the mercury tends to amalgamate with metals. The low charge–carrier mobilities associated with HgI$_2$ cause incomplete charge collection, which limits the sensitive thickness of the detector, even when very high electric fields are applied [1.24]. Furthermore, the yields of both compound semiconductors are very low, their availabilities are restricted and their prices are high. Thus, although CdTe and HgI$_2$ detectors have demonstrated good performances as room temperature X–ray and gamma photon spectrometers,

their crystal growth methods and their long term stabilities have to be improved.

GaAs was also investigated for its usefulness in nuclear–radiation detection in the early 1960s, when high–resistivity, compensated crystals became available [1.20, 1.23]. However, the performances of the fabricated detectors were poor due to strong trapping effects. Upon the development of liquid– and vapor–phase epitaxial techniques to grow high–purity GaAs films on either GaAs or on Si substrates, Schottky diodes $60 - 80 \, \mu m$ thick and 1.5 mm in diameter were fabricated, which obtained excellent energy resolutions of gamma photons [1.23]. However, as high–quality epilayers cannot be grown in excess of $100 \, \mu m$, the efficiencies of such devices are very small and therefore they cannot find applications in X–ray or in gamma photon detection [1.23].

Due to their well–developed processing technologies, silicon and germanium were the first semiconductor materials used to fabricate semiconductor–radiation detectors [1.20]. Silicon was primarily used to image light photons, while germanium, with its higher atomic number, was used in the detection of higher energy electromagnetic radiation. However, the material requirements for the fabrication of semiconductor–radiation sensors are very different from those requirements for the fabrication of standard integrated circuits. Extremely pure material is required, so that deep depletion depths, long effective charge–collection lengths and low concentrations of deep trap centers can be obtained. The lithium–ion compensation technique was introduced in the early 1960s to increase the purity of silicon and germanium substrates and to allow the production of thicker detectors that would require lower reverse–bias voltages for full depletion. Lithium–drifted detectors up to 10 mm thick can currently be fabricated and are known for their excellent energy resolutions [1.25].

The lithium–drift procedure involves the initial diffusion of lithium on one side of a p–type wafer (with a nominal resistivity of 1000 Ω–cm), thus forming an n^+–contact. A groove is then cut into this side of the wafer with an ultrasonic cutter. The evaporation of gold follows on the reverse side of the wafer to form the p^+–contact. The surface is subsequently treated to minimize leakage currents.

The detector is then heated to $110 - 150$ ºC and a reverse–bias voltage (on the order of $500 - 1000$ V) is applied. This procedure causes the lithium ions to drift from the n^+–contact into the p–type bulk. The lithium ions compensate the boron impurities, thus producing a nearly intrinsic device [1.25].

The lithium–drift process is relatively simple and very little equipment is necessary. However, surface passivation techniques are very difficult. In addition, lithium tends to form complexes with oxygen, which is generally present in silicon and germanium crystals. This effect and the presence of microdefects in the crystals cause interferences in the drift process. Moreover, lithium ions drift at relatively low temperatures, especially in germanium crystals. Both Ge(Li) and Si(Li) detectors must be stored at liquid nitrogen temperatures. Ge(Li) detectors must also be operated at 77 ºC, although Si(Li) detectors can be utilized in some applications at room temperature [1.25].

High–purity germanium ingots with excellent crystal structures, extremely small trap concentrations and impurity concentrations on the order of 1×10^{10} cm^{-3} became available in the early 1970s, primarily for use in the fabrication of gamma photon detectors [1.20, 1.22]. The purification procedures were based on float–zone refining techniques rather than on compensation techniques. Room temperature handling and storage of high–purity Ge is possible, although these detectors must be operated below 150 K in order to

eliminate the effects of thermally—generated leakage—current noise. As this material has almost all the advantages of Ge(Li) without the problems associated with lithium drift, it basically replaced Ge(Li) [1.22].

More recently, high—purity silicon crystals with resistivities from $500 - 50{,}000\ \Omega$—cm, lifetimes from $100 - 5000\ \mu$sec and low defect densities have become available. This material is fabricated either through the use of the float—zone growth and refinement methods or by neutron transmutation, Sect. 4.2 [1.21]. High—purity silicon is used in the fabrication of devices that must operate under a high voltage, i.e. power devices, thyristors and radiation sensors. Due to its higher bandgap, in most applications, high—purity silicon does not need to be cooled. However, cooling the detector will lower its leakage current and noise, Sect. 2.2.1.

1.3 SOFT X—RADIATION

1.3.1 Soft X—ray sources

Significant research has been devoted to the development of sensors to detect electromagnetic radiation in the light spectrum, as well as in the X— and gamma radiation regions. However, very little effort has been expended for the development of sensors for the detection of soft X—rays, i.e. electromagnetic radiation with energies from approximately $2 - 25$ keV. In the past, there has been little need for such sensors, because there have been very few sources of soft X—rays and therefore very few applications. However, due to the recent development of intense soft X—ray sources and efficient optics, soft X—ray systems have been found to be powerful research tools for use in many areas of science and medicine, e.g. in such applications as X—ray microscopy, X—ray spectrometry and digital—subtraction angiography [1.26–1.28]. An urgent need now exists for the development of both one— and two—dimensional position—sensitive soft X—ray sensors.

A summary of the fundamental properties of three different X—ray sources: X—ray tubes, plasma sources and storage (or synchrotron) rings, is given below. Additional sources of soft X—rays originating from the decay of radioactive elements, which are used in preliminary experimental work and for the purpose of calibrating detectors, are also discussed.

Photons in the soft X—ray region are emitted due to X—ray transitions during the decay of certain radioactive sources. ^{241}Am decays by alpha decay with a 432.4 year half—life producing ^{237}N$_P$ L and M X—rays, which have energies below 25 keV. Since the early 1970s, radioactive ^{241}Am sources have been extensively used in the absolute efficiency calibration of Si(Li) detectors. ^{241}Am is ideal for the absolute efficiency calibration of detectors within the $1 - 60$ keV energy range, as it has M X—ray lines between $2 - 6$ keV, a well—defined Lα line at 13.9 keV and Lβ and Lγ transitions, which cover the energy range $15 - 23$ keV. It also has gamma photon transitions at 26.3, 33.1, 43.5 and 59.5 keV [1.29].

The relatively broad X—ray spectrum emitted from an X—ray tube is determined by the target material and typically consists of a few characteristic

lines. Spectral shaping of the radiation is possible by means of filters. The radiation has isotropic characteristics with typical focal spots on the order of a few millimeters. The quality of the X–rays produced can be adjusted by varying the voltage across the tube or the current flow through the tube [1.30–1.31].

Plasmas are ionized gases. Conditions within a plasma are described by several parameters: the density of the electrons, the ionization states of the constituent atoms and the electron and ion energy distributions. Plasmas hotter than 10^6 K emit radiation in the X–ray region. High–temperature plasmas have been used since the early 1970s for the production of controlled fusion reactions, but have more recently been investigated for the production of intense soft X–ray sources [1.32–1.37].

Three methods to generate plasma sources involve the electrical discharge of a capacitor bank. The discharge occurs across a vacuum gap in the vacuum spark method, across a fine wire in the exploding wire method and through a low–pressure gas existing between two cylindrical electrodes in the plasma focus method. Plasmas can also be generated when a high–power laser pulse is focused on a solid material (the laser focus method) [1.36–1.37].

Considerable research is currently being carried out on laser plasmas. The spectra from laser plasmas consist of many lines that originate from resonant transitions. The range of the radiation emitted falls between approximately $1 - 6$ keV, while the available repetition rates are from approximately $1 - 10$ nsec. The soft X–ray intensity can be manipulated by varying the target and the laser pulse characteristics. Up to 10^{12} photons per pulse can be emitted at a brightness of 2 x 10^{16} (a.u.) [1.36]. The brightness is defined as the flux emitted by the source per unit source area and per unit of solid angle. Spot sizes from 50 μm to 100 μm have been realized [1.35]. The ability of laser plasma sources to provide the rapid emission of an intense, soft X–ray spectrum from a small volume has recently led to investigations of its use in such applications as X–ray microscopy, X–ray spectrometry and X–ray diffraction [1.35–1.37].

Synchrotron radiation is white electromagnetic radiation emitted by electrons $(h\nu > 100$ MeV) moving at relativistic velocities through an external magnetic field [1.38]. The most effective sources of synchrotron radiation are electron storage rings, as they cycle and accumulate beams with very high intensities. The emitted radiation is strongly focused in the forward direction of the particle motion due to the relativistic velocity [1.38].

Synchrotron radiation is naturally collimated and is characterized with a broad spectral range, a high polarization and a pulsed–time structure, in addition to a high intensity [1.39]. Moreover, an electron storage ring produces synchrotron radiation with a small beam spot size in a stable, high–vacuum environment. Spot sizes on the order of 0.5 mm are typical. Synchrotron radiation provides five orders of magnitude more continuum vacuum ultraviolet and soft X–radiation than X–ray tubes. The wavelength of synchrotron radiation can be finely tuned and selected with crystal monochromators over a wide energy range, from approximately $1 - 35$ keV. Due to its high original intensity, the intensity of the monochromatic radiation remains sufficiently high for experimental use. The intensity after monochromation of the other radiation sources is too low for practical use. Due to the fine collimation and low divergence of the beam, sharply defined reflections are obtained making high data resolution accessible. This unique combination of properties in one soft X–ray source has opened up wide new areas of research in many scientific disciplines [1.39].

1.3.2 Methods of soft X—ray detection

There are four basic soft X—ray imaging topologies. These are based on soft X—ray photon to visible—light photon conversion, on soft X—ray photon to electron conversion, on soft X—ray photon to heat conversion and on direct soft X—ray photon detection.

The first detection scheme, i.e. soft X—ray photon to visible—light conversion, is based on the coupling of a scintillator crystal or a phosphor layer to an image—intensifier module (termed a fiber—optic demagnifier or a demagnifying electro—optic unit). The image—intensifier module is further coupled to a silicon photodiode or to a CCD imaging array [1.40]. Problems with this type of detection scheme involve the loss in the overall efficiency due to the intermediate conversions and due to the demagnification process. These problems include matching the emission of the scintillator or the phosphor to the spectral response of the silicon detector and the transmission losses involved in the fiber—optic coupling system [1.40]. In addition, the elevated cost of fiber—optic faceplates, priced at approximately US$ 500 each, eliminates this as a possible method of soft X—ray detection for most applications.

The second topology involves the use of materials that convert incident soft X—rays to electrons. Although several different materials that provide this conversion are currently being investigated, this field is still relatively undeveloped at this time [1.40].

Another method of soft X—ray detection is based on the transduction of incident soft X—rays into heat with the subsequent measurement of the temperature increase, i.e. it is based on the use of a (tandem) thermal sensor. The soft X—ray is first absorbed in a material, possibly one other than silicon. Its energy is then converted to heat and the temperature increase is measured by the change in the resistance of a thermistor. One type of thermal detector used is a bolometer, which consists of three parts: an energy absorber, a semiconducting thermometer and a support structure to carry away the applied heat and to establish electrical contact to the thermometer [1.41]. The advantage of this type of detector is that, due to the very small measurement uncertainty, an energy resolution of 1 eV full—width at half—maximum (FWHM) can be expected, if the detector is operated at 0.1 K and if there is no noise associated with the thermalization of the soft X—rays. This can be compared to a minimal $100 - 200$ eV FWHM for direct silicon detectors operating at room temperature conditions. However, the sensing material must have a very small heat capacity so that very small temperature rises can be sensed (the energy of a 1 keV X—ray only corresponds to 4×10^{-17} calories or 1.6×10^{-16} J) and so that random fluctuations of the temperature of the sensing material will have a small magnitude. The detector must also be thick enough, to insure a high efficiency for the absorption of incident soft X—rays, and be able to operate at 0.1 K. In addition, to optimize the performance of thermal detectors, the temperature sensor must have a high temperature coefficient of resistance, as well as a resistance that can be matched to the preamplifier to minimize noise. Due to all the constrictions placed on bolometers for the detection of soft X—rays, they have to date found very little application in this area [1.41].

Another type of thermal detector that may have application in the soft X—ray region is that based on the use of a thermopile. This type of thermal detector

system also consists of three basic elements: a radiation absorber with an absorbance close to unity, a temperature sensor to measure the temperature increase of the absorber due to radiation absorption and a heat sink to serve as a temperature reference. Thermopile–type sensors have been used extensively in the infrared, visible and ultraviolet spectral regions, but have not yet been applied in the soft X–ray region [1.42]. One major problem exists in the search of a suitable radiation absorbing material.

The final topology, direct X–ray detection, involves no loss in overall efficiency through intermediate energy conversions. The range of photon energies for which high–purity silicon sensors can serve as direct detectors depends on their sensitive volumes. When fully depleted, high–purity silicon sensors 0.38 mm thick are employed, the intrinsic quantum efficiencies for (soft) X–rays with energies between $2-25$ keV are $95-15\,\%$, Sect. 2.1.4. However, two difficulties are associated with this type of detector, namely their small physical size and the reduction of the useful detector lifetime through the radiation damage caused by the direct exposure of the silicon sensor to soft X–rays [1.40]. The small physical size of the detection system can be overcome if many individual sensors or sensor arrays are placed in the formation of a large array, given that a reasonable uniformity exists between the individual sensors. Moreover, silicon sensors based on $p-n$ junctions are less prone to radiation damage than MOS–based devices and experiments have shown that this damage can be annealed by ultraviolet illumination, Sect. 2.2.6 [1.18].

1.3.3 Direct soft X–ray sensors

Standard methods for direct photon detection in the soft X–ray region include the use of photographic films, gaseous detectors and high–purity Ge diodes and Si(Li) diodes, all of which have been described in Sects. $1.2.4.1 - 1.2.4.4$. More recently, silicon detectors designed for operation in the optical and near infrared region of the electromagnetic spectrum, i.e. P–I–N diodes, photodiode matrices and CCD arrays, have also been employed as direct soft X–ray sensors [1.43–1.45].

As mentioned above, the instantaneous response provided by solid–state detectors gives them a distinctive edge over photographic films. Due to their higher densities and lower ionization energies, solid–state detectors have better stopping powers and energy resolutions than gaseous detectors. Because silicon has a larger bandgap than germanium, silicon detectors can be operated at room temperature, whereas germanium detectors need to be cooled to around 77 K in order to limit their leakage currents.

Through slight device modifications, silicon–based optical imaging devices such as P–I–N diodes, photodiode matrices and CCD arrays have been successfully used as detectors for the lower soft X–ray region [1.43–1.45]. However, these devices are not optimally suited for the detection of soft X–rays at the higher energy confines of the soft X–ray region. Soft X–rays are primarily absorbed in silicon by the photoelectric process, Sect. 2.1.2. The efficiency of the sensing device for the photoelectric absorption of incident electromagnetic radiation at intermediate photon energies (including the soft X–ray region) is

determined by the absorption coefficient for photoelectric interactions, α_{pe}, and the photon absorption length, which is the inverse of the absorption coefficient, α_{pe}^{-1}. In order to ensure the total useful absorption of incident electromagnetic radiation, the thickness of the sensitive region (depletion region plus one diffusion length) must be several times the absorption length. This thickness is comparatively small for standard silicon optical–imaging devices. In addition, the photoelectric absorption coefficient, α_{pe}, for photons of intermediate energy decreases by a factor proportional to the incident photon energy to the power $-7/2$, Eqn. (2.5). Therefore, for the total absorption of photons, the thickness of the sensitive region of the device must increase by the same factor. There is also an intrinsic problem associated with the absorption of intermediate and high–energy photons in silicon due to its low atomic number ($Z = 14$), as the photoelectric absorption coefficient, α_{pe}, is also proportional to the atomic number of the absorbing material to the power 5, Eqn. (2.5). For this reason, semiconductors with high atomic numbers are often used for the detection of gamma photons.

In order to directly detect photons at the higher energy confines of the soft X–ray region, large sensitive volumes can be obtained in silicon through the use of high–resistivity or compensated silicon material, Sect. 4.2. Higher efficiencies can often be obtained with devices processed on Si(Li) substrates due to the increased thicknesses of the starting materials. However, compared with compensated silicon material, high–purity silicon contains fewer generation–recombination centers, which makes the fabrication of devices with lower leakage currents and lower device noise possible. Moreover, the deterioration of detector performance through the redistribution of compensating doping atoms is avoided when high–purity silicon is used as the substrate. Other advantages associated with the use of high–purity silicon include the ability to utilize standard integrated–circuit fabrication techniques in order to process multielement detectors with high quality surface–passivation layers, asymmetric, nearly abrupt p–n junctions and thin, noninjecting contacts, as well as the ability to anneal radiation damaged detectors [1.26].

Si(Li) detectors have successfully been used in many soft X–ray applications. However, problems in the material selection, fabrication and evaluation of these detectors still exist [1.46].

In the sphere of high–purity silicon, deep–depletion MOS CCD imagers fabricated on high–ohmic silicon (substrate resistivity in the range of $2 - 5$ kΩ–cm) have been reported [1.45] and the first results of a fully depleted p–n junction CCD using the principle of the semiconductor drift chamber have been announced [1.47]. The fabrication of such structures however is very complex. Another disadvantage of MOS CCD structures as X–ray detectors is their insufficient radiation hardness [1.18]. When CCD imaging devices based on MOS capacitors are directly irradiated with soft X–rays, radiation damage results. Evidence of this damage is demonstrated by increased reverse currents, flat–band voltage changes and reduced charge–transfer efficiencies. Radiation damage due to the exposure of p–n junction devices to soft X–rays is also associated with an increase in the reverse current. However, significant damage (i.e. increases in the reverse current by a factor of 10) generally does not become evident until after an exposure dose of approximately 1×10^7 rads. In addition, investigations have shown that this damage can be annealed by ultraviolet illumination, Sect. 2.2.6.

Soft X–ray sensors fabricated on high–purity silicon (substrate resistivity

4 kΩ–cm) have the potential to overcome the material problems associated with lithium–drifted silicon detectors and the fabrication complexity of deep–depleted CCD detectors and thus become useful in scientific imaging applications.

1.3.4 Applications

Recently, there has been much interest in developing synchrotron radiation and repeatedly–pulsed plasma soft X–ray sources for use in scientific and medical applications. High–purity silicon soft X–ray sensors and sensor arrays are ideal devices for use in those measurement techniques that employ low–energy X–rays, which include X–ray microscopy, X–ray spectrometry, X–ray tomography, nondestructive evaluation and structural analyses, digital–subtraction angiography and mamography [1.26–1.28, 1.40–1.46].

Many beam lines have become available at synchrotron and pulsed–plasma facilities around the world. This presents an opportunity for a great variety of experiments to take place with a wide range of photon intensities. It also creates a demand for one– and two–dimensional position–sensitive soft X–ray sensors for the collection of high–quality data. Other applications arise in the maintenance of quality control of these radiation sources. Diagnostic procedures must be carried out to monitor the performance of these sources in terms of the beam dosimetry and the beam tracking. Soft X–ray sensors are also required in beam monitoring applications [1.32–1.40].

1.4 AIM OF RESEARCH

Due to the recent progress made in the fundamental research and technological applications of soft X–radiation and due to the current availability of soft X–ray sources, the development of one– and two–dimensional position–sensitive soft X–ray sensors for the collection of high–quality data has become necessary. The aim of this work was to investigate the fundamental properties of two–dimensional position–sensitive soft X–ray sensor arrays fabricated on high–purity silicon.

In order to accomplish this aim, a processing sequence first had to be developed. A simple process involving the fabrication of two junctions, i.e. a frontside p^+-n^- junction and a backside high–low n^+-n^- junction on high–purity silicon, was initially investigated to realize basic soft X–ray sensors. Two additional steps were then added to the initial sequence in order to realize resistive structures to be used for resistive coupling purposes. These steps included the low–pressure chemical–vapor deposition (LPCVD) of a polysilicon layer and the subsequent doping of this layer by phosphorous diffusion, performed in order to dope the polysilicon and lower its resistivity. Two groups of fundamental structures were thereby obtained, i.e. the basic $p^+-n^--n^+$ diodes and these diodes, each with a polysilicon resistive structure in series. These two groups of basic structures came to form the fundamental elements of two groups

of sensor arrays. One group of arrays consisted of matrices of $p^+-n^--n^+$ diodes, while two–dimensional arrays of such diodes, each with a resistive structure in series, made up the second group.

However, a double–layer conduction process was necessary in order to realize two–dimensional position–sensitive high–purity soft X–ray sensor arrays. Initial attempts involved the use of polysilicon lower conductors and aluminum conductors in the second layer. However, high–purity soft X–ray sensor arrays with improved characteristics were obtained upon the perfection of a double–layer metalization process. This process was based on the initial basic process with the addition of two processing steps: a low–temperature deposition of silicon dioxide and a second layer metalization.

The organization of the thesis is centered on the theoretical characterizations of the elemental soft X–ray sensors and the two–dimensional soft X–ray sensor arrays (Chapters 2 and 3, respectively), on the fabrication of the sensors and sensor arrays (Chapter 4) and on the experimental results obtained from measurements performed on the sensors and sensor arrays (Chapter 5). A summary concludes the work.

REFERENCES

[1.1]   S. Middelhoek and S.A. Audet, Silicon sensors, Academic Press, London, 1989.

[1.2]   K. Petersen, Silicon as a mechanical material, Proc. IEEE, 70 (1982) 420–457.

[1.3]   C.E. Jowett, The engineering of microelectronic thin and thick films, Macmillan Press Ltd., London, 1976.

[1.4]   S. Middelhoek and J. Van der Spiegel (eds.), Sensors and Actuators: State of the art of sensor research and development, Elsevier Sequoia S.A., Lausanne, 1987.

[1.5]   W. von Ammon and H. Herzer, The production and availability of high–resistivity silicon for detector applications, Nucl. Instr. and Meth., 226 (1986) 94–102.

[1.6]   J. Buechler, E. Kasper, P. Russer and K.M. Strohm, Silicon high–resistivity substrate millimeter–wave technology, IEEE Trans. on Electr. Dev., ED–33 (1986) 2047–2052.

[1.7]   C.D. Fung, P.W. Cheung, W.H. Ko and D.G. Fleming (eds.), Micromachining and micropackaging of transducers, Elsevier, Amsterdam, 1985.

[1.8]   S. Middelhoek and S.A. Audet, Silicon sensors: full of promises and pitfalls, J. Phys. E: Sci. Instr., 20 (1987) 1080–1086.

[1.9]   S.M. Sze, Physics of semiconductor devices, 2nd ed., John Wiley and Sons, New York, 1981.

[1.10]   S.M. Sze (ed.), VLSI Technology, 2nd ed., McGraw Hill, New York, 1988.

[1.11]   P.A. Tipler, Physics, 2nd ed., Worth Publ., New York, 1976.

[1.12]   N.H. de Heathcote, Nobel prize winners in physics $1901 - 1950$, Schuman, New York, 1953.

[1.13]   G. Dearnaley and D.C. Northrop, Semiconductor counters for nuclear radiations, E. & F. Spon Ltd., London, 1964.

[1.14]   B. Culshaw, Photodetectors and photodetection, Sensors and Actuators, 10 (1986) 263–285.

[1.15]   W.H. Tait, Radiation detection, Butterworths, London, 1980.

[1.16]   G.F. Knoll, Radiation detection and measurement, John Wiley and Sons, New York, 1979.

[1.17]   M.C. Peckerar, W.D. Baker and D.J. Nagel, X–ray sensitivity of a charge–coupled device array, J. of Appl. Phys., 48 (1977) 2565–2569.

[1.18]   B.G. Magorrian and N.M. Allinson, Soft X–ray damage in CCD detectors, Nucl. Instr. and Meth., A273 (1988) 599–604.

[1.19]   M.R. Farukhi, $Bi_4GE_3O_{12}$ (BGO) – A scintillator replacement for NaI(Tl), in Nuclear radiation detection materials, E.E. Haller, H.W. Kraner and W.A. Higinbotham (eds.), North–Holland, New York, 1983, 115–130.

[1.20]   P.A. Tove, Review of semiconductor detectors for nuclear radiation, Sensors and Actuators, 5 (1984) 103–107.

[1.21]   D. Itoh, S. Kawamoto, S. Miki, I. Namba and Y. Yatsurgi, Fabrication of ultra high purity silicon single crystals, in Nuclear radiation detection materials, E.E. Haller, H.W. Kraner and W.A. Higinbotham (eds.),

North—Holland, New York, 1983, 47—76.

[1.22]   W. L. Hansen and E.E. Haller, High purity germanium crystal growing, in Nuclear radiation detection materials, E.E. Haller, H.W. Kraner and W.A. Higinbotham (eds.), North—Holland, New York, 1983, 1—16.

[1.23]   P. Siffert, Cadmium telluride detectors and applications, in Nuclear radiation detection materials, E.E. Haller, H.W. Kraner and W.A. Higinbotham (eds.), North—Holland, New York, 1983, 87—114.

[1.24]   J.R. Howes and J. Watling, The fabrication of mercuric iodide detectors for use in wavelength dispersive X—ray analyzers and backscatter photon measurements, in Nuclear radiation detection materials, E.E. Haller, H.W. Kraner and W.A. Higinbotham (eds.), North—Holland, New York, 1983, 207—216.

[1.25]   J.T. Walton and E.E. Haller, Silicon radiation detectors, in Nuclear radiation detection materials, E.E. Haller, H.W. Kraner and W.A. Higinbotham (eds.), North—Holland, New York, 1983, 141—160.

[1.26]   J. Kirz, New Developments in X—ray microscopy, Nucl. Instr. and Meth., A266 (1988) 293—295.

[1.27]   T.A. Callcott, K.—L. Tsang, C.H. Zhang, D.L. Ederer and E.T. Arakawa, Area detectors for X—ray spectroscopy, Nucl. Instr. and Meth., A266 (1988) 578—585.

[1.28]   A.C. Thompson, R. Hofstadter, J.N. Otis, H.D. Zeman, R.S. Kernoff, E. Rubenstein, J.C. Giacomini, H.J. Gordon, G.S. Brown and W. Thomlinson, Transvenous coronary angiography using synchrotron radiation, Nucl. Instr. and Meth., A266 (1988) 252—259.

[1.29]   D.D. Cohen, X—rays from an ^{241}Am source and their relative intensities, Nucl. Instr. and Meth., A267 (1988) 492—498.

[1.30]   A. Heuberger, Comparison of different X—ray sources: X—ray tubes, laser induced plasma sources, compact and conventional storage rings, SPIE, 48 (1983) 8—16.

[1.31]   S. Batter, State of the art of conventional X—ray equipment, IEEE Trans. on Nucl. Sci., NS—27 (1980) 1034—1041.

[1.32]   P. Jaegle, G. Jamelot, A. Klisnick and A. Carillon, Plasma sources and X—ray lasers, SPIE, 733 (1986) 1—14.

[1.33]   P. Choi, A.E. Dangor and C. Deeney, Small gas puff Z—pinch X—ray source, SPIE, 733 (1986) 52—58.

[1.34]   D.J. Nagel, X—ray emission from high—temperature laboratory plasmas, in Advances in X—ray analysis, W.L. Pickles (ed.), Plenum Press, New York, 1974, 1—25.

[1.35]   F. O'Neill, Laser—plasma XUV sources generated by KrF lasers, SPIE, 733 (1986) 15—22.

[1.36]   A. Michette, C.P.B. Hills, A.M. Rogoski and P. Charalambous, Laser plasma sources for scanning X—ray microscopy, SPIE, 733 (1986) 28—33.

[1.37]   M. Chaker, H. Pepin, V. Bareau, S. Boily, B. Lafontaine, R. Fabbro, I. Toubhans, B. Faral, J.F. Currie, D. Nagel and M. Peckerar, Laser created X—ray sources for microlithography, SPIE, 733 (1986) 58—64.

[1.38]   K. Wille, Design considerations for storage rings for synchrotron radiation, in Advances in X—ray analysis, W.L. Pickles (ed.), Plenum Press, New York, 1974, 74—79.

[1.39]   H. Winick and S. Doniach (eds.), Synchrotron radiation research, Plenum Press, New York, 1980.

[1.40]   N.M. Allinson, Solid–state imaging arrays for X–ray detection, Nucl. Instr. and Meth., 201 (1982) 53–64.

[1.41]   S.H. Moseley, R.L. Kelley, J.C. Mather, R.F. Mushotzky and A.E. Symkowiak, Thermal detectors as single photon spectrometers, IEEE Trans. on Nucl. Sci., NS–32 (1985) 134–138.

[1.42]   M. Kuhne and B. Wende, Vacuum UV and soft X–ray radiometry, J. Phys. E. Sci. Instr., 18 (1985) 637–647.

[1.43]   J.P. Kirkland, T. Jach, R.A. Neiser and C.E. Bouldin, PIN diode detectors for synchrotron X–rays, Nucl. Instr. and Meth., A266 (1988) 602–607.

[1.44]   N.M. Allinson, G. Baker, G.N. Greaves and J.K. Nicoll, PDA system for energy dispersive EXAFS, Nucl. Instr. and Meth., A266 (1988) 592–597.

[1.45]   H.–Y. Tsoi, J.P. Ellul, M.I. King, J.J. White and W.C. Bradley, A deep–depletion CCD imager for soft X–ray, visible and near infrared sensing, IEEE Trans. on Electr. Dev., ED–32 (1985) 1525–1530.

[1.46]   J.T. Walton, H.A. Sommer, A.C. Thompson, E.B. Hughes and H.D. Zeman, 300–element silicon–lithium position–sensitive imaging detector for angiography, IEEE Trans. on Nucl. Sci., NS–33 (1986) 537–541.

[1.47]   L. Struder, P. Predehl, M. Meier, C. Reppin, M. Sterzik, G. Lutz, D. Hauff, A. Schwartz, K.F. Schuster, V. Radeka, P.Rehak, S. Rescia, E. Gatti, A. Longoni, M. Sampietro, P. Holl, J. Kemmer, U. Prechtel, T. Ziemann and W. Butler, The MPI/AIT X–ray imager, Proc. 5th European Symposium on Semiconductor Detectors, New Developments in Radiation Detectors, Munich, Feb. 21–23, 1989.

2

THEORY OF HIGH–PURITY SILICON
SOFT X–RAY SENSORS

2.1 INTERACTIONS OF ELECTROMAGNETIC RADIATION WITH SILICON

2.1.1 Introduction

The theoretical operation of high–purity silicon soft X–ray sensors is analyzed in this chapter. Two types of basic elemental structures are examined. Both consist of $p^+-n^--n^+$ diodes realized on high–resistivity silicon. The readout of one group of elemental structures is direct, i.e. via nearly perfect conductors (aluminum) to aluminum bonding pads, while each elemental structure in the second group is first connected in series with a highly–doped polysilicon resistive structure before being connected to an aluminum bonding pad. To confirm the theory, both types of elemental structures were fabricated by the author in the Integrated–Circuit Laboratory at Delft University of Technology with the support of the staff members. The fabrication of the sensors is thoroughly discussed in Chapter 4, while the experimental results are presented in Chapter 5.

Realization of the $p^+-n^--n^+$ diodes involved the fabrication of two junctions on high–resistivity n^-–type silicon substrates: a frontside p^+-n^- junction surrounded by a p^+–guard ring and a backside n^--n^+ high–low junction. The diodes and guard rings were realized through the same frontside boron implantation, while arsenic was implanted on the wafer backsides to fabricate the high–low junctions. The resistive structures were realized through the deposition and doping of polysilicon by low–pressure chemical–vapor deposition (LPCVD) and phosphorous diffusion techniques, respectively. Lithographical techniques were employed to define their geometrical areas.

These sensors are designed to be used for the detection of incident soft X–radiation. The theoretical characterizations below deal primarily with the $p^+-n^--n^+$ diode structures. However, the polysilicon resistive structures are analyzed in all applicable subtopics.

In Sect. 2.1, the interactions of electromagnetic radiation with silicon are discussed. The detection of electromagnetic radiation in high–purity silicon sensors is a two step process. First, the incident radiation must be absorbed within the device. The absorption of electromagnetic radiation in silicon is thoroughly described in Sect. 2.1.2. Free carriers are generated upon the absorption of electromagnetic radiation in silicon. The number of carriers produced per incident photon can be predicted by the quantum yield, which is analyzed in Sect. 2.1.3. The second step involves the collection of the free charge. For optimum collection of generated electrons and holes, the sensors should be placed under reverse–bias conditions. Due to the applied electric field, the electrons and holes will quickly be separated and swept to the n^+- and p^+-contacts, respectively, and collected. The efficiency of the overall detection process is described by the absolute quantum efficiency, the analysis of which is delineated in Sect. 2.1.4.

In Sect. 2.2 the theoretical analyses involved in the operation of the devices are detailed. The most important criteria to optimize in terms of a soft X–ray sensor's performance include the device's leakage current, which necessitates an optimum charge–carrier lifetime, and the device's energy resolution and noise. These topics are theoretically discussed in Sect. 2.2 along with a theoretical description of the charge collection process and the damage incident radiation creates within the device.

The analyses in this section are limited to one dimension, as calculations, Sect. 2.2.5, have shown that the electric fields generated beneath the fully depleted diode structures described above follow one–dimensional theory. This is due to the presence of guard–ring structures, which reduce the effects of junction curvature and prevent the introduction of two–dimensional field effects beneath the fully depleted diode structures.

2.1.2 Absorption

It is important to be aware of all the possible interactions of electromagnetic radiation with silicon in order to understand the proper operation of the radiant sensor, as well as the measurement system as a whole. The interactions concern the attenuation of the incident radiant beam as it penetrates through silicon. The most important interactions of electromagnetic radiation in the light spectrum with silicon include absorption, refraction, transmission, interference and diffraction [2.1]. However, most of these phenomena, with the exception of absorption, play a nonessential role in the detection of electromagnetic radiation in the (soft and hard) X–ray and gamma photon regions due to their high energies and therefore will not be discussed in this text.

Absorption of photons refers to their attenuation by the process of conversion to other forms of energy. When a photon interacts with an atom, part or all of its energy is transferred to that atom depending on the energy of the initial photon.

There are a wide range of absorption interactions that occur between photons and silicon. Some interactions result in the conversion of the photons into electrical charge (the photoelectric effect), while other interactions convert impinging photons into entities that have no net electrical charge (phonons, excitons, etc.). The only phenomena under consideration here will be those involving the absorption of photons in the silicon lattice structure so as to cause the liberation of electron–hole pairs. Upon collection of the charge carriers, the transformation of radiant energy into electrical energy is completed.

When the energy of an incident light photon exceeds silicon's bandgap value E_g, i.e. $h\nu > E_g$, absorption of the photon can take place through the excitation of a valence electron into the conduction band. This is called band–to–band or fundamental absorption and results in the creation of an electron–hole pair. The free electron and hole then become excess carriers and are free to contribute to the conductivity of the material, while they exist in their respective bands.

The maximum wavelength to which silicon can usefully respond is found by equating the photon energy to the bandgap E_g. As E_g decreases with increasing temperature, Sect. 2.2.1, the maximum useful wavelength will therefore increase as the temperature increases [2.2].

$$\lambda_{\max} = hc/E_g \tag{2.1}$$

Intrinsic silicon is generally transparent to electromagnetic radiation of wavelengths longer than $\lambda_{\max}$, but absorption can occur by free carriers in the conduction band moving to higher energy levels upon the absorption of low–energy photons. In pure silicon, this interaction is very weak, because there are so few free carriers.

The photon absorption process is allowed only under strict observation of the laws of conservation of energy and momentum. The energy of the interaction is conserved, in that the magnitude of the energy increase experienced by the valence electron equals that lost by the incident photon. However, the momentum of a photon in the light spectrum ($h\lambda^{-1}$, where λ is on the order of thousands of angstrom), is very small compared to that of an electron or compared to the crystal momentum (ha^{-1}, where a is the lattice constant of a few angstrom).

In order for an incident light photon to excite a valence electron into the conduction band of an indirect semiconductor such as silicon, the electron must change its k–vector, Fig. 2.1. This requires a change in its momentum. Incident photons are not able to provide this momentum. The probability of such an interaction taking place thus depends on the presence of a third particle, called a phonon or a lattice–vibration quantum, in order to conserve momentum [2.2].

Phonons are vibrational–wave particle entities that have relatively small energies compared to the bandgap energy, but have momentum values covering the entire range of electronic transitions within the silicon crystal. Because a relatively smaller change in momentum is required to generate electron–hole pairs of higher energy light photons, absorption increases with increasing photon energy until the direct bandgap energy, approximately 3.4 eV, is achieved. The threshold energy for indirect transitions therefore equals the energy of a phonon having the required momentum ($h\nu_q$) subtracted from the indirect

semiconductor's bandgap energy, i.e. the minimum energy difference between the conduction and the valence bands [2.3]. The absorption coefficient related to indirect transitions α_i is given by [2.3]

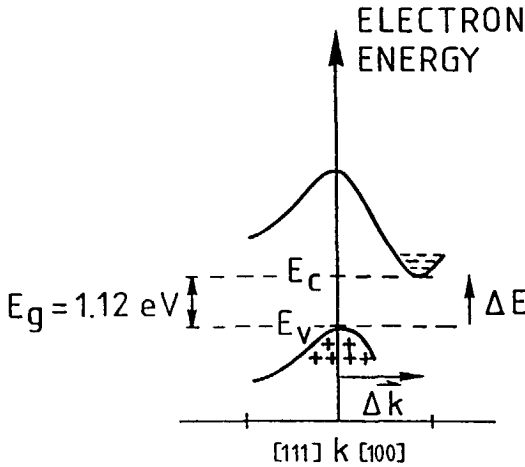$$\alpha_i \propto \left(h\nu - E_g \pm h\nu_q\right)^2 \tag{2.2}$$

Fig. 2.1 *General features of the energy–band structure at 300 K for Si, an indirect bandgap semiconductor* [2.2].

Photons are removed from their incident beam as they penetrate through silicon, interacting with silicon either through absorption or scattering mechanisms, with the result that the intensity of the radiation decreases with distance into the silicon. The decrease in intensity per unit path length is given by

$$\partial \mathscr{I}(x) / \mathscr{I} = \alpha \, \partial x \tag{2.3}$$

where $\mathscr{I}(x)$ is the intensity of the beam at a depth x and α is the absorption coefficient. The value of the absorption coefficient depends on the material under consideration, as well as on the energy of the incident photons, Figs. 2.2 and 2.3 [2.3]. The energy of the incident beam does not decrease with distance, but remains constant. Each interaction is a singular event in which one photon is effectively absorbed or scattered. The attenuation function for a beam with initial intensity $\mathscr{I}_0$ can thus be obtained by solving Eqn. 2.3 [2.3]

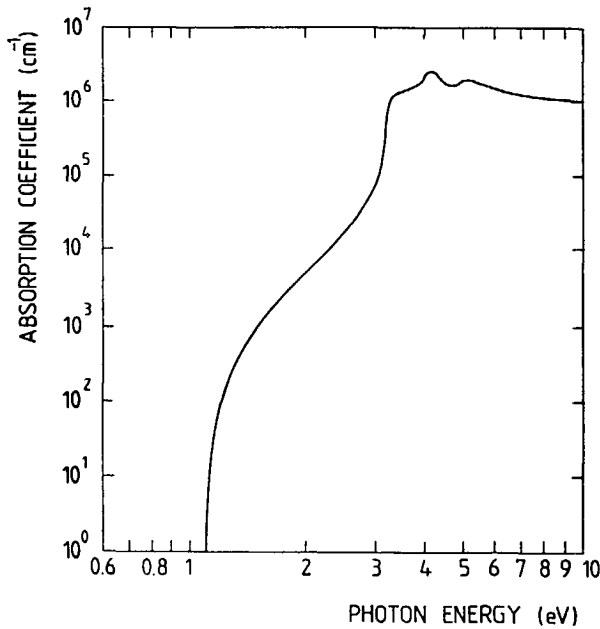$$\mathscr{I}(x) = \mathscr{I}_0 \exp(-\alpha x) \tag{2.4}$$

Fig. 2.2 *Measured absorption coefficients at 300 K for Si as a function of incident photon energy in the range of 0.6 to 10 eV* [2.2].

Photons with higher energies, i.e. soft and hard X—rays and gamma photons, are able to produce direct transitions in silicon. As this requires no third particle interaction, the probability of direct transitions is greater than that for indirect transitions. This explains the rapid increase in the absorption coefficient at approximately 3.4 eV. Interactions of higher energy photons occur with atomic electrons either through absorption or scattering mechanisms. Absorption occurs through one of three main interaction mechanisms, each characterized by its own absorption coefficient: photoelectric absorption (α_{pe}), Compton scattering (α_{cs}) or pair production (α_{pp}). The total absorption coefficient (α_t) is the sum of these three. The process that takes place depends on the incident photon energy, Fig. 2.3 [2.4].

The photoelectric effect dominates at lower energies, from visible light up to approximately 100 keV. If a photon interacts in a photoelectric process, it will transfer all of its energy to an electron (most probably to a K—shell electron) within the interacting atom, Fig. 2.4. This electron is then emitted from the atom with a kinetic energy of ($h\nu - E_b$), where $h\nu$ is the energy of the incident photon and E_b is the binding energy of the K—shell electron [2.5]. This kinetic energy is dissipated by ionization, creating other electron—hole pairs. The interacting atom, being in an excited condition, returns to equilibrium through a cascade of electron transitions from the outer to the inner shells. The total energy liberated by these de—excitation processes, primarily in the form of secondary X—rays, is equal to the binding energy of the K—shell electron, E_b. These X—rays can be

reabsorbed by the photoelectric effect. A separate process, which rarely occurs, termed the Auger effect, involves the transfer of the de–excitation energy to atomic electrons from electron shells with lower energies. These atomic electrons are then emitted instead of the secondary electrons. The total amount of charge created is directly proportional to the energy of the incident radiation, Eqn. (1.2). The absorption coefficient for photoelectric interactions is given by [2.3]

$$\alpha_{\mathrm{pe}} \propto (h\nu)^{-7/2} \rho_{\mathrm{d}} Z^{5} \tag{2.5}$$

where ρ_{d} and Z are the density and the atomic number of the absorbing material, respectively [2.3]. As can be observed in Fig. 2.3, the photoelectric effect dominates the absorption of soft X–rays, i.e. electromagnetic radiation with photon energies between approximately $2 - 25$ keV.
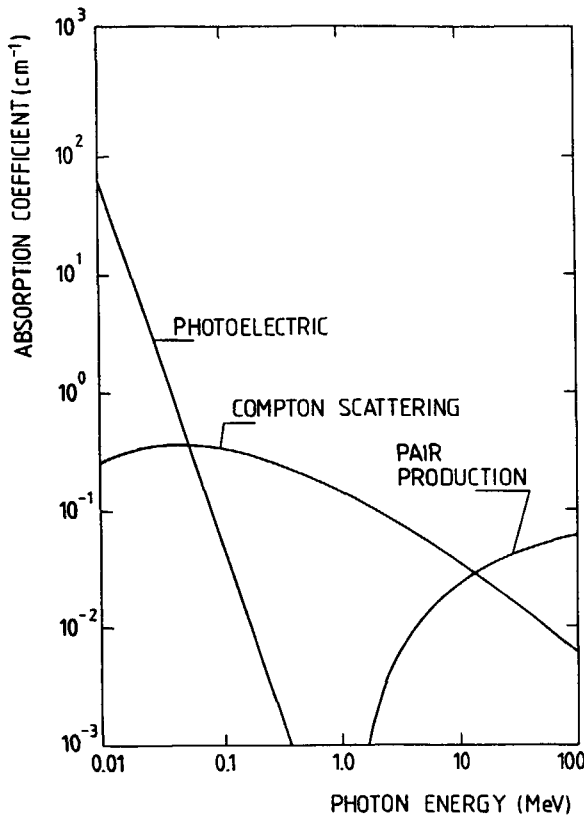

Fig. 2.3 *Measured absorption coefficients at 300 K for Si as a function of incident photon energy in the range of 10 keV to 100 MeV [2.4].*
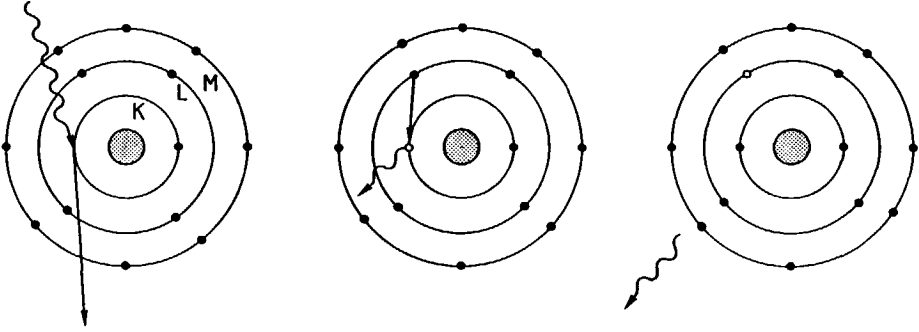
Fig. 2.4 *(a) Incident photon interacting with a K–shell electron. (b) The de–excitation process in which an electron transition occurs from the outer L shell to the inner K shell, (c) which is followed by the emission of a characteristic secondary X–ray photon.*

From 100 keV up to approximately 10 MeV, the Compton process dominates, Fig. 2.3. In this type of interaction, only part of the photon energy is transferred to the electron. The original photon is scattered and decreased in energy. Again, the kinetic energy of this electron will be dissipated by ionization with the resultant creation of electron–hole pairs. The deflected photon can then be reabsorbed through photoelectric or Compton processes or can escape from the silicon [2.5]. The absorption coefficient for the Compton process is given by [2.3]

$$\alpha_{cs} \propto (h\nu)^{-1} \rho_d \tag{2.6}$$

At the highest energies, the production of electron–positron pairs will occur, the creation energy of which is 1.022 MeV. In this interaction, the original photon disappears, while the excess energy is imparted to the electron–positron pair. The electron and positron lose their energy through collisions and eventually come to a rest. The positron then annihilates with an electron from the crystal. This interaction produces two gamma photons, each having an energy of 511 keV, which are emitted in opposite directions. The gamma photons can then be reabsorbed through photoelectric or Compton processes or can escape from the silicon [2.5]. The absorption coefficient for pair production is given by [2.3]

$$\alpha_{pp} \propto \ln[h\nu] \, \rho_d Z^2 \tag{2.7}$$

2.1.3 Quantum yield

The number of free charge carriers generated per incident photon is termed the intrinsic quantum yield and is signified by Q_i. When the energy of incident electromagnetic radiation resides within the light spectrum, but is greater than that associated with the semiconductor's bandgap $(h\nu > E_g)$, one electron–hole pair will be created for each incident photon. The intrinsic quantum yield in this case will equal one [2.5].

When the energy of the incident radiation is greater than approximately 5 eV, $h\nu/\epsilon$ electron–hole pairs will be created for each absorbed photon of energy $h\nu$, where ϵ is termed the ionization energy, which is defined as the average energy necessary to create an electron–hole pair (3.6 eV in Si). With respect to radiation of this kinetic energy, the ionization energy is independent of the photon energy. Therefore, the number of electron–hole pairs generated will be proportional to the incident photon energy, Eqn. (1.2) [2.5].

Inbetween these two regions, i.e. as the incident photon energy increases above the bandgap energy ($E_g = 1.12$ eV in Si) up to approximately 5 eV, the quantum yield will equal unity, but the electron–hole pair generated per incident photon will have additional kinetic energy, which will be dissipated through interactions with the lattice [2.5].

However, a detector is more properly characterized by the effective quantum yield. This is equal to the number of charge carriers successfully transferred out of the device per incident photon. It is signified by Q_e and is always smaller than Q_i due to various loss mechanisms.

2.1.4 Quantum efficiency

The overall detection process not only involves the absorption of incident photons within the radiation sensor and the ensuing charge generation, but also involves the collection of the generated charge. The absolute quantum efficiency, η_a, engrosses the overall process and is defined as the ratio of the number of holes collected to the theoretical number of electron–holes pairs that would be created if all the incident photons emitted from the source were to be converted to electron–hole pairs [2.3].

The sensing device currently under investigation is an abrupt $p^+–n^-–n^+$ diode characterized with a constant substrate doping density of donor impurities N_{dn}^-, a uniform front–surface doping density of acceptor impurities N_{ap}^+, a uniform back–surface doping density of donor impurities N_{dn}^+, a $p^+–n^-$ junction depth x_{pn} and a high–low junction depth x_{hl}, Fig. 2.5. In this figure, x_p and x_n are the extensions of the depletion region into the $p^+–$ and the n^-–regions, respectively, while x_d is the thickness of the entire structure, excluding the metalization layers. Two–dimensional arrays of such diode structures are examined in Chapter 3. The device is assumed to be reverse–biased. Four regions can then be defined within the diode, Fig. 2.5: region i $(0 < x < x_{pn})$; a p^+–type quasi–neutral region on the frontside, region ii $(x_{pn} < x < x_n$); an n^-–type depleted bulk region, region iii $(x_n < x < x_{hl})$; an n^-–type undepleted bulk region and region iv $(x_{hl} < x < x_d)$; an

n^+–type quasi–neutral region on the backside [2.6].

Note that the extension of region *i* to $x = x_{pn}$ is based on the fact that $x_p \approx x_{pn}$, as $N_{ap}^+ >> N_{dn}^-$, i.e. the acceptor concentration in the p^+–region is much greater than the donor concentration in the n^-–region. Given a typical reverse–bias voltage of 75 V, the depletion region will extend only approximately 3 nm into the p^+–region, which typically lies between $200 - 700$ nm below the surface of the device. Therefore, x_{pn} is taken to be approximately equal to x_p.
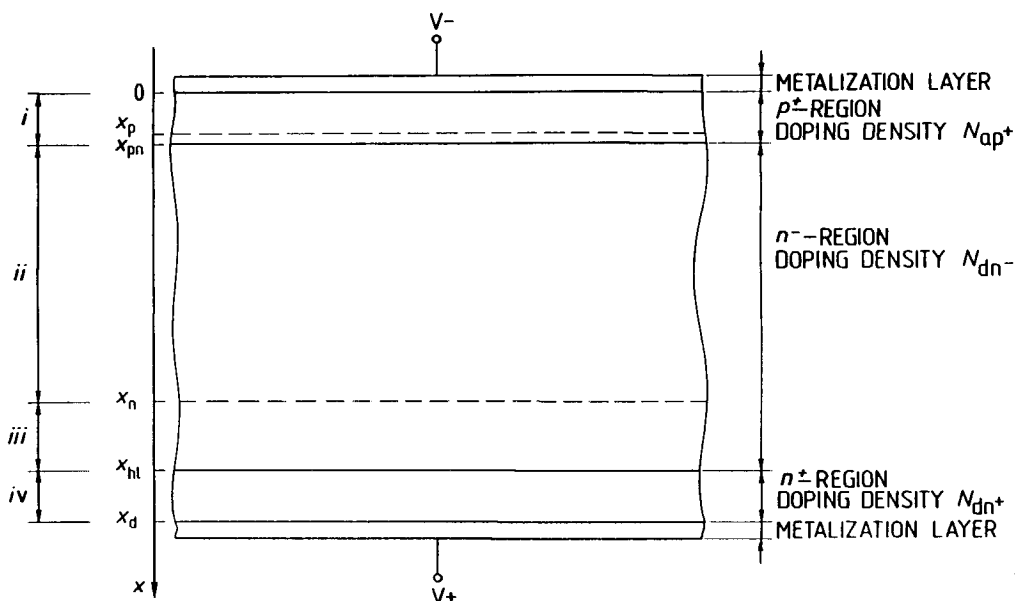

Fig. 2.5 *Generalized structure of a $p^+ -n^- -n^+$ diode indicating doping densities and regional divisions* [2.6].

Although a backside aluminum layer is generally present in standard $p^+-n^--n^+$ diodes, its absence will not significantly reduce the quality of the devices, as long as the high–low junction is present. The sensors and sensor arrays in this work were fabricated without a backside metal layer in order to simplify the processing and in order to allow the backside illumination of the structures. Backside illumination of a fully depleted sensor array provides higher and more uniform responsivity than standard frontside illumination. It also shields the frontside functional layers of the device from radiation damage, depending on the energy and the type of radiation being detected. In addition, if the backside method of illumination is employed, the imaging of photons in the visible and near infrared

regions of the electromagnetic spectrum (400 − 950 nm) also becomes possible.

Abrupt *p–n* junctions can be realized through the use of the ion–implantation method of dopant introduction. The devices described in Sect. 2.1 have been fabricated using a boron implantation on the frontside and an arsenic implantation on the backside. The interface between regions *i* and *ii* therefore forms an abrupt *p⁺–n⁻* junction, while an abrupt high–low junction is formed at the interface between regions *iii* and *iv*.

Mobile electrons and holes generated from electromagnetic radiation absorbed within the depleted bulk region, region *ii*, will quickly drift out of this region toward their respective contacts (the *n⁺*–contact in the case of electrons and the *p⁺*–contact in the case of holes) due to the presence of a strong electric field within this region, which is generated through the application of a reverse–bias voltage. Complete collection of the holes generated within region *ii* is assumed to occur at the front *p⁺*–contact. This assumption is based on exact calculations [2.7]. That charge generated beneath the depletion region however, will not experience a strong electric field and will therefore only slowly diffuse. A fraction of those holes generated within one diffusion length of the depletion region will diffuse to the depletion region and thereafter will be collected. The remainder, and those holes generated further than one diffusion length away from the depletion region, will recombine with majority carriers or will become trapped and therefore will not be collected [2.7].

Complete collection of all holes generated within the device is therefore only guaranteed if the device is fully depleted. For this reason, sensors for the detection of high–energy electromagnetic and nuclear–particle radiation are more efficient when they are fabricated on a substrate material that can easily be fully depleted, i.e. on high–resistivity silicon. When the substrate material is not necessarily high ohmic, but is characterized with a high minority–carrier lifetime and therefore a long minority–carrier diffusion length, Eqn. (1.4b), a high percentage of the generated charge can also be collected, given a sufficient collection time period. However, collection by diffusion is comparatively slow and this would seriously limit the count rate of the device.

$$J_e = q\mu_e n \mathscr{E} + qD_e \frac{\partial n}{\partial x} \tag{2.8a}$$

$$J_h = q\mu_h p \mathscr{E} - qD_h \frac{\partial p}{\partial x} \tag{2.8b}$$

$$\frac{\partial n}{\partial t} = G_e + \frac{1}{q}\frac{\partial J_e}{\partial x} \tag{2.9a}$$

$$\frac{\partial p}{\partial t} = G_h - \frac{1}{q}\frac{\partial J_h}{\partial x} \tag{2.9b}$$

Equations can be obtained for the absolute quantum efficiency within each region by solving the current and continuity equations for electrons and holes, Eqns. (2.8a) and (2.8b), and Eqns. (2.9a) and (2.9b), respectively, (note that all symbols are given in the symbol table) and by assuming a Shockley–Read–Hall recombination mechanism and steady–state conditions [2.8].

The partial quantum efficiencies for each region will now be given, Eqns. (2.10 − 2.12) [2.8]. The total quantum efficiency of the device η_t is the sum of all the regional contributions, i.e. $\eta_t = \eta_p + \eta_{dr} + \eta_n$.

In region i, the partial quantum efficiency η_p equals

$$
\eta_p = \frac{\alpha L_e^2}{1 - \alpha^2 L_e^2} \left\{ \alpha \exp(-\alpha x_{pn}) - \right.
$$

(2.10)

$$
\left. \frac{L_e(s + \alpha D_e) - \exp(-\alpha x_{pn}) [sL_e \cosh(x_{pn}/L_e) + D_e \sinh(x_{pn}/L_e)]}{L_e \{sL_e \sinh(x_{pn}/L_e) + D_e \cosh(x_{pn}/L_e)\}} \right]
$$

given that $x_p \approx x_{pn}$, where s is the surface recombination velocity, L_e is the diffusion length of electrons in the p^+–region and D_e is the diffusion constant of electrons in the p^+–region. Note that region i extends from $(0 < x < x_{pn})$. Following classical approximations [2.8], the quantum efficiency of the quasi–neutral region described in Eqn. (2.10) should include that region which extends from $(0 < x < x_p)$. However, given a typical reverse–bias voltage of 75 V, the depletion region will extend only approximately 3 nm into the p^+–region from the p^+–n junction. Typically, this junction will lie between 200 − 700 nm below the surface. It can therefore be assumed that $x_p \approx x_{pn}$. Note that the depletion region will extend approximately 100,000 times as far, i.e. approximately 300 μm, into the lower doped n^-–region.

In region ii the partial quantum efficiency η_{dr} equals

$$
\eta_{dr} = \exp(-\alpha x_{pn}) - \exp(-\alpha x_n)
$$

(2.11)

given that $x_p \approx x_{pn}$.

In region iii the partial quantum efficiency η_n equals

$$
\eta_n = \frac{\alpha L_h^2}{\alpha^2 L_h^2 - 1} \left\{ \alpha \exp(-\alpha x_n) + \right.
$$

(2.12)

$$
\left. \frac{\exp(-\alpha x_{hl}) - \exp(-\alpha x_n) \cosh[(x_{hl} - x_n)/L_h]}{L_h \sinh[(x_{hl} - x_n)/L_h]} \right]
$$

where L_h and D_h are the diffusion length and the diffusion constant of holes in the n^-–region, respectively. This equation is valid given the assumption that region *iv* and the backside metalization layer form a perfect ohmic contact, i.e. the quantum efficiency within this region is negligible. A more complicated expression is obtained when these points are not assumed, but calculations have shown that the difference in the total quantum efficiency is insignificant.

The absolute quantum efficiencies for six different devices have been calculated and are plotted in Figs. 2.6 and 2.7. The parameter values used in the calculations are given in Table 2.1 [2.10–2.13].

Table 2.1 *Parameter values used in the calculation of η_P, η_{dr} and η_n, Figures 2.6 and 2.7.*

Constant parameter values

D_e	35 cm²/s
D_h	12 cm²/s
s	10 cm/s
x_{Pn}	1 μm
x_{hl}	370 μm

Variable parameter values

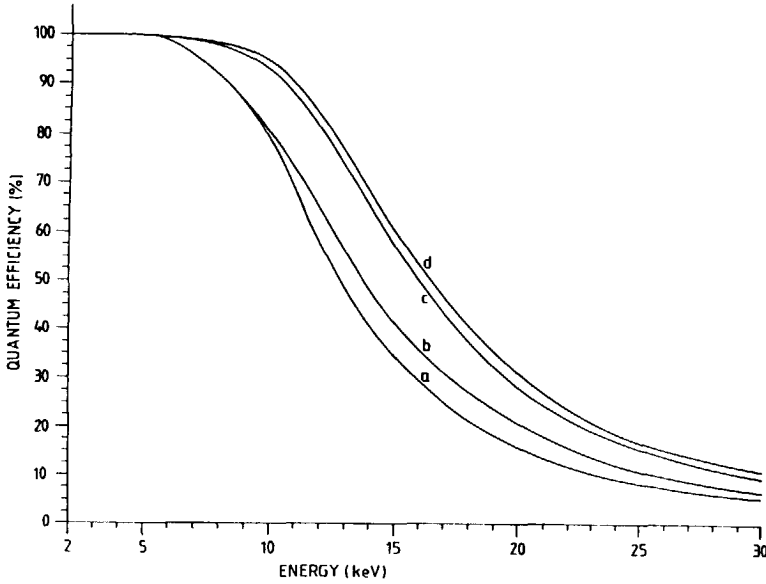|	τ_e [μs]	τ_h [μs]	L_e [μm]	L_h [μm]	N_d [cm⁻³]	V_b [V]	x_n [μm]
Figure 2.6 (a)	10	10	187	109.5	1 x 10¹²	5	85
Figure 2.6 (b)	500	500	1320	775	1 x 10¹²	5	85
Figure 2.6 (c)	500	500	1320	775	1 x 10¹²	75	313
Figure 2.6 (d)	500	500	1320	775	1 x 10¹²	125	370
Figure 2.7 (a)	10	10	187	109.5	1 x 10¹⁴	5	8.5
Figure 2.7 (b)	500	500	1320	775	1 x 10¹⁴	5	8.5

Fig. 2.6 *Calculated quantum efficiencies for devices fabricated on (a) high–ohmic silicon with a low lifetime under a low reverse–bias voltage, (b) high–ohmic silicon with a high lifetime under a low reverse–bias voltage, (c) high–ohmic silicon with a high lifetime under a medium reverse–bias voltage and (d) high–ohmic silicon with a high lifetime under a high reverse–bias voltage.*
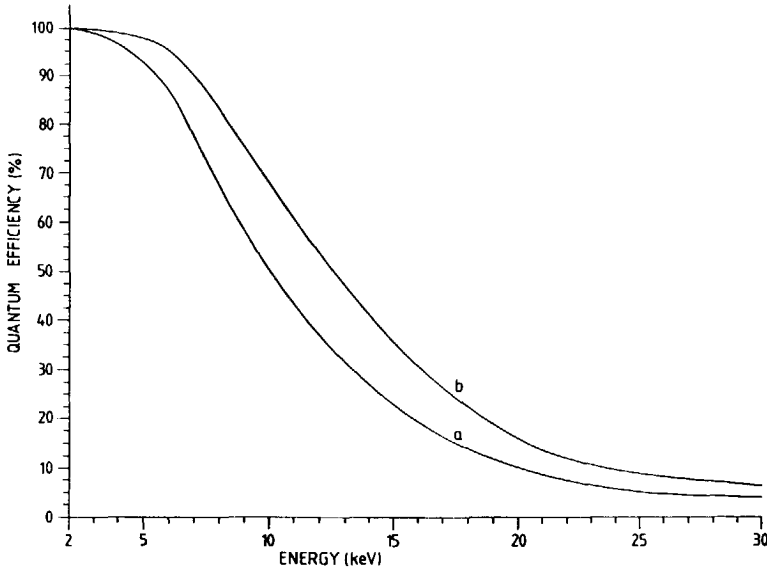

Fig. 2.7 *Calculated quantum efficiencies for devices fabricated on (a) low–ohmic silicon with a low lifetime under a low reverse–bias voltage and (b) low–ohmic silicon with a high–lifetime under a low reverse–bias voltage.*

As can be observed in Figs. 2.6 and 2.7, devices fabricated on high–ohmic silicon ($N_d = 1 \times 10^{12}$ cm^{-3}) consistently have higher quantum efficiencies than those fabricated on standard ohmic silicon ($N_d = 1 \times 10^{14}$ cm^{-3}). In addition, as the reverse bias across the device increases, the partial quantum efficiency η_{dr} increases and as the minority–carrier lifetime increases, the partial quantum efficiency η_n increases, both of which cause the total quantum efficiency η_t to increase. Note that the magnitude of the reverse–bias voltage that can safely be placed across devices fabricated on standard ohmic silicon is limited by the breakdown phenomenon, Sect. 4.2, while a relatively high reverse–bias voltage can be placed across devices fabricated on high–ohmic silicon.

These calculations have been performed with the assumption that no absorbing materials cover the exposed surfaces of the devices. However, in many standard electromagnetic radiation detectors, a thin layer of silicon dioxide is present over the exposed surface in order to protect the device from surface contamination. The wavelength dependence of the absorption coefficient of silicon dioxide is similar to that of silicon, but its magnitude is slightly larger [2.9]. The presence of a 1 μm thick layer of silicon dioxide will theoretically decrease the quantum efficiency of a silicon electromagnetic radiation sensor in the spectral regions with energies less than 6 keV by a factor of five to ten, while a 3 μm thick layer of SiO$_2$ will theoretically decrease the quantum efficiency in these areas by a factor of ten to ten thousand [2.9]. When the energy of the incident radiation is above approximately 10 keV, the presence of a SiO$_2$ layer makes little difference [2.9]. The presence of one or two aluminum layers will however cause an attenuation of the incident beam intensity. If the device is operated in the fully depleted mode of operation, backside illumination of a device fabricated without a backside metal layer can solve this problem.

The detector quantum efficiency, η_d, is a more fundamental design parameter than the absolute quantum efficiency for one– and two–dimensional radiation sensors. It is defined as the absolute quantum efficiency divided by the effective quantum yield, i.e. η_a/Q_e, and equals the ratio of interacting photons to incident photons per pixel [2.3].

2.2 THEORY OF HIGH–PURITY SILICON SOFT X–RAY SENSORS

2.2.1 Leakage current

The leakage or reverse current of a reverse–biased p^+–n^-–n^+ junction diode is that current that flows in the absence of any incident radiation source whatsoever. The leakage current greatly influences the operating characteristics of a silicon soft X–ray sensor. The leakage current increases the device noise and deteriorates the energy resolution of the sensor. In attempting to limit or reduce the total leakage current, it is important to understand its elemental composition, as well as the origin and magnitude of each elemental contribution. In this section, the elemental composition of the leakage current in high–purity silicon soft X–ray sensors is first described, followed by the derivation of theoretical expressions for each component and their relative contributions to the

total leakage current.

The leakage current is expressed as the sum of four regional current contributions, Fig. 2.5, which originate from three sources: surface leakage, thermal generation in the depletion region and thermal generation in undepleted regions [2.10].

Surface leakage current originates from surface charge generated through interface states and Tamm defects existing at the surface and from surface contamination. The surfaces of radiation detectors are passivated, most commonly with a thermal silicon dioxide layer, in order to reduce the number of surface states and thus the amount of surface charge generated. The degree of surface state reduction depends on the technique used to fabricate the passivation oxide layer.

There are four types of charge associated with oxide films: mobile ionic charge, oxide trapped charge, fixed oxide charge and interface trapped charge [2.11]. The mobile ionic charge originates from alkali ions (e.g. Na^+ and K^+) and heavy metal ions. Electrons and holes, trapped in the bulk of the oxide layer, are the sources of oxide trapped charge [2.11]. This charge may originate from defects in the oxide layer or from exposure of the device to radiation, avalanche injection or high currents. If the processing is well–controlled, i.e. if the thermal oxidation is performed in an atmosphere containing $1-6\%$ Cl^- ions in the form of HCL or TCE, the original concentrations of mobile ionic charge and oxide trapped charge will be insignificant [2.12]. Thermal treatments at low temperatures have been shown to effectively anneal the externally induced oxide trapped charge [2.11].

The fixed oxide charge is almost always positive and is located in the oxide layer within approximately 3 nm from the Si/SiO_2 interface [2.11]. It originates from incomplete oxidation near this interface, which creates silicon dangling bonds. This charge density is related to the oxidation process itself and cannot be charged or discharged. The (111)–crystal orientation will have a higher concentration of fixed oxide charge than the (100)–crystal orientation due to the greater density of silicon bonds at that surface [2.13]. In addition, the wet thermal oxidation technique tends to be associated with a higher concentration of fixed positive charges than does the dry thermal oxidation technique, as wet thermal oxidation is a rapid process resulting in relatively porous films. However, it is the last temperature treatment, usually an anneal step performed at $400-500$ ℃, that primarily determines the final fixed oxide charge density [2.11].

The interface trapped charge can be positive or negative and is associated with energy states lying within the forbidden bandgap of silicon. The origins of interface trapped charge include structural defects related to the oxidation procedure, metallic impurities and bond breaking procedures [2.11]. This charge density can be reduced by charge–center neutralization in a 10% hydrogen atmosphere. After neutralization, positive fixed oxide charges will dominate the influence surface leakage currents have on the total leakage current [2.11]. These positive fixed oxide charges will attract electrons to the surface. In p^+-n-n^+ junction devices, this situation is desirable, as individual strip or pixel diodes become isolated from their neighbors, which allows the possibility of fabricating a device with one– or two–dimensional position resolution, respectively. In addition, the presence of p^+–guard rings surrounding the p^+-n^- diodes will prevent surface currents originating outside the diode area from reaching this region when the guard rings are placed at the same reverse–bias potential as the diodes [2.11].

Oxide films however, are not good barriers to the diffusion of mobile ions, i.e.

Na$^+$ and K$^+$. Additional passivation layers of silicon nitride and phosphorous glass will eliminate this migration and protect the device from contamination once it is fabricated.

The second source arises from the thermal generation of carriers within the depletion region. Thermal generation occurs due to the existence of recombination centers, which are created from the presence of impurity atoms or structural imperfections [2.10]. To minimize this current contribution, homogeneous, high–resistivity, monocrystalline silicon substrates, which have minimal concentrations of bulk charge–trapping centers, should be employed.

Diffusion leakage currents arise from minority carriers generated within one diffusion length of the depletion layer or from carriers injected from the backside contact, when this contact is within one diffusion length of the depletion layer. These carriers will then diffuse to the depletion region and become collected [2.14]. However, high–resistivity silicon contains a low number of generation–recombination centers, which will limit the degree of minority–carrier generation. In addition, the diffusion length of the minority carriers can be decreased through the presence of a high–low junction on the backside, which also prevents minority–carrier injection from the back contact. Moreover, high–purity silicon soft X–ray sensors are most often employed in the fully depleted state. In this case, diffusion currents can essentially be neglected.

An analytical expression for the leakage current of the device can be derived through the use of the current and continuity equations for electrons and holes, Eqns. (2.8a) and (2.8b) and Eqns. (2.9a) and (2.9b), respectively. For this analysis, the diode is again divided into four regions, Fig. 2.5. The surface current described above originates from surface generation at the front surface, from minority–carrier injection at the back surface and from minority–carrier reflection at the high–low junction between regions *iii* and *iv*. The thermal generation current in the depletion region only originates from region *ii*, as it is the only depleted region. Diffusion currents will arise from regions *i*, *iii* and *iv*, as these regions are quasi–neutral, undepleted regions. However, thermal generation of carriers occurs within each region. The total leakage current is therefore the sum total of the current contributions from each region.

In deriving the thermal generation current in the depletion region, it is first assumed that the generation rate is uniform throughout this region. The generation current then equals [2.7]

$$I_{\mathrm{ii}} = qAx_{\mathrm{dr}}G \tag{2.13}$$

where q is the electronic charge, A and x_{dr} are the area and width of the depletion region with x_{dr} equal to $(x_{\mathrm{n}} - x_{\mathrm{p}})$, Fig. 2.5, and G is the generation rate. This rate in an n–type silicon substrate under dark, low–field conditions is given by [2.7]

$$G = \frac{v_{\mathrm{th}}\sigma_{\mathrm{e}}\sigma_{\mathrm{h}}N_{\mathrm{t}}\left(n_{\mathrm{i}}^2 - n_{\mathrm{n}}p_{\mathrm{n}}\right)}{\sigma_{\mathrm{h}}\left[p_{\mathrm{n}} + n_{\mathrm{i}}\exp\left[\dfrac{-(E_{\mathrm{t}} - E_{\mathrm{i}})}{kT}\right]\right] + \sigma_{\mathrm{e}}\left[n_{\mathrm{n}} + n_{\mathrm{i}}\exp\left[\dfrac{(E_{\mathrm{t}} - E_{\mathrm{i}})}{kT}\right]\right]} \tag{2.14}$$

where all the symbols are defined in the symbol table. Note that $(|E_t - E_i|)$ is the energy difference between the energy level of the traps and the intrinsic Fermi level. Equation. (2.14) is the Shockley–Read–Hall (SRH) expression for generation via localized states. In the case of recombination, $R = -G$ [2.7].

This expression can be simplified if a number of points are taken into consideration. In the depleted region of an n–type silicon substrate, there are few free carriers and therefore, p_n and $n_n \approx 0$. Furthermore, if τ_{ho} and τ_{eo} are defined as $(\nu_{th}\sigma_h N_t)^{-1}$ and $(\nu_{th}\sigma_e N_t)^{-1}$, respectively, the rate of thermal generation in the depletion region can be obtained. Under the assumption that the traps are either uniformly distributed through the bandgap or have their energy level at the midgap,

$$G = -R = \frac{n_i}{\tau_{eo} \exp\left[\dfrac{-(E_t - E_i)}{kT}\right] + \tau_{ho} \exp\left[\dfrac{(E_t - E_i)}{kT}\right]} \tag{2.15a}$$

$$= \frac{n_i}{\tau_g} \tag{2.15b}$$

where

$$\tau_g = \tau_{eo} \exp\left[\frac{-(E_t - E_i)}{kT}\right] + \tau_{ho} \exp\left[\frac{(E_t - E_i)}{kT}\right] \tag{2.16}$$

Therefore,

$$I_{ii} = qA x_{dr} n_i / \tau_g \tag{2.17}$$

However, this result must be slightly modified. It has been revealed through different analyses of p–n junctions that thermal generation of carriers occurs in a volume whose width, x_g, is slightly less than the width of the depletion layer [2.15]. This generation zone is situated in the center of the depletion layer. Recombination within the generation zone can be neglected, as no free carriers exist within this region. At both the upper and lower interfaces of the depletion region however, recombination is seen to increase, as the number of free carriers (p_n or n_n) is seen to increase, which results in a decrease within these edge regions in the net generation [2.15].

The trap energy level in these edge regions E_t' differs from that level in the generation zone, E_t. When $|E_t'| > |E_{qn,p}|$, where E_{qn} and E_{qp} are the quasi–Fermi energy levels on the n– and p–side, respectively, the recombination of holes or electrons, depending on the particular interface in question, increases. The edges of the generation zone can be determined. The n–concentration at one border is derived from the generation rate equation, Eqn. (2.14), and the

p–concentration at the other border can similarly be interpreted [2.15].

If x, Fig. 2.5, is situated within the depletion region so that the hole concentration satisfies the inequality

$$p_n(x) < n_i \exp\left[\frac{-(E_t - E_i)}{kT}\right] \tag{2.18}$$

and

$$G = \frac{n_i^2}{\tau_{eo}\left[n_i \exp\left[\frac{-(E_t - E_i)}{kT}\right]\right] + \tau_{ho}\left[n_n + n_i \exp\left[\frac{(E_t - E_i)}{kT}\right]\right]} \tag{2.19}$$

and if, in addition, the electron concentration $n_n(x)$ satisfies the condition

$$n_n(x) < \frac{\tau_{eo}\left[n_i \exp\left[\frac{-(E_t - E_i)}{kT}\right]\right] + \tau_{ho}\left[n_i \exp\left[\frac{(E_t - E_i)}{kT}\right]\right]}{\tau_{ho}} \tag{2.20}$$

then

$$G = \frac{n_i^2}{\tau_{eo}\left[n_i \exp\left[\frac{-(E_t - E_i)}{kT}\right]\right] + \tau_{ho}\left[n_i \exp\left[\frac{(E_t - E_i)}{kT}\right]\right]} \tag{2.21}$$

and the condition for net generation will be satisfied [2.15]. When Eqn. (2.20) becomes an equality, the border between a region in which net recombination can be ignored and a region where this is not the case can be defined. The *n*–concentration at one border has thus been derived from the generation rate equation. The *p*–concentration at the other border can similarly be derived. The borders are therefore determined by the electron and hole concentrations [2.15]

$$n_n(x = x_{bn}) = \frac{\tau_{eo}\left[n_i \exp\left[\frac{-(E_t - E_i)}{kT}\right]\right] + \tau_{ho}\left[n_i \exp\left[\frac{(E_t - E_i)}{kT}\right]\right]}{\tau_{ho}} \tag{2.22}$$

$$p_n(x = x_{bp}) = \frac{\tau_{eo}\left[n_i \exp\left[\frac{-(E_t - E_i)}{kT}\right]\right] + \tau_{ho}\left[n_i \exp\left[\frac{(E_t - E_i)}{kT}\right]\right]}{\tau_{eo}} \qquad (2.23)$$

If x_{bp} and x_{bn} are defined to mark the upper and lower borders, respectively, the width of the generation zone, x_g, is equal to, Fig. 2.5

$$x_g = (x_{bn} - x_{bp}) \qquad (2.24)$$

Eqn. (2.17) must therefore be modified to take this into consideration

$$I_{ii} = qAx_g\, n_i/\tau_g \qquad (2.25)$$

Regions *i*, *iii* and *iv* all contribute diffusion currents. These diffusion currents consist of two components: that arising from thermal generation in the quasi–neutral part and that arising from the surface. The surface component originates from surface generation at the front surface, from minority–carrier injection at the back surface and from minority–carrier reflection at the interface between regions *iii* and *iv* (i.e. at the high–low junction). If regions *iii* and *iv* are considered together (region *iii,iv*), a similar expression can be derived for the leakage–current originating from region *i* as that originating from region *iii,iv*. This current will first be derived for region *iii,iv* and then modified to provide an expression for the leakage current associated with region *i*.

The diffusion currents in both regions *iii* and *iv* are determined by the diffusion of the minority carriers, i.e. the diffusion of the holes, within these regions. An interface, i.e. the high–low junction, exists between these two regions. When an effective surface generation velocity s^* is introduced, which encompasses effects arising from the reflecting properties of the high–low junction, as well as the effects contributed from the backside surface, the diffusion current contributions of the two regions can simultaneously be derived.

This effective surface generation velocity can be modeled. First, the reflecting properties of the high–low junction have to be taken into account, as the minority–carrier concentration is reduced when going from the n–side to the n^+–side of the high–low junction. Assuming that the change in the minority–carrier (hole) quasi–Fermi level is negligible across the interface and that charge neutrality exists at the edges of the junction [2.6]

$$p_n{}^+ = p_n{}^- \left[1 + \frac{p_n{}^-}{N_{dn}{}^-}\right] \frac{N_{dn}{}^-}{N_{dn}{}^+} \qquad (2.26)$$

where all symbols are given in the symbol table. In the case of relatively low

injection of minority carriers from the n^-– to the n^+–side, Eqn. (2.26) simplifies to [2.6]

$$p_n^+ = p_n^- \left[\frac{N_{dn}^-}{N_{dn}^+} \right] \tag{2.27}$$

The effective surface generation velocity depends on the width of the n^+–region and the minority–carrier (hole) lifetime within this region. For uniform doping within the n^+–region and relatively low concentrations of excess carriers, the effective surface generation velocity is defined as [2.6]

$$s^* = \frac{D_{hn}^+}{L_{hn}^+} \frac{p_n^+}{p_n^-} \left[\coth \left[\frac{x_d - x_{hl}}{L_{hn}^+} \right] \right] \tag{2.28}$$

where p_n^+/p_n^- is given by Eqn. (2.26) in general and by Eqn. (2.27) in the case where the minority–carrier injection is relatively low. Given the latter situation, Eqn. (2.28) then becomes

$$s^* = \frac{D_{hn}^+}{L_{hn}^+} \frac{N_{dn}^-}{N_{dn}^+} \left[\coth \left[\frac{x_d - x_{hl}}{L_{hn}^+} \right] \right] \tag{2.29}$$

The diffusion current in region iii,iv is given by the derivative of the minority–carrier concentration at the edge of the depletion layer [2.14]

$$I_{iii,iv} = qAD_h \left. \frac{\partial p}{\partial x} \right|_{x_{dr}} \tag{2.30}$$

This is calculated by solving the current and continuity equations for electrons and holes, Eqns. (2.8a) and (2.8b) and Eqns. (2.9a) and (2.9b), respectively. The diffusion current can be written as [2.15–2.18]

$$I_{iii,iv} = \frac{qA\Delta p(x_{dr})D_{hn}^-}{L'} \tag{2.31}$$

where

$$L' = L_{hn}^- \frac{(s^* L_{hn}^-/D_{hn}^-) \sinh \alpha^* + \cosh \alpha^*}{\sinh \alpha^* + (s^* L_{hn}^-/D_{hn}^-) \cosh \alpha^*} \tag{2.32}$$

and

$$\alpha^* = \frac{x_d - x_n}{L_{hn}^-} \tag{2.33}$$

and where $\Delta p(x_{dr})$ is the deviation of the hole concentration at the interface of regions *ii* and *iii* from its equilibrium value, s^* is the effective surface generation velocity, L_{hn}^- is the diffusion length for holes in region *iii*, D_{hn}^- is the diffusion constant for holes in region *iii* and $(x_d - x_n)$ is the total width of the regions *iii* and *iv*. Note that $\Delta p(x_{dr})$ increases with increasing reverse–bias voltage and reaches a maximum of $p_n^- = (n_i^2/N_{dn}^-)$.

In the case where the regional width $(x_d - x_n)$ is much greater than the diffusion length of holes in region *iii*, L_{hn}^-, i.e. $\alpha^* \gg 1$, that part of the generation current originating from minority–carrier injection from the backside becomes negligible. The expression for the leakage current in this region, Eqn. (2.31) can then be simplified [2.15]

$$I_{iii,iv} = \frac{qA \Delta p(x_{dr}) D_{hn}^-}{L_{hn}^-} \tag{2.34}$$

When the diffusion length of holes in region *iii* is long compared to the regional width, i.e. $\alpha^* \ll 1$, as is typically the case in high–resistivity silicon substrates, minority–carrier injection may now influence the leakage current. Further simplifications of Eqn. (2.31) can be obtained when this condition is taken into consideration together with a very high effective surface recombination velocity, Eqn. (2.35), or a very low effective surface generation velocity, Eqn. (2.36) [2.15–2.16].

$$I_{iii,iv} = \frac{qA \Delta p(x_{dr}) D_{hn}^-}{(x_d - x_n)} \tag{2.35}$$

$$I_{iii,iv} = \frac{qA \Delta p(x_{dr}) (x_d - x_n) D_{hn}^-}{(L_{hn}^-)^2} \tag{2.36}$$

In region *i*, the leakage current is also given by Eqn. (2.31), where all the parameters will be those of region *i* and s^* will now equal the frontside surface generation velocity. In this case however, the regional diffusion length is generally

greater than the regional width, especially if thin junctions $(100 - 200$ nm$)$ are fabricated through ion–implantation. If in addition, an infinite surface generation velocity, a constant doping profile and no degeneracy effects are taken into account, the leakage current contribution can be equated to Eqn. (2.35), with the parameters changed to equal those of region i [2.15]

$$I_i = \frac{qAn_p^+D_{ep^+}}{x_{pn}} \tag{2.37}$$

The total current will be the sum of the partial current contributions

$$I_t = I_i + I_{ii} + I_{iii,iv} \tag{2.38}$$

Table 2.2 *Parameter values used in calculating I_i, I_{ii} and $I_{iii,iv}$.*

A	1 cm²
D_{ep^+}	10 cm²/s
D_{hn^+}	2.0 cm²/s
D_{hn^-}	12.5 cm²/s
L_{hn^+}	10 μm
L_{hn^-}	448 μm
n_i	1.4 x 10¹⁰ cm⁻³
n_p^+	19.6 cm⁻³
N_{ap^+}	1 x 10¹⁹ cm⁻³
N_{dn^+}	1 x 10¹⁹ cm⁻³
N_{dn^-}	1 x 10¹² cm⁻³
q	1.6 x 10⁻¹⁹ C
x_{dr}	100 μm
$(x_d - x_n)$	280 μm
x_{pn}	1 μm
$\Delta p(x_{dr})$	1.96 x 10⁸ cm⁻³
τ_{ep^+}	0.5 μs
τ_{hn^+}	0.5 μs
τ_g	1 ms
τ_r	160 μs

In general, if the processing of the diode is well–controlled, the greatest contribution to the total leakage current in high–resistivity silicon p^+–n^-–n^+

diodes will be due to thermal generation in region *ii*, i.e. it will arise due to thermal generation in the depletion region. This statement can be verified and an insight into the significance of each current contribution can be obtained by calculating each regional contribution given the necessary data [2.13].

Values have been given for each parameter in Table 2.2. In addition, the area A is given to be 1 cm² and the generation zone is assumed to be equal to the width of the depletion region. For standardization purposes, the depletion depth used in the calculation of I_{ii} is 100 μm. The regional current contributions per cm² per 100 μm depletion depth can then be calculated for this region. The theoretical value may then be compared with the experimental values presented in Chapter 5. Note that the value for the lifetime in the undepleted bulk, i.e. τ_r, which is used to calculate the minority–carrier diffusion length in region *iii*, L_{hn}^-, is taken to be the experimentally measured value, Sect. 5.2.3. All other parameter values have been either specified by the manufacturer of the high–purity silicon or obtained from the semiconductor data handbook [2.13].

Upon calculation, one finds that the current contribution for region *i* is less than 1 pA and can therefore be considered negligible. Note that the assumptions made, which led to the equation for the current contribution from region *i*, Eqn. (2.37), are valid. The minority–carrier diffusion length in this region (22 μm) is much greater than the regional width (1 μm), and high values for the surface recombination velocity s^* ensue, as the front surface of the (111)–oriented (i.e. associated with a relatively large number of surface states) high–purity silicon soft X–ray sensor is not covered with an oxide layer.

Calculation of the current contribution from region *ii* is straight forward and, using the parameter values given in Table 2.2, is equal to 22.4 nA/cm² per 100 μm depletion depth.

It can be shown that the presence of a high–low junction on the backside of the sensor and the presence of a low number of generation–recombination centers in the undepleted bulk, i.e. a long recombination lifetime, significantly diminish region *iii,iv*'s contribution to the total leakage current.

When a high–low junction is present, the effective minority–carrier diffusion length is diminished and minority–carrier injection from the back contact is avoided. These factors lead to a very low value (2 x 10⁻⁴ cm/s) of the effective surface recombination velocity s^*, Eqn (2.29). When this parameter is normalized through the multiplication of s^* by the factor (L_{hn}^-/D_{hn}^-), which occurs in the derivation of the current contribution of region *iii,iv*, Eqn. (2.32), the normalized effective surface recombination velocity is equal to 7.2 x 10⁻⁷.

In addition, when there are a low number of generation–recombination centers in the undepleted bulk, i.e. when the recombination lifetime is very long, then the minority–carrier diffusion length in the undepleted bulk region, $(L_{hn}^- = \sqrt{\tau_r D_{hn}^-})$ will increase. If it is much greater than the regional width, then $\alpha \ll 1$. Under these two conditions, Eqn. (2.36) becomes valid. From this equation, it can be seen that the higher L_{hn}^- is, the lower region *iii,iv*'s contribution to the total leakage current will be. Using that experimentally measured value of the recombination lifetime, Sect. 5.2.3, and a fully reverse–biased sensor, a current on the order of a nanoampere per centimeter squared will arise from this region.

Under the conditions mentioned above, the greatest contribution to the total theoretical reverse current therefore arises from thermal generation in region *ii*, i.e. from thermal generation in the depletion region.

As the temperature of the high–resistivity silicon sensor is increased, the

number of thermally generated carrier pairs contributed by the silicon atoms increases, whereas the number of carrier pairs contributed by the impurities remains constant. The leakage current increases with increasing temperature due to increased generation in the depletion region and diffusion from the neighboring undepleted regions to the depletion region. The dependence of the leakage current on temperature is revealed by examining all the temperature dependent parameters affecting the total leakage current, which includes all the temperature dependent parameters of the generation–dependent leakage current, i.e. I_{ii} Eqn. (2.25), as well as those of the diffusion–dependent leakage currents, essentially $I_{iii,iv}$ Eqn. (2.36), as I_i Eqn. (2.37) was shown to be negligible. From Eqns. (2.25) and (2.36), those temperature–dependent parameters are seen to include the intrinsic carrier concentration n_i, the electron concentration n, the change in the hole concentration from its equilibrium value at the depletion–region edge $\Delta p(x_{dr})$, the generation lifetime τ_g, the diffusion constants $D_{e,h}$ and the diffusion lengths $L_{e,h}$.

The intrinsic carrier concentration is given by [2.7]

$$n_i{}^2 = np \tag{2.39a}$$

$$= N_c N_v \exp(-E_g/kT) \tag{2.39b}$$

$$= 4 \left[\frac{2\pi m_n{}^* kT}{h^2} \right]^{3/2} \left[\frac{2\pi m_p{}^* kT}{h^2} \right]^{3/2} \exp(-E_g/kT) \tag{2.39c}$$

$$= BT^3 \exp(-E_g/kT) \tag{2.39d}$$

where B is a constant, and therefore

$$n_i = BT^{3/2} \exp(-E_g/2kT) \tag{2.40}$$

It is now clear that n_i is a very sensitive function of T and E_g (which is also dependent on T). The bandgap in silicon depends on temperature according to [2.7]

$$E_g = 1.17 - \frac{(4.73 \times 10^{-4}) T^2}{(T + 636)} \tag{2.41}$$

Parameters that are less significantly affected by temperature include the electron concentration n, the change in the hole concentration from its equilibrium value at the depletion–region edge $\Delta p(x_{dr})$, the generation lifetime τ_g, the diffusion constants $D_{e,h}$ and the diffusion lengths $L_{e,h}$.

At high temperatures, the low–doped silicon substrate becomes intrinsic. The

electron concentration of the substrate can be determined from the fact that the electron concentration times the hole concentration equals the intrinsic carrier concentration squared, Eqn. (2.39a), and that it also equals the doping concentration N plus the hole concentration p. Therefore,

$$n = \frac{N + (N^2 + 4n_i^2)^{1/2}}{2} \tag{2.42}$$

The electron concentration no longer equals the doping concentration alone, as it is taken to equal at room temperature. The change in the hole concentration from its equilibrium value at the depletion–region edge $\Delta p(x_{dr})$ must now be given as (where n is given by Eqn. (2.42))

$$\Delta p(x_{dr}) = \frac{n_i^2}{n} \tag{2.43}$$

The generation lifetime exponentially depends on the difference between the trap and intrinsic energy levels, Eqn. (2.16), which will be repeated here for convenience

$$\tau_g = \tau_{eo} \exp\left[\frac{-(E_t - E_i)}{kT}\right] + \tau_{ho} \exp\left[\frac{(E_t - E_i)}{kT}\right] \tag{2.44}$$

As the bandgap shrinks with increasing temperature, the difference between these two energy levels will be affected. The parameters τ_{eo} and τ_{ho}, defined to equal $(N_t v_{th} \sigma_e)^{-1}$ and $(N_t v_{th} \sigma_h)^{-1}$, respectively, also depend on temperature due to the change in the capture cross section with temperature. Impurity scattering increases as the temperature increases, which decreases the distance, $r_{e,h}$, necessary for effective impurity scattering to occur. This distance is inversely proportional to temperature, i.e. $r_{e,h} \propto T^{-1}$. Therefore, the scattering cross section of the impurities $\sigma_{e,h}$, given by $\pi(r_{e,h})^2$, will decrease with increasing temperature according to T^{-2} and the parameters τ_{eo} and τ_{ho}, inversely proportional to the scattering cross sections, will increase with temperature according to T^2.

From Einstein's equation, the diffusion constants depend on the carrier mobilities according to

$$D_{e,h} = \frac{kT}{q} \mu_{e,h} \tag{2.45}$$

where the mobilities in turn depend on temperature. Carrier mobilities are influenced by lattice and impurity scattering, both of which have a temperature dependence, but in opposing manners. Lattice vibrations increase in magnitude as the temperature increases, which makes the mean free path of a carrier between lattice scattering events decrease as the temperature increases. As the mean free path of a carrier between lattice scattering events is directly proportional to the mobility due to lattice scattering events, it will also decrease as the temperature increases. The dependence of the mobility on lattice scattering alone, μ_l, is given by

$$\mu_l \propto T^{-3/2} \tag{2.46a}$$

As stated above, impurity scattering increases as the temperature increases, which decreases the distance, r, necessary for effective impurity scattering to occur. Therefore, the scattering cross section of the impurity, given by πr^2, will decrease with increasing temperature. The mean free path between impurity scattering events, which is directly proportional to the mobility due to impurity scattering events, is inversely proportional to this area and will therefore increase as the temperature increases. The dependence of the mobility on impurity scattering events alone, μ_i, is given by

$$\mu_i \propto T^{3/2} \tag{2.46b}$$

The mobilities μ_l and μ_i contribute to the total mobility according to

$$\mu_t^{-1} = \frac{1}{\mu_l} + \frac{1}{\mu_i} \tag{2.47}$$

At high temperatures, μ_l will dominate the dependence of the mobility on temperature.

Lastly, as the diffusion lengths depend on the diffusion constants,

$$L_{e,h} = (D_{e,h} \tau_{e,h})^{1/2} \tag{2.48}$$

they will accordingly change with temperature.

It can now be stated that very few parameters are free from the effects of temperature. The absolute maximum temperature T_{max} for the high–resistivity silicon sensor can be found by equating the intrinsic carrier concentration, which increases with temperature according to Eqn. (2.40), to the impurity concentration of the silicon substrate, N_{dn}^-. For optimum operation of the sensor however, the working temperature should remain well below this maximum

value.

$$T_{\max} = \frac{E_{\mathrm{g}}}{2k \, \ln\left[\dfrac{(N_{\mathrm{c}}N_{\mathrm{v}})^{1/2}}{N_{\mathrm{dn}}^{-}}\right]} \tag{2.49}$$

The absolute maximum temperature is therefore approximately 390 K or 117 °C. However, from Eqn. (2.42) it can be seen that the electron concentration n will equal the doping concentration from room temperature up to the point where the intrinsic carrier concentration has increased to the value of $n_{\mathrm{i}} = 0.1 \, N_{\mathrm{dn}}^{-}$. When the substrate resistivity is 4 kΩ–cm, i.e. when it has a doping concentration of $N_{\mathrm{dn}}^{-} = 1 \times 10^{12} \, \mathrm{cm}^{-3}$, the silicon will begin to behave intrinsically at temperatures above 50 °C.

2.2.2 Recombination and generation lifetimes

The free electron– and hole–carrier concentrations in thermodynamic equilibrium, n and p, respectively, are equal in intrinsic silicon. This concentration is called the intrinsic carrier concentration, n_{i}, and is a constant in thermodynamic equilibrium. In the intrinsic case therefore, $n = p = n_{\mathrm{i}}$. In the extrinsic case, $n \neq p$, but their product in thermodynamic equilibrium still equals n_{i}^2, i.e. $np = n_{\mathrm{i}}^2$.

Disturbances in the equilibrium condition result in $np \neq n_{\mathrm{i}}^2$. Different processes exist to restore the system to equilibrium. The particular restoring process will depend on the situation that has been created by the disturbance, $np \gg n_{\mathrm{i}}^2$ or $np \ll n_{\mathrm{i}}^2$ and on the type of semiconductor, direct or indirect bandgap [2.7, 2.14]. The following discussion only applies to indirect bandgap semiconductors such as silicon and is treated with the assumption of the existence of a single energy trap level which is homogeneously distributed. As several nonhomogeneously distributed trap levels usually occur in most integrated devices, this single trap level is theoretically designed to represent their mean.

A disturbance, such as the injection of excess carriers, created through the introduction of an incident radiation source onto the surface of a semiconductor device or through the application of a forward bias on a p–n junction device, would result in the first situation, i.e. $np \gg n_{\mathrm{i}}^2$. The mechanism that would restore equilibrium in this case involves the recombination of the injected minority carriers with majority carriers. This restoring process is therefore called recombination. The time involved from the point of injection to the point equilibrium is reached is termed the recombination lifetime [2.14].

If however, a p–n junction device is placed under reverse–bias conditions, a paucity of free carriers will exist in the depletion region and the second situation will result, i.e. $np \ll n_{\mathrm{i}}^2$. The restoring mechanism in this case is called generation, as carriers will continually be generated through generation–recombination centers in order to restore the system to equilibrium.

This process can also be described by a lifetime. However, in this case the parameter involved is termed the generation lifetime [2.14].

Three recombination mechanisms exist: Shockley–Read–Hall (SRH), radiative and Auger [2.18]. The SRH process involves the use of localized states or intermediate energy levels within silicon's forbidden gap to carry out the recombination process. Conversely, the radiative process is a band–to–band process simultaneously involving electrons and holes. This process only occurs when incident radiation is present. The energy released from the SRH process is dissipated as heat to the lattice in the form of lattice vibrations, while that energy created by the radiative process is emitted as photons. The Auger recombination process occurs only in the presence of high electric fields. It is inverse to the process of impact ionization, where avalanche multiplication occurs. An electron and a hole recombine and the excess energy is given to a third carrier, either an electron or a hole. When the silicon device is placed under dark, low–field conditions, the SRH recombination process is the only mechanism available to restore equilibrium conditions [2.18].

Three generation mechanisms also exist. They are the inverse of the three recombination mechanisms: thermal generation of electron–hole pairs, optical electron–hole pair generation and avalanche multiplication, respectively. Under dark, low–field conditions, again the only process available to restore equilibrium will be the inverse SRH process, i.e. the thermal generation of electron–hole pairs via intermediate energy levels existing within the forbidden gap.

The SRH expression for recombination via localized states in n–type silicon is given by Eqn. (2.14), but will be repeated here in the general case. Note that $R = -G$.

$$R = \frac{v_{th}\sigma_e\sigma_h N_t \ (np - n_i^2)}{\sigma_h\left[p + n_i \exp\left[\frac{-(E_t - E_i)}{kT}\right]\right] + \sigma_e\left[n + n_i \exp\left[\frac{(E_t - E_i)}{kT}\right]\right]} \tag{2.50}$$

As stated in Sect. 2.2.1, in general, if the processing of the diode is well–controlled and both the p–n junction and the high–low junction function properly, the leakage current in fully reverse–biased high–resistivity silicon p^+–n^-–n^+ diodes will be mainly due to thermal generation in the depletion region, i.e. in region *ii*, Fig. 2.5. The lifetime in the depleted region is termed the generation lifetime τ_g, while that in the undepleted quasi–neutral region is termed the recombination lifetime τ_r.

The generation lifetime is given by Eqn. (2.15b)

$$\tau_g = n_i/G \tag{2.51}$$

The expression for τ_g has been derived in Sect. 2.2.1. The reader is referred to this section for the details of the derivation. This expression is given as Eqn. (2.16) and is repeated here for convenience

$$\tau_{\rm g} = \tau_{\rm eo} \exp\left[\frac{-(E_{\rm t} - E_{\rm i})}{kT}\right] + \tau_{\rm ho} \exp\left[\frac{(E_{\rm t} - E_{\rm i})}{kT}\right] \tag{2.52}$$

However, as discussed in Sect. 2.2.1, it has been revealed through different analyses of p–n junctions that thermal generation of carriers occurs in a volume whose width, $x_{\rm g}$, is slightly less than the width of the depletion layer. This generation zone is situated in the center of the depletion layer. Recombination within the generation zone can be neglected, as no free carriers exist within this region. At both the upper and lower edges of the depletion region however, recombination is seen to increase, which results in a decrease within these edge regions in the net generation. In Sect. 2.2.1, $x_{\rm g}$ was derived and given in Eqn. (2.24). However, it is repeated here for convenience

$$x_{\rm g} = (x_{\rm bn} - x_{\rm bp}) \tag{2.53}$$

where $x_{\rm bn}$ and $x_{\rm bp}$ are defined to mark the upper and lower interfaces of the generation zone, as derived in Sect. 2.2.1, Eqns. (2.22) and (2.23), respectively.

For the purpose of deriving the recombination lifetime, again two time constants, $\tau_{\rm ho}$ and $\tau_{\rm eo}$, are introduced, defined as $(\nu_{\rm th}\sigma_{\rm h}N_{\rm t})^{-1}$ and $(\nu_{\rm th}\sigma_{\rm e}N_{\rm t})^{-1}$, respectively. In the depletion region, both electrons and holes will be depleted so that the product np in the numerator of Eqn. (2.50) can be neglected with respect to $n_{\rm i}^2$ when deriving the generation lifetime. In the undepleted region, this is no longer true. This equation can be modified somewhat however, by substituting n and p with their equivalent values within the undepleted region

$$n = N_{\rm dn}^- \tag{2.54a}$$

$$p = n_{\rm i}^2/N_{\rm dn}^- - \Delta p \tag{2.54b}$$

When each term is divided by $N_{\rm dn}^-$, the insignificant terms are neglected, and n, which in this case equals $N_{\rm dn}^-$, is replaced with its definition, i.e. $n = n_{\rm i} \exp[(E_{\rm qn} - E_{\rm i})/kT]$, (where $E_{\rm qn}$ is the quasi–Fermi level of electrons), Eqn. (2.50) simplifies to

$$R = \frac{\Delta p}{\tau_{\rm ho}\left[1 + \exp\left[\frac{E_{\rm t} - E_{\rm qn}}{kT}\right]\right] + \tau_{\rm eo}\left[\exp\left[\frac{E_{\rm i} - E_{\rm t}}{kT}\right] + \exp\left[\frac{E_{\rm i} - E_{\rm qn}}{kT}\right]\right]} \tag{2.55}$$

The lifetime in the quasi–neutral n–type undepleted bulk, i.e. the recombination lifetime, is defined to be [2.7]

$$\tau_{\mathrm{r}} = \Delta p / R \qquad\qquad (2.56)$$

Comparison of Eqns. (2.55) and (2.56) leads to the equation for the recombination lifetime in the quasi–neutral bulk region

$$\tau_{\mathrm{r}} = \tau_{\mathrm{ho}} \left[1 + \exp \left[\frac{E_{\mathrm{t}} - E_{\mathrm{qn}}}{kT} \right] \right] + \qquad\qquad (2.57)$$
$$\tau_{\mathrm{eo}} \left[\exp \left[\frac{E_{\mathrm{i}} - E_{\mathrm{t}}}{kT} \right] + \exp \left[\frac{E_{\mathrm{i}} - E_{\mathrm{qn}}}{kT} \right] \right]$$

Two important parameters related to the carrier lifetime are the drift length and the diffusion length. The drift length is the average distance a carrier can drift under an applied electric field in its lifetime, is applicable only to region *ii* and is given by Eqn. (1.4a). The diffusion length represents the distance a carrier can travel by diffusion in a time equal to its lifetime and is applicable in this situation to regions *i*, *iii* and *iv*. The diffusion length is given by Eqn. (1.4b).

Several measurement techniques exist to experimentally determine the generation and recombination lifetimes. The transient of a MOS capacitor is extensively used to investigate generation mechanisms and to measure the generation lifetime, Sect. 4.7.2.1. A new contactless microwave technique has recently been developed at Delft University of Technology in cooperation with Philips Research Laboratories, Eindhoven, the Netherlands, in order to investigate recombination mechanisms and to measure recombination lifetimes, Sect. 4.7.2.2. The problem with MOS capacitor analysis techniques is that the surface generation and the bulk generation cannot be distinguished. The two are distinguishable in the contactless–microwave measurement technique.

2.2.3 Energy resolution

The ability of a detector to measure the energy of incident radiation is quantified by its energy resolution. This resolution is a measure of the degree to which the detection system is able to separate or distinguish between two or more radiations with nearly equal energies. The result of an energy measurement is $E + \mathrm{d}E$, where $\mathrm{d}E$ is the sum of all the calibration and resolution errors. In order to perform this measurement, the detection system must produce a voltage pulse output signal, whose height is proportional to the amount of energy deposited in the detector, per incident photon. Since the objective is to determine the energy of the incident radiation, the photons must be absorbed within the detector and must deposit all their energy there.

Theoretically, the emission spectrum of a monoenergetic source should be an impulse on an intensity versus energy curve. However, the detector output spectrum, i.e. the pulse–height spectrum, of such a source is recorded as a

relatively broad peak on a counts (which is proportional to intensity) versus pulse height (which is proportional to energy) curve. Unequal pulse heights are produced for photons of equal energy. The distribution of pulse heights is usually Gaussian or nearly Gaussian in nature [2.3]. This effect is termed line broadening and is caused by statistical fluctuations in the number of created carriers and in the magnitudes of the reverse currents and electronic noise currents.

Line broadening effects that are intrinsic to the signal generation in the sensitive volume of the detector are a source of noise and are detrimental to the intrinsic resolution, while all other line broadening effects, also sources of noise, cause the external resolution to deteriorate. The intrinsic resolution is the main factor that determines the degree of total line broadening and is derived from statistical variations in the number of charge carriers created in the sensitive volume by each photon.

The intrinsic energy resolution, given by the intrinsic full–width at half–maximum (FWHM), can be obtained assuming Gaussian statistics. The width of a peak on a pulse–height spectrum is given by the standard deviation from the mean, σ, which is half of the peak width at 61 % of its maximum value [2.3]

$$\sigma = (\bar{N})^{1/2} \epsilon \tag{2.58}$$

where $\bar{N}$ is the mean number of charge carriers produced and ϵ is the ionization energy. The FWHM is related to the standard deviation by [2.3]

$$\text{FWHM} = \frac{\mathrm{d}E}{E} \bar{N}\epsilon = 2.35\,\sigma \tag{2.59}$$

Using Eqn. (2.58) and the fact that $\bar{N} = E/\epsilon$, Eqn. (2.59) reduces to

$$\frac{\mathrm{d}E}{E} = \frac{2.35}{\sqrt{E}} \sqrt{\epsilon} \tag{2.60}$$

Thus, the intrinsic resolution is proportional to the square root of the ionization energy and inversely proportional to the square root of the energy of the incident radiation. The resolution of a given detector for radiation at a particular energy can be roughly predicted by this formula. The ionization energy, ϵ, is a fundamental property of the detector material and values for a semiconductor, a gas and a scintillator detector are approximately 3 eV, 30 eV and 300 eV, respectively. It is now clear that semiconductor detectors, having lower ionization energies, will be able to produce more charge carriers and therefore will have better intrinsic energy resolutions than the other two types of detectors. In addition, for any given detector, as the energy resolution is inversely proportional

to $\sqrt{E}$, it deteriorates with decreasing photon energy.

However, as the pulse–height spectrums of most peaks are asymmetrical, an empirical factor, F, called the Fano factor must be added to Eqn. (2.60). This factor was theoretically introduced by Fano and can be calculated and determined experimentally [2.19]. In silicon, F has been found to lie between 0.1 and 0.3 [2.19].

$$\frac{dE}{E} = \frac{2.35 \ \sqrt{F\epsilon}}{\sqrt{E}} \tag{2.61}$$

The actual intrinsic energy resolution is therefore better than that assumed using Gaussian statistics. Fano related this effect to the fact that when the photon is completely absorbed within the detector and deposits all its energy there, the total amount of energy loss is fixed [2.5].

There are two main sources of noise that affect the extrinsic resolution: detector noise and electronic noise. Detector noise is mainly due to random fluctuations in the leakage currents, while electronic noise is mainly due to random fluctuations in the currents originating from the electronic readout circuitry. Contributions to the extrinsic resolution are independent of the energy of the radiation and therefore add whole increments of dE to the total energy resolution. Since all the effects mentioned above are statistical in nature, they add in quadrature. The total resolution is therefore given by

$$dE^2 = dE_{int}^2 + dE_{ext}^2 \tag{2.62}$$

2.2.4 Noise

Detector and electronic noise sources were discussed above with respect to the effect they have on the determination of a detector's energy resolution. The three main sources of noise have been given: that due to the stochastic nature of the energy loss process of the incident radiation, that originating from the detector itself and that originating from the electronic circuitry. The first source of noise is fully described in Sect. 2.2.3. The other noise sources are more fully detailed below.

The detector itself produces noise from a variety of origins, but the main contributor is that arising from statistical fluctuations in the leakage current. The main sources of current noise in reverse–biased junction detectors, which are assumed to be independent, are generation–recombination noise, shot noise and flicker or $1/f$ noise.

Generation–recombination noise is caused by fluctuations in current–carrier generation and recombination. These fluctuations are created by effects which disrupt the current flow, i.e. the trapping of the carriers. The magnitude of the generation–recombination noise current is [2.20]

$$\overline{i}_{\mathrm{gr}}^{2} = 4 I_{\mathrm{r}}^{2} \left[\frac{\tau_{\mathrm{c}} \Delta f}{N_{0}[1 \; + \; (\; 2 \, \pi f \tau_{\mathrm{c}})^{2}]} \right] \tag{2.63}$$

where I_{r} is the average reverse current, τ_{c} is the minority–carrier lifetime, Δf is the electrical bandwidth, N_{0} is the total number of free carriers and f is the frequency at which the noise is measured.

Shot noise occurs in systems where each current carrier crosses continuously from one electrode to the other with the same transit time. Assuming there is no correlation between carriers, the shot noise in detectors irradiated by a Poisson distributed source is given by [2.20]

$$\overline{i}_{\mathrm{s}}^{2} = [2 \mathrm{q} I_{\mathrm{r}} \Delta f] \tag{2.64}$$

where q is the charge of an electron, I_{r} is the average reverse current and Δf is the electrical bandwidth. This formula gives a maximum value for the case where no correlation between carriers exists. This may occur in a fully depleted semiconductor detector with no trapping centers or ionized impurities. Note that in this case the generation–recombination current will equal zero. When ionized impurities and trapping centers exist, there will be a correlation between the charge carriers. As the percentage of ionized impurities and traps increases, the shot noise will decrease and the generation–recombination noise will increase. These sources are to some extent mutually exclusive [2.5]. It is generally accepted that if the shot noise has been accounted for, the generation–recombination noise need not be and that the photon contribution to the noise current is equal to Eqn. (2.64) times a small correction factor ($\sqrt{2}$) [2.20].

Flicker noise originates from crystal defects and dislocations, from surface–state traps and from the lack of an ohmic contact. These sources produce traps, which randomly capture and release carriers. The time constants associated with these processes give rise to a noise current whose energy is concentrated at low frequencies. The empirical expression for this noise current is given by [2.20]

$$\overline{i}_{\mathrm{f}}^{2} = B \left[\frac{I_{\mathrm{r}}^{a} \Delta f}{f^{b}} \right] \tag{2.65}$$

where B is a proportionality constant of the device, I_{r} is the average reverse current through the detector, a is a constant in the range of 0.5 to 2, b is a constant of approximately unity and Δf is the electrical bandwidth. As crystal imperfections can vary randomly even on the same substrate, the constant B varies widely for different devices. The flicker noise is negligible when the detector is fabricated properly.

Thermal or Johnson noise is due to the random thermal motion of the charge carriers. For detectors with a series resistance R_{s}, the thermal noise current is [2.20]

$$\bar{i}_t^2 = \left[\frac{4kT\Delta f}{R_s}\right] \tag{2.66}$$

where k is Boltzmann's constant, T is the temperature in K and Δf is the electrical bandwidth. The thermal noise will decrease with decreasing temperatures and can be negligible in those detectors with small series resistances, i.e. in fully depleted detectors that have low contact resistances [2.5].

For the high–purity silicon soft X–ray sensors with series resistors, one additional noise source must be taken into account. The heavily–doped polysilicon resistor will introduce an additional source of thermal noise. This noise source can be modeled as a shunt current generator whose magnitude is given by Eqn. (2.66).

The primary sources of electronic noise originate from the input transistor of the preamplifier and from the bias resistor placed between the external voltage source and the detector. The bias resistor contributes thermal noise, which can be represented by a shunt current generator. The magnitude of this noise source, Eqn. (2.66), is inversely proportional to the resistance value of the bias resistor and is negligible for resistance values on the order of tens of megaohms [2.5].

As the preamplifier is a two–port network, it can be represented by two equivalent input noise generators, provided that correlation is considered between the two noise generators. The value of the equivalent noise voltage is obtained by first short–circuiting the input of each circuit and equating the output noise in each case, while the value of the equivalent noise current is found by open–circuiting the input of each circuit and equating the output noise in each case.

The equivalent circuit for a high–purity silicon soft X–ray sensor is shown in Fig. 2.8(a), while the same sensor with a heavily–doped polysilicon resistor in series is shown in Fig. 2.8(b). In these figures, $I(t)$ represents the current due to the motion of the charge carriers generated in the depletion region by the absorption of an incident photon, V_b and R_b represent the bias voltage and bias resistor, respectively, R_d and C_d represent the depletion layer resistance and capacitance, respectively, R_s and C_s account for the resistance and the capacitance of the undepleted bulk material, R_c represents the contact resistance, R_r represents the resistance of the polysilicon resistive structure and A represents the amplification unit.

As the depletion region is depleted of free carriers, its resistance, especially if the device is fully depleted, is on the order of hundreds of megaohms. The effect of R_d can therefore be neglected with respect to the reactance of C_d. When the sensor is operated in the fully depleted mode, R_s and C_s do not have to be accounted for and can be replaced in Figs. 2.8(a) and (b) with a short circuit. In well fabricated and packaged sensors, the contact resistance, R_c, will also be negligible. Figures 2.8(a) and (b) can be revised taking these considerations into account.

The revised equivalent circuit for a fully depleted sensor–amplifier system with noise sources included is shown in Fig. 2.9(a). The revised equivalent circuit for the same sensor and amplifier unit, but connected through an on–chip series polysilicon resistor, is shown in Fig. 2.9(b).
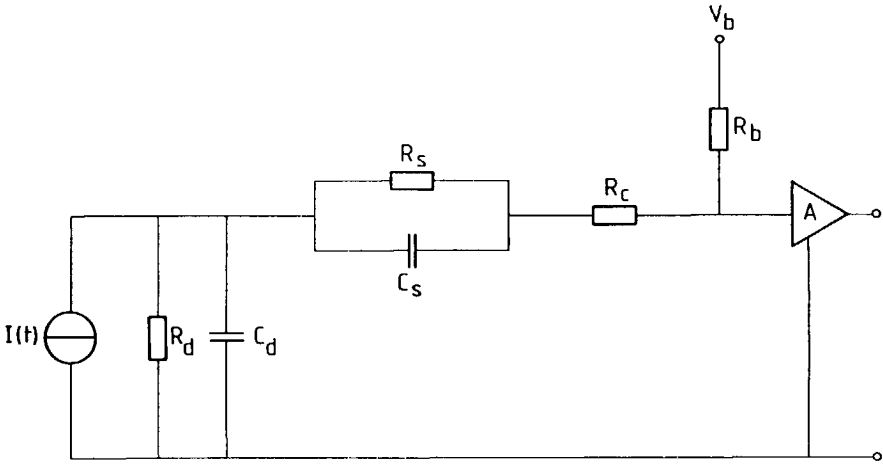
Fig. 2.8 (a) *Equivalent circuit for a silicon soft X–ray sensor and associated electronics* [2.19].
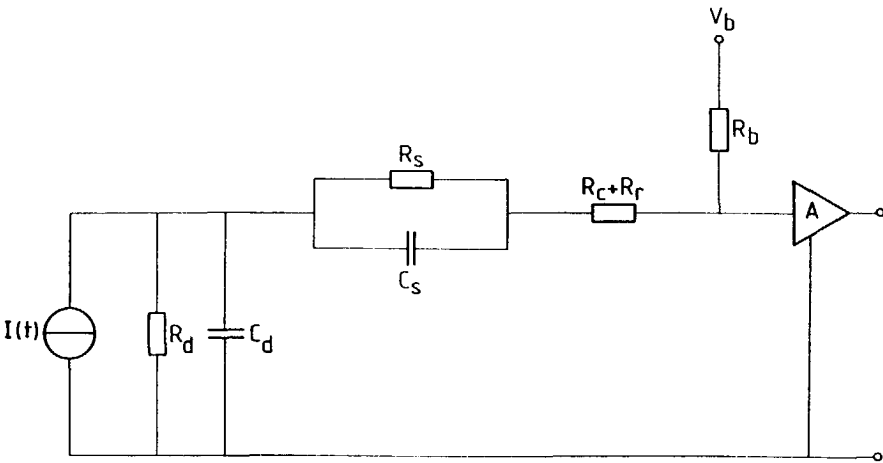

Fig. 2.8 (b) *Equivalent circuit for a silicon soft X–ray sensor with a polysilicon resistor in series and associated electronics* [2.19].
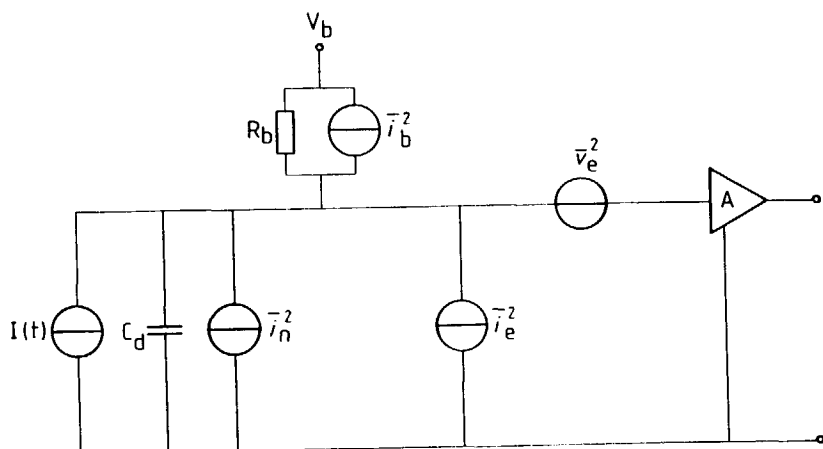
Fig. 2.9 (*a*) *Equivalent circuit for a fully depleted high–purity silicon soft X–ray sensor and associated electronics with noise sources included* [2.19].
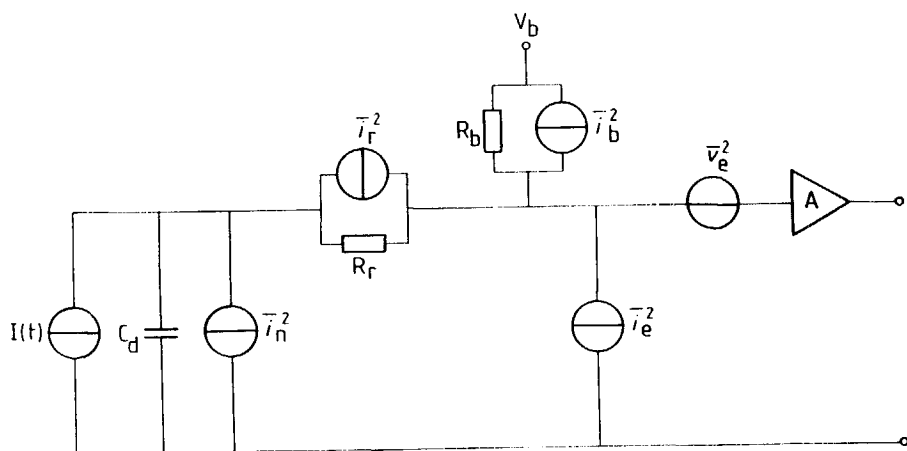

Fig. 2.9 (*b*) *Equivalent circuit for a fully depleted high–purity silicon soft X–ray sensor with a polysilicon resistor in series and associated electronics with noise sources included* [2.19].

In Figs. 2.9(a) and (b), $\bar{i}_n^2$, $\bar{i}_b^2$, $\bar{i}_r^2$, $\bar{i}_e^2$ and $\bar{v}_e^2$ represent, respectively, the sum total of all the noise current sources from the detector, (i.e. the sum of the generation–recombination noise, Eqn. (2.63), the shot noise, Eqn. (2.64), the flicker noise, Eqn. (2.65) and the thermal noise, Eqn. (2.66)), the noise current source due to the bias resistor, (i.e the thermal noise, Eqn. (2.66)), the noise current source due to the polysilicon resistor, (i.e. the thermal noise, Eqn. (2.66)) and the equivalent noise current and noise voltage from the amplification–unit load, respectively.

As the signal from the high–purity silicon soft X–ray sensor is in the form of an electrical charge, the noise contributions from the sensor and from the electronics can be summed and expressed in terms of an equivalent noise charge (EQN) in units of the electron charge [2.19]. The EQN is related to the FWHM by the equation [2.19]

$$EQN = \frac{FWHM}{2.35\epsilon} \tag{2.67}$$

2.2.5 Charge collection

The shape of the signal pulse obtained from a sensor after a soft X–ray is absorbed is determined by the motion of the charge carriers from the time of their creation until the time of their collection. Analytical expressions for the time required for the ionization process to reach its completion following the absorption of a photon, for the radius of the cloud of (positive or negative) charge carriers when the cloud reaches the respective contact, for the electric field within the device, for the time needed for the created carriers to reach their relevant electrodes, for the change in the induced charge on the electrodes, for the current at a particular time during the collection process and for the amount of charge that will be collected are developed in the following analyses.

The equation of motion of a charge carrier is given by [2.5]

$$v_d = \mu_{e,h} \mathscr{E} \tag{2.68}$$

where v_d is the drift velocity, $\mu_{e,h}$ is the carrier mobility of electrons or holes, respectively and $\mathscr{E}$ is the electric–field strength. In these analyses, a constant charge density throughout the detector volume is assumed, as well as the existence of ideal electrodes. In addition, relatively low values of the electric field strength are assumed, and therefore, to a first approximation, μ_e and μ_h are assumed to be independent of the electric field.

An incident soft X–ray will produce an energetic electron by the photoelectric process, Sect. 2.1.2. This energetic electron is a charged particle and loses its energy through the creation of secondary electrons. Each of these secondary electrons rapidly loses its energy through impact ionization, until the remaining

kinetic energy is insufficient to create another electron–hole pair. The ionization tracks are folded and complex. An estimate of the time required for the ionization process to reach completion in silicon is given by [2.5]

$$t_i = \frac{\tau E_g}{h\nu} \tag{2.69}$$

where τ is the relaxation time for lattice scattering by optical modes and $h\nu$ is the energy of the secondary optical photons.

The created electrons and holes begin to separate due to the action of the applied electric field. If a great many charge carriers are produced, the area of ionization can become polarized and an opposing space–charge field can develop, which can completely counteract the applied electric field within its center. Within the center, separation would then continue by ambipolar diffusion, while the applied electric field would continue to separate those carriers near the edges. Diffusion would eventually enlarge the area to the extent that the electric field could penetrate it. Each carrier would then be attracted to its relevant electrode by the full electric field. In the case of soft X–ray absorption however, space–charge effects can be neglected, as the charge carriers are not generated in a high density, although repulsive forces may exist, depending on the size of the charge density.

Assuming the charges spread out as a cloud from their points of origin, by the time the positive charges reach the front electrode the radius of the diffusive cloud, r, can be estimated to be

$$r = (2D_h t_h)^{1/2} \tag{2.70}$$

where D_h is the diffusion coefficient for holes and t_h is the time necessary for the holes at the center of the cloud to reach the front electrode. Using the Einstein relation, i.e. $D_h = \mu_h kT/q$, where μ_h is the hole mobility and q is the electronic charge, Eqn. (2.70) becomes

$$r = \left[\frac{2\mu_h kT t_h}{q}\right]^{1/2} \tag{2.71}$$

If the detector could be characterized by a constant electric field throughout the device $\mathscr{E}$,

$$\mathscr{E} = -\frac{V_b}{x_d} \tag{2.72}$$

where V_b is the applied bias voltage and x_d is the thickness of the depletion region, the collection time for the positive carriers generated at a point x within the volume of the device would be

$$t_h = \frac{x}{\mu_h \mathscr{E}} \tag{2.73}$$

Then, using Eqns. (2.68) and (2.71) – (2.73), Eqn. (2.71) would become

$$r = \left[\frac{2kT x_d{}^2}{q V_b}\right]^{1/2} \tag{2.74}$$

However, in the case of p^+–n^-–n^+ step junction detectors, the electric field is not constant throughout the device. The electric field decreases linearly from the junction contact. If V_d is given as the voltage needed to deplete the detector of thickness x_d, for reverse–bias voltages equal to or greater than the depletion voltage, $\mathscr{E}(x)$ is given by

$$\mathscr{E}(x) = \frac{2 V_d}{x_d}\left[1 - \frac{x}{x_d}\right] \tag{2.75}$$

where x is the point of carrier generation within the device. The collection time then becomes

$$t_h = \frac{1}{\mu_h}\int_0^{x_d}\frac{1}{\mathscr{E}(x)}\,dx \tag{2.76}$$

The time for the electrons to reach the back contact is determined by the same formula, except the mobility of electrons is used instead of that for holes. Using Eqns. (2.58), (2.71) and (2.75) – (2.76), the radius of the diffusive cloud, Eqn. (2.71), becomes

$$r = \left[\left[\frac{2kT x_d{}^2}{V_d}\right]\frac{-\ln}{2}\left[1 - \frac{x}{x_d}\right]\right]^{1/2} \tag{2.77}$$

The amount of original charge qN_o created at a point x within a detector of

thickness x_d will decrease to an amount N during its transport toward the front electrode by a factor of $\exp(-t/\tau)$.

According to Ramo's theorem, the change in the induced charge on the electrodes at a particular time t when the cloud has moved through a distance δx within the detector is [2.21]

$$\delta Q = qN \frac{\delta x}{x_d} \tag{2.78}$$

This theorem has been experimentally confirmed by several authors [2.22–2.23]. When recombination and trapping effects are not negligable, the current is

$$i(t) = \frac{\delta Q}{\delta t} = \frac{qN_0}{x_d} \exp(-t/\tau) \frac{\delta x}{\delta t} \tag{2.79}$$

and the amount of charge collected at the electrodes is

$$
\begin{aligned}
Q(t) &= \int_0^{x/\mu\mathscr{E}} i(t) \, dt \\
&= \frac{qN_0}{x_d} \int_0^x \exp(-x/\mu\mathscr{E}\tau) \, dx \\
&= \frac{qN_0\mu\mathscr{E}\tau}{x_d} [1 - \exp(-x/\mu\mathscr{E}\tau)] \, dx
\end{aligned}
\tag{2.80}
$$

Some of the charge carriers generated in the sensitive volume of the detector may not contribute to the pulse signal due to charge–carrier trapping and recombination. This results in a spread in the pulse–rise times and pulse–height distributions. These effects can be reduced by increasing the strength of the applied electric field, if the drift velocity is not already at its maximum.

As the detector is assumed to be operated in a mode in which the time constant of the external circuit is much longer than the detector charge–collection time, the time required for the signal pulse to reach its maximum is determined by the detector charge–collection time and is not influenced by any properties of the external or load circuit. However, the time required to restore the signal to zero, the decay time, is determined solely by the time constant of the load circuit. The amplitude of the analog–voltage signal pulse from the preamplifier is therefore determined by the ratio of the total charge collected during one event divided by the capacitance of the load circuit. As this capacitance is normally fixed, the maximum height of the analog signal pulse is directly proportional to the charge

generated within the detector and therefore to the energy of the incident radiation, E_P

$$V_{max} = \frac{Q}{C} = \frac{qE_P}{\epsilon C} \qquad\qquad (2.81)$$

In a photon–counting detector system (the systems described in this work), as opposed to an integrating system such as a CCD, the count rate determines the maximum source intensity or flux that can be incident upon the sensor. The limit on the count rate is set by the system dead time. High intensities are desired in most applications employing synchrotron radiation. When high–resistivity silicon is used as the substrate, fast charge collection and high count rates ensue. Therefore, high–resistivity silicon, rather than material with a high lifetime but a low resistivity, is utilized.

2.2.6 Radiation damage

The high–purity silicon crystal is often assumed to be a perfect periodic structure of silicon atoms. In actuality, deviations from this condition in the form of foreign impurities and structural defects, which are introduced during the manufacturing process and by incident radiation, exist within the crystal. Radiation incident upon Si or SiO_2 can cause damage through the generation of lattice displacement defects or through the generation of electron–hole pairs [2.24].

The degree of radiation damage that results through the generation of lattice displacement defects depends on the energy and the type of the radiation. The energy of the radiation should be sufficient to overcome the binding energy of an atom and bring the recoil atom out of the neighborhood of the vacancy. Single vacancies can be created by the excitation of a silicon atom from its lattice position, the binding energy of which is approximately 25 eV.

The level of damage also depends on the type of radiation. A classification is made into neutrons, α–particles and energetic electrons. Soft X–rays are able to damage the lattice through the creation of energetic electrons [2.25]. Of the three types, energetic electrons are the least damaging. Compared to neutrons, which produce clusters of lattice defects, energetic electrons produce only single defects. Energetic electrons can remove an atom from the lattice by imparting to it sufficient kinetic energy to knock it out of its lattice site. This results in the creation of a vacancy and an interstitial. These local defects give rise to acceptor and donor levels in the bandgap, respectively. Vacancies are mobile above 55 K and tend to travel through the lattice forming pairs or recombining with other vacancies, impurities or surface defects to form stable point defects. Displacement damage also increases the rate of nonequilibrium carrier trapping, recombination and generation. If many defects occur in one place, n–type material can transform into p–type material, causing a degradation in the detector performance. The levels in the bandgap also influence the resistivity, lifetime and mobility of the

material. High–purity silicon is particularly sensitive to these effects. An increase in the resistivity and a decrease in the lifetime and mobility create an increase in the detector leakage current and noise. Local changes can create a transverse electric field, which will disturb the sensor's position linearity.

The rate of defect introduction greatly increases with increasing electron energy due to the increase of the collision angle over which the threshold energy can be transferred, to the increase of the solid angle through which the recoil atom can be scattered and still be displaced and to the increase of the separation of the interstitial from the vacancy. However, the introduction of a significant amount of defects is not seen to occur at incident photon energies below 130 keV [2.25]. The soft X–ray spectrum is well below this energy.

Radiation damage due to the exposure of p–n junction devices to soft X–rays is associated with an increase in the reverse current. However, significant damage (i.e. increases in the reverse current by a factor of 10) generally does not become evident until after an exposure dose of approximately 10^7 rad. In addition, investigations have shown that this damage can be annealed by ultraviolet illumination [2.24–2.25]. When the material with defects is heated to a temperature where the defects are mobile, structural changes appear. This process is termed annealing and offers a possibility to reduce or eliminate the defects. It has been experienced however that once annealed, these detectors suffer from significant damage upon repeat exposure to radiation at lower doses than those associated with the original exposure. The function of a radiation detector appears to be inherently coupled to its own destruction and thus it only has a limited lifetime.

Radiation damage caused through the creation of electron–hole pairs tends to affect the SiO_2 and the Si/SiO_2 interface more than the Si bulk material. Electron–hole pairs in the Si bulk will recombine or eventually will be swept out of the device by the electric field. However, a significant proportion of the charge carriers tend to remain trapped in the SiO_2. Long term ionization effects can occur due to the build up of trapped charge in the insulator layer. Because of this, devices which employ functional oxide layers are more sensitive to this type of radiation damage than their junction counterparts. This fact must not be overlooked when attempting to integrate (bipolar or MOS) electronic circuitry close to the sensor on a high–resistivity substrate.

Soft X–rays incident upon the MOS device will be absorbed by the photoelectric effect within the oxide layer, as well as within the silicon. Electron–hole pairs will thus be generated in both regions. The electron–hole pairs created will separate due to the applied electric field. Due to the high mobility of electrons in the silicon dioxide layer, the photon–generated electrons within this region tend to rapidly drift to the metal electrode and be collected. Very little trapping of these electrons occurs. However, the hole mobility in silicon dioxide is relatively low. The photon–generated holes tend to slowly drift to the Si/SiO_2 interface. Up to 30 % of the holes become trapped near the interface [2.24].

At radiation doses above 10^4 rad, the incident ionizing radiation forms interfacial trapping states. The formation of these interface states is thought to lead to an increase in the reverse current, cause a shift in the flat–band voltage and decrease the charge–transfer efficiency [2.24]. This sensitivity to soft X–ray damage is shared by all MOS devices and, in conventional devices, becomes significant after doses of approximately 10^5 rad of exposure. The positive charge

build–up in the oxide affects p–n junction devices as well. As the positive charge builds up, the surface leakage currents increase and the inter–element resistance decreases. Devices fabricated with inverted structures reportedly have increased soft X–ray hardness [2.26]. Backside illumination of deep– or fully–depleted p–n junction and MOS devices will reduce the radiation damage, depending on the efficiency of the detector for the particular radiation of interest.

2.3 CONCLUSIONS

In this chapter, the theoretical operation of two basic types of high–purity silicon soft X–ray sensors is analyzed: directly read out p^+–n^-–n^+ diodes and p^+–n^-–n^+ diodes coupled in series to highly–doped polysilicon resistive structures. The interactions that take place when electromagnetic radiation is incident upon silicon are discussed, the most important of which is absorption. From a curve of the absorption coefficient versus the energy of the incident radiation, it is seen that soft X–rays are primarily absorbed by the photoelectric effect in silicon. The number of free carriers generated upon the absorption of electromagnetic radiation in silicon can be predicted by the quantum yield. An analytical expression for the total quantum efficiency of the sensor is derived and used to calculate the quantum efficiencies of six different devices. It is graphically demonstrated that devices fabricated on high–purity silicon consistently have higher quantum efficiencies than those fabricated on standard ohmic silicon.

The theoretical characterization also consists of analyses of the sensors' leakage currents and lifetimes. The total leakage current is shown to originate from three sources: from the surface, from the depletion region and from undepleted regions. Analytical expressions for each component are derived and their relative contributions to the total leakage current are analyzed. It is shown that the greatest contribution to the total leakage current in high–resistivity silicon p^+–n^-–n^+ diodes is due to thermal generation current arising from the depletion region.

Disturbances in system equilibrium result in either an excess or a paucity of free carriers. The processes of recombination or generation, respectively, exist to restore the system to equilibrium. These processes are described and analytical expressions for the lifetime involved in both cases, i.e. the recombination and the generation lifetimes, respectively, are derived.

In addition, the energy resolution and the noise of the sensors, as well as the charge–collection process and the damage incident radiation can cause, are discussed. The energy resolution of a radiation sensor, i.e. its ability to distinguish between two or more radiations with nearly equal energies, is shown to consist of intrinsic and extrinsic contributions. Effects intrinsic to the signal generation in the sensitive volume of the sensor contribute to the intrinsic energy resolution, while all other effects, i.e. electronic noise, contribute to the extrinsic energy resolution. Since all the effects are statistical in nature, they add in quadrature.

The three main sources of noise are described: that due to the stochastic nature of the energy loss process of the incident radiation, that originating from the detector itself and that originating from the electronic circuitry. The main source

of the detector noise originates from the statistical fluctuations in the leakage current, while the primary sources of the electronic noise originate from the input transistor of the preamplifier and from the bias resistor. Equivalent circuits for a basic high–purity silicon soft X–ray sensor and one with a polysilicon resistive structure in series are portrayed, as well as equivalent circuits for a basic fully depleted high–purity silicon soft X–ray sensor (with noise sources included) and one with a polysilicon resistive structure in series (with noise sources included).

Analytical expressions for the time required for the ionization process to reach its completion following the absorption of a photon, for the radius of the cloud of (positive or negative) charge carriers when it reaches the respective contact, for the electric field within the device, for the time needed for the created carriers to reach their relevant electrodes, for the change in the induced charge on the electrodes, for the current at a particular time during the collection process and for the amount of charge that is collected are developed and presented.

Radiation incident upon Si or SiO_2 can cause damage through the generation of lattice displacement defects or through the generation of electron–hole pairs. The degree of radiation damage that results depends on the energy and the type of the incident radiation, as well as on the structure of the device. Soft X–rays damage the lattice through the creation of energetic electrons. However, the introduction of a significant amount of defects through this mechanism does not occur at incident energies below 130 keV and the soft X–ray spectrum is well below this energy. *P–n* junction based sensors are more radiation hard than their MOS counterparts.

REFERENCES

[2.1]   S. Middelhoek and S.A. Audet, Silicon sensors, Academic Press, London, 1989.

[2.2]   S.M. Sze, Semiconductor devices, Physics and Technology, John Wiley and Sons, New York, 1985.

[2.3]   W.H. Tait, Radiation detection, Butterworths, London, 1980.

[2.4]   H.L. Malm, T.W. Raudorf, M. Martini and K.R. Zanio, Gamma–ray efficiency comparisons of Si, Ge, CdTe and HgI_2 detectors, IEEE Trans. on Nucl. Sci., NS–20 (1973) 500–509.

[2.5]   G. Dearnaley and D.C. Northrop, Semiconductor counters for nuclear radiations, E. & F.N. Spon, London, 1966.

[2.6]   J.R. Hauser and P.M. Dunbar, Minority carrier reflecting properties of semiconductor high–low junctions, Solid State Electr., 18 (1975) 715–716.

[2.7]   A. Bar–Lev, Semiconductors and electronic devices, 2nd ed., Prentice Hall Inc., Englewood Cliffs, 1984.

[2.8]   P.G. Jespers, F. Van de Wiele and M.H. White, Solid state imaging, Noordhoff, Leyden, 1976.

[2.9]   EG&G Reticon application notes, Number 101, Application of Reticon photodiode arrays as electron and X–ray detectors, EG&G Reticon, 345 Potrero Avenue, Sunnyvale, California, U.S.A.

[2.10] J. Kemmer, Improvement of detector fabrication by the planar process, Nucl. Instr. and Meth., 226 (1984) 89–93.

[2.11] S.M. Sze (ed.), VLSI Technology, 2nd ed., McGraw Hill, New York, 1988.

[2.12] J. Walton, Silicon detectors: new challenges, Nucl. Instr. and Meth., 226 (1984) 1–11.

[2.13] H.F. Wolf, Silicon semiconductor data, Pergamon Press, Oxford, 1969.

[2.14] A.S. Grove, Physics and technology of semiconductor devices, John Wiley and Sons, New York, 1967.

[2.15] J. Van der Spiegel and G.J. Declerck, Theoretical and practical investigation of the thermal generation in gate controlled diodes, Solid State Electr., 24 (1981) 869–877.

[2.16] G. Vanstraelen, Generation lifetime monitoring on high resistivity silicon using gated diodes, Proc. 5th European Symp. on Semiconductor Detectors, New Developments in Radiation Detectors, Munich, Feb. 21–23, 1989.

[2.17] D.K. Schroder, Effective lifetimes in high–quality silicon devices, Solid State Electr., 27 (1984) 247–251.

[2.18] D.K. Schroder, The concept of generation and recombination lifetimes in semiconductors, IEEE Trans. on Electr. Dev., ED–29 (1982) 1336–1338.

[2.19] G. Bertolini and A. Coche, Semiconductor detectors, North–Holland Publishing Co., Amsterdam, 1968.

[2.20] E.L. Dereniak and D.G. Crowe, Optical radiation detectors, John Wiley and Sons, New York, 1984.

[2.21] S. Ramo, Currents induced by electron motion, Proc. IRE, 27 (1939) 584–585.

[2.22]   N.B. Strokan, V.K. Yeryomin, S.A. Lomashevich and N.I. Tisnek, Final results on the nature of the pulse–height spectrum from semiconductor detectors, IEEE Trans. on Nucl. Sci., NS–19 (1972) 365–369.

[2.23]   R.N. Williams and E.M. Lawson, Formation of current pulses in semiconductor nuclear radiation detectors, Nucl. Instr. and Meth., 113 (1973) 597–598.

[2.24]   B. Magorrian and N.M. Allinson, Soft X–ray damage in CCD detectors, Nucl. Instr. and Meth., A273 (1988) 599–604.

[2.25]   V.A.J. van Lint, Mechanisms of radiation effects in electronic materials; Vol. 1, John Wiley and Sons, New York, 1980.

[2.26]   S. Lerose, D. Pons and C. Fonne, Microstrip detectors with inverted structure for hardening against radiation damage, IEEE Trans. on Nucl. Sci., 33 (1986) 347–350.

3

THEORY OF HIGH–PURITY SILICON
SOFT X–RAY SENSOR ARRAYS

3.1 INTRODUCTION

A one–dimensional position–sensitive high–purity silicon radiation sensor can be realized by dividing the front electrode, i.e. the p^+–implantation covered with aluminum, Fig. 2.5, into strips. This device is referred to as a silicon strip detector [3.1]. Under operating conditions, the n^-–substrate separating the p^+–strips will be accumulated with electrons, which are present in order to match the positive fixed oxide charges always associated with Si/SiO_2 interfaces, Sect. 2.2.1. Each strip therefore acts as a separate collecting electrode.

A two–dimensional position–sensitive radiation sensor can be realized if, instead of one continuous front electrode, as shown in Fig. 2.5, many smaller rectangular electrodes are fabricated in the n^-–type substrate [3.2–3.9]. When the size of each electrode is on the order of $1 \, \text{mm}^2$ or less, this type of device is referred to as a pixel detector. Again, due to the presence of the positive fixed oxide charges, each pixel acts as a separate collecting electrode. However, in this case, readout of the electrodes is not straightforward and special techniques must be used in order to collect the charges induced on the electrodes following the exposure of the device to electromagnetic radiation [3.2–3.9].

The principles of operation of the sensor arrays are discussed in Sect. 3.1.1 and array design specifications for typical soft X–ray applications are outlined in Sect. 3.1.2. Simulation circuits for modeling the high–purity silicon soft X–ray sensor arrays are discussed in Sect. 3.2. The theoretical operation of the sensor arrays is then developed in Sect. 3.3, based on the theory presented in Sect. 2.2.

3.1.1 Principles of array operation

Five different high—purity silicon soft X—ray sensor arrays have been fabricated by the author in the I.C. Laboratory at Delft University of Technology with the help of the laboratory staff. However, one of the processing steps, i.e. the low—temperature deposition of silicon dioxide, was carried out at Philips Research Laboratories in Eindhoven, the Netherlands. The principles of operation of the five different arrays are similar.

The operation of the arrays is based on both the resistive and the capacitive coupling of the elements in a matrix of sensing diodes. In a given array, the columnar elements are resistively coupled to one output connection. In three of the five arrays, Figs. 3.1(a), (b) and (c), this was accomplished through the use of highly—doped polysilicon structures, while in the other two, Figs. 3.1(d) and (e), only the small resistance associated with the aluminum interconnection lines was utilized. In all but one of the arrays, Figs. 3.1(b), (c), (d) and (e), those elements lying in the same row in a given array are capacitively coupled through the use of the double—layer metalization technique. Capacitive coupling was achieved in the remaining array, Fig. 3.1(a), through a double—layer conduction scheme, which consisted of a lower conductor of heavily—doped polysilicon and an upper conductor of aluminum.
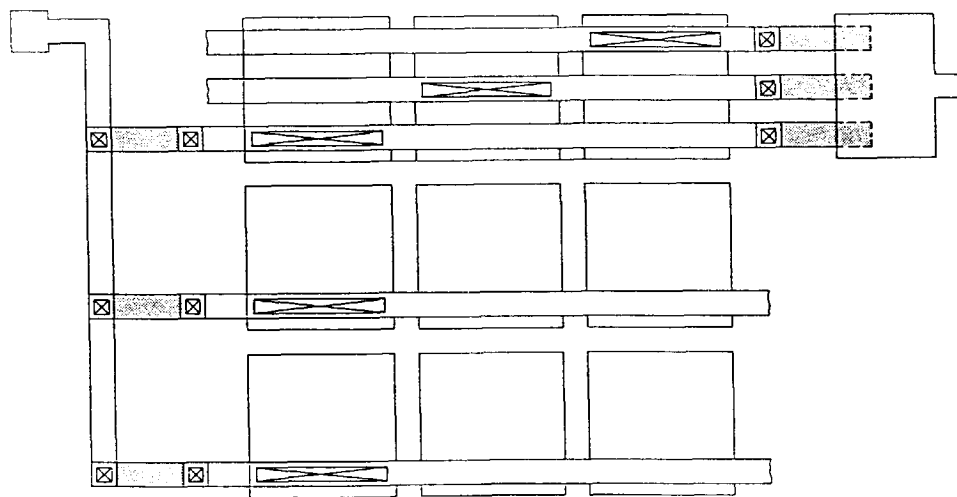
Fig. 3.1 *(a) Schematic of the high—purity silicon soft X—ray sensor array based on a double—layer conduction scheme, IS—502.*

The technique of using resistive and capacitive coupling for the incorporation of a passive multiplexing readout scheme onto a high—purity silicon radiation sensor was initially tested and successfully demonstrated on a one—dimensional silicon strip detector [3.10]. This readout technique enables the one—dimensional position resolution of incident radiation to be obtained with a significant
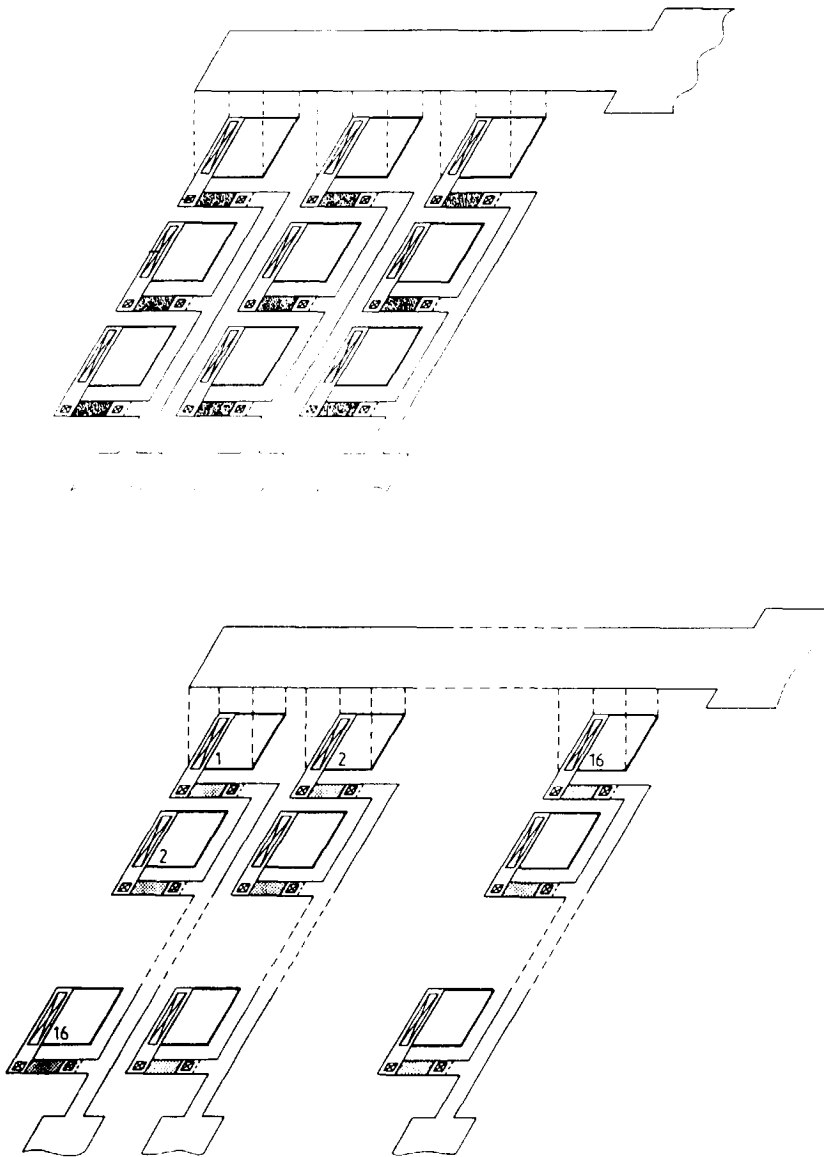
Fig. 3.1 *Schematics of the two high—purity silicon soft X—ray sensor arrays based on the double—layer metalization technique which employ highly—doped polysilicon structures to realize the resistive coupling: (b) a 3 x 3 array, IS—531 and (c) a 16 x 16 array, IS—562.*
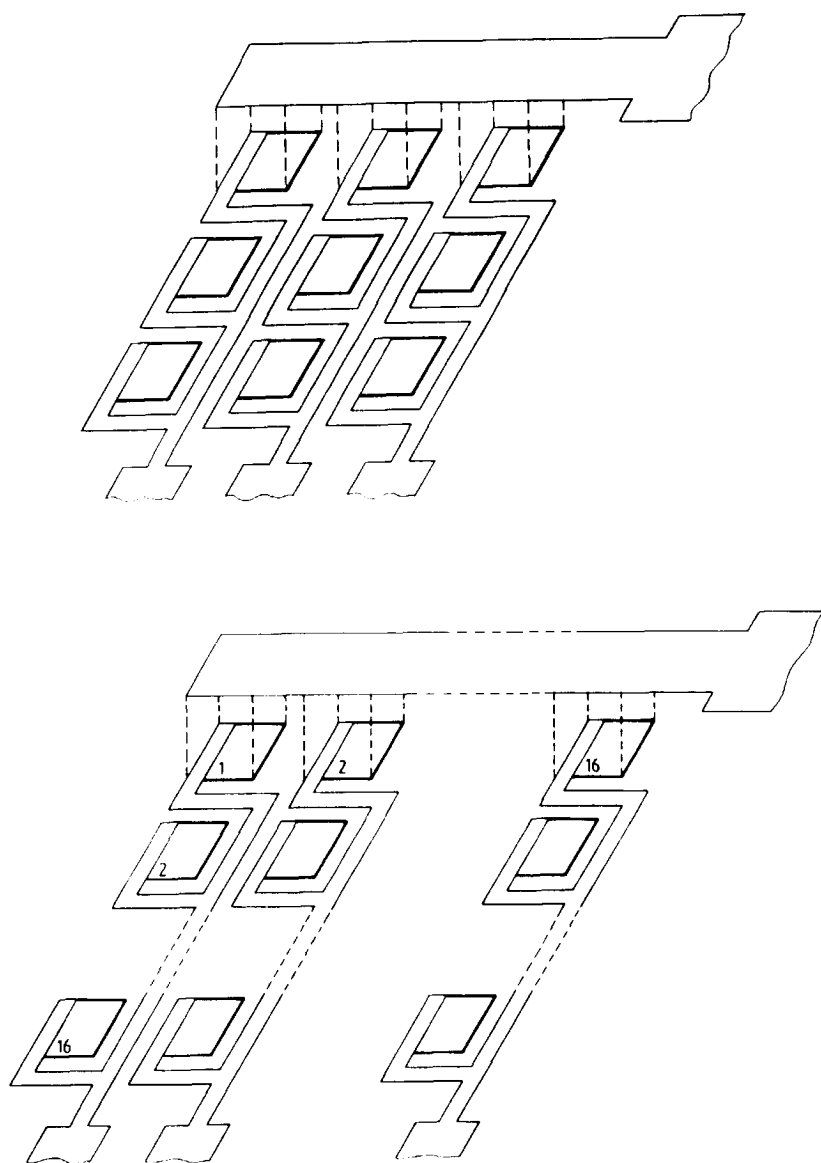
Fig. 3.1　*Schematics of the two high−purity silicon soft X−ray sensor arrays based on the double−layer metalization technique which employ aluminum interconnections to realize the resistive coupling: (d) a 3 x 3 array, IS−559 and (e) a 16 x 16 array, IS−560.*

reduction in the number of bonding pads. The number of output pads necessary is reduced from n, the number of strips, to $2n^{1/2}$ [3.10].

This design was modified to produce devices for application in the two–dimensional position detection of incident electromagnetic radiation. The operation of the modified devices is also based on both the resistive and the capacitive coupling of the elements in arrays of sensing diodes, but the arrays are now two–dimensional in geometry. Two–dimensional position resolution is achieved by the direct collection through resistive coupling of radiation–generated charge in the x–dimension and the indirect capacitive coupling of this charge in the y–dimension.

The array of Fig. 3.1(b) will now be specifically addressed. Variations in the operation of the other arrays shown in Fig. 3.1 will then be explained.

As can be observed in Fig. 3.1(b), the first element (a p^+–n^- junction diode contacted to an overlying aluminum layer) in every row is resistively coupled to one x–addressed output connection through the use of heavily–doped polysilicon structures. The second element (as well as the third) in every row is resistively coupled in the same manner to a separate x–addressed output connection. In order to capacitively couple each of the three elements lying in the same row, an aluminum band is patterned in a second metalization layer over each row. Each of the three bands is separated from the first layer metal by a dielectric (silicon dioxide) and directly connected to a y–addressed output connection.

Given that electromagnetic radiation enters and interacts within the reverse–biased sensor in such a way as to cause the photon–generated charge to become collected within one diode element, two output signals will be obtained: one at that element's x–addressed (resistive–coupled) output and one at its y–addressed (capacitive–coupled) output. The charge will be directly readout by flowing through the polysilicon resistive structure into the preamplifier associated with the x–address. The signal obtained after the preamplifier will be a voltage pulse. It can be used for energy as well as position resolution purposes and as a trigger signal.

Due to the capacitor fabricated above the irradiated diode, during the same period of time, a signal will also be observed at the output associated with the y–address. This signal is only used to discriminate within which row the irradiated diode element is lying and therefore must only be distinguishable above the noise.

The operation of the arrays depicted in Figs. 3.1(b), (c), (d) and (e) are identical with the exception that in two of the four arrays, Figs. 3.1(b) and (c), the resistive coupling was accomplished through the use of highly–doped polysilicon structures, while in the other two, Figs. 3.1(d) and (e), only the small resistance associated with the aluminum interconnection lines was utilized. The size of the array elements in Figs. 3.1(b) and (d) is 0.5 x 0.5 mm², while size of the array elements in Figs. 3.1(c) and (e) is 0.25 x 0.25 mm².

As the double–layer metalization fabrication technique was not yet perfected in the I.C. Laboratory at Delft University of Technology at the time the first sensor array was being designed, Fig. 3.1(a), double–layer conduction was first realized through the use of heavily–doped polysilicon bands as the lower conductors and aluminum bands as the upper conductors. This sensor array is composed of a 3 x 3 matrix of sensing elements (i.e. p^+–n junctions), each element measuring 1 mm² in area. Each row of three elements was first traversed by three

parallel aluminum strips, 10 μm in diameter. These strips were separated from the sensing elements by a layer of thermal silicon dioxide. The bottom strip was then contacted directly to the left–most row element, the middle to the middle element and the top to the right–most element. Through an extension of the strips off to the left side of the matrix, the first (as well as the second and third) elements in each row were connected via polysilicon resistive structures, to the same output node. In this way, the resistive coupling was realized.

The aluminum strips were also extended off to the right side of the matrix. Heavily–doped polysilicon bands were then connected to the aluminum strips to serve as the lower conductor in the double–layer conduction scheme. A silicon dioxide layer was then deposited by an LPCVD high–temperature oxide (HTO) technique to serve as the insulator. Finally, one aluminum band per row was then patterned above the three polysilicon strips associated with the same row to serve as the upper conductor in the double–layer conduction scheme.

This design has the disadvantage that large arrays of small elements cannot be fabricated, due to the fact that as the number of elements per row increases, the number of aluminum strips traversing the row elements must increase. This increases the necessary size of the elements in the vertical dimension. Through the use of the improved double–layer aluminum conduction technique, the size of the sensor can be reduced, but more importantly, large arrays of small elements can be fabricated.

3.1.2 Soft X–ray sensor array design specifications

The most important factors which determine if a particular sensor or sensor array is suitable for the detection of radiation within a certain part of the electromagnetic spectrum are the magnitude of the system noise and the quantum efficiency of the sensor or sensor array in the wavelengths of interest. As mentioned in Sect. 1.3.3, high–purity silicon sensors and sensor arrays are ideal devices for the direct detection of low–energy (soft) X–rays. The detectable energy range is limited on the low energy end of the soft X–ray spectrum by the system noise and by the absorption of the radiation in any dead layers that exist on the exposing surface of the sensor. The detector is limited on the high energy end of the soft X–ray spectrum by the quantum efficiency of the sensor at those wavelengths, Sect. 2.1.4.

The system noise presents itself as a signal with very high count rates at the lowest energies in a pulse–height spectrum. The lower the system noise, the lower the detectable energy range can extend.

When high–resistivity silicon is employed as the substrate material, the entire volume of the substrate can be depleted at relatively low reverse voltages. The high energy cutoff is then limited by the substrate thickness and by the percent efficiency that is required for a particular application. Note that high lifetime material can also be used as the substrate. However, the collection times in this case will be relatively long, which will limit the count rate.

Most of the applications listed in Sect. 1.3.4 are performed with X–ray energies in the range of $8-25$ keV. An exception is digital–subtraction angiography, which is performed at approximately 33 keV. The soft X–ray sensors and sensor

arrays presented in Chapters 2 and 3 provide useful detectors for applications employing electromagnetic radiation in the higher energy limits of the soft X–ray spectral range. The quantum efficiencies of fully depleted sensors and sensor arrays for soft X–radiation, i.e. for radiation in the $2-30$ keV energy range, are given in Figs. 2.6 and 2.7.

In addition to the quantum efficiency, other important parameters of the radiation sensor include the detector diameter and pixel width, as well as the detector's spatial and energy resolutions, the degree of inter–elemental crosstalk, the count rate and the degree to which the sensor is radiation hard. These parameters are discussed with respect to high–purity silicon soft X–ray sensors in Sect. 2.2 and with respect to high–purity silicon soft X–ray sensor arrays in Sect. 3.3. The ideal detector specifications for a number of soft X–ray applications are given in Table 3.1. It is nearly impossible for any one detector to simultaneously meet all aspects of the ideal specifications, even for only one experiment.

Table 3.1 *Ideal detector specifications for a number of soft X–ray applications.*

Application	Detector diameter [mm]	Pixel width [μm]	Spatial resolution [μm]	Energy resolution [Yes,No]
DSA	15	1000	300 (2D)	No
EXAFS	10	75	20 (1D)	Yes
Low–angle scattering	25	250	75 (1D)	Yes
Muscle diffraction	40	125	40 (2D)	Yes

3.2 SIMULATION OF HIGH–PURITY SILICON SOFT X–RAY SENSOR ARRAYS

In order to test the design concept, the sensor arrays were first simulated by the program SPICE. The simulation circuit for one row of three elements of the sensor array of Fig. 3.1(b), IS–531, is shown in Fig. 3.2(a). The same simulation
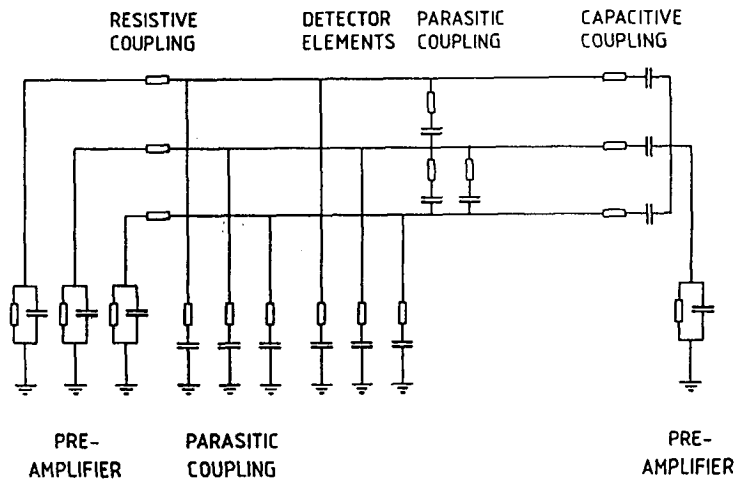
Fig. 3.2 (*a*) *Simulation circuit for one row of three elements of the sensor array IS–531, Fig. 3.1(b).*
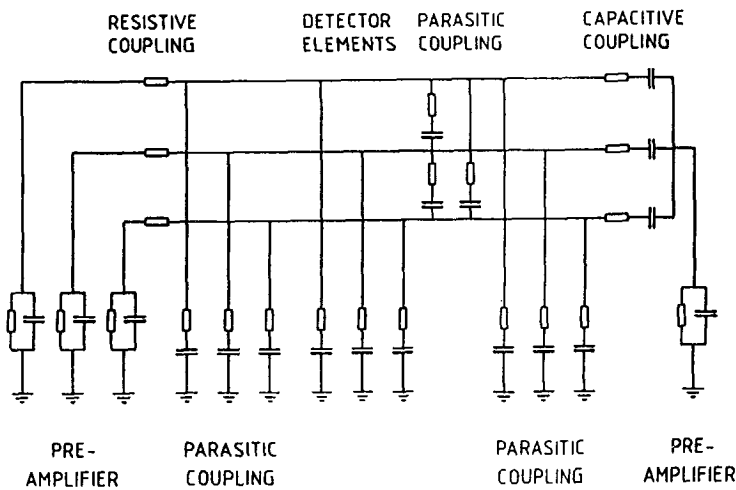
Fig. 3.2 (*b*) *Simulation circuit for one row of three elements of the sensor array IS–502, Fig. 3.1(a).*

circuit was used for the arrays of Figs. 3.1(c), (d) and (e), IS–562, IS–559 and IS–560, respectively, varying only in the number and constitutent values of the parameters. A slightly different simulation circuit was used for the array of Fig. 3.1(a), IS–502, which is shown in Fig. 3.2(b). The major difference is the existence in Fig. 3.2(b) of simulated impedances, (a capacitor and a resistor in series) from each polysilicon conductive structure to ground, as well as to the overlying aluminum band. The circuit description that follows, i.e. that of Fig. 3.2(a), therefore pertains to Fig. 3.2(b) as well.

Each diode in the matrix was simulated by a capacitor and a resistor in series, the capacitance simulating that associated with the capacitance of the depletion region and the resistance simulating the impedance associated with the undepleted region and the contact resistance. In well–fabricated and packaged, fully depleted detectors, this resistance value is negligible. The capacitance value was estimated to be that given by a parallel plate capacitor, i.e. $C = A\epsilon_0\epsilon_{si}/d$, where A is the diode area, ϵ_0 and ϵ_{si} are the permittivity of free space and the dielectric constant of silicon, respectively, and d is the depth of the depletion region. The resistance associated with the depletion region has not been included, because the depletion region is depleted of free carriers, and its resistance, especially if the device is fully depleted, is on the order of hundreds of megaohms. The effect of this resistance can therefore be neglected with respect to the reactance value associated with the capacitor, Sect. 2.2.4.

The first diodes in each row were connected by series resistors to one output node, as were the second and the third (not shown in Fig. 3.2(a)) in order to simulate the resistive coupling. For every row, the diodes in the same row were coupled together with a series capacitor (representing the capacitive coupling of the double–layer metalization) and resistor (representing the small resistance associated with the aluminum interconnections) leading to a separate output node. The capacitance was again estimated to be that of a parallel plate capacitor, where A is the area overlapped by the two metal layers and d is the thickness of the silicon dioxide layer, but the dielectric constant in this case is that of silicon dioxide. The output nodes were connected to the parallel connection of a capacitor and a resistor, which together represent the input impedance of the charge–sensitive preamplifiers to ground. Charge–sensitive preamplifiers generally consist of a differential first stage, incorporating a capacitor, C_f, and a resistor, R_f, in parallel. The input capacitance and resistance of the preamplifier are then given by $C_{in} = C_f|A|$ and $R_{in} = R_f|A|^{-1}$, respectively, where A is the amplifier open–loop gain. In addition, the parasitic coupling between elements was simulated by placing the series connection of a capacitor and a resistor between each diode and its neighboring diode or guard–ring structure.

One of the most important criteria to optimize in terms of an imaging array's performance is the degree of inter–elemental crosstalk. The resistance value of the resistors associated with the resistive coupling and the capacitance value of the capacitors associated with the capacitive coupling were optimized in order to minimize this crosstalk. A current pulse, whose magnitude and duration simulate that current pulse which would be associated with the collection of the charge generated after a soft X–ray photon of 10 keV had been absorbed within the sensitive volume of a fully depleted sensor, was applied to one sensing element, Fig. 3.3(a) and all the output voltage pulses were observed, Figs. 3.3(b) and (c).
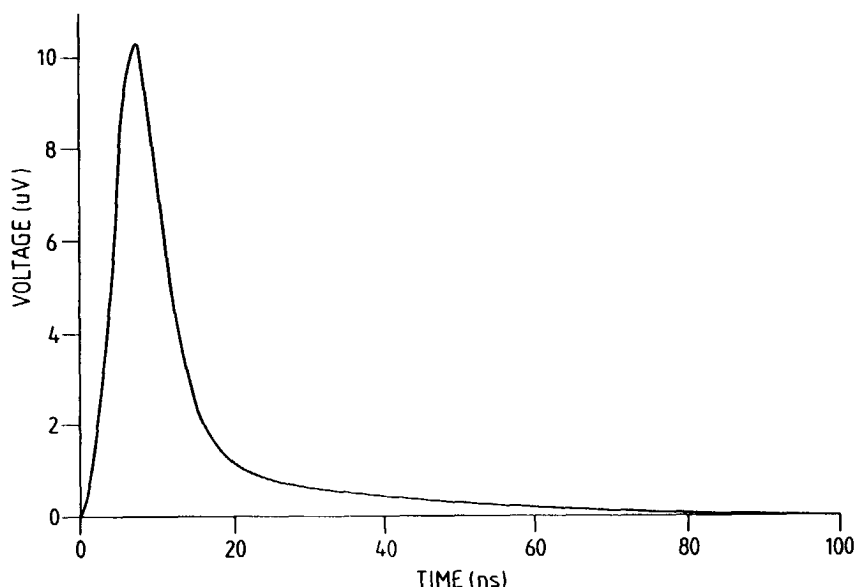
Fig. **3.3** (*a*) *Simulation input: voltage across a 1 Ω resistor when the input current pulse passes through it.*

For illustration purposes, the simulation results for the sensor of Fig. 3.1(b), IS–531, have been detailed. The output voltage peaks associated with the irradiated element's resistive– and capacitive–coupled outputs were on the same order of magnitude, Fig. 3.3(b), while the magnitudes of the output voltage peaks associated with the nonirradiated elements, i.e. the crosstalk to the other four outputs, was less than 10 %, Fig. 3.3(c). It is important to note the change in scales between the three figures.

Similar crosstalk simulation results were obtained for the sensors of Figs. 3.1(c), (d) and (e), IS–562, IS–559 and IS–560, respectively, as well as for the sensor of Fig. 3.1(a), IS–502, i.e. given proper parameter values for the coupling resistors and capacitors and a proper pulse–shaping network, a simulated crosstalk of less than 10 % was obtained in each case. It should be noted however that when simulating the two sensor arrays based on the double–layer metalization technique which employ aluminum interconnections in order to realize the resistive coupling, i.e. IS–559 and IS–560, the output voltage peaks associated with the irradiated elements' resistive–coupled outputs were twice the order of magnitude of their capacitive–coupled outputs. However, the signals from the capacitive outputs are only used to discriminate within which row the irradiated element lies and therefore must only be distinguishable above the noise. Given the simulated parameter values, the fabrication could then begin, Chapter 4.

Note that the pulses associated with the irradiated elements resistive– and capacitive–coupled outputs follow the input current pulse with minimal delays (0 – 20 ns). The count–rate limitations are therefore only determined by the pulse–shaping network, Sect. 2.2.5.
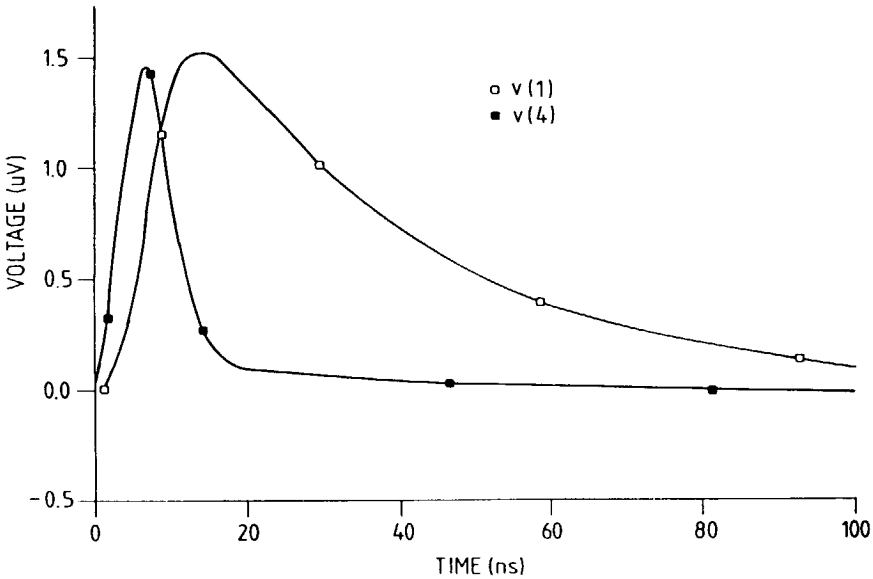
Fig. 3.3 (*b*) *Simulation output: output voltage pulses associated with the irradiated elements resistive [v(1)] and capacitive [v(4)] coupled outputs. Note the change of scales from Fig. 3.3(a)*
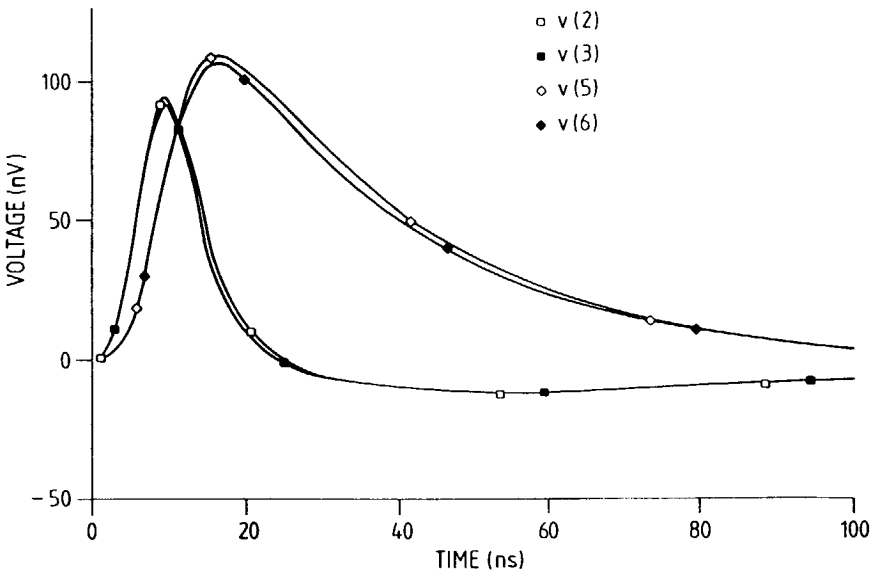
Fig. 3.3 (*c*) *Simulation crosstalk: output voltage pulses associated with the resistive [v(2) and v(3)] and the capacitive [v(5) and v(6)] coupled outputs of the nonirradiated neighboring elements. Note the change of scales from Figs. 3.3(a) and (b).*

3.3 THEORY OF HIGH—PURITY SILICON SOFT X—RAY SENSOR ARRAYS

3.3.1 Introduction

Due to the fact that the high—purity silicon soft X—ray sensor arrays are composed of high—purity silicon soft X—ray sensor elemental units, many of the device characterization parameters, as discussed with respect to the elemental units in Sects. 2.2.1 through 2.2.6, apply directly to the arrays. The leakage current associated with one resistive output of a sensor array (that output which will be used for energy resolution purposes, if this is required) will be the sum total of the leakage currents of the individual elements in that column. The leakage current of the individual elements is discussed in Sect. 2.2.1. The lifetime associated with a particular radiation sensor is not dependent on the sensor design and therefore does not have to be redefined for the sensor arrays, Sect. 2.2.2.

Furthermore, the intrinsic energy resolution associated with a resistive output of a sensor array is described by the same theoretical expressions as the intrinsic energy resolution of the individual elements and depends only on such factors as the energy of the incident radiation, the ionization energy, the Fano factor and the number of charge carriers created, Sect. 2.2.3. The extrinsic energy resolution has the same two main sources, i.e. detector noise and electronic noise. Detector noise is mainly due to random fluctuations in the leakage currents, while electronic noise is mainly due to random fluctuations in the currents originating from the electronic readout circuitry. The noise associated with a resistive output of a sensor array is dependent on the noise of the individual elements, as discussed in Sect. 2.2.4. However, as the equivalent circuits of the sensor arrays are different than those of the elemental units, the equivalent circuits for a high—purity silicon radiation sensor array (with and without polysilicon resistors) and associated electronics with noise sources included are given in Figs. 3.4(a) and (b), respectively. The principles of charge—carrier collection are the same for both the sensors and the sensor arrays. However, parameters that do differ for the sensor arrays include spatial resolution, crosstalk and radiation damage. These are discussed in Sects. 3.3.3, 3.3.4 and 3.3.5, respectively.

3.3.2 Noise

The discussion of noise in Sect. 2.2.4 applies to two different types of sensor arrays, as well as to the individual sensors. One type is composed of a matrix of basic units which embody an individual sensor associated with a polysilicon resistive structure, while the other type is composed of a matrix of sensing elements which consist only of individual sensors. The noise of the two different types of sensor arrays is based on the noise of their compositional units.

The three main sources of noise have been fully described in Sect. 2.2.4, i.e. that due to the stochastic nature of the energy loss process of incident radiation, that originating from the sensor itself and that originating from the electronic

circuitry.

The sensor itself produces noise from a variety of origins, as stated in Sect. 2.2.4, with the main contribution arising from statistical fluctuations in the leakage current. The main sources of current noise in reverse–biased junction detectors, which are assumed to be independent, are generation–recombination noise, Eqn. (2.63), shot noise, Eqn. (2.64) and flicker or 1/f noise, Eqn. (2.65). Thermal or Johnson noise is due to the random thermal motion of the charge carriers. For detectors with a series resistance R_s, the thermal noise is given by Eqn. (2.66). The thermal noise will decrease with decreasing temperatures. The thermal noise, in theory, must be included in the total noise contribution of the sensor, but can be neglected in those sensors with small series resistances, i.e. in fully depleted detectors which have low contact resistances [3.11].

For the sensors with the basic units consisting of an individual sensor associated with a polysilicon resistive structure, one additional noise source must be taken into account. The heavily–doped polysilicon resistor will introduce an additional source of thermal noise. This noise source can be modelled as a shunt current generator whose magnitude is given by Eqn. (2.66).

As described in Sect. 2.2.4, the primary sources of electronic noise originate from the input transistor of the preamplifier and from the bias resistor placed between the external voltage source and the detector. The bias resistor contributes thermal noise, which can be represented by a shunt current generator. The magnitude of this noise source, Eqn. (2.66), is inversely proportional to the resistance value of the bias resistor and is negligible for resistance values on the order of tens of megaohms [3.11]. As the preamplifier is a two–port network, it can be represented by two equivalent input noise generators, providing that correlation is considered between the two noise generators. The value of the equivalent noise voltage is obtained by first short–circuiting the input of each circuit and equating the output noise in each case, while the value of the equivalent noise current is found by open–circuiting the input of each circuit and equating the output noise in each case.

The equivalent circuit for the basic sensor–amplifier systems, i.e. a high–purity silicon soft X–ray sensor and an amplification unit, and the same sensor with a heavily–doped polysilicon resistor in series and an amplification unit, are shown in Figs. 2.8(a) and (b), respectively. The equivalent circuits for fully depleted sensor–amplifier systems with noise sources included are shown in Figs. 2.9(a) and (b), respectively. The equivalent circuits for fully depleted sensor arrays (with and without the polysilicon resistances) and amplifier systems with noise sources included are based on those of Figs. 2.9(a) and (b), respectively, and are shown in Figs. 3.4(a) and (b), respectively.

The effect of detector and electronic noise was discussed in Sect. 2.2.4 with respect to its reduction in the energy resolution. The signals from the high–purity silicon soft X–ray sensor array, as with the individual sensors, are in the form of electrical charges. Therefore, the noise contributions from the array and from the electronics can be summed and expressed in terms of an equivalent noise charge (EQN) in units of the electron charge. The EQN is related to the FWHM by Eqn. (2.67), which is repeated here for convenience [3.12]

$$EQN = \frac{FWHM}{2.35\epsilon} \qquad (3.1)$$
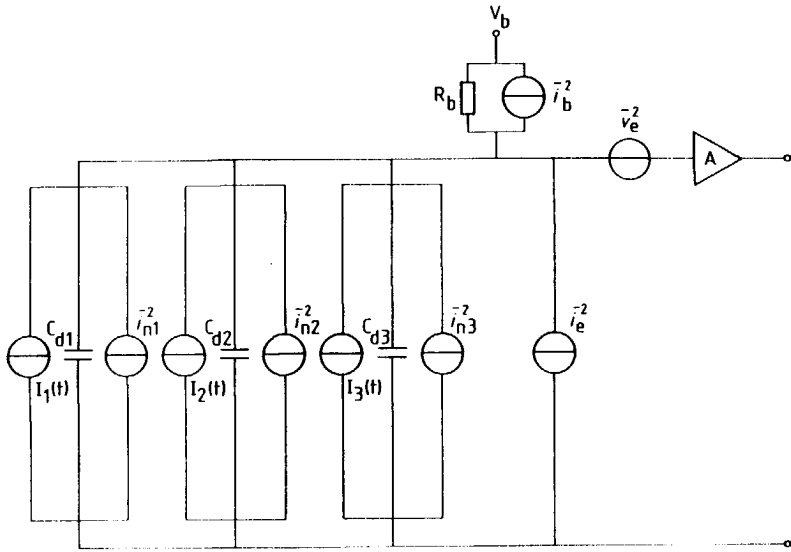
Fig. 3.4 (*a*) *Equivalent circuit for a fully depleted high—purity silicon soft X—ray sensor array (consisting only of the individual sensing elements) and associated electronics with noise sources included* [3.12].
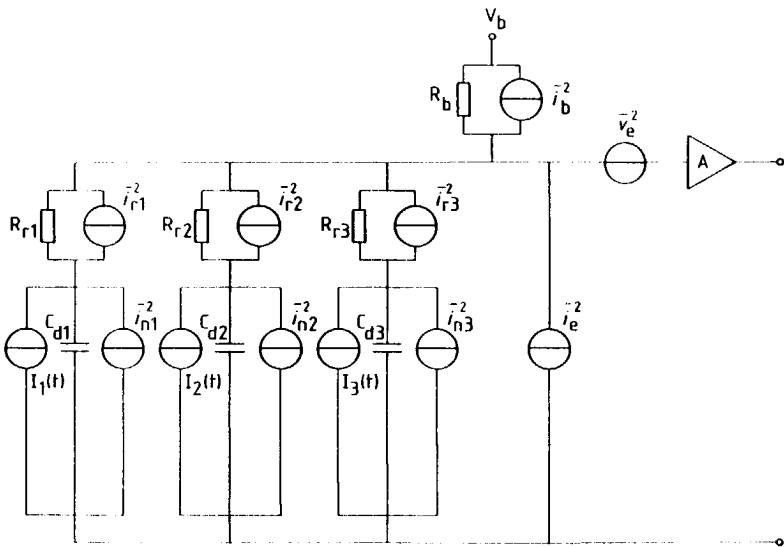
Fig. 3.4 (*b*) *Equivalent circuit for a fully depleted high—purity silicon soft X—ray sensor array (consisting of the individual sensing elements and polysilicon resistive structures) and associated electronics with noise sources included* [3.12].

3.3.3 Spatial resolution

Spatial resolution describes the ability of a sensor to distinguish the incident positions of two adjacent events. The length (and width) of the sensor's one– (two–) dimensional response to a given point event is (are) termed the one– (two–) dimensional track resolution(s). The one– (two–) dimensional track resolution(s) is (are) the minimum value(s) of the width (the length and width), which allow(s) two events, rather than one, to be observed [3.13].

Detectors, such as cloud and bubble chambers, with differential spatial resolutions are able to locate events within their sensitive volumes. Other detectors, such as most semiconductor detectors, have integral spatial resolutions, i.e. they merely indicate whether or not an event has taken place somewhere within a specific sensitive volume.

The input–output function of an ideal sensor array, with no outdiffusion, noise or crosstalk effects, will have a top–hat distribution $f(x)$ with a standard deviation σ

$$\sigma^2 = \frac{\int_{-\infty}^{+\infty} (x - x_0)^2 \, f(x) \, \mathrm{d}x}{\int_{-\infty}^{+\infty} f(x) \, \mathrm{d}x}$$

$$= \frac{1}{P} \int_{-1/2\,P}^{1/2\,P} x^2 \, \mathrm{d}x$$

$$= \frac{P^2}{12} \tag{3.2}$$

where P is the pitch, i.e. the distance from the center of one element to the center of its neighboring element. This will be the position accuracy of sensors when their pitch is relatively large. When taking nonidealic factors into consideration, a Gaussian distribution will usually be added to the top–hat distribution [3.13].

The pixel and the pitch dimensions of the sensor arrays described in this work, i.e. IS–502, IS–531, IS–562, IS–559 and IS–560, are 1×1 mm^2/1.050 mm, 0.5×0.5 mm^2/0.550 mm, 0.25×0.25 mm^2/0.30 mm, 0.5×0.5 mm^2/0.550 mm and 0.25×0.25 mm^2/0.30 mm, respectively. In these cases, the pitches are much greater than the widths of the collected charge distributions, Sect. 2.2.5. The spatial resolutions can therefore be estimated in both the x– and the y–dimensions using Eqn. (3.2) as approximately 300 μm, 160 μm, 90 μm, 160 μm and 90 μm, respectively.

When energy resolution is not a requirement in a given application, the position of the incident radiation can be measured digitally. The two–dimensional position can be dictated by those x– and y– addresses with the

highest output voltage pulse−height amplitudes. In this situation, the noise level of the sensor and the amount of crosstalk are less critical.

In the case where energy resolution is necessary, all the charge must be collected from all the resistive−coupled outputs. The position in the x−dimension is then determined by weighing the voltage pulse heights from the resistive outputs through analog techniques [3.14]. The y−dimension can still be determined digitally, as it is not involved in energy measurements.

The integral spatial resolution of high−purity silicon soft X−ray sensor arrays is determined by four factors: the geometrical structure, the degree of cross−diffusion of photogenerated carriers, charge transfer or crosstalk effects and the presence or absence of a magnetic field.

The absorption of soft X−rays involves primarily the photoelectric effect, Sect. 2.1.2. When a soft X−ray of energy 10 keV is absorbed, approximately 2778 charge carriers are created within $1\,\mu$m of the point of absorption. Due to diffusion, the charge cloud (in a fully depleted $300\,\mu$m thick detector) will widen to a maximum of approximately $8\,\mu$m in diameter during collection, Sect. 2.2.5, which occurs typically within $10-20$ ns. Therefore, depending on the sensor array geometry, the charge may be collected by more than one element. The collection of photogenerated carriers at more than one element occurs when the sensor pitch is on the same order of magnitude as the collected charge distribution. Analog weighing techniques can then be used to determine the position resolution.

Cross−diffusion of photogenerated carriers on the other hand occurs in undepleted sensor arrays. If the depletion layer only extends partially into the bulk, a significant proportion of photons with energies at the higher energy confines of the soft X−ray spectrum will be absorbed well below the depletion layer. The generated charge carriers then have the opportunity to cross diffuse into neighboring elements, especially if the bulk material is high resistivity with a long carrier lifetime. As this effect will cause a loss in the spatial resolution, soft X−ray sensors and sensor arrays are usually operated in the fully depleted mode. Crosstalk effects are discussed in Sect. 3.3.4.

The presence of a magnetic field perpendicular to the electric field affects the position sensing of the detector. A magnetic field perpendicular to the electric field will cause the charge carriers to drift at an angle θ with respect to the electric field given by

$$\tan\theta = \mu_{\text{hall}}\mathscr{B} \tag{3.3}$$

where μ_{hall} is the Hall mobility and equals 310 cm^2/Vs for holes and 1650 cm^2/Vs for electrons. A systematic shift in the position coordinates therefore occurs when the sensor is in the presence of a magnetic field perpendicular to the electric field, e.g. approximately a $5\,\mu$m shift in the center−of−gravity of the collected charge distribution will occur if holes are collected from a $300\,\mu$m thick sensor in the presence of a 1 T magnetic field perpendicular to the electric field [3.14].

3.3.4 Crosstalk

Crosstalk occurs when charge collected at one element induces an output at another element. This can occur through the existence of (parasitic) impedances within the sensor array design. This phenomenon can be used beneficially. In the sensor arrays of Fig. 3.1, the charge induced on one element produces an output at its associated x–address, but also one at its y–address, due to the capacitive coupling between the two aluminum layers. The dielectric between the two layers is fabricated as thin as possible to enhance this effect.

However, this phenomenon is detrimental as well. Parasitic capacitances and resistances exist between each element, Sect. 3.2. In order to avoid crosstalk, the preamplifiers associated with the resistive–coupled outputs should have low resistive– and high capacitive–input impedances compared with those inter–element impedances.

In order to determine the degree of crosstalk, two (neighboring) outputs could be measured in coincidence. Coincidence techniques are used to select events detected in true coincidence with each other. A coincidence unit accepts two (or more) input pulses and outputs one pulse if and only if the input pulses are coincident within a certain resolving time. A given output would produce a pulse whenever radiation was incident upon it. Its (neighboring) output, measured in coincidence, would only give an output if charge was induced at that electrode at the exact same incident. This could only occur when radiation was incident upon the two elements at the exact same time, when radiation was incident between the two elements or when true crosstalk occurs. If the source used has a very low intensity and if the pitch of the sensor elements is relatively large (as is the case in the sensor arrays discussed in this work), the first two possibilities can generally be excluded. The degree of crosstalk can then be estimated from the pulse–height spectrums of the two coincident outputs.

3.3.5 Radiation damage

High–purity silicon soft X–ray sensor arrays may be more sensitive to radiation damage than the high–purity silicon sensors discussed in Chapter 2, as they contain two additional layers above the first metalization layer, i.e. a second aluminum layer and an oxide layer that separates the two metal layers. Due to the presence of the additional oxide layer, it is suspected that the arrays will not be as radiation hard as the p–n junction devices alone.

In MOS devices, the electron–hole pairs produced within the oxide layer will separate due to the applied electric field. The electrons tend to drift to the metal electrode and be collected due to the high mobility of electrons in SiO_2, whereas the holes tend to become trapped due to their relatively low mobility in SiO_2. The lack of an electric field across this oxide layer in the high–purity silicon soft X–ray sensor arrays on the other hand will tend to cause a continual build–up of permanently trapped electrons as well as holes. A beneficial aspect of the array design is that the only interfaces with the oxide layer are the metal layers, so that no modulation of the leakage current is anticipated. Long term ionization effects

due to the trapped charge may still occur however. The functioning of the SiO_2 layer as a dielectric may be influenced or the dielectric constant could change. The noise associated with the capacitive–coupled outputs could increase. On the other hand, if the electron–hole pairs are created in high density, many of the electron–hole pairs may come sufficiently close together so that their mutual Coulomb attraction would cause them to recombine. Once again, backside illumination of the fully depleted array will reduce the possibility of this damage from occurring.

3.4 CONCLUSIONS

The principles of operation of five different high–purity silicon soft X–ray sensor arrays are similar and are all based on both the resistive and the capacitive coupling of the elements in matrices of sensing diodes. Design specifications for typical soft X–ray imaging applications are outlined in Table 3.1.

Device simulation studies using the circuit simulation program SPICE predict that if proper impedance values are given, i.e. proper resistance values for the resistors associated with the resistive coupling and proper capacitance values for the capacitors associated with the capacitive coupling, and if proper readout electronics are utilized, the crosstalk can be minimized to a value below 10 %.

Analyses concerning the theoretical operation of high–purity silicon soft X–ray sensor arrays can be developed based on the theory presented in Chapter 2. Due to the fact that the high–purity silicon soft X–ray sensor arrays are composed of high–purity silicon soft X–ray sensor elemental units, many of the device characterization parameters, as discussed with respect to the elemental units in Chapter 2, apply directly to the arrays. The leakage current associated with one resistive output of a sensor array is the sum total of the leakage currents of the individual elements in that column. In addition, the lifetime associated with a particular radiation sensor is not dependent on the sensor design and therefore does not have to be redefined for the sensor arrays.

Furthermore, the intrinsic energy resolution associated with a resistive output of a sensor array is described by the same theoretical expressions as the intrinsic energy resolution of the individual elements and depends only on such factors as the energy of the incident radiation, the ionization energy, the Fano factor and the number of charge carriers created. The extrinsic energy resolution has the same two main sources for both the sensors and the sensor arrays, i.e. detector noise and electronic noise. Detector noise is mainly due to random fluctuations in the leakage currents, while electronic noise is mainly due to random fluctuations in the currents originating from the electronic readout circuitry.

The noise associated with a resistive output of a sensor array is dependent on the noise of the individual elements. However, as the equivalent circuits of the sensor arrays are different than those of the elemental units, the equivalent circuits for a high–purity silicon soft X–ray sensor array (with and without polysilicon resistors) and associated electronics with noise sources included are given in Figs. 3.4(a) and (b), respectively.

The principles of charge–carrier collection are also the same for both the sensors and the sensor arrays. However, parameters that do differ for the sensor

arrays include spatial resolution, crosstalk and radiation damage.

The high–purity silicon soft X–ray sensors presented in Chapter 2 are not position sensitive. However, the sensor arrays presented in this chapter have two–dimensional track resolution. As the pitch in both the x– and the y–dimensions in each of the five arrays is much greater than the diameters of the collected charge distributions, the position accuracy in each case is determined by the standard deviation of a top–hat distribution, i.e. by the equation $P/\sqrt{12}$, where P is the pitch.

Crosstalk occurs when charge collected at one element induces an output at another element. Crosstalk can be minimized through the use of preamplifiers with low resistive– and high capacitive–input impedances at the resistive–coupled outputs. Coincidence techniques can be used to determine the degree of crosstalk.

As the high–purity silicon soft X–ray sensor arrays have a second metalization layer and a dielectric, which separates the two metal layers, it is suspected that the sensor arrays will not be as radiation hard as the p^+–n^-–n^+ junction devices themselves. Long term ionization effects due to trapped charge may affect the functioning of the dielectric. Backside illumination will reduce the possibility of this damage from occurring.

REFERENCES

[3.1]   W.R.Th. ten Kate, Detectors for nuclear radiation, Sensors and Actuators, 10 (1986) 83–101.

[3.2]   S.A. Audet, Radiation–sensor array fabricated on high–purity silicon with coupling impedances realized through polysilicon and double–layer metalization layers, Proc. Int. Electr. Dev. and Mat. Symp., Kaohsiung, Aug. 29–31, 1988, 212–217.

[3.3]   S.A. Audet and E.M. Schooneveld, High–purity silicon radiation–sensor array, Nucl. Instr. and Meth., A275 (1989) 517–526.

[3.4]   S.A. Audet, Two–dimensional silicon sensor for imaging radiation, Sensors and Actuators, 16 (1989) 155–163.

[3.5]   S.A. Audet, High–purity silicon radiation–sensor array for imaging synchrotron radiation in digital–subtraction angiography procedures, Rev. of Sci. Instr., 60 (1989) 2276–2279.

[3.6]   S.A. Audet, Silicon sensor array for imaging soft X–rays and IR, Sensor Technology, 5 (1989) 2.

[3.7]   S.A. Audet, S.E. Wouters, E.M. Schooneveld and M.H. Kim, High–purity silicon soft X–ray imaging sensor array, Proc. 5th Int. Conf. on Sensors and Actuators, Transducers '89, Montreux, June 25–30, 1989, 175.

[3.8]   S.A. Audet, High–purity silicon sensor array for imaging soft X–ray and infrared radiation, Proc. IEDM '89, Washington, D.C., Dec. 3–6, 1989, 177–180.

[3.9]   S.A. Audet and S.E. Wouters, Monolithic integration of a nuclear radiation sensor and transistors on high–purity silicon, to be published in IEEE Trans. on Nucl. Sci.

[3.10] W.R.Th ten Kate and H.M. Heijne, Capacitive multiplexing on a silicon microstrip detector, Nucl. Instr. and Meth., A234 (1985) 398–401.

[3.11] G. Dearnaley and D.C. Northrop, Semiconductor counters for nuclear radiations, E. & F.N. Spon, London, 1966.

[3.12] G. Bertolini and A. Coche, Semiconductor detectors, North–Holland Publishing Co., Amsterdam, 1968.

[3.13] W.H. Tait, Radiation detection, Butterworths, London, 1980.

[3.14] E. Belau, J. Kemmer, R. Klanner, U. Koltz, G. Lutz, W. Manner, E. Neugebauer, H.J. Seebrunner and A. Wylie, Silicon detectors with 5 μm spatial resolution for high energy physics, Nucl. Instr. and Meth., 217 (1983) 224–228.

4

FABRICATION OF HIGH–PURITY SILICON SOFT X–RAY SENSORS AND SENSOR ARRAYS

4.1 INTRODUCTION

The optimal operation of high–purity silicon soft X–ray sensors and sensor arrays depends on the existence of minimal reverse currents in reverse–biased $p^+-n^--n^+$ junctions. As the magnitude of the reverse current for a given device is dependent on temperature, Sect. 2.2.1, the most obvious approach to leakage current reduction is to operate the device at a low (e.g. liquid nitrogen) temperature. However, in view of the great technological difficulties such an approach entails, it is highly desirable to reduce the leakage currents in high–purity silicon soft X–ray sensors without the requirement of operating them at low temperatures.

It has been shown that the magnitude of the leakage current of a given high–purity silicon radiation sensor depends on the processing technologies used in its fabrication [4.1–4.2]. Leakage current limitation and reduction are the primary goals to achieve in the optimal design of all process sequences involved in the fabrication of high–purity silicon soft X–ray sensors and sensor arrays. When high–purity silicon is used as the starting material, the associated trap density, the number of scattering centers per unit volume and the density of donors or acceptors fully ionized at room temperature are relatively low. This allows for the fabrication of devices that have longer minority–carrier lifetimes, higher charge–carrier mobilities and larger sensitive volumes than those devices fabricated on wafers typically used in standard integrated–circuit processing. Large sensitive volumes can also be obtained through the use of compensated silicon. The unique characteristics of, and the technologies used to produce, high–purity and compensated silicon are discussed in Sect. 4.2.

From an initial investigation [4.1], the process which resulted in the lowest leakage currents was selected for the fabrication of high–purity silicon soft X–ray

sensors. After a brief description of silicon planar technology in Sect. 4.3, the basic high–purity silicon soft X–ray sensor processing steps are detailed in Sect. 4.4. However, as this basic process can only be employed in the fabrication of zero– or one–dimensional high–purity silicon soft X–ray sensors, extra processing steps are required in order to fabricate two–dimensional high–purity silicon soft X–ray sensor arrays. These advanced procedures are discussed in Sect. 4.5. The actual process sequences utilized are pictorially outlined in Sect. 4.6. The effects the additional processing steps had on the quality of the resulting devices could directly be tested through the measurement of various test structures fabricated on the same chip as the sensors. The test structures and the procedures used to characterize the success of the processing are described in Sect. 4.7.

4.2 HIGH–PURITY AND COMPENSATED SILICON

High–purity silicon is used as the starting material for a number of reasons in the fabrication of silicon soft X–ray sensors. First, high–purity silicon contains a relatively low number of impurities, which leads to the minimization of the thermal generation component of the leakage current contributed from the depletion region [4.3–4.4]. The second reason has to do with the absorption of soft X–rays in the silicon bulk and the subsequent collection of the generated charge carriers. In order for 10 keV soft X–rays to be absorbed with a 95 % efficiency, the wafer must be on the order of 400 μm thick. Collection of the generated charge carriers could be envisioned given high–lifetime, rather than high–purity, material. However, collection by diffusion is not efficient or fast enough to allow a total contribution to the output signal of all the charge carriers created by incident radiation in high count–rate experiments, which is necessary in the majority of current soft X–ray applications. Therefore, the detector should be fabricated on high–resistivity material and should be fully depleted for optimal operation. As the depletion depth is directly proportional to the reverse–bias voltage and inversely proportional to the substrate doping, relatively high and low values of these parameters, respectively, assure large depletion depths. In one–sided $p^+–n^-$ junctions, where $N_a >> N_d$, the depth of the depletion region, x_n, is given by Eqn. (1.3), but it is repeated here for convenience [4.5]

$$x_n = \left[\frac{2\epsilon_0\epsilon_{s\,i}V_t}{qN_d}\right]^{1/2} \tag{4.1}$$

Note that if the junction is very shallow, $x_{dr} \approx x_n$, as $x_p \approx 0$.

The avalanche breakdown voltage is also inversely proportional to the substrate doping. Therefore, high–purity silicon sensors are characterized with high breakdown voltages. In one–sided $p^+–n^-$ junctions, where $N_a >> N_d$ [4.5],

$$BV = \frac{\epsilon_0 \epsilon_{s\,i}\, \mathscr{E}_{bv}^2}{2qN_d} \qquad (4.2)$$

where $\mathscr{E}_{bv}$ is the the electric field at the breakdown voltage and is a property of the material. For lightly doped silicon ($N_d < 10^{14}$ cm^{-3}), this value is on the order of 10^5 V/cm [4.5]. Silicon wafers 380 μm thick with a substrate doping of 1×10^{12} cm^{-3} will be fully depleted at a reverse–bias voltage of approximately 140 V, which is significantly less than the breakdown voltage ($\approx 3 \times 10^4$ V) [4.5].

Just as important as the process itself is the manner in which the processing is carried out. Relatively little is known about the processing of high–purity silicon, but avoidance of contamination, auto–doping and thermal shock are necessary in order to retain the resistivity of the starting material throughout the sensor fabrication. Very pure chemicals, glass– and plastic–ware must be used. Rigorous furnace cleaning is necessary immediately prior to all high temperature steps. All heavily–doped regions on the wafer, which have the potential to act as dopant sources, should be capped before succeeding thermal treatments. In addition, the introduction of extended defects and the generation of dislocations in the active zones during processing must be avoided. In order to avoid thermal stresses, the processing temperatures should be kept as low as possible with the avoidance of temperatures over 1100 ºC. Slow insertion and retraction of the wafers will minimize dislocation propagation. In addition, the utilization of gettering techniques counteracts the existence of harmful impurities in the active region of the sensor. If these processing precautions are taken into account, the resistivity of the starting material can be maintained during high–purity silicon soft X–ray sensor fabrication, Sect. 5.3.2.

High–resistivity single–crystal silicon wafers with resistivities on the order of $1 - 50$ kΩ–cm are currently available with diameters up to approximately 100 mm (4 in.) [4.3]. High–purity silicon is prepared through the use of the float–zone growth and refining techniques [4.3–4.4, 4.6].

High–purity float–zone silicon is fabricated from a hyperpure starting material, which then undergoes the floating–zone refinement technique numerous times until the required purity grade is achieved. P–type silicon will have a lower compensation level than n–type silicon of the same doping level, as boron tends to remain in the silicon during the refinement procedure, whereas phosphorous tends to be removed [4.3–4.6].

Large sensitive volumes can also be obtained in silicon through the use of compensated silicon material, i.e. lithium–drifted silicon, Si(Li), or through the use of neutron–doped material. The preparation of Si(Li) material is thoroughly described in Sect. 1.2.4.4. The compensation technique of neutron transmutation is based on the irradiation of high–purity p–type silicon with neutrons. Upon the absorption of neutrons, silicon increases its atomic weight, which results in the disintegration of the atom when it reaches an atomic weight of 31. Decay of the material atoms by the release of β–particles results in the production of phosphorous atoms, which overcompensate the p–type silicon through the creation of n–type silicon [4.7].

Higher efficiencies can be obtained with devices processed on Si(Li) substrates compared to high–purity substrates due to the increased thickness of the starting material. However, compared with compensated silicon material, high–purity silicon contains fewer generation–recombination centers, which makes the

fabrication of devices with lower leakage currents and lower detector noise possible. Moreover, the deterioration of the detector performance through the redistribution of compensating doping atoms is avoided when high–purity silicon is used as the starting material. Other advantages associated with the use of high–purity silicon include the ability to utilize standard integrated–circuit fabrication techniques in order to process multielement detectors with high quality surface–passivation layers, asymmetric, nearly–abrupt $p–n$ junctions and thin, noninjecting contacts, as well as the ability to anneal radiation damaged detectors.

High–purity (specified resistivity 4 kΩ–cm ± 35 %), n–type, (111)–oriented silicon wafers, 2 inches in diameter and 380 μm thick, with a specified recombination lifetime of 500 μsec., polished on the frontside and etched damage free on the backside, were used as the starting material for the fabrication of the sensors and sensor arrays described in this work.

4.3 SILICON PLANAR TECHNOLOGY

The silicon planar process is a fabrication technology in which silicon wafers, usually in bulk quantities, are sequentially led through a well–characterized sequence of processing steps in the production of microelectronic (and/or micromechanical) circuits, devices and sensors. Silicon planar technology is currently the principle processing method used in the fabrication of most silicon integrated circuits and devices [4.5]. It has evolved from the early grown–junction and alloy–junction methods, the developments of which were motivated by the continual advancements made in the realm of theoretical semiconductor physics in the mid–1900s. Theoretical and experimental investigations into the physical properties of semiconductors in the 1930s and 1940s followed von Laue's discovery of crystal diffraction in 1912. With this procedure, the crystal structures of various semiconductor materials were uncovered. Cooperation between many scientists in the fields of physics, electrical engineering, chemistry and metallurgy at Bell Laboratories began in the late 1940s in an effort to fabricate a solid–state field–effect device. The realizations of the first point–contact transistor by Bardeen and Brattain and the junction transistor by Shockley followed from this research in the late 1940s and early 1950s, respectively [4.8].

The first diodes, which were used to experimentally verify the theory of $p–n$ junction characteristics, were produced by the grown–junction method. This method necessitates the sudden change of the doping concentration of the melt at a certain point in the growth of a semiconductor single–crystal ingot. Bars containing $p–n$ junctions are then sectioned from the resulting ingot [4.9–4.10].

The alloy–junction method proved to be more suitable than the grown–junction method for mass production. It involves the positioning of a pellet of material containing $p–$ ($n–$) type impurities within a specific region on the surface of an $n–$ ($p–$) type semiconductor wafer and the subsequent placement of this wafer in an inert atmosphere at a temperature near the eutectic point. In this manner, the pellet material will alloy into the semiconductor material. As the wafer gradually becomes cooled, the pellet material will recrystallize in

single–crystal form with the same lattice structure as the underlying semiconductor material and thereby form a *p–n* junction [4.9–4.10].

The major difficulty associated with the alloy–junction method proved to be the predetermination and control of the junction depth. Other methods for the fabrication of *p–n* junctions were therefore sought. One outcome was the diffused–junction method, which provided the foundation for semiconductor planar technologies.

Much of the early work on semiconductor fabrication technology was performed with the semiconductor germanium (Ge). The electron and hole drift mobilities at 300 K are more than twice as high in pure, defect–free Ge (3900 and 1900 cm^2/Vs, respectively) than in pure, defect–free Si (1350 and 480 cm^2/Vs, respectively). However, attention inevitably turned from Ge to Si due to silicon's high reliability, to its improved temperature capabilities and to the fact that the thermal oxide of silicon is unparalleled in its dielectric and interfacial properties [4.9].

Silicon planar technology, and devices fabricated with it, were first reported in 1960 [4.8]. The state–of–development of the material processing of silicon is currently more advanced than that of any other semiconductor material. State–of–the–art silicon planar–processing technologies allow for the reliable fabrication of complex circuits, devices and sensors. The essential, core processing steps required for the fabrication of silicon planar devices are thoroughly examined [4.9–4.11]. The basic silicon planar–processing steps employed in the fabrication of high–purity silicon soft X–ray sensors are briefly reviewed below.

4.4 BASIC HIGH–PURITY SILICON SOFT X–RAY SENSOR PROCESS TECHNIQUES

4.4.1 Passivation oxidation

Oxide passivation is a useful surface treatment technique employed in the fabrication of high–purity silicon soft X–ray sensors for reducing the number of surface states, the amount of surface charge and the magnitude of the surface leakage current. As described in Sect. 2.2.1, surface leakage current originates from surface charge generated through interface states and Tamm defects existing at the surface and from surface contamination. Section 2.2.1 details the four types of charge associated with oxide films: mobile ionic charge, oxide trapped charge, fixed oxide charge and interface trapped charge.

The degree of leakage current reduction depends on the technique used to fabricate the oxide layer. The technique chosen must minimize the number of dangling bonds near the Si/SiO$_2$ interface, i.e. it must minimize incomplete oxidation. The chosen technique must also minimize the production of defects in the oxide layer, the growth of stacking faults during the heat treatment and the introduction of heavy metals, alkali ions and silicon interstitials into the silicon bulk, all of which have been shown to be detrimental to leakage current reduction.

The (111)–crystal orientation will have a higher concentration of oxide charge

than the (100)–crystal orientation due to the greater density of silicon bonds at that surface. However, high–purity silicon wafers are often more widely available in the (111) orientation. It has been reported that thermal oxidation performed in an atmosphere containing $1 - 6\%$ Cl⁻ ions in the form of HCl or TCE helps to avoid the growth of stacking faults during the heat treatment, aids in the gettering of heavy metals and alkaline ions and appears to provide sinks for silicon interstitials [4.10]. The wet thermal oxidation technique tends to be associated with a higher concentration of oxide charges than does the dry thermal oxidation technique, as wet thermal oxidation is a rapid process resulting in relatively porous films. In addition, this technique is associated with the injection of silicon interstitials into the silicon bulk. These interstitials reportedly can nucleate into defects under certain conditions [4.11]. Thermal treatments at low temperatures in a 10% hydrogen atmosphere have been shown to be able to anneal oxide trapped charge [4.10]. In addition, the presence of guard rings surrounding the diodes will prevent surface currents originating outside the diode area from reaching this region.

Oxide films however, are not good barriers to the diffusion of mobile ions, i.e. Na^+ and K^+. An additional passivation layer of silicon nitride will eliminate this migration and protect the device from contamination once it is fabricated [4.10].

The growth of a dry thermal oxide passivation layer was the first step of each process sequence used in the fabrication of the high–purity silicon sensors and sensor arrays described in this work (except IS–502, which employed a wet oxidation technique). The thermal treatments were performed in atmospheres of dry (wet) oxygen following the thorough cleaning of the ovens with an HCl/H_2O solution. The oxidations were performed at 1100 °C for various times, depending on the desired thicknesses of the oxide layers. A warm–up step and a cool–down step performed in nitrogen atmospheres preceded and succeeded each oxidation, respectively. This was done in order to bring the wafers into thermal equilibrium with the environment before the oxidations began in an effort to obtain uniform oxide passivation layers with minimal stresses.

4.4.2 Low–pressure chemical–vapor deposition

Polysilicon and dielectric deposited films are widely used in the fabrication of modern silicon circuits, devices and sensors. The most common deposition methods in silicon planar technology include various chemical–vapor deposition (CVD) techniques: atmospheric–pressure chemical–vapor deposition (APCVD), low–pressure chemical–vapor deposition (LPCVD) and plasma–enhanced chemical–vapor deposition (PECVD) [4.10]. Deposition temperatures and pressures in these techniques can vary from $100 - 1000$ °C and from atmospheric pressure down to 0.05 Torr, respectively. Film deposition methods must reproducibly be able to generate high–quality films with predictable compositions and structures and with excellent uniformities and good step coverages.

APCVD systems are characterized with marginally acceptable uniformities (no better than $\pm 10\%$ across the wafer or down the boat) and low throughputs and they require frequent cleaning. LPCVD systems tend to have better uniformities ($\pm 5\%$) and higher throughput rates than APCVD systems. In addition, they

provide more precise control over the film composition and structure. The main advantage of PECVD systems is their low deposition temperature. The throughput in these systems is however severely restrictive [4.9–4.10].

The reactors used in LPCVD systems are low–pressure $(0.25 - 2.0\,\text{Torr})$, hot–wall reactors, which typically consist of quartz tubes heated by three–zone furnaces with gas inlet and outlet ports, wherein quartz boats that accommodate vertically standing wafers are placed.

4.4.2.1 Polysilicon

Polysilicon is produced by pyrolyzing silane, SiH_4, at $575 - 625\,^{\circ}\text{C}$. When polycrystalline silicon contains several percent oxygen, it can serve as a semi–insulating material, but normally it is doped during or after deposition to serve as resistive or conductive layers. It is also used in the fabrication of gate electrodes in the self–aligned gate technology of MOS devices [4.10].

The polysilicon layers described in this work were deposited at $600\,^{\circ}\text{C}$ by an LPCVD reactor and doped after deposition by phosphorous diffusion in order to produce layers 400 nm thick with sheet resistivities on the order of $10 - 15\,\Omega/\text{sqr.}$, Sect. 4.6. The heavily–doped polysilicon was patterned by standard photolithographic techniques in the formation of geometrical structures which performed resistive or conductive functions. The highly–doped polysilicon served as resistive structures in that group of high–purity silicon soft X–ray sensors that were associated with polysilicon resistive structures in series, Sect. 4.6.1.2, in the high–purity silicon soft X–ray sensor arrays based on those elemental units, Sect. 4.6.2.2 and in the high–purity silicon soft X–ray sensor arrays based on the double–layer conductive technique, Sect. 4.6.2.1. In addition, the patterned heavily–doped polysilicon served as conductive structures in the high–purity silicon soft X–ray sensor arrays based on the double–layer conductive technique, Sect. 4.6.2.1. The layer's sheet resistivity, R_{sh}, and the surface geometry of the structure, i.e. its length (l) and the width (w), determine the resistance of the structure

$$R_{\text{r}} = R_{\text{sh}} \frac{l}{w} \tag{4.3}$$

4.4.2.2 High–temperature oxide

Silicon dioxide can be deposited with excellent uniformity in LPCVD systems at temperatures of around $900\,^{\circ}\text{C}$ by reacting dichlorosilane, $SiCl_2H_2$, with nitrous oxide, N_2O. This type of oxide is frequently deposited over polysilicon layers to serve as insulators in double–layer conduction schemes [4.10]. High–temperature oxide (HTO) was employed in the fabrication of only one type of sensor (IS–502) described in this work for this very purpose. The layers were

deposited at 912 ºC for approximately 90 minutes to produce layers 500 nm thick, Sect. 4.6.2.1.

4.4.3 Junction fabrication

Two types of junctions are realized in the fabrication of high–purity silicon soft X–ray sensors: the p^+-n^- junction and the high–low junction. Various junction fabrication techniques are briefly described in this section. Advantages and disadvantages of the different techniques and which techniques were used to fabricate the sensors described in this work are mentioned.

4.4.3.1 *P–n* junctions

Impurities are introduced into pure silicon for the specific purpose of altering its electrical characteristics. Shallow–level, pentavalent–impurity atoms such as phosphorous with donor ionization energies given by $(E_c - E_d)$ readily donate their fifth valence electrons to the silicon crystal at room temperature resulting in the formation of n–type silicon. Shallow–level, trivalent–impurity atoms such as boron with acceptor ionization energies of $(E_a - E_v)$ readily accept electrons from the silicon crystal at room temperature, thereby creating p–type silicon. Virtually all shallow level impurities will be ionized at normal operating temperatures.

A p–n junction is fabricated in silicon by the deliberate introduction of shallow–level, trivalent (pentavalent) dopant atoms into a predefined area of n–type (p–type) silicon. The location where the impurity changes from p–type to n–type defines the p–n junction. As described in Sect. 4.3, the first diodes, which were used to experimentally verify the theory of p–n junction characteristics, were produced by the grown–junction method. As this was unsuitable for mass production, the alloy–junction method was subsequently introduced. However, predetermination and control of the junction depth using this technique proved to be a major difficulty. Research into other methods for the fabrication of p–n junctions led to the development of such procedures as epitaxy, diffusion and ion–implantation.

Epitaxy is a process of preserved, ordered growth of a thin, monocrystalline layer upon a crystalline substrate. The epitaxial layer is usually doped opposite to that of the substrate for insulation purposes. Silicon epitaxial layers serve in bipolar, JFET and VMOS technologies, as well as in some NMOS and CMOS technologies, as regions of proper resistivity and conductivity within which the device is fabricated. The silicon substrate in these cases serves as the seed crystal for the epitaxial growth and as a mechanical support.

As epitaxial layers are characteristically thin layers, and as it is very difficult to grow an epitaxial layer with a resistivity over 500 Ω–cm, this technology is rarely used in the fabrication of sensors for the detection of high–energy electromagnetic or nuclear–particle radiation.

Diffusion as a fabrication step in silicon planar processing is an important method for the introduction of a predetermined concentration of impurity atoms into a specific region of the silicon lattice in order to alter its conductivity. Diffusion is performed through window openings in a (silicon dioxide) mask, which overlies the silicon substrate. Common n—type dopants used in silicon planar technology include phosphorous (P), arsenic (As) and antimony (Sb), while boron (B) is the most widely used p—type dopant. All these dopants are substitutional diffusers, i.e. they move through the crystal lattice by jumping from one lattice site to another. The rate of movement is different for each dopant and is characterized by the diffusion coefficient. Assuming this coefficient is concentration independent, the diffusion of shallow impurities into silicon of the opposite type at elevated temperatures ($700\,^{o}C < T < 1200\,^{o}C$) can be approximated by the linear diffusion equation [4.10]. From the large amount of research conducted in the area of shallow impurity diffusion in silicon, solutions have been found for the linear diffusion equation when the diffusion is carried out under constant—source conditions, under limited—source conditions and under conditions where an initial constant—source diffusion is performed (predeposition) followed by a limited—source diffusion (drive—in) [4.10]. Dopant interactions which occur during diffusion are well—documented [4.9–4.10].

Ion—implantation is an alternative technique for the introduction of impurity atoms into the single—crystal silicon substrate in order to alter its electrical properties. In this technique, an ion implanter is used to first convert neutral dopant atoms into ions. These ions are then purified, collimated into an ion beam and accelerated to an energy between $50 - 500$ keV. The ion beam is then directed at the silicon surface and subsequently deflected to scan the wafer. The energy of the beam is chosen so that the ions can be implanted somewhere between $50 - 1,000$ nm below the silicon surface, wherever it is not protected by a sufficiently thick insulating mask [4.9]. Retrograde ion implantation, a relatively new technique used in some CMOS and specialty processes (e.g. the process used to fabricate microelectronics and radiation sensors on the same high—purity silicon substrate), uses energies between $700 - 1200$ keV in order to obtain comparatively deep implantations.

The accelerated ions lose their energy through collisions with the substrate or with the insulating mask. The total travelled distance from the surface entry point is termed the range. The projection of this range along the direction of the incident beam is called the projected range, which is characterized by a mean value (R_p) and a standard deviation along the direction of the ion (ΔR_p), also called the straggle. Light ions, e.g. B^+, tend to transfer very little energy with each collision and thus are able to be deflected through large scattering angles. The range and the straggle in this case are comparatively large. Heavy ions, e.g. As^+, transfer large amounts of energy with each collision and therefore the range and the straggle tend to be relatively small.

The concentration of dopants introduced into the material is determined by the dose, while the range is determined by the ion energy. The statistical target distribution of the ion implantation of the silicon substrate is satisfied by a one—dimensional Gaussian function [4.9]. The doping profile due to the ion—implantation results from the integration of this function over the limits $\pm \infty$ [4.9].

The collision of the implanted ions with the substrate atoms causes material

damage. Heavy ions tend to create considerably more damage than light ions. In both situations however, a process of thermal annealing must occur in order to restore the crystal structure, to recover the minority–carrier lifetime and to recover the charge–carrier mobilities, as well as to activate the implanted carriers. This annealing procedure commonly takes place in conventional furnaces at temperatures between 600 – 900 ºC.

P–n junctions were fabricated in the sensors described in this work through the application of boron–ion implantations through windows in the passivation oxide layers into the high–resistivity *n*–type silicon substrates. Thermal annealing followed these procedures. The doses and energies of the implantations and the temperatures of the anneals are given specifically for each type of sensor in Sect. 4.6.

Diffusion is a high temperature procedure (800 ºC < T < 1200 ºC), whereas ion implantation is a room temperature technique (although the wafers may heat up to approximately 100 – 200 ºC during the operation). The use of ion implantation therefore avoids the material deterioration that often results from high temperature processing, e.g. stresses in the material can form during the warm–up and cool–down stages, which can create dislocations in the crystal structure. In addition, asymmetric, nearly–abrupt *p–n* junctions can be realized with ion implantations through the use of proper ion energies, ion doses and mask profiles. Moreover, very thin junctions can be fabricated (R_P values of 50 nm have been realized) using the ion–implantation technique in order to reduce the effects of energy straggling. However, ion implantation does damage the crystal structure. If the subsequent anneal procedure is insufficient, low minority–carrier lifetimes and mobilities and high leakage currents will result.

The effect the type of junction processing performed had on the device parameters was tested in conjunction with the application of gettering techniques. Although the *p–n* junctions of all the sensors and sensor arrays were realized with ion–implantations, the high–low junctions were realized with either diffusions or ion implantations. The resulting device parameters (i.e. the recombination lifetimes and leakage currents) were then compared. The process sequences are detailed in Sect. 4.6.1.3 and the measurement results are presented in Sect. 5.2.3.

4.4.3.2 High–low junctions

A high–low junction is fabricated in silicon by the deliberate introduction of shallow–level, trivalent (pentavalent) dopant atoms into a predefined area of *p*–type (*n*–type) silicon, i.e. the type of silicon does not change, only the doping impurity concentration. The location where the impurity concentration changes defines the high–low junction. A high–low junction is commonly fabricated on the backside of most high–purity silicon radiation sensors through the utilization of a phosphorous or an arsenic diffusion or ion implantation. The presence of a high–low junction tends to reduce the diffusion contribution to the leakage current by diminishing the effective diffusion length and by minimizing carrier injection from the backside contact.

High–low junctions were fabricated in the sensors described in this work through the application of either a phosphorous diffusion or an arsenic ion implantation. The processing specifics are detailed in Sect. 4.6.1.3 and the measurement results are presented in Sects. 5.2.3.

4.4.3.3 Gettering techniques

Techniques employed to selectively remove atoms of a given class are known as gettering techniques [4.10–4.17]. Several different gettering methods compatible with standard integrated–circuit fabrication techniques for the reduction or removal of transition group elements, such as heavy metals, from the active regions of microelectronic devices are frequently used in order to reduce leakage currents in junctions and capacitors (e.g. in dynamic and static RAMs, ROMs and microprocessors) and to reduce quiescent device dissipations (e.g. in CMOS devices). Metallic impurities form generation–recombination centers for carriers.

Independent of the gettering method employed, three physical effects are necessary in order for effective gettering to take place: impurity release, impurity diffusion and impurity capture. The impurities must first be released if they are captured in extended bulk defects. The impurities must then be able to diffuse to a capture zone, which often exists on the wafer back surface, i.e. the proper time and temperature conditions must be present for complete diffusion of the impurities existing within the bulk to diffuse to a capture zone fabricated on the wafer backside. Finally, the impurities must be captured at some sink within the capture zone [4.10].

In Sect. 2.2.1, it was concluded that the leakage current in high–purity silicon sensors is dominated by generation in the depletion region. The presence of impurities that introduce energy levels near the center of the silicon bandgap, e.g. metals such as gold, iron and copper, causes a significant increase in this component of the leakage current and a significant decrease in the generation lifetime [4.10–4.11]. Many gettering techniques are based on the high affinity of heavy metals for damaged regions. Damaged regions and defects can be produced through the use of several different methods. The most common include the intrinsic gettering technique of oxygen precipitation [4.10], as well as extrinsic gettering techniques, such as mechanical abrasion [4.10], thin–film polysilicon and silicon nitride deposition [4.11–4.13], ion implantation [4.14–4.15] and phosphorous doping [4.15–4.17].

Silicon wafers, prepared from ingots grown by the Czochralski (CZ) technique, contain substantial amounts of interstitial oxygen. Oxygen is an impurity which arises from the dissolution of the crucible during growth [4.10]. When the oxygen concentration exceeds a threshold concentration of approximately 6×10^{17} atoms/cm^3, the oxygen will precipitate at common processing temperatures, usually heterogeneously [4.10]. A gettering treatment, called intrinsic gettering, is based on this oxygen precipitation and it produces a variety of defects. A high–temperature cycle first removes oxygen from the surface by evaporation. The depth of the oxygen–free region is a function of the time and the temperature of the cycle. Additional thermal cycles then promote the precipitation of oxygen and the formation of defects in the wafer bulk.

Microelectronic devices can then be fabricated in the surface defect–free zone.

In the majority of microelectronic devices, the bulk of the wafer serves no other function than providing mechanical support. In these cases, intrinsic gettering is a very useful gettering technique. However, as the active regions of the majority of high–purity silicon soft X–ray sensors extend through the entirety of the bulk, this technique cannot be applied. Moreover, most high–purity silicon ingots are prepared by the floating–zone (FZ) method. No crucible is involved in this silicon growth technique and oxygen is present only in very small quantities. However, extrinsic gettering techniques, i.e. mechanical abrasion, thin–film polysilicon and silicon nitride deposition, ion implantation and phosphorous doping, are applicable.

Damaged regions in high–purity silicon radiation sensors are characteristically produced on the back surface of the wafer, far from the active region. Mechanical abrasion methods include such techniques as lapping or sand–blasting. Damage can also be created by a focused laser beam. The backside of the silicon lattice becomes damaged by this mechanical abrasion and during thermal processing, dislocations, which act as trapping sites for fast–diffusing species (i.e. most heavy metals), emanate from the backside. Provided that the stresses placed on the wafer during processing are minimal, the dislocations will remain localized on the backside [4.10].

The deposition of approximately 1 μm of polysilicon on the backside of the wafer, after the chemical etching and polishing of the surface, is another useful gettering technique [4.10–4.11]. In this case, the highly disordered grain boundary regions in the polysilicon act as trapping sites for fast–diffusing species. When this polysilicon layer is heavily doped with phosphorous, its gettering properties are enhanced and it can also serve as a backside contact [4.11–4.15]. Ion implantation is an additional extrinsic gettering technique, as it also produces mechanical damage [4.14–4.15].

Finally, the diffusion of phosphorous, often performed on the backsides of wafers, has also accomplished the effective gettering of heavy metals [4.15–4.17]. Classical phosphorous–doping gettering methods have been based on a heavy phosphorous (POCl$_3$) deposition followed by a high temperature anneal, while modern methods employ moderate to low annealing temperatures after the deposition [4.15]. It has been explained that if heavy metals are present in the form of precipitates in the silicon wafer before processing begins, a phosphorous deposition followed by a high temperature anneal will dissolve and effectively getter the metal impurities, as the solid solubility of metal impurities increases rapidly as the temperature increases. However, silicon ingots (especially float–zone silicon ingots) can presently be prepared with extremely low heavy metal concentrations. Any heavy metals introduced during processing must be segregated far from the active zones by selective segregation, which is most effective at moderate annealing temperatures [4.12].

Recently, phosphorous diffusion has been found only to be effective in the removal of heavy metals when the phosphorous surface concentration C_s and the diffusion temperature T are kept within a well–defined domain, with C_s high and T low. Gettering has been found to be ineffective if the opposite is true. The boundary between effective and ineffective gettering has been found to be an iso–Fermi level curve with $(E_c - E_f) = 0.15$ eV [4.15]. However, in addition to the phosphorous surface concentration C_s and the temperature of the diffusion T, the diffusion time is also of vital importance to the success of the gettering step,

especially if the entire thickness of the wafer is to be depleted of heavy metal impurities. The anneal time must be long enough to allow the transport of the heavy metal impurities across the entire thickness of the wafer.

In the phosphorous doping method of gettering, two mechanisms have been found to be responsible for serving as the sinks in the gettering of heavy metals. Phosphorous has been shown to getter by an ion–paring mechanism [4.15–4.17]. In addition to phosphorous ions, the defects and dislocations introduced by the phosphorous and the strain field around the localized dislocations also contribute to gettering [4.16].

In order to investigate two different gettering techniques: a backside arsenic implantation and a backside phosphorous diffusion, two different groups of basic high–purity silicon soft X–ray sensors were fabricated, Sect. 4.6.1.3. The process sequences used were based on the initial basic process for the fabrication of high–purity silicon soft X–ray sensors; the difference lying in the realization of the backside high–low junction. The first group employed an arsenic implantation as a gettering technique (thus being identical to the basic process) and the second group employed a phosphorous diffusion. In order to assess the degree of success the specific gettering technique had on the quality of the resulting sensors, recombination lifetime measurements were taken using the contactless–microwave measurement technique described in Sect. 4.7.2.2 after several steps during the processing and leakage current measurements were performed upon completion of the fabrication. The measurement results are presented in Sect. 5.2.3.

4.4.4 Metalization and interconnection

Interconnections between device contacts and external terminations are provided by conductive films. These films must satisfy a very demanding set of requirements. The material must be highly conductive, i.e. have a low sheet resistance, and must be able to form low resistive, ohmic contacts. It must be able to withstand high current densities without electromigration or material failure. A low temperature deposition procedure must be available for its procurement and the deposited film must be highly adherent to insulator surfaces. It must also be easy to pattern and etch and be reliable throughout long term operation [4.9, 4.10].

Most of these requirements are met by aluminum and gold films. Other metals with well–developed deposition technologies include Al–Si–Cu, Al–Cu–Cr, Ti–Al and Ti–W alloys, Ti and Mo and silicides of Mo, Pd, Pt and Ta. Other films used for interconnection purposes include heavily–doped silicon and polysilicon.

Aluminum and aluminum with $1-2$ % silicon are the films most widely used in silicon planar technology. The addition of $1-2$ % silicon to aluminum prevents the creation of aluminum spikes through shallow junctions. Aluminum is easily deposited by vacuum evaporation and has a resistivity of approximately $2.7 \ \mu\Omega$–cm. Good ohmic contacts can be made with aluminum to both p^+– and n^+–type silicon when the metal deposition is followed by an alloying procedure performed at $400-450$ °C. It adheres well to insulator surfaces and it is easy to pattern and etch. However, there are disadvantages associated with the use of

aluminum. Under high current densities aluminum atoms tend to migrate in the direction of current flow and in the presence of moisture, corrosion of the aluminum layer can occur. These electromigration and corrosion problems can be reduced and workable solutions (i.e. the addition of copper) are available [4.9, 4.10].

Gold is a more difficult metal to work with, as it requires the concurrent use of titanium or tungsten in order to form interconnections. In addition, it produces deep–level recombination centers in silicon. This last problem is intensified by the fact that gold is a rapid diffuser in silicon. Heavily–doped diffused silicon and polysilicon interconnections have sheet resistivities that are too high to satisfy the demands for a general use interconnection material, but they serve well for short under–crosses, for gate materials and for local interconnections.

Double–layer metalizations and interconnections can be made between heavily–doped silicon, heavily–doped polysilicon or aluminum first level conductive layers and aluminum second level conductive layers, if an insulating layer separates the two conducting layers.

As the *p–n* junctions of the sensors described in this work were shallow, realized through ion implantations, aluminum saturated with silicon was evaporated to produce thin–film metal layers. Due to the different sticking coefficients of aluminum and silicon, the final composition of the deposited metal was aluminum with approximately $1 - 2\%$ silicon.

The second metalization layers associated with the sensor arrays consisted of pure aluminum, as no threat of junction short–circuiting existed at this stage. The layer thicknesses are given in Sect. 4.6.

4.5 ADVANCED MULTILEVEL–CONDUCTION PROCESS TECHNIQUES

With the current international efforts to increase the number of circuit elements per chip and to reduce the minimum line widths came the introduction and perfection of multilevel–conduction techniques. Two of the most frequently used techniques include the use of heavily–doped polysilicon and aluminum, and the use of multilevel aluminum layers, as the conductors.

4.5.1 Polysilicon and aluminum

In the design of the first sensor array, IS–502, Fig. 3.1(a), double–layer conduction was realized through the use of heavily–doped polysilicon bands, which served as the lower conductors, and aluminum bands, which served as the upper conductors. As described in Sect. 3.1.1, the aluminum strips connected to the sensing elements were extended off to the right side of the matrix. Heavily–doped polysilicon bands were then connected to the aluminum strips to serve as the lower conductors in the double–layer conduction scheme. The polysilicon was deposited by LPCVD techniques and doped by phosphorous diffusion to obtain a sheet resistivity of $10 - 15\,\Omega/\text{sqr.}$, as described in

Sect. 4.4.2.1. A silicon dioxide layer was then deposited by LPCVD, high–temperature oxide (HTO) techniques, Sect. 4.4.2.2, to serve as the insulator. The polysilicon was first slightly oxidized before the HTO deposition in order to fabricate an optimal interface between the two layers. Finally, one aluminum band was then patterned above each set of three polysilicon strips associated with the same row to serve as the upper conductor in the double–layer conduction scheme. This design, IS–502, Fig 3.1(a), has the disadvantage that large arrays of small elements cannot be fabricated, due to the fact that as the number of elements per row increases, the number of aluminum strips traversing the row elements must increase, which increases the necessary size of the elements in the vertical dimension.

4.5.2 Double–layer aluminum

Through the use of the double–layer aluminum technique, the size of the sensor array can be reduced, but more importantly, large arrays of small elements can be fabricated.

In the designs IS–531, IS–562, IS–559 and IS–560, the first layer metalization was performed as stated in Sect. 4.4.4. The dielectric employed was silicon dioxide deposited at low temperatures $(250 - 400 \,^{o}C)$ either by PECVD or silox low–temperature SiO_2 deposition techniques [4.11]. The second metalization layers associated with the sensor arrays consisted of pure aluminum, as no threat of junction short–circuiting existed at this stage. The layer thicknesses are given in Sect. 4.6.

4.6 PROCESS SEQUENCES

The fabrication of the basic high–purity silicon soft X–ray sensors described in this work is described in Sect. 4.6.1. The process sequence developed is pictorially illustrated in a simplistic style. Details about the processing are given in the text. The modifications that were made to this basic process in order to realize the high–purity silicon soft X–ray sensors with polysilicon resistive structures in series and in order to investigate two gettering techniques are then outlined in Sects. 4.6.1.2 and 4.6.1.3, respectively.

The process sequences developed to fabricate the high–purity silicon soft X–ray sensor arrays are subsequently illustrated in Sect. 4.6.2. The first sequence, outlined in Sect. 4.6.2.1, is based on the use of highly–doped polysilicon as a lower conductor and aluminum as the upper conductor in a double–layer conduction technique. At the time of its development, the technique of double–layer metalization had not yet been perfected in our laboratory. However, upon its perfection, the process sequence of Sect. 4.6.1.2, i.e. the basic process sequence modified in order to realize polysilicon resistive structures in addition to the sensors, could directly be utilized with the addition of two subsequent steps: a low–temperature deposition of silicon dioxide and a second layer metalization.

These steps are illustrated and described in Sect. 4.6.2.2.

4.6.1 High–purity silicon soft X–ray sensors

4.6.1.1 Basic process sequence

The process sequence developed to fabricate the basic high–purity silicon soft X–ray sensors described in this work is simplistically illustrated below.

The necessity of employing high–purity silicon as the starting material is thoroughly explained in Sect. 4.2. All the cautionary measures described in that section, which are necessary to perform in order to maintain the original substrate resistivity throughout the processing, were taken.

The basic process begins with a dry thermal oxidation of the silicon substrate. The surface is passivated with an oxide layer in order to reduce the number of surface states, the amount of surface charge and the magnitude of the surface leakage current, Sect. 4.4.1. The thermal treatment was performed in an atmosphere of dry oxygen five to six hours subsequent to the thorough cleaning of the ovens with an HCl/H_2O solution. A warm–up in a nitrogen atmosphere was initially performed at 1100 ºC for 15 minutes in order to allow the wafers to come into thermal equilibrium with their environment before the oxidation began in an effort to obtain a uniform oxide layer. The oxidation was performed at 1100 ºC for approximately 140 minutes to obtain an oxide layer approximately 200 nm thick. In order to avoid thermal stress, this step was followed by a cool–down at 900 ºC in a nitrogen atmosphere for 120 minutes. In addition, the wafers were inserted and retracted at slow rates.

Windows, defining the subsequent diode areas, were then opened in the SiO_2 layer after the wafers were coated with 1 μm of positive photoresist, soft–baked, exposed to the photomask, developed, hard–baked and etched in a wet chemical SiO_2 etch, (1:6; HF (40 %): Ammonium fluoride).

Subsequently, a dry oxidation at 950 ºC for 40 minutes was performed in order to cover the previously defined window areas with a thin layer (40 nm) of oxide. This oxidation provides a layer of known thickness. The presence of the oxide layer significantly reduces the occurrence of ion channeling during ion–implantation procedures. Again, warm–up and cool–down operations were performed in nitrogen atmospheres at 950 ºC for 15 minutes and at 900 ºC for 60 minutes, respectively.

Ion implantation was chosen as the technique to realize the p^+-n^- and the n^+-n^- junctions, as this process was shown to produce high–purity silicon sensors with the best characteristics [4.1]. The wafers were implanted through the thin oxide at an angle of approximately 7 ºC to the (111) axis in order to avoid channeling effects. For the p^+-n^- junction fabrication, a p–type implantation was performed using boron atoms at an energy of 70 keV and a dose of 5 x 10^{14} ions/cm^2. Given these specifications, and taking the protecting oxide layer into consideration, the junction was calculated to form at a depth of 180 nm. The n^+-n^- junctions were

HIGH–PURITY SILICON

DRY OXIDATION

DEFINE DIODE AREAS

DRY OXIDATION

IMPLANTATION
ANNEAL

METALIZATION
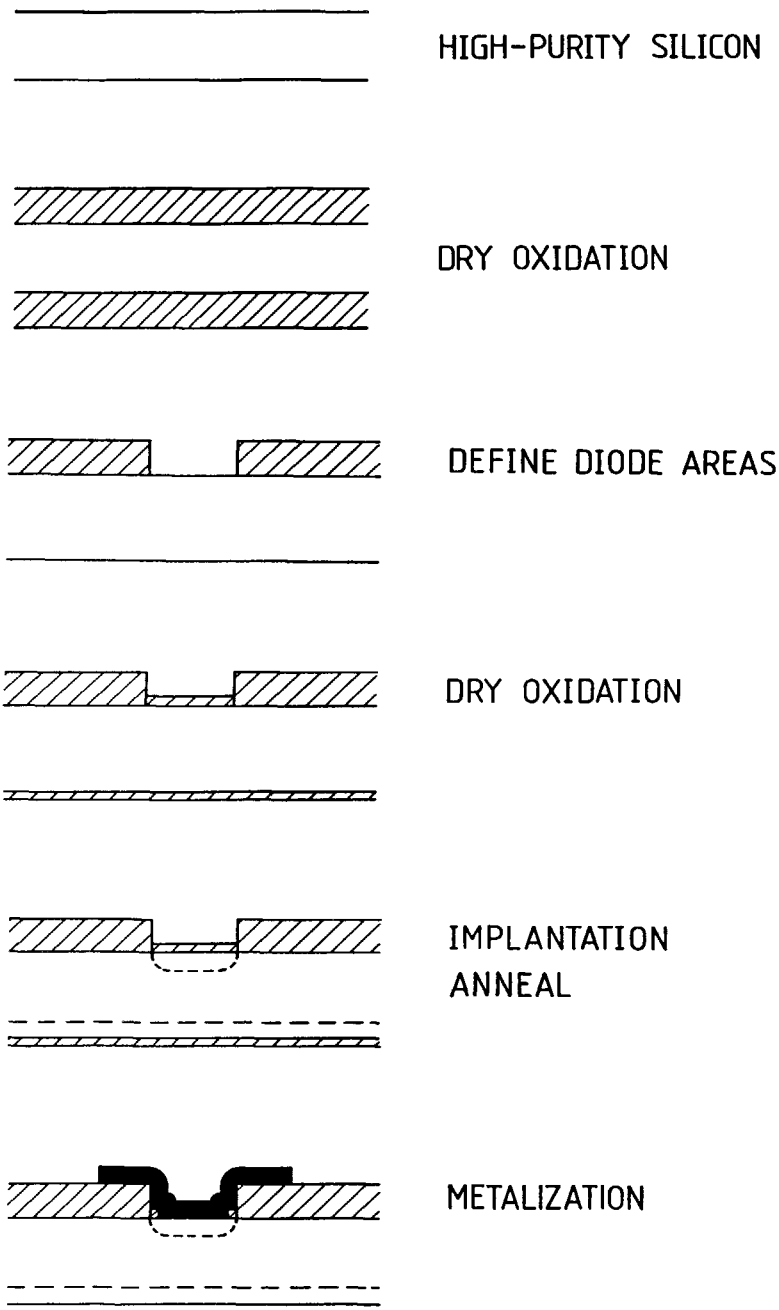
Fig. 4.1   *Process sequence used to fabricate basic high–purity silicon soft X–ray sensors.*

fabricated by an arsenic implantation performed on the backside of the wafer at an energy and dose of 150 keV and 5×10^{15} atoms/cm^2, respectively. Given these specifications, and taking the protective oxide layer into consideration, the junction was calculated to form at a depth of 50 nm. The implantations were annealed at 600 °C for 30 minutes.

Following contact window opening, an aluminum/silicon composition was vacuum evaporated to obtain a layer of aluminum with $1-2$ % silicon 500 nm thick, which was subsequently patterned by standard lithographic techniques. Finally, an aluminum alloy step was performed at 450 °C for $10-20$ minutes in an atmosphere of 75 % N$_2$ and 25 % H$_2$ to obtain good contact and to reduce the contact resistivity.
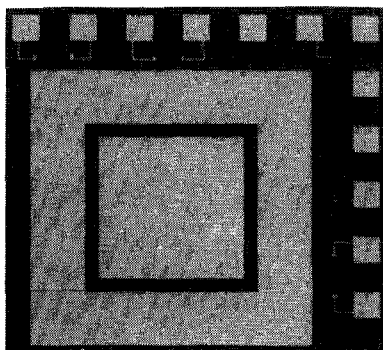
Fig. 4.2 *Photograph of a basic high–purity silicon soft X–ray sensor, i.e. a 0.25 mm^2 diode surrounded by a guard ring.*

4.6.1.2 Modifications to realize resistive structures

The modifications made to the basic process in order to fabricate polysilicon resistive structures in series with high–purity silicon soft X–ray sensors are illustrated and discussed in this section.

The first modification to the basic process occurs after the initial oxide passivation step and involves the deposition of polysilicon. The polysilicon was deposited by LPCVD techniques, Sect. 4.4.2.1. The deposition temperature was 625 °C, while the time was set after an initial test run in order to obtain a layer approximately 400 nm thick.

After its deposition, the polysilicon was doped through the use of a phosphorous deposition technique. The source used was POCl$_3$, the temperature: 950 °C, the time: 15 minutes and the atmosphere: a combination of oxygen and hydrogen. Immediately following this step, the thin layer of phosphorous glass covering the doped layer's surface was removed by a quick dip (20 seconds) in a phosphorous–glass wet chemical etch, (3:6:91; HNO$_3$ (65 %):HF (40 %): H$_2$O). Sheet resistivities of $10-15$ Ω/sqr. were obtained.
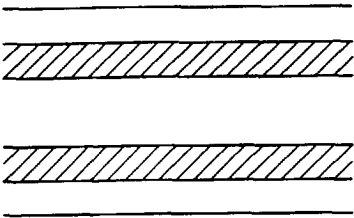
POLYSILICON DEPOSITION
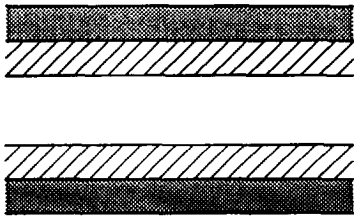
PHOSPHOROUS DEPOSITION

DEFINE DIODE AREAS
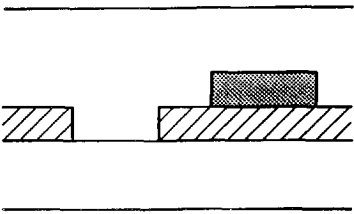
DEFINE RESISTIVE
STRUCTURES
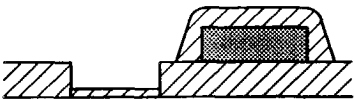
DRY OXIDATION
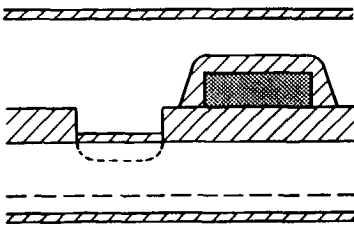
IMPLANTATION ANNEAL

Fig. 4.3 *Modifications made to the basic process (Fig. 4.1) in order to fabricate high–purity silicon soft X–ray sensors in series with polysilicon resistive structures.*

Identical windows, defining the subsequent diode areas, were then opened in the polysilicon and SiO_2 layers after the wafers were coated with 1 μm of positive photoresist, soft–baked, exposed to the first photomask, developed, hard–baked and successively etched in a polysilicon wet chemical etch (70:2:28; HNO_3 (65 %): HF (40 %): H_2O), followed by a SiO_2 wet chemical etch, (1:6; HF (40 %): Ammonium fluoride). The desired polysilicon structures were then defined by standard photolithographic techniques. The highly–doped polysilicon patterns serve as resistive structures whose resistance values can easily be altered by changing the time and/or the temperature of the $POCl_3$ deposition and thereby changing the polysilicon sheet resistivity, Eqn. (4.3).

Subsequently, a dry oxidation at 950 ºC for 170 minutes was performed in order to drive in the phosphorous, oxidize the polysilicon and cover the previously defined window areas with a thin layer of oxide. Warm–up and cool–down operations were carried out prior to and subsequent to the oxidation at 950 ºC for 15 minutes and at 900 ºC for 60 minutes, respectively, in nitrogen atmospheres. The thickness of the oxide layer above the polysilicon typically measured 100 nm, while the thickness of the oxide grown in the windows and on the wafer backside typically measured 80 nm. A SiO_2 back etch established the backside oxide thicknesses to 40 nm.

Ion implantation and metalization steps identical to those described in Sect. 4.6.1.1 were then performed. The thickness of the aluminum layer was in this case 600 nm.
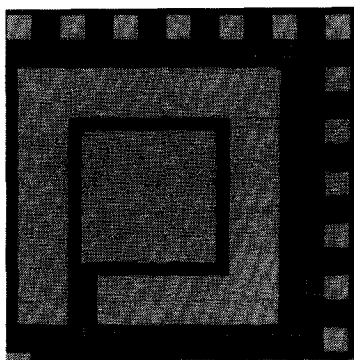
Fig 4.4 *Photograph of a high–purity silicon soft X–ray sensor, i.e. a 0.25 mm² diode surrounded by a guard ring, with a polysilicon resistive structure in series.*

4.6.1.3 Modifications to investigate gettering techniques

The modifications made to the basic process in order to investigate two gettering techniques are illustrated and discussed in this section.

The first gettering technique involved the use of a backside arsenic implantation to realize the n^+–n^- junction and therefore involved no alterations to

the basic process, Sect. 4.6.1.1.

The second gettering technique investigated the use of a backside phosphorous deposition to realize the n^+-n^- junction. In order to accomplish this, after the initial oxide passivation step, the SiO_2 layer was removed from the backside and a phosphorous deposition, identical to that used to dope the polysilicon layers, Sect. 4.6.1.2, was performed. The only other modification was that the arsenic implantation of the backside was not carried out.
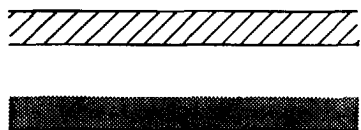
ETCH OXIDE ON BACKSIDE

PHOSPHOROUS DEPOSITION

Fig. 4.5 *Modifications made to the basic process (Fig. 4.1) in order to investigate the phosphorous gettering technique.*

The structures fabricated in this investigation are identical in appearance to the diode shown in Fig. 4.2.

4.6.2 High–purity silicon soft X–ray sensor arrays

The process sequences developed to fabricate the high–purity silicon soft X–ray sensor arrays based on double–layer conduction and double–layer metalization techniques are illustrated in Sects. 4.6.2.1 and 4.6.2.2, respectively.

4.6.2.1 Double–layer conduction arrays

The process sequence based on the double–layer conduction technique developed to fabricate high–purity silicon soft X–ray sensor arrays is illustrated and described in this section.

The first four processing steps are identical to those described in Sect. 4.6.1.2, except that the oxide passivation was achieved through a wet thermal technique. This technique was performed due to the fact that a thick oxide passivation layer was essential in this design and wet oxidation is a faster procedure than its dry counterpart. An oxide passivation layer 500 nm thick was necessary, as it served the additional purpose of acting as a dielectric separating the sensing diodes from those aluminum bands not directly connected to them.

Modifications then made are shown pictorially in Fig. 4.6. The polysilicon structures were first defined by standard photolithographic techniques. These structures serve two functions in this design. In one instance, they act as resistive structures, whose resistance values can easily be altered by changing the time and/or the temperature of the $POCl_3$ deposition. In the other case, they serve as the lower conductors in the double–layer conduction technique. The resistive and conductive structures are defined by standard photolithographic techniques.

A dry oxidation step followed to oxidize the polysilicon, as this material forms an optimal interface with LPCVD deposited oxide. The oxidation took place in a dry oxygen atmosphere at 950 ℃ for 170 minutes with the resulting growth of an oxide layer 100 nm thick above the polysilicon. Warm–up and cool–down operations took place prior to and subsequent to the oxidation procedure at 950 ℃ for 15 minutes and at 900 ℃ for 60 minutes, respectively.

A silicon dioxide layer was then deposited by LPCVD techniques, Sect. 4.4.2.2, at a temperature of 910 ℃ for 90 minutes in the formation of a layer approximately 500 nm thick.

The diode areas were defined by standard photolithographic techniques. The last three steps, i.e. the dry oxidation, the implantation and anneal and the metalization, were identical to those depicted in Fig. 4.3, with the exception that the metal layer was 1500 nm thick.

A photograph of a fully fabricated high–purity silicon soft X–ray sensor array whose principle of operation is based on a double–layer conduction technique, IS–502, is shown in Fig. 4.7. The resistive coupling is clearly portrayed on the left–hand side of the photograph, while the capacitive coupling is clearly portrayed on the right–hand side. The schematic of this sensor array is shown in Fig. 3.1(a).

4.6.2.2 Double–layer aluminum arrays

The process sequence based on the double–layer metalization technique developed to fabricate high–purity silicon soft X–ray sensor arrays is illustrated and described in this section.

The process sequence of Sect. 4.6.1.2, i.e. the basic process sequence modified in order to realize polysilicon resistive structures in series with the high–purity silicon soft X–ray sensors, could directly be utilized for the fabrication of high–purity silicon soft X–ray sensor arrays with the addition of two subsequent steps: a low–temperature deposition of silicon dioxide and a second layer metalization. Note that the two arrays designed without resistive structures within the matrices, i.e. IS–559 and IS–560, were fabricated using the same sequence that was used to fabricate those arrays with resistive structures, i.e. IS–531 and IS–562. However, the mask defining the polysilicon structures was altered. This was done in order to make sure that any differences between the two groups of arrays with respect to the device noise originated from the differences in the device design and not from differences in the device processing.

DEFINE RESISTIVE
AND CONDUCTIVE
STRUCTURES

DRY OXIDATION

SILICON DIOXIDE
DEPOSITION

DEFINE DIODE
AREAS

DRY OXIDATION

IMPLANTATION
ANNEAL
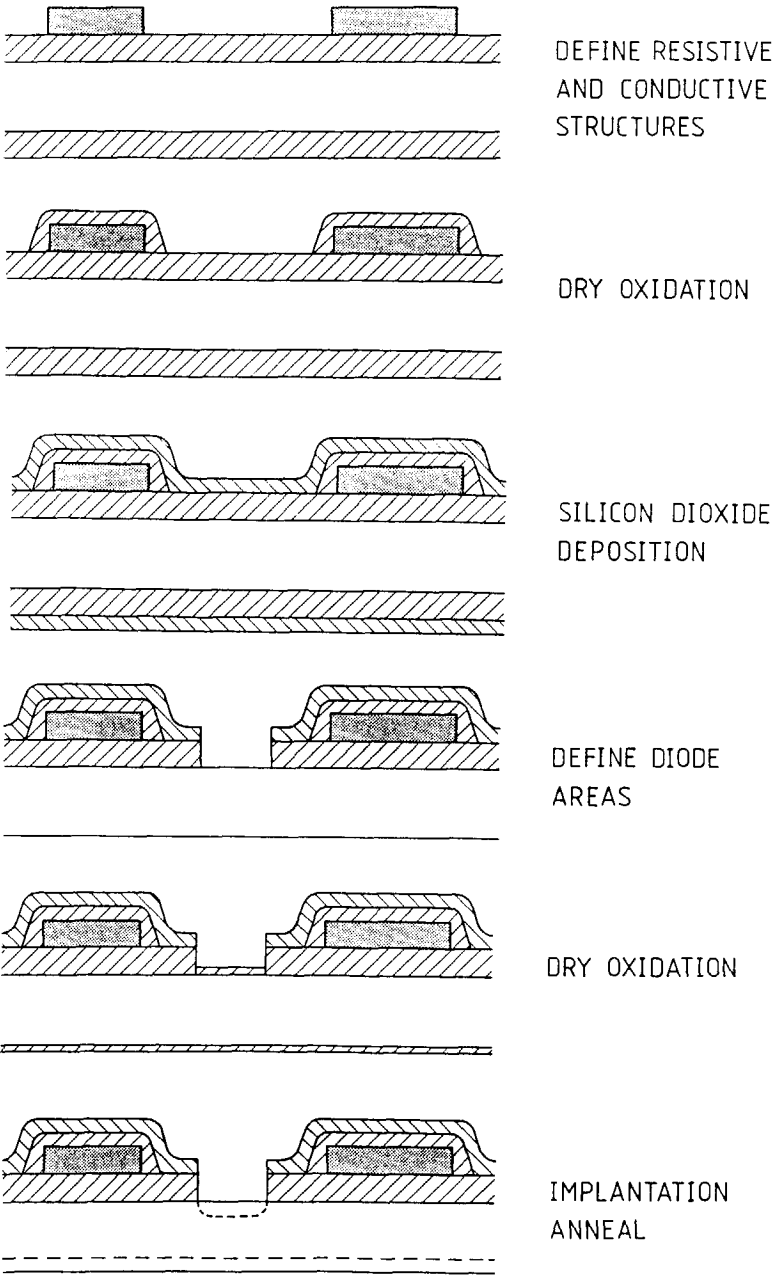
Fig. 4.6 *Modifications made to the process sequence used to fabricate high–purity silicon soft X–ray sensors in series with polysilicon resistive structures (Fig. 4.3) in order to realize two–dimensional high–purity silicon soft X–ray sensor arrays based on the double–layer conduction technique.*
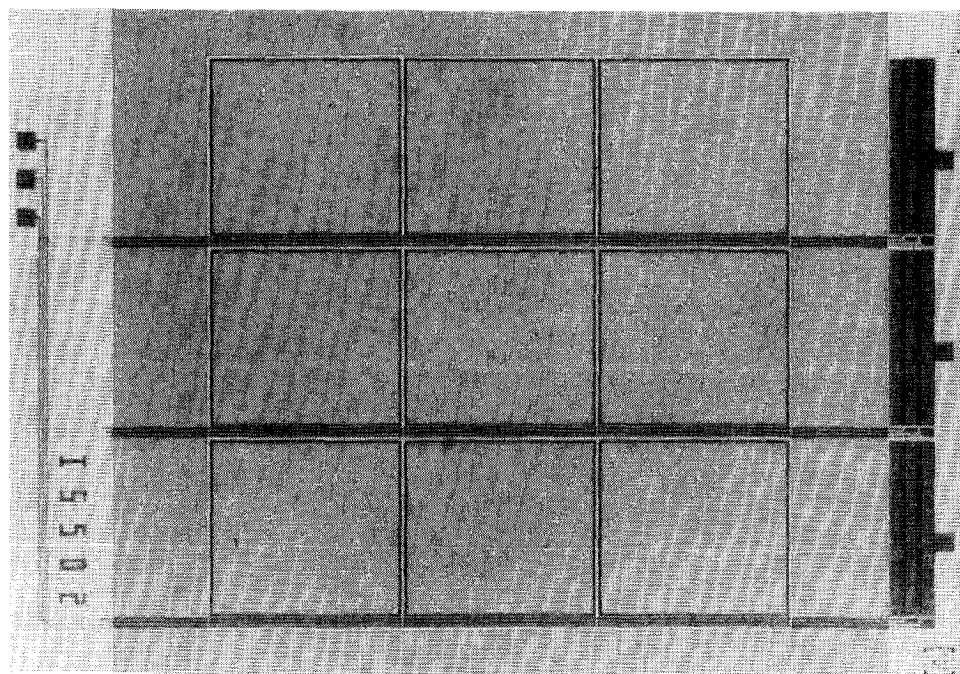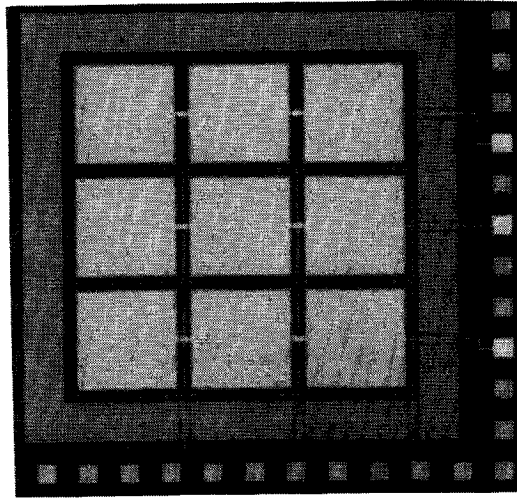
Fig. 4.7   *Photograph of a high–purity silicon soft X–ray sensor array after full fabrication whose principle of operation is based on a double–layer conduction technique (IS–502). The resistive coupling is portrayed on the left–hand side of the photograph, while the capacitive coupling is portrayed on the right–hand side.*

After the first layer aluminum had been vacuum evaporated, patterned and scintered, the first of the two additional steps took place, i.e. the low–temperature deposition of silicon dioxide, Fig. 4.8. This step was performed at Philips Research Laboratories in Eindhoven, the Netherlands with one of two different techniques. One technique was the low–temperature PECVD of silicon dioxide (employed with IS–531) and the other was the low temperature silox deposition of silicon dioxide (employed with IS–559, IS–560 and IS–562), Sect. 4.5.2. It was evident from measurements taken before and after each technique was performed that neither technique influenced the device characteristics, Sect. 5.3.2. Which technique is utilized therefore makes little difference. The low–temperature PECVD was performed at a temperature of 250 ℃, while the silox deposition took place at a temperature of 400 ℃. The time for both operations was set after initial test runs in order to obtain layers approximately $100-120$ nm thick.

The second additional step involved the vacuum evaporation of pure aluminum in the formation of a second metalization layer 150 nm thick, Fig. 4.8. The second

LOW TEMPERATURE
SILICON DIOXIDE
DEPOSITION

SECOND LEVEL
METALIZATION
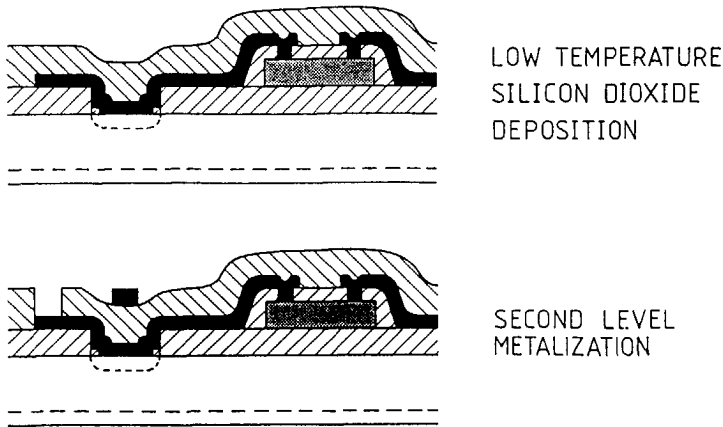
Fig. 4.8 *Modifications made to the process sequence used to fabricate high–purity silicon soft X–ray sensors in series with polysilicon resistive structures (Fig. 4.3) in order to realize two–dimensional high–purity silicon soft X–ray sensor arrays based on the double–layer metalization technique (IS–531, IS–559, IS–560 and IS–562).*

metalization layers were composed of pure aluminum, as there was no threat of junction short–circuiting at this stage. Finally, the aluminum was patterned and contact windows were opened in the deposited oxide layer.

Photographs of the high–purity silicon soft X–ray sensor arrays based on the double–layer metalization technique fabricated up to the first level metalization, i.e. IS–531, IS–562, IS–559 and IS–560, are shown in Figs 4.9(a), (b), (c) and (d), respectively. These photographs display the elemental diode structures, the resistive structures (if present) and the guard ring structures. The resistive coupling is clearly portrayed. Photographs of the sensor arrays after full fabrication were also taken, as they clearly portray the capacitive coupling. So as to avoid repetition, only one of the four photographs is shown. A photograph of the sensor IS–531 is shown after full fabrication, Fig. 4.10, depicting the second metalization layer and clearly portraying the capacitive coupling. In addition, photographs of this sensor array are shown with the different test structures in Figs. 4.11(a) and (b).

4.7 CHARACTERIZATION OF PROCESS STEPS

In order to develop a high–purity silicon soft X–ray sensor fabrication process, careful step–by–step monitoring of the process sequence is necessary in addition to the standard electrical parameter testing, which takes place upon completion of the device. This is achievable through the employment of a new
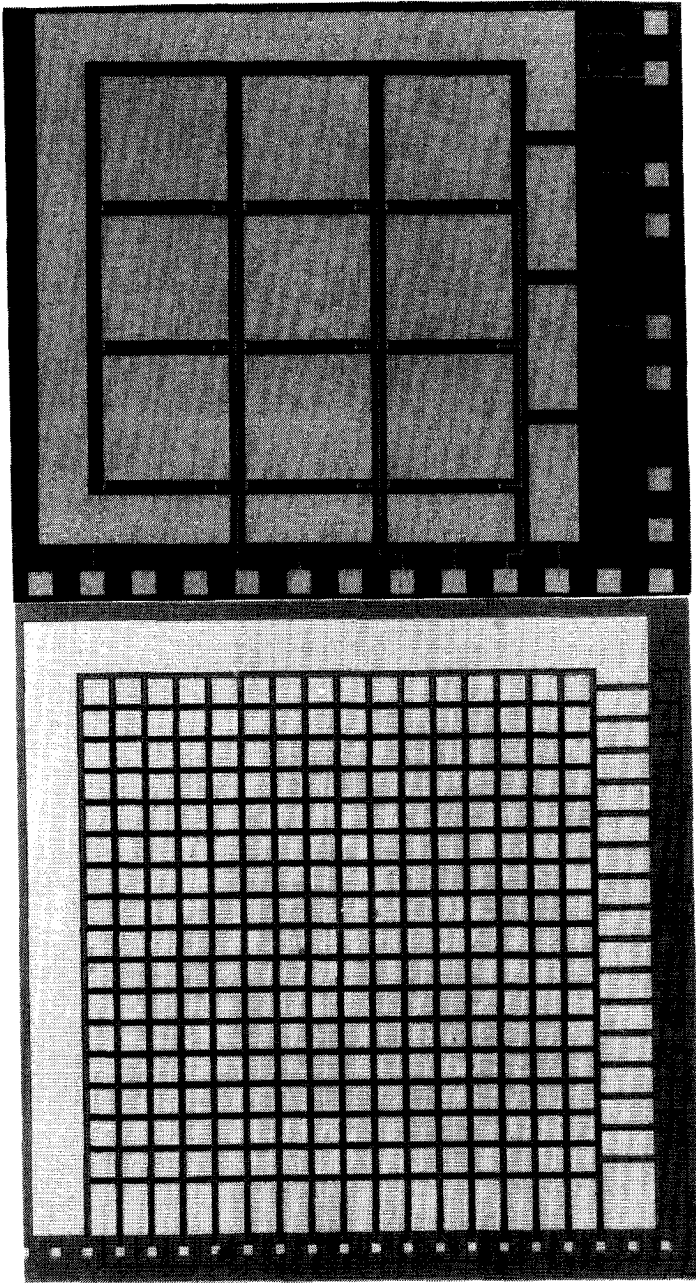
Fig. 4.9 *Photographs of high–purity silicon soft X–ray sensor arrays after the first level metalization whose principles of operation are based on a double–layer metalization technique and which employ polysilicon resistive structures to realize the resistive coupling: (a) IS–531 and (b) IS–562. The resistive coupling is clearly portrayed.*
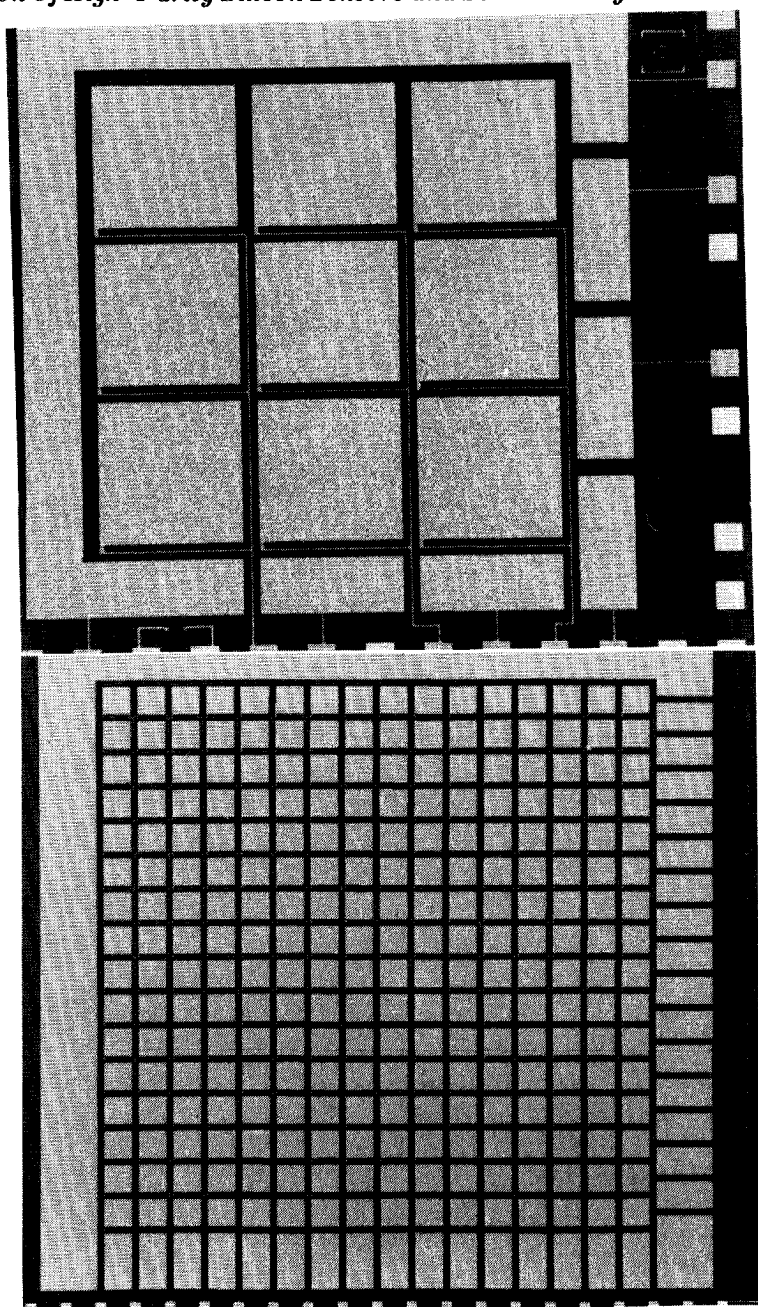
Fig. 4.9   *Photographs of high–purity silicon soft X–ray sensor arrays after the first level metalization whose principles of operation are based on a double–layer metalization technique and which employ aluminum interconnections to realize the resistive coupling: (c) IS–559 and (d) IS–560. The resistive coupling is clearly portrayed.*

Fig. 4.10 *Photograph of the high–purity silicon soft X–ray sensor array IS–531 after full fabrication clearly portraying the capacitive coupling.*

contactless–microwave technique, which is capable of monitoring the recombination lifetime after each processing step, in addition to the use of appropriate test structures for performing electrical parameter measurements. The test structures employed are first described in Sect. 4.7.1. An overview of lifetime measurement techniques follows in Sect. 4.7.2.

4.7.1 Test structures

Several test structures, which are particularly useful in characterizing the performance of a high–purity silicon soft X–ray sensor upon the completion of its fabrication, have been fabricated on the same chip as the sensor. These include several different diode structures, MOS capacitor structures and polysilicon resistive structures. Such test structures are not only important for the development and evaluation of a soft X–ray sensor fabrication process, but also for radiation damage evaluation. As radiation damage increases, the leakage current of diode structures is seen to increase and the flat–band voltage of MOS capacitor structures is seen to shift [4.18].

4.7.1.1 Diodes

There is no unique method of fabricating well–functioning high–purity silicon soft X–ray sensors. Processes are designed based on previous experience and on

the instrumentation available. The most important criteria to optimize in terms of sensor performance include the diode leakage current and energy resolution.

The diode is one of the simplest test structures to realize. As a test diode will be fabricated with the same technologies used to fabricate the soft X–ray sensor, it can be implemented in nearly every fabrication process without the need for extra processing steps.

Within the same chip as every high–purity silicon soft X–ray sensor array, diode structures with the same area as that of an array element were fabricated, Fig. 4.11(a). Some of these structures were directly read out, while others were connected in series to polysilicon resistive structures (with the same geometry as those within the array) before being read out. In this way, the elemental contributions of the leakage current and noise could be determined, as well as the effect the polysilicon structures had on the energy resolution.
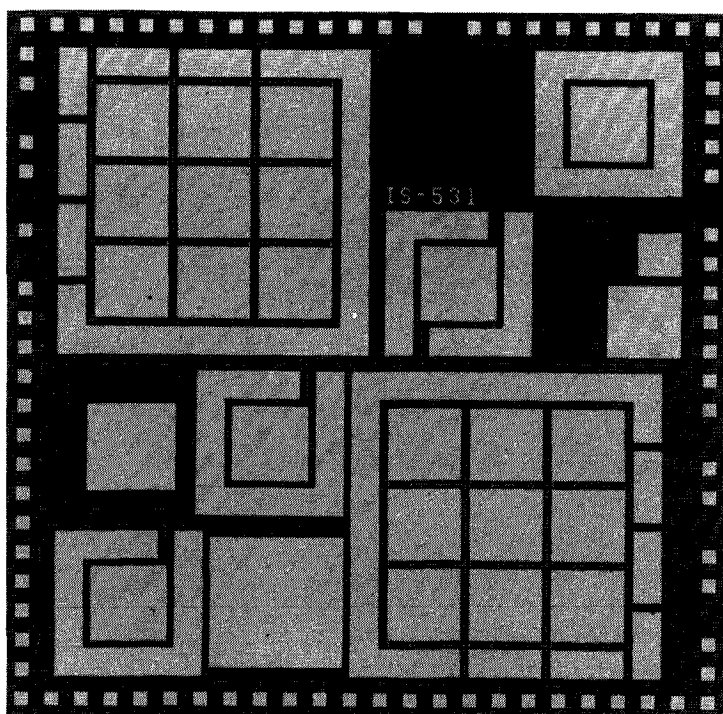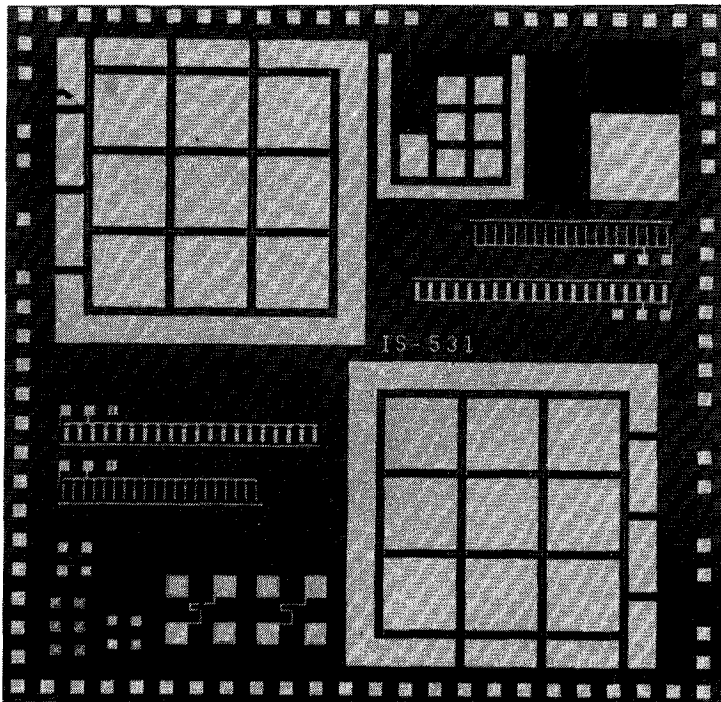

Fig. 4.11 (a) *Photograph of IS–531 (version A) after the first level metalization illustrating the sensor array with various diode test structures.*

4.7.1.2 MOS capacitors

The MOS capacitor is a very useful test structure and can deliver extensive

information. Like the diode test structure, it can be implemented in nearly every fabrication process without the requirement of extra processing steps.

The MOS capacitor consists of a metal gate (typically aluminum) separated by an insulating layer (typically silicon dioxide) from a semiconductor (high–purity silicon in this case). When a voltage is placed across the metal and the semiconductor, it is possible for the semiconductor surface to exist in one of four possible states: accumulation, flat–band, depletion or inversion.

The application of a positive voltage on the gate causes a sufficient number of electrons to collect at the semiconductor surface in order to match the applied positive charge. When the semiconductor material is n–type, the MOS capacitor will now be in the state of accumulation.

As there are always positive charges associated with a Si/SiO_2 interface, when no voltage is applied, the surface will already exist in the state of accumulation. At the surface, the energy bands will bend in the direction of a higher n–doped material. In order to flatten the energy bands, a specific negative voltage must be applied to the gate. That applied voltage which makes the bands flat is called the flat–band voltage V_{fb} and is given by

$$V_{fb} = V_{ms} - \frac{Q_{ox}}{C_{ox}} \tag{4.4}$$

where V_{ms} is the difference in potential between the metal and the semiconductor, Q_{ox} is the positive oxide charge near the Si/SiO_2 interface and C_{ox} is the capacitance of the fabricated oxide layer per unit area defined by the oxide dielectric divided by the oxide thickness.

Upon an increase in the magnitude of the negatively applied voltage, the bands at the surface will begin to bend in the opposite direction, because positive charges are attracted to the surface to match that negative voltage on the gate in excess of the flat–band voltage. The majority carriers will be depleted from the surface and a depletion layer will exist. This state is called depletion.

A point is reached when the silicon at the surface begins to turn from its original n–type to p–type. This point is called the beginning of effective inversion. The voltage at which effective inversion is reached is called the threshold voltage. With a further increase in the magnitude of the applied negative voltage, the MOS capacitor will go into strong inversion. The excess applied voltage requires a matched increase in the free charge concentration at the surface, which must be supplied by thermal generation.

When the capacitance is measured in the inversion state, C_{min}, and in the accumulation state, C_{ox}, the width of the depletion layer can be obtained

$$x_d = \frac{A \epsilon_0 \epsilon_{si}}{C_d} \tag{4.5}$$

where A is the area of the gate and C_d is the depletion layer capacitance, which

equals

$$C_d^{-1} = \frac{(C_{ox} - C_{min})}{C_{ox}C_{min}}$$ (4.6)

However, these equations are only true if the situational problem is determined to be one–dimensional in nature. Due to the lateral extension of the depletion region in high–purity silicon substrates, it becomes a multi–dimensional problem, and the measurement results are significantly dependent on the perimeter–to–area ratio of the gate.

In order to eliminate this lateral dependence, two MOS capacitor test structures, with the same perimeter but different areas, were fabricated on the same chip as the soft X–ray sensors and sensor arrays, Figs. 4.11(b). The C–V data of the two structures were obtained and then subtracted, thereby eliminating the sidewall capacitance and the effects of the lateral extension of the depletion layer, Sect. 5.3. From the subtracted C–V data, the doping profile of the substrate can be obtained, Sect. 5.3 [4.5].

Fig. **4.11** (*b*) *Photograph of IS–531 (version B) after the first level metalization illustrating the sensor array with various MOS capacitor and polysilicon resistive test structures.*

In addition, the MOS capacitor can be used to measure the generation lifetime. Various techniques are described in Sect. 4.7.2.1.

4.7.1.3 Polysilicon resistive structures

From test polysilicon resistive structures placed around the periphery of the chips with the same as well as different dimensions as those structures designed within the sensor arrays, the resistance value of the resistive structures within the matrices could be estimated, Figs. 4.11(b). The measurement results are provided in Sects. 5.2 and 5.3.

4.7.2 Lifetime measurements

One of the most important material parameters characterizing the quality of a high–purity silicon soft X–ray sensor is the lifetime. Several methods have been developed to measure the generation as well as the recombination lifetime [4.19–4.26].

The generation lifetime can be calculated from the I–V characteristic of a diode test structure or from the sensor itself [4.19–4.20]. The I–V curve displays a square–root behavior, as the depletion layer width is proportional to the square root of the reverse–bias voltage. An I^2–V plot of the same data displays a linear section, from which the generation lifetime can be estimated.

Most other methods of measuring the generation lifetime involve the use of MOS capacitor test structures [4.22–4.24] and are discussed in Sect 4.7.2.1. A new contactless–microwave technique has been developed for the measurement of the recombination lifetime [4.2, 4.25–4.26] and is outlined in Sect. 4.7.2.2.

4.7.2.1 MOS capacitor techniques

The standard, most frequently used technique for measuring the generation lifetime is the pulsed MOS capacitor method [4.22]. In this method, a MOS capacitor is initially reverse biased. A negative voltage step is then applied to the gate and the capacitance response is measured. The additional charge on the gate creates an additional requirement for free holes in the substrate. As free holes in the depletion region are only available through thermal generation, the depletion layer must initially increase sufficiently to a deep–depletion value in order to provide the extra charge. The depletion of the bulk is a majority response and is several times faster than the generation of minorities. With time, free holes become available through thermal generation and the depletion layer will subsequently decrease to its original equilibrium state. The time required for this response to occur characterizes the generation lifetime. Another method involves

the application of a negative voltage ramp in place of a voltage step [4.23]. The response is seen as a rapid decrease in the capacitance of the structure to a certain deep–depletion value. While the voltage follows a ramp, the device remains in quasi–equilibrium and the capacitance is measured. At this point, the charging current of the gate, which is calculated as the measured capacitance times slope of the voltage ramp, is equal to the internal generation current, from which the generation lifetime can be obtained.

These methods have been developed for structures fabricated on silicon of standard resistivity and cannot be directly used for structures fabricated on high–purity silicon. In high–purity silicon, several significant effects create a situation that deviates from ideal discussed above. These effects include a lateral expansion of the depletion layer (which will cause an increase in the measured capacitance and an increase in the generation current and thereby will affect the accuracy of the measured depletion layer width and the current–depletion layer relation), the significant bulk resistance in series with the depletion capacitance (for which the measurement results have to be corrected) and the dependence of the diffusion current on the depletion depth.

It has been found that through the use of a slightly modified method, these effects can be minimized and measurements can be made on high–purity silicon [4.24]. In addition, two– and three–dimensional lateral effects can be taken into account, an effective diffusion length can be defined and the measured capacitance can be corrected. The method involves the application of a voltage step onto the gate of a MOS capacitor in order to force the structure into deep depletion with the subsequent application of a voltage ramp, which will maintain the MOS capacitor in the deep depletion state until the maximum allowed gate bias voltage is reached [4.24]. The measured capacitances must then be corrected through the use of an impedance conversion method [4.24].

Although the detrimental effects can be minimized, this measurement remains extremely difficult. For this reason, measurements of the lifetime were performed using a new lifetime measurement technique, Sect. 4.7.2.2. With this technique, the recombination lifetime, rather than the generation lifetime, is obtained.

4.7.2.2 Contactless–microwave technique

Contactless measurement of many different parameters associated with semiconductor wafers and devices is currently receiving a great deal of attention. This type of measurement is nondestructive and does not damage or contaminate the material under test or affect its properties in any way. The recently developed contactless, nondestructive method to measure the lifetime of a silicon sample after each successive processing step during the fabrication of a device (e.g. a soft X–ray sensor) allows the monitoring of any changes in the material quality. The material quality may change due to impurity contaminations or removals or due to the introduction of structural irregularities during the fabrication procedure [4.2]. Contactless measurements are based on the excitation of a material from a distance, typically through the use of an electromagnetic or a mechanical source, and subsequently measuring the energy reflected from or transmitted through the material [4.2].

It is known that a change in the concentration of free carriers in a semiconductor sample will affect a probing microwave field. The contactless method for the measurement of the recombination lifetime of the free carriers in a semiconductor sample developed at Delft University of Technology is cooperation with Philips in Eindhoven, the Netherlands is based on the measurement of the reflected microwave power following an electromagnetic (optical) excitation of a semiconductor sample through the use of a light–emitting diode (LED) source with a characteristic wavelength of 875 nm, which results in the generation of free carriers.

Upon the generation of free carriers in the semiconductor sample, either the reflected or the transmitted microwave power can be measured. The measurement is more straightforward if the reflected microwave power is determined. The reflection coefficient of the microwave power from a semiconductor sample is dependent on the sample's conductivity and permeability and on the frequency of the microwaves [4.25]. However, as the frequency of the microwaves remains constant during the measurement and as silicon is a nonmagnetic material, the conductivity of the sample is the only parameter that changes as a consequence of the optical excitation of the free carriers [4.26]. The reflection coefficient is therefore assumed to be only a function of the sample's conductivity, which is in turn, directly proportional to the concentration of free carriers in the sample [4.26].

A functional diagram of the measurement system is shown in Fig. 4.12. Microwaves, with a constant frequency of 2.8 GHz, are provided by a generator at a power of 80 mW (1). The microwave power is directed via a waveguide to an attenuator (2) in order to adjust the emitting power level. The microwave power is then directed to a splitter (3), which divides the power into two equal parts. One part is directed to an antenna (6) in order to irradiate the wafer (7) by means of a circulator (4) and a stub tuner (5). The stub tuner is used to match the impedance of the antenna and the wafer to the system. The microwave power reflected from the wafer is directed via the circulator to a combiner (10), through which this power is added to half the original power. However, as thermal generation of free carriers causes an offset in this sum of the powers, the phase shifter (8) and the attenuator (9) can be adjusted, which will result in a partial elimination of this offset. The resulting power is then directed to an attenuator (11), a microwave power amplifier (12) and a microwave detector. The detector provides an output voltage proportional to the reflected microwave power (13). The output voltage can be visualized by a digital oscilloscope (14).

A pulse generator (15) drives the optical source, an LED (16), the wavelength of which is 875 nm. The pulsed radiation emitted by the LED optically excites free carriers in the semiconductor sample. A change in the output voltage of the microwave detector, i.e. a change in the reflected microwave power, occurs after the wafer is irradiated, due to the change in the sample's conductivity upon irradiation. The digital oscilloscope is coupled to a computer, which analyzes the output voltage signal and calculates the value of the lifetime.

As free carriers will exist at the surface as well as in the bulk of the semiconductor sample after optical excitation, the recombination process that ensues will consist of both surface and bulk contributions. However, it has been shown that when the level of injection of free carriers is low, the surface contribution is negligible [4.26]. Therefore, when low injection levels are

employed, the recombination lifetime in the semiconductor bulk can be obtained. This recombination process has been thoroughly investigated and described for semiconductor wafers of both low and high resistivity [4.2, 4.26].

Lifetime measurements have been obtained on preprocessed and processed high–purity silicon soft X–ray sensors. The results are given in Sect. 5.2.3.
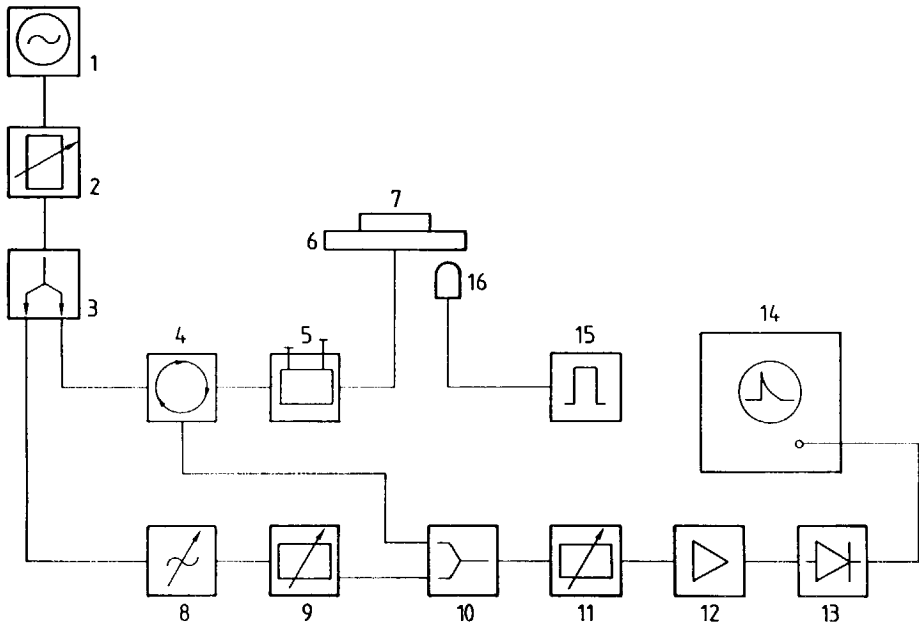
Fig. 4.12 *Functional diagram of a contactless–microwave recombination lifetime measurement system* [4.26].

4.8 CONCLUSIONS

Leakage current limitation and reduction are the primary goals to achieve in the optimal design of all process sequences involved in the fabrication of high–purity silicon soft X–ray sensors and sensor arrays. As high–purity silicon has a relatively low trap density and contains relatively low numbers of impurities fully ionized at room temperature and scattering centers per unit volume, the thermal generation component of the leakage current contributed from the depletion region is minimized. In addition, the minority carrier lifetime,

the charge carrier mobilities and the depletion–region depth are maximized.

High–lifetime material, which does not necessarily have a high resistivity, also has a relatively low trap density and also contains a relatively low number of scattering centers per unit volume. However, collection by diffusion, which would be the mode of operation in such a detector, is not efficient or fast enough to allow a total contribution to the output signal of all the charge carriers created by incident radiation in high–count rate experiments. Furthermore, compared with high–lifetime and with compensated silicon material, high–purity silicon contains fewer generation–recombination centers, which makes the fabrication of devices with lower leakage currents and lower detector noise possible. The sensors and sensor arrays in this work were therefore fabricated on high–purity silicon. They should be operated in the fully depleted mode for optimal operation.

After a brief description of silicon planar technology, the processing steps used in the fabrication of the high–purity silicon soft X–ray sensors and sensor arrays are detailed. The actual process sequences used are pictorially outlined.

The process which resulted in the fabrication of diodes with the lowest leakage current measurements was selected for the fabrication of high–purity silicon soft X–ray sensors. This process was modified in order to realize polysilicon resistive structures in series with the sensors and in order to investigate gettering techniques.

An initial process to realize two–dimensional position–sensitive high–purity silicon soft X–ray sensor arrays employed a double–layer conduction technique based on polysilicon and aluminum conductors. As this design would not permit the fabrication of a large array of small elements, an alternate array was designed. In developing an alternate process sequence for its fabrication, the basic process modified to realize the polysilicon resistive structures in series with the sensors could directly be utilized with the addition of two subsequent steps: a low temperature deposition of silicon dioxide and a second layer metalization. With this process, based on the double–layer metalization technique, large arrays of small elements can be realized.

Test structures allow more information to be obtained about the quality of a fabricated device. The test structures and measurement procedures employed in this work are described.

In order to develop a high–purity silicon soft X–ray fabrication process, careful step–by–step monitoring of the process sequence is necessary. This is achievable through the use of a new contactless–microwave lifetime measurement technique. The lifetime of a silicon device is an important parameter. The knowledge of the magnitude of the lifetime after each processing step provides a powerful means of characterizing the bulk quality by detecting possible sources of contamination or lattice damage that may occur during the fabrication of the device. The usual lifetime measurement methods, including the MOS capacitor technique, require the formation of ohmic contacts and special test structures, which may contaminate or damage the sample. In addition, the MOS capacitor technique is not directly applicable to devices fabricated on high–purity silicon. The advantages of the contactless–microwave method include the freedom from damage caused by a probe and the avoidance of contamination, as well as the ability to perform in situ and fast measurements. The sample needs no preparation, contact resistance effects are eliminated and the measurement can readily be carried out after each processing step. An additional benefit of this method is that if a sample has been contaminated during fabrication, full

processing of the device in order to perform the standard lifetime measurement techniques, is unnecessary. This measurement technique is described and a functional diagram of the measurement system is given.

REFERENCES

[4.1]   W.R.Th. ten Kate and S.A. Audet, Processing high–purity silicon used for sensor applications, Sensors and Actuators, 16 (1989) 287–298.

[4.2]   T. Otaredian and S.A. Audet, Contactless lifetime measurement in processed and preprocessed silicon radiation detectors, Proc. 5th Int. Conf. on Sensors and Actuators, Transducers '89, Montreux, June 25–30, 1989, 180–181.

[4.3]   W. von Ammon and H. Herzer, The production and availability of high–resistivity silicon for detector applications, Nucl. Instr. and Meth., 226 (1986) 94–102.

[4.4]   D. Itoh, S. Kawamoto, S. Miki, I. Nambe and Y. Yatsurugi, Fabrication of ultra high purity single crystals, in Nuclear radiation detector materials, E.E. Haller, H.W. Kraner and W.A. Higinbotham (eds.), North Holland, Amsterdam, 1983.

[4.5]   S.M. Sze, Semiconductor devices; physics and technology, John Wiley and Sons, New York, 1985.

[4.6]   W. Keller and A. Muhlbauer, Floating–zone silicon, in Preparation and properties of solid state materials, W.R. Wilcox (ed.), Dekker, New York, 1981.

[4.7]   J. Messier, Y. le Coroller and J.M. Flores, Thick junctions made with nuclear compensated silicon, IEEE Trans. on Nucl. Sci., NS–11 (1964) 276–279.

[4.8]   J. Nishizawa, The transistor: a look back and a look ahead, Solid–State Tech., 30 (1987) 73–76.

[4.9]   S.K. Ghandhi, VLSI fabrication principles: silicon and gallium arsenide, John Wiley and Sons, New York, 1983.

[4.10]   S.M. Sze (ed.), VLSI Technology, 2nd ed., McGraw Hill, New York, 1988.

[4.11]   S. Holland, Fabrication of detectors and transistors on high–resistivity silicon, Nucl. Instr. and Meth., A275 (1989) 537–541.

[4.12]   L. Baldi, G. Cerofolini and G. Ferla, Heavy metal gettering in Si devices, J. Electrochem. Soc., 127 (1980) 164–169.

[4.13]   D.E. Hill, Gettering of gold in silicon wafers using various backside gettering techniques, Proc. Symp. on Defects in Silicon, W.M. Bullis and L.C. Kimerling (eds.), The Electrochem. Soc., Pennington, 1983.

[4.14]   T.M. Buck, K.A. Pickar, J.M. Poate and C.–M. Hsieh, Gettering rates of various fast–diffusing metal impurities at ion–damaged layers on silicon, Appl. Phys. Lett., 21 (1972) 485–487.

[4.15]   D. Lecrosnier, J. Paugam, G. Pelous, F. Richou and M. Salvi, Gold gettering in silicon by phosphorous diffusion and argon implantation: mechanisms and limitations, J. Appl. Phys., 52 (1981) 5090–5097.

[4.16]   W.F. Tseng, T. Koji, J.W. Mayer and T.E. Seidel, Simultaneous gettering of Au in silicon by phosphorous and dislocations, Appl. Phys. Lett., 33 (1978) 442–444.

[4.17]   D. Lecrosnier, J. Paugam, F. Richou, G. Pelous and F. Beniere, Influence of phosphorous–induced point defects on a gold–gettering mechanism in silicon, J. Appl. Phys., 51 (1980) 1036–1038.

[4.18]   B.G. Magorrian and N.M. Allinson, Soft X–ray damage in CCD

detectors, Nucl. Instr. and Meth., A273 (1988) 599–604.

[4.19]   J. Kemmer, Fabrication of low noise silicon radiation detectors by the planar process, Nucl. Instr. and Meth., 169 (1980) 499–502.

[4.20]   J. Kemmer, Improvement of detector fabrication by the planar process, Nucl. Instr. and Meth., 266 (1984) 89–93.

[4.21]   H.R. Huff and T.L. Chiu, Minority–carrier lifetime: correlation with IC process parameters, J. Electrochem. Soc., 126 (1979) 1142–1147.

[4.22]   F.P. Heiman, On the determination of minority carrier lifetime from the transient response of a MOS capacitor, IEEE Trans. on Electr. Dev., ED–14 (1967) 781–784.

[4.23]   R.F. Pierret, A linear sweep MOS–C technique for determining minority carrier lifetimes, IEEE Trans. on Electr. Dev., ED–19 (1972) 869–873.

[4.24]   P.J. van Wijnen and W.R.Th. ten Kate, Charge carrier lifetime measurements on high–purity silicon, Nucl. Instr. and Meth., A253 (1987) 351–359.

[4.25]   M. Kunst and G. Beck, The study of charge carrier kinetics in semiconductors by microwave conductivity measurements, J. Appl. Phys., 60 (1986) 3558–3566.

[4.26]   T. Otaredian, S. Middelhoek and M.J.J. Theunessen, The theory and application of contactless microwave lifetime measurement, Materials Science and Engineering, B5 (1990) 151–156.

5

EXPERIMENTAL RESULTS

5.1 MEASUREMENT SYSTEM

Successful application of high–purity silicon soft X–ray sensors and sensor arrays depends critically on the availability of small, fast, low–noise amplification and signal–conditioning electronics with low power dissipations. Especially the preamplifiers must be small, as the detector and the initial amplifying unit have to be mounted close together to minimize the input capacitance caused by cabling and thereby minimize the noise associated with this unit. In addition, the preamplifier must intrinsically be of low noise, so as not to mask the small soft X–ray induced signals. The amplifying and signal–conditioning electronics should be fast, as the detection system count rate is limited by the dead–time associated with the circuitry, Sect. 2.2.5. Finally, a low power dissipation is required, due to the fact that as the substrate increases in temperature, the leakage current and therefore the noise increases. Moreover, if the substrate increases in temperature above approximately 50 ºC, it will no longer retain its original resistivity, Sect. 2.2.1.

5.1.1 Sensor

In all the applications mentioned in Sect. 1.3.4, the information desired involves the position and/or the energy of a particular soft X–radiation source. The aim of the soft X–ray sensor or sensor array is to absorb the incident radiation and to collect the electron–hole pairs subsequently generated within its volume in order to provide a measure of the energy of the incident radiation and, in the case of the array, to indicate in one or two dimensions the radiation's

position of incidence. Such sensors have been thoroughly described in Chapters 1 – 4.

5.1.2 Signal–processing units

The collected charge must subsequently be processed. The signal–processing units used in soft X–ray detection systems typically consist of preamplifiers, spectroscopy amplifiers, analog–to–digital converters (ADCs), coincidence units and multichannel analyzers (MCAs), Fig. 5.1. However, conventional MCAs are equipped with the capability of performing all functions from data acquisition to display and typically have internal ADCs with level discrimination and coincidence capabilities, as well as memory and display units [5.1]
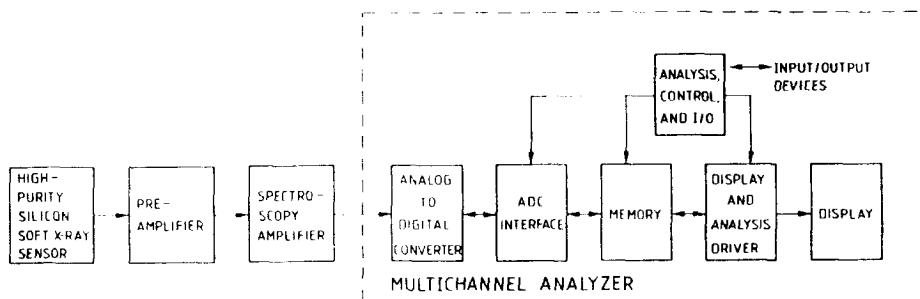
Fig. 5.1 *Measurement system for the detection of soft X–radiation* [5.1].

5.1.2.1 Preamplifiers

As the amount of collected charge is limited and as no gain is involved with the sensor itself, preamplification of the signal becomes necessary. A preamplifier is specifically designed to accept a signal from a radiation sensor and amplify it with the addition of as little noise as possible in order to preserve the maximum signal–to–noise ratio. Minimal signal shaping occurs in preamplification units. There are three basic types of preamplifiers: charge sensitive, current sensitive and voltage sensitive.

A charge–sensitive preamplifier ideally integrates all the charge generated within a radiation sensor onto a feedback capacitor. Charge–sensitive preamplifiers generally consist of a differential first stage, incorporating a capacitor, C_f, and often a high–value resistor, R_f, in parallel. The feedback resistor is a source of noise and when present is made as large as possible in order to minimize its contribution to the preamplifier's total noise. The capacitive and

the resistive input impedances of the preamplifier are then given by

$$C_{in} = C_f |A|$$ (5.1)

$$R_{in} = R_f |A|^{-1}$$ (5.2)

where A is the open loop gain. With a specified C_f of 2 pF and an open loop gain of 1000, the capacitive input impedance of the preamplifier, C_{in}, will equal 2 nF. This value must be compared to that associated with the detector, C_{det}, which is typically on the order of a few pF or less. For a charge–collection deficit of less than 1 %, the capacitance of the detector must be at least 100 times less than C_{in}. In this case, the output voltage will be linearly related to the amount of charge, Q, collected at the electrode associated with the preamplifier

$$|V_{out}| = \frac{|Q|}{C_f}$$ (5.3)

Note that the output is not sensitive to any of the detector's parameters, including its capacitance, as long as the capacitive input impedance C_{in} is much greater than the other sources of capacitance on the preamplifier input, such as the detector capacitance, input cabling, etc. The rise time of the output pulse is ideally equal to the detector current pulse width and the decay time constant τ_t is equal to [5.1]

$$\tau_t = R_f C_f$$ (5.4)

In applications where a parameter of interest is the quantity of the generated charge or the energy of the incident radiation (which is proportional to the charge as given by Eqn. (1.2)) and/or in applications where the time of occurrence of an event is important, this type of preamplifier is ideal [5.1].

Charge–sensitive preamplifiers were used with the resistive– and the capacitive–coupled outputs of the high–purity silicon soft X–ray sensors and sensor arrays described in this work. The additional source of capacitance associated with the capacitive–coupled outputs increases the noise associated with their corresponding preamplifiers. The noise in charge–sensitive preamplifiers is controlled by three components: the input FET, the input resistance and the input capacitance (i.e. the detector capacitance, the cabling capacitance and in the case of the sensor arrays the coupling capacitance). However, as long as the capacitive input impedance of the preamplifier C_{in} is much greater than the other sources of capacitance on the preamplifier input, the output will not significantly deteriorate. In addition, as the capacitive–coupled output signal is only used to discriminate within which row the irradiated diode element is lying, this signal must only be distinguishable above the noise. It is not

used for energy resolution purposes.

Current–sensitive preamplifiers include only a resistor in the feedback network. Therefore, the signal from the detector must subsequently be integrated. Integration is performed by the following unit, the spectroscopy amplifier. However, as such, the current–sensitive preamplifier is designed to convert fast current signals into voltage signals and therefore can be used for timing applications [5.1]. In such a configuration, the output is proportional to the amount of charge collected at the electrode associated with the preamplifier, Q, and to the feedback resistor, R_f.

$$|V_{out}| = |Q|R_f\delta(t) \tag{5.5}$$

Voltage–sensitive preamplifiers are rarely used because the output voltage is inversely proportional to the detector capacitance, C_{det}. As the capacitance of the detector is defined by the magnitude of the reverse–bias voltage, fluctuations in this voltage cause instabilities in the output voltage. This instability is minimized when the detector is operated in the fully or over–depleted mode [5.1]. The resistive feedback configuration will determine the value of the constant B.

$$|V_{out}| \propto B\frac{|Q|}{C_{det}} \tag{5.6}$$

5.1.2.2 Spectroscopy amplifiers

Spectroscopy amplification units accept input signals from preamplifiers and amplify, shape and filter the signals. The shaping and filtering is performed in such a way as to improve the signal–to–noise ratio and shorten the response time, thereby precluding overlap or pile–up effects. Spectroscopy amplifiers are usually composed of shaping circuits that have provisions which allow for user selection of the pulse–shape parameters. The pulse–shaping networks are generally operated with time constants much longer than the rise time of the signal delivered by the preamplifier, but much shorter than the signal's decay time. The necessary information from the preamplifier's output signal is given by the pulse rise time and the amplitude of the pulse. The gain range is generally adjustable from 1 × up to 1500 ×, while the pulse shaping is typically unipolar [5.1].

5.1.2.3 Analog–to–digital converters, coincidence units and multichannel analyzers

Signals from the spectroscopy amplifier must subsequently be digitized and

input into a multichannel analyzer for spectrum analysis and storage. The digitization is performed with an analog–to–digital converter (ADC). The ADC samples an analog signal and provides, through Wilkinson or successive–approximation processes, a digital representation of the signal. A capacitor is charged to the amplitude of the input pulse in the Wilkinson technique with the subsequent discharging of the capacitor at a constant rate. During the discharge time, a crystal–controlled pulse timer is counted in a register and the total number of pulses produced results in the event address. In the successive–approximation technique, a number of comparators is used to successively re–estimate the amplitude of the pulse to the required precision. Eight or twelve comparators are normally required to produce the necessary precision. ADCs are normally provided with level discrimination and coincidence capabilities in order to select and/or eliminate signals [5.1].

In the case of the sensor arrays, the coincidence capabilities of the ADCs must be utilized or separate coincidence units must be employed. Coincidence techniques are used to select events detected in true coincidence with each other. A coincidence unit accepts two (or more) input pulses and outputs one (or more) pulse(s) if and only if the input pulses are coincident within a certain resolving time. Pulses received from one x–addressed output and from one y–addressed output within a very short, predefined period of time will indicate the two–dimensional position of incident radiation, while pulses from two x–addressed or from two y–addressed outputs, which occur within this specified time period, will indicate photon absorption between two elements, double hits or crosstalk.

Multichannel analyzers (MCAs) collect and store spectral data acquired from a detection system for the purposes of display and/or further analysis. The acquisition modes most often used include the pulse–height analysis (PHA) mode, the multichannel scaling (MCS) mode and the sample (list) mode [5.1].

In the PHA operating mode, a pulse–height spectrum or spectrum histogram is formed, i.e. a frequency distribution is made of the heights from a sequence of input pulses. This is performed through the measurement of the amplitude of each input event and the subsequent conversion of the amplitude into a channel address. MCAs typically have internal ADCs and memory storage capabilities. The memory is composed of individual channels. Most MCAs consist of either 2048 or 4096 channels. At the end of the measurement, the number of counts associated with a particular channel will equal the number of pulses processed whose amplitudes correspond to that channel number. A histogram of the number of counts versus the channel number is thus obtained and can be visualized on the MCA display, Fig. 5.1. The channel numbers can be calibrated with a source of known energy distribution so that a final histogram of the number of counts versus the energy can be produced.

In the MCA mode, an analysis of the count rate versus the elapsed time is performed. Each channel is programmed to count the data for a predetermined period of time. Upon the elapse of this time, the next channel automatically resumes the counting operation. This mode is useful for decay–rate measurements of short–lived isotopes. Individual channels store digitized energy values of the analog input voltage in the sample (list) mode. This mode is used for multi–parameter PHA and for time–related spectroscopy.

The PHA mode was utilized in performing all the measurements described in Sects. 5.2 and 5.3.

5.2 MEASUREMENTS ON HIGH–PURITY SILICON SOFT X–RAY SENSORS

The most important criteria to optimize in terms of the performance of soft X–ray sensors include the diode reverse $I-V$ characteristics (a low leakage current measurement obtained from a sensor or sensor array assures that the sensor or sensor array will have a good energy resolution, Sect. 5.3.2), the magnitudes of the breakdown voltages and the diode $C-V$ characteristics. These measurements are therefore described first in the three subsections below (basic sensors, basic sensors with resistive structures and gettering techniques), followed by the results of the measurements performed on the test structures and the measurements of the recombination lifetime.

5.2.1 Basic sensors

The measurements presented in this section were performed on high–purity silicon soft X–ray sensors fabricated with the basic process illustrated in Sect. 4.6.1.1. A photograph of a basic high–purity silicon soft X–ray sensor is shown in Fig. 4.2.
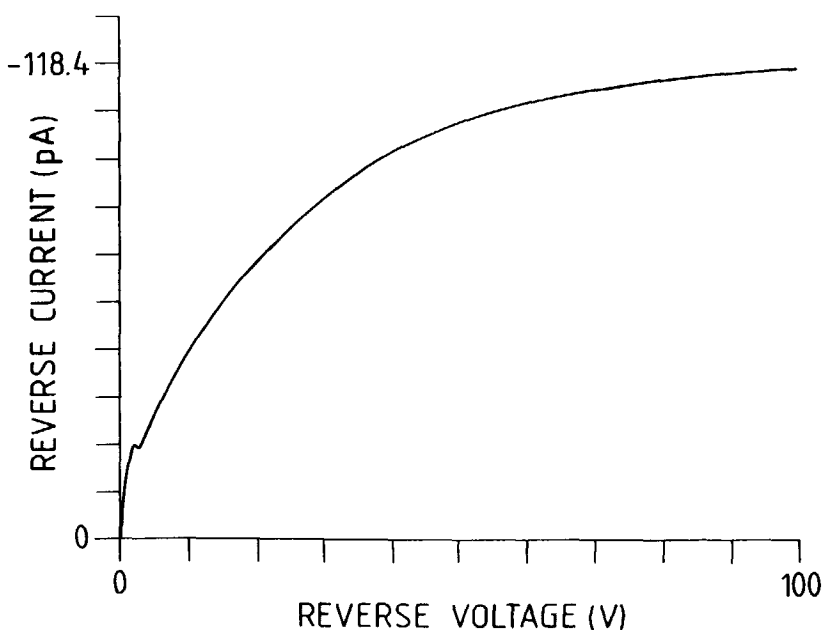
Fig. 5.2   *Typical reverse $I-V$ characteristic of a basic high–purity silicon soft X–ray sensor 0.25 mm² in area.*

Figure 5.2 shows a typical reverse I–V characteristic of a basic high–purity silicon soft X–ray sensor 0.25 mm^2 in area. As explained in Sects. 2.2.3 and 2.2.4, the main source of noise in high–purity silicon soft X–ray sensors originates from that reverse current present in the absence of any radiation source, i.e. from the leakage current. The reverse I–V characteristics are affected by the process in which the sensor is fabricated, Chapter 4. A low leakage current signifies a well–functioning device. Excellent results for the leakage current are on the order of $1 - 10$ nA/cm^2 per 100 μm depletion depth, although the yield is often defined by the upper limit of 50 nA/cm^2 per 100 μm depletion depth [5.2].

Using Eqn. (1.3) and given a donor impurity concentration of $N_d = 1 \times 10^{12}$ cm^{-3}, a 10 V reverse bias will theoretically deplete a layer approximately 100 μm in depth. From Fig. 5.2, the leakage current at 100 μm depletion depth (10 V reverse bias) is seen to be approximately 47 pA. Dividing by the diode area (0.0025 cm^2) reveals a leakage current on the order of 19 nA/cm^2 per 100 μm depletion depth. This is in good agreement with the theoretical value calculated in Sect. 2.2.1, i.e. $20 - 30$ nA/cm^2 per 100 μm depletion depth.

The theoretical breakdown voltage, Eqn. (4.2), is on the order of 3×10^4 V and from Fig. 5.2, the experimental breakdown voltage can be seen to be over 100 V.

A typical C–V characteristic measured on the diode is shown in Fig. 5.3. Stray capacitances have been taken into account. The depletion depth of the device should increase, given a sufficiently high–resistivity substrate, as the reverse–bias voltage across the device increases. Because the capacitance of the device is
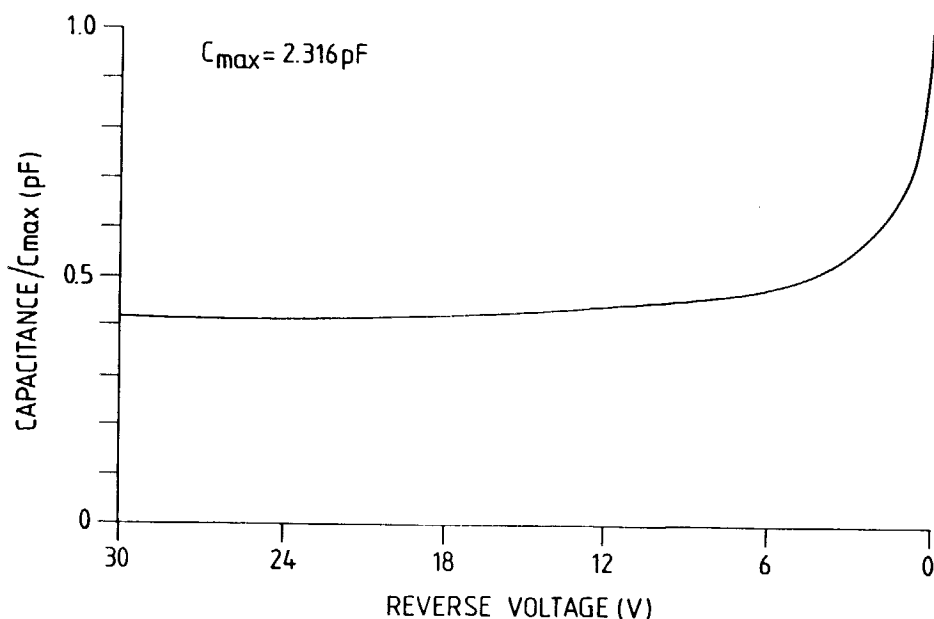
Fig. 5.3 *Typical C–V characteristic of a basic high–purity silicon soft X–ray sensor 0.25 mm^2 in area.*

inversely proportional to the depletion depth, this capacitance should decrease as the reverse–bias voltage increases. This is seen to occur in Fig. 5.3. The capacitance value is larger than that predicted by one–dimensional theory, i.e. $C = A\epsilon/x_d$, where A is the area of the diode, ϵ the dielectric constant of silicon and x_d the depletion region depth, due to the extension of the depletion region outside the diode area. Given appropriate test structures, developed and used with the sensor arrays, Sects. 5.3.1 and 5.3.2, the sidewall capacitance can be eliminated.

5.2.2 Basic sensors with resistive structures

The measurements presented in this section were performed on high–purity silicon soft X–ray sensors, each fabricated with a polysilicon resistive structure in series, with the process illustrated in Sect. 4.6.1.2. A photograph of a basic high–purity silicon soft X–ray sensor connected in series with a polysilicon resistive structure is shown in Fig. 4.4. Figure 5.4 shows a typical reverse I–V characteristic of a basic high–purity silicon soft X–ray sensor 0.25 mm^2 in area fabricated with a polysilicon resistive structure in series.

Using Eqn. (1.3) and given a donor impurity concentration of $N_d = 1 \times 10^{12}$ cm^{-3}, a 10 V reverse bias will theoretically deplete a layer
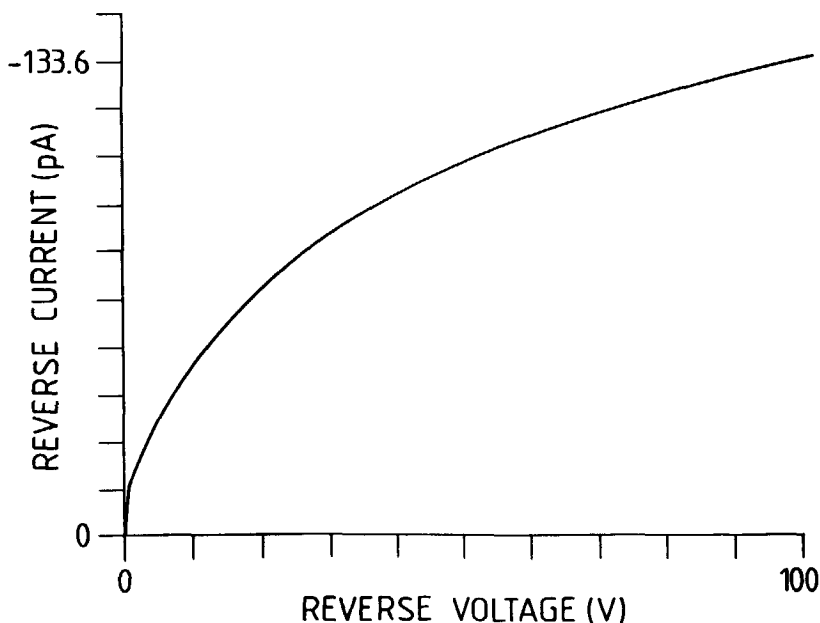
Fig. 5.4 *Typical reverse I–V characteristic of a high–purity silicon soft X–ray sensor 0.25 mm^2 in area with a polysilicon resistive structure in series.*

approximately 100 μm in depth. From Fig. 5.4, the leakage current at 100 μm depletion depth (10 V reverse bias) is seen to be approximately 50 pA. Dividing by the diode area reveals a leakage current on the order of 20 nA/cm^2 per 100 μm depletion depth. This result can be compared with that presented in Fig. 5.3, as the diodes were fabricated simultaneously. It can be seen that the polysilicon structures only minimally affect the reverse *I–V* and the *C–V* measurements.

The theoretical breakdown voltage, Eqn. (4.2), is on the order of 3 x 10^4 V and from Fig. 5.4, the experimental breakdown voltage can be seen to be over 100 V.

The *C–V* characteristic obtained from the diode is shown in Fig. 5.5. Stray capacitances have been taken into account. As described in Sect. 5.2.1, this capacitance should decrease as the reverse–bias voltage increases. This is seen to occur in Fig. 5.5. Again, the capacitance value is larger than that predicted by one–dimensional theory, i.e. $C = A\epsilon/x_{\mathrm{d}}$, where A is the area of the diode, ϵ the dielectric constant of silicon and x_{d} the depletion region depth, due to the extension of the depletion region outside the diode area. Given appropriate test structures, developed and used with the sensor arrays, Sects. 5.3.1 and 5.3.2, the sidewall capacitance can be eliminated.
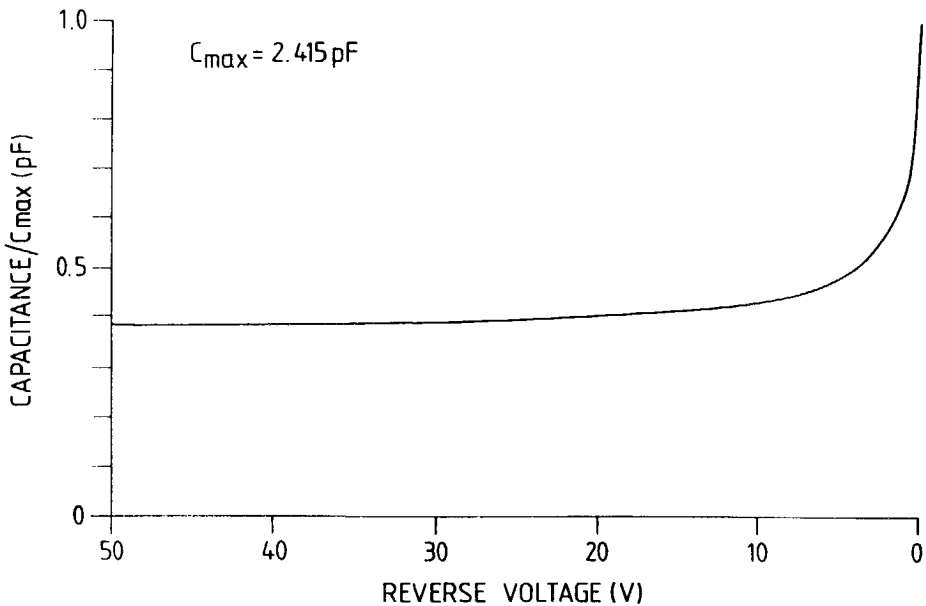
Fig. 5.5 *Typical C–V characteristic of a high–purity silicon soft X–ray sensor 0.25 mm^2 in area with a polysilicon resistive structure in series.*

From test resistors placed around the periphery of the chip (14 in total) with the same, as well as different dimensions as those in series with the diodes, the resistance values of the resistive structures within the elemental units could be estimated. The theoretical resistance values of the resistive structures are

calculated according to Eqn. (4.3). The resistance values of the fourteen test resistive structures were measured on all those chips containing the test resistive structures on ten different wafers. The theoretical and the average experimental measurements are listed in Table 5.1.

Table 5.1 *Theoretical and average experimental values of fourteen test resistive structures, process Sect. 4.6.1.2.*

	THEORETICAL			EXPERIMENTAL
	LENGTH [μm]	WIDTH [μm]	RESISTANCE [Ω]	RESISTANCE [Ω]
1.	50	10	162.5	162.3
2.	100	20	162.5	156.8
3.	150	30	162.5	159.0
4.	120	20	195	200.1
5.	170	30	184	188.6
6.	250	10	812.5	820.3
7.	40	10	130	135.9
8.	80	20	130	134.0
9.	120	30	130	134.4
10.	160	40	130	130.2
11.	200	50	812.5	816.9
12.	500	20	812.5	823.0
13.	500	10	1625	1691.0
14.	1000	20	1625	1678.4

Table 5.2 *Rms noise measurements obtained from the fourteen test resistive structures, process Sect. 4.6.1.2.*

RMS NOISE MEASUREMENTS [mV]	
1.	0.110
2.	0.110
3.	0.110
4.	0.110
5.	0.082
6.	0.110
7.	0.097
8.	0.110
9.	0.110
10.	0.110
11.	0.085
12.	0.100
13.	0.110
14.	0.100

Note that the theoretical resistance values are calculated given a certain sheet resistivity value, Eqn. (4.3). This value was measured to be $10 - 15 \, \Omega/\text{sqr.}$ after the initial phosphorous deposition, Fig. 4.3. However, after the oxidation of the polysilicon, Fig. 4.3, the measured sheet resistivity increased to $30 - 35 \, \Omega/\text{sqr.}$, as some of the phosphorous was lost to the growing oxide layer. Therefore, the sheet resistivity used to calculate the theoretical resistance values in Table 5.1 was $32.5 \, \Omega/\text{sqr.}$ Note that the experimental values are all within $\pm 5 \, \%$ of their theoretical values.

The geometry of the polysilicon structures used in the two different sensor arrays of design IS–531 were identical to those of test resistors 4 and 5, i.e. they are associated with theoretical resistance values of 200.1 and $188.6 \, \Omega/\text{sqr.}$,

respectively, while that geometry of test resistor 4 was used in the sensor arrays of design IS–562.

In addition to the resistance value, the rms noise was measured for each resistor (in series with a preamplifier) on one chip. The results are presented in Table 5.2. As the measured values are approximately 100 – 1000 times larger than the theoretical values, it can be concluded that the noise of the preamplifier is far greater than the noise of the resistors. Therefore, in order to observe what effect the resistor noise has on the energy resolution of a detection system, that resistor with the largest noise value and that with the smallest value were selected for a further investigation. These resistors were sequentially placed in series with a high–purity silicon radiation sensor. The energy resolution was measured for the sensor itself, the sensor in series with that resistor with the smallest noise value and the sensor in series with that resistor with the largest noise value. The results are shown in Figs. 5.6(a), (b) and (c).
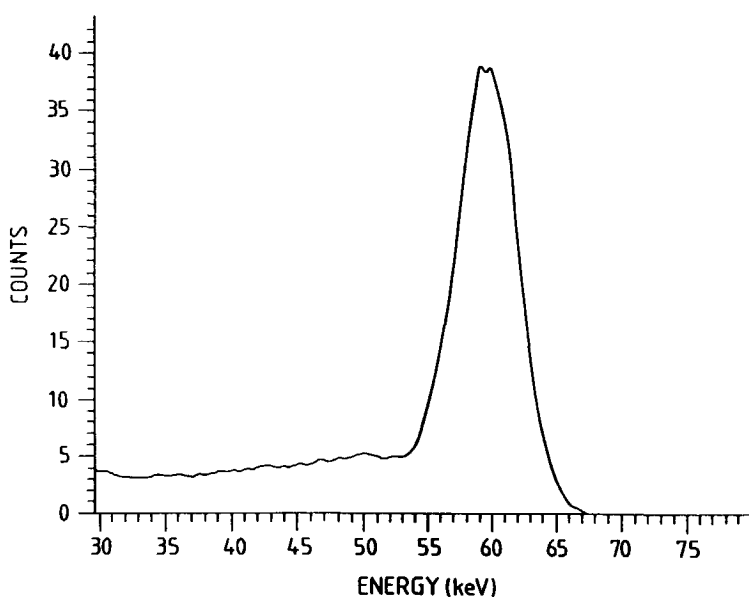
Fig. 5.6 *(a) Pulse–height spectrum of a 10 mm² high–purity silicon radiation sensor upon exposure to* ^{241}Am.

The full–width–at–half–maximum (FWHM) of the sensor on its own was measured to be 5.0 keV, while those values for the sensor in series with the resistor having the smallest noise value and the sensor in series with the resistor having the largest noise value were 5.5 and 5.7 keV, respectively. The difference in the FWHM values are insignificant. This implies that the noise of the sensor is greater than the noise of the polysilicon resistors and that sensor arrays based on an elemental unit composed of a sensor and a polysilicon resistive structure in series are feasible.
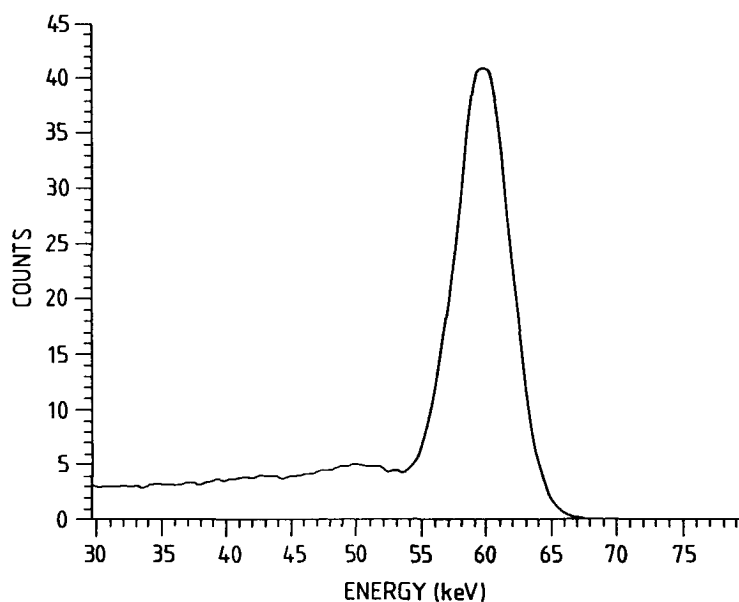
Fig. 5.6 *(b) Pulse—height spectrum of a 10 mm² high—purity silicon radiation sensor in series with that resistor with the smallest noise value (Table 5.2) upon exposure to ^{241}Am.*
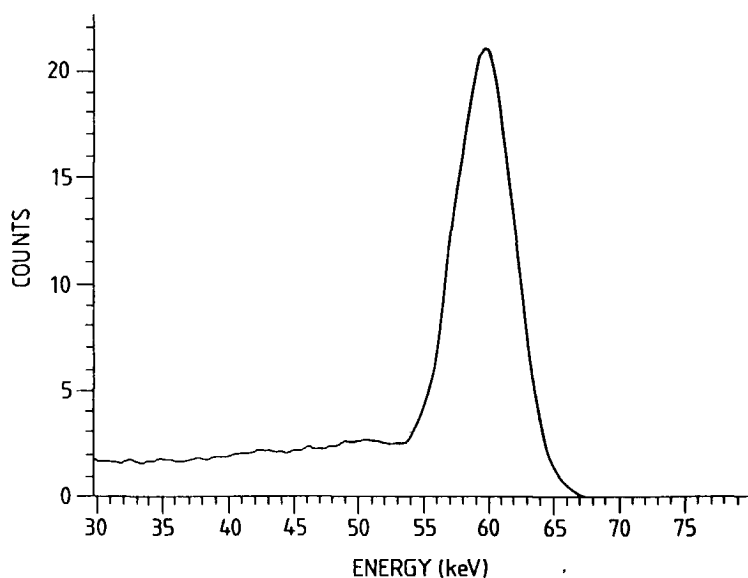
Fig. 5.6 *(c) Pulse—height spectrum of a 10 mm² high—purity silicon radiation sensor in series with that resistor with the largest noise value (Table 5.2) upon exposure to ^{241}Am.*

5.2.3 Gettering techniques

Two different groups of high–purity silicon soft X–ray sensors were fabricated in order to investigate two different gettering techniques: a backside arsenic implantation and a backside phosphorous diffusion. The process sequences used were based on the initial basic process for the fabrication of high–purity silicon soft X–ray sensors, Sect. 4.6.1.1, the difference lying in the realization of the backside high–low junction. The first group (Group 1) employed arsenic implantation as a gettering technique, while the second group (Group 2) utilized phosphorous diffusion. The process sequence for the first group is therefore the same as that depicted in Sect. 4.6.1.1, while that of the second group is depicted in Sect. 4.6.1.3.

In order to assess the degree of success the specific gettering technique had on the quality of the resulting sensors, recombination lifetime measurements were taken using the contactless–microwave measurement technique described in Sect. 4.7.2.2 after several steps during the processing and reverse diode I–V characteristics were measured upon completion of the fabrication.

Recombination lifetime measurements performed on preprocessed wafers from both groups were on the order of 160 μsec, although the manufacturer specified recombination lifetime was stated to be 500 μsec. Wafers from the two groups were then fabricated according to the sequences depicted in the Figs. 4.1 and 4.5 for Groups 1 and 2, respectively. An ungettered wafer was used as a control.

The introduction of phosphorous occurred in the wafers of Group 2 after the initial passivation oxidation, Fig. 4.3. The predeposition step involved a phosphorous diffusion at a temperature of 950 oC for 15 minutes using a POCl$_3$ source. The step resulted in the formation of an n^+–layer on the backside of the wafers from Group 2 (the frontsides being protected by thick oxide layers), with a thickness and a doping concentration of approximately 500 nm and 1×10^{20} cm^{-3}, respectively. Since the diffusion time at this stage was very short, i.e. 15 minutes, the lifetime in the bulk was expected to be unaffected, as one of the requirements for effective gettering to take place, Sect. 4.4.3.3, is that sufficient time should be allowed, at a specific diffusion temperature, for any impurities existing in the bulk to diffuse to the capture zone on the wafer backside (the n^+–layer). Thereafter, the impurities should essentially be unable to influence the characteristics of the fabricated sensors.

The normalized results of the recombination lifetime measurements carried out on an ungettered wafer and on a wafer from Group 2 are shown in Figs. 5.7(a) and (b), respectively. The effective lifetime for the wafer from Group 2 is almost constant over the entire recombination process and is approximately 160 μsec. The result of the ungettered wafer shows a fast initial decay followed by a slow decay with a constant effective lifetime of approximately the same value as that of the wafer from Group 2.

The only difference between the two measurement results of Fig. 5.7 is the value of the recombination lifetime at the beginning of the recombination process. The initial part of the recombination process has been shown to be mainly determined by surface recombination [5.3]. As the concentration of free carriers at the surface decreases, the bulk recombination becomes more dominant. That concentration at which the surface contribution becomes negligible is dependent on the concentration of surface states and on the height of the potential barriers

at the surfaces. The concentration of surface states is assumed to be on the same order of magnitude for both wafers. However, the $n^+–n^-$ junction formed by the phosphorous diffusion step in the wafer of Group 2 results in an additional potential barrier at the backside surface. This influences the diffusion of free carriers from the bulk towards that surface. The surface contribution in this wafer therefore becomes negligible at a higher free carrier concentration than that associated with the ungettered wafer. This explains the difference in the recombination lifetimes at the beginning of the recombination process, i.e. it explains the comparatively fast initial decay of the ungettered wafer in Fig. 5.7. As expected, the values of the effective recombination lifetimes at the end of both recombination processes shown in Fig. 5.7 are the same. The quality of the bulk of the wafers at this stage must therefore be the same.
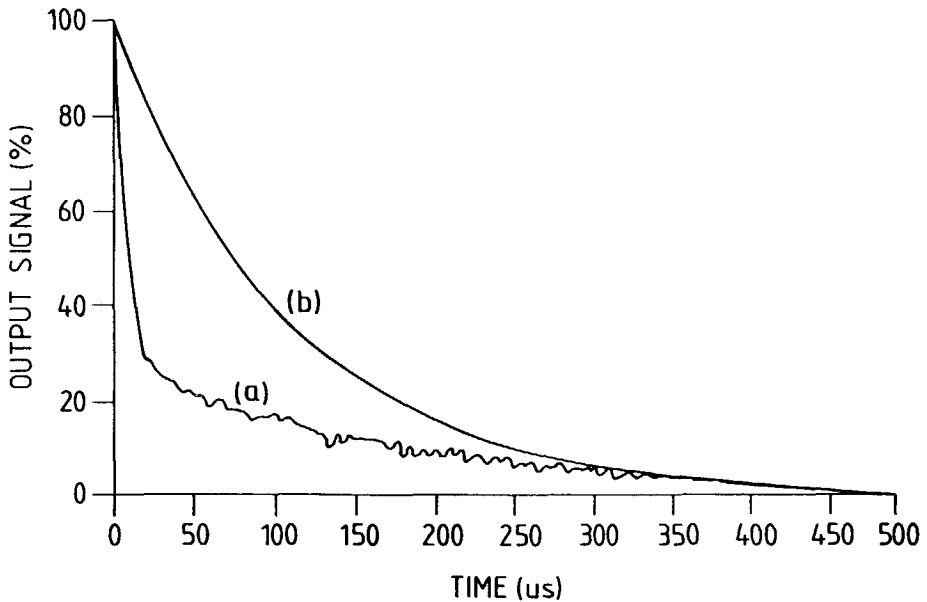
Fig. 5.7 *Results of the effective recombination lifetime measured (a) on an ungettered wafer and (b) on a wafer from Group 2.*

However, it is expected that given a sufficient diffusion time (at a specific diffusion temperature), any impurities existing in the bulk will be able to diffuse to the capture zone on the wafer backside, thus ridding the bulk of any contaminants and thereby improving the quality of the bulk and the recombination lifetime. During the oxidation step, which followed the phosphorous predeposition in the process sequence of the wafer from Group 2,

Sect. 4.6.1.3, a (diffusion) time of 185 minutes was allowed at a temperature of 950 °C, as well as a cool–down time of 60 minutes at 900 °C. According to previous investigations, Sect. 4.4.3.3 [5.4], this time should be sufficient to allow the diffusion of all impurities existing in the bulk of the wafer of Group 2 to diffuse to the capture zone on the wafer backside, thereby allowing effective gettering to take place. Measurements taken at this stage however revealed similar results to those presented in Fig. 5.7. Two conclusions can now be derived. Either the time–temperature combination of the diffusion step was such that ineffective gettering took place or the bulk of the wafer contained an insignificant number of impurities.

The effective recombination lifetime was measured on a wafer from Group 1 after an arsenic implantation was performed. The dose and energy of the implantation were selected to produce an n^+–layer on the wafer backside with an approximate thickness and doping concentration of 50 nm and 1×10^{20} cm^{-3}, respectively. This step, like the phosphorous diffusion step, also produces an addition potential barrier on the backside of the wafer, which will influence the diffusion current of free carriers from the bulk towards the surface. The surface contribution will therefore become negligible at a higher concentration than that associated with the ungettered wafer. The initial recombination process is therefore expected to be affected, as it was with the wafer from Group 2, but the bulk recombination process should also be affected, if this method, i.e. the creation of a damaged, heavily–doped arsenic region on the wafer backside, is an effective method to getter bulk impurities.

The measurement results showed that the beginning of the process followed a curve whose decay was similar to that of the Group 2 wafer, shown in Fig. 5.7, and whose effective recombination lifetime at the end of the process was similarly on the order of 160 μsec. Due to complications in the recombination lifetime measurement procedure, no further measurements were carried out, i.e. no measurements could be obtained after the anneal step.

The reverse $I–V$ characteristics were then measured upon completion of the fabrication. The results are shown in Figs. 5.8(a) and (b) for the wafers of Group 1 and 2, respectively.

The leakage currents for the sensors of the two groups, i.e. Group 1 and Group 2, are 24 and 30 nA/cm^2 per 100 μm depletion depth, respectively. The magnitudes of the leakage currents are approximately the same as those values presented in Sects. 5.2.1 and 5.2.2 and are in good agreement with the theoretical value calculated in Sect. 2.2.1. In addition, it would be expected that the leakage currents from the two wafers would be approximately the same, given similar effective bulk recombination lifetime measurements.

Given the acceptable leakage current results obtained from the wafers from both groups, i.e. Group 1 and Group 2, it cannot be concluded that these two types of gettering were ineffective. It must therefore be concluded that the bulks of the wafers contained insignificant numbers of impurities and that the gettering abilities of the two techniques are approximately equal.
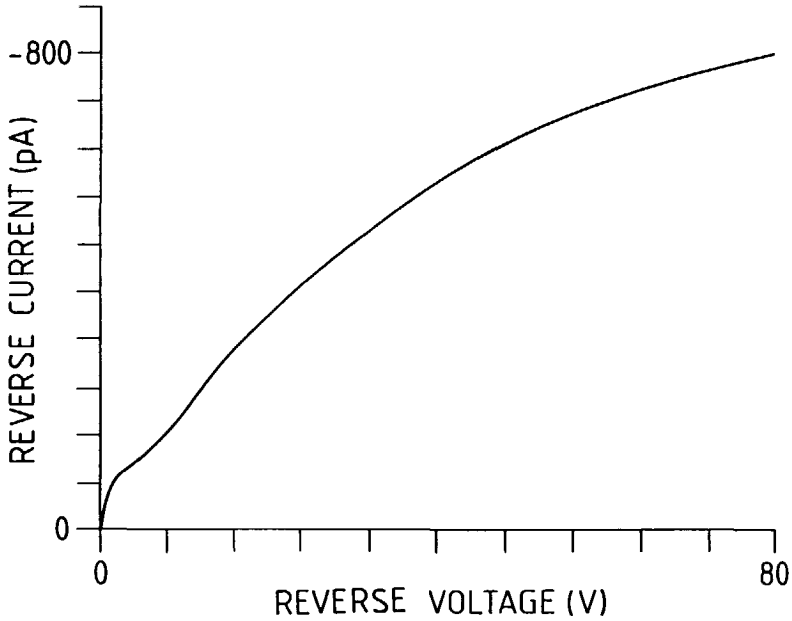
Fig. 5.8 (*a*) *Typical reverse I–V characteristic of a high–purity silicon soft X–ray sensor 1 mm² in area from Group 1.*
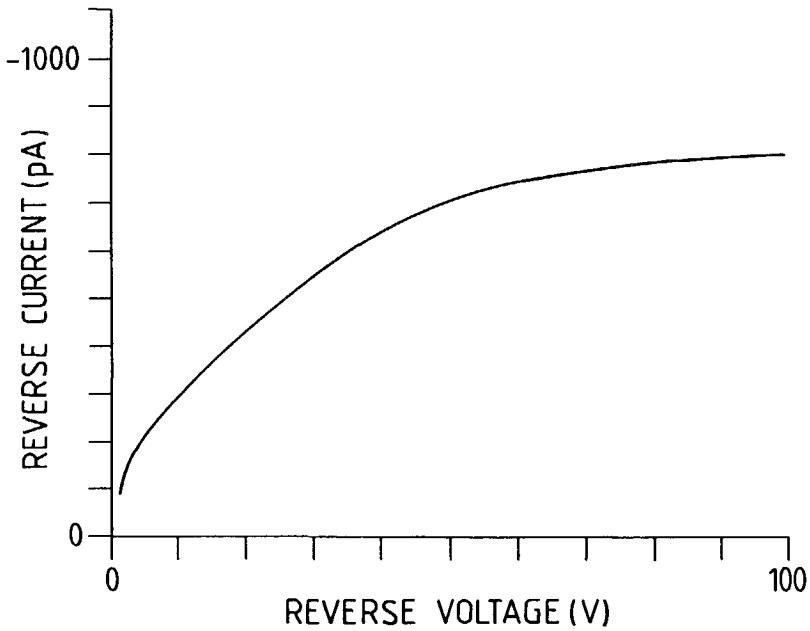
Fig. 5.8 (*b*) *Typical reverse I–V characteristic of a high–purity silicon soft X–ray sensor 1 mm² in area from Group 2.*

5.3 MEASUREMENTS ON HIGH–PURITY SILICON SOFT X–RAY SENSOR ARRAYS

The most important criteria in terms of the performance of high–purity silicon soft X–ray sensor arrays include, as for the sensors described in Sect. 5.2, the diode reverse I–V characteristics, the magnitudes of the breakdown voltages and the diode C–V characteristics, while in addition, the crosstalk is of primary importance in determining the ability of a sensor array to function as an imager. These measurements are therefore described first for each of the five different types of sensor arrays, followed by measurements performed on various diode, MOS capacitor and polysilicon resistive test structures.

5.3.1 Double–layer conduction arrays

5.3.1.1 Introduction

The measurements presented in this section were performed on high–purity silicon soft X–ray sensor arrays of the design IS–502 fabricated with the process sequence depicted in Sect. 4.6.2.1. A schematic of this sensor array design is
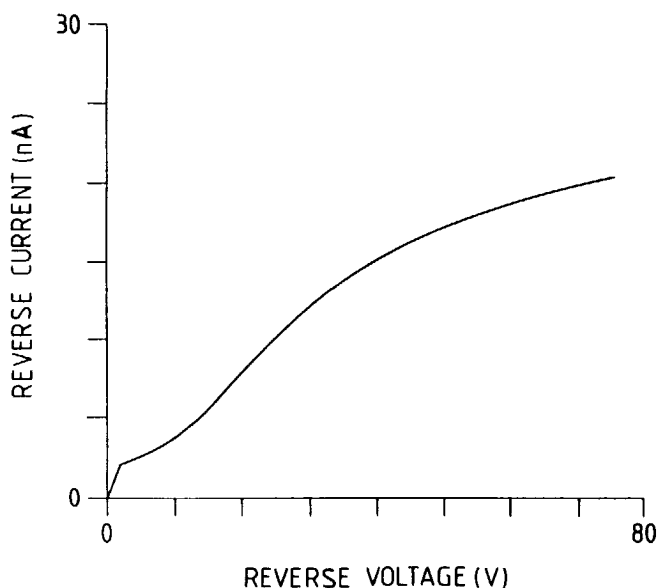
Fig. 5.9 *Typical reverse I–V characteristic of a resistive output from a high–purity silicon soft X–ray sensor array (IS–502).*

shown in Fig. 3.1(a) and a photograph of a fully fabricated sensor array with this design is shown in Fig. 4.7.

5.3.1.2 Reverse *I–V* characteristics

Figure 5.9 shows a typical reverse *I–V* characteristic of a resistive–coupled output from a high–purity silicon soft X–ray sensor array of the design IS–502, i.e. based on the double–layer conduction technique.

The theoretical breakdown voltage, Eqn. (4.2), is on the order of 3×10^4 V and from Fig. 5.9, the experimental breakdown voltage can be seen to be over 80 V.

5.3.1.3 *C–V* characteristics

The *C–V* characteristic of a resistive–coupled output from a high–purity silicon soft X–ray sensor array fabricated with the double–layer conduction technique (IS–502) is shown in Fig. 5.10(a). Stray capacitances have been taken into account. As described in Sect. 5.2.1, this capacitance should decrease as the reverse–bias voltage increases. This is seen to occur in Fig. 5.5. In addition, the
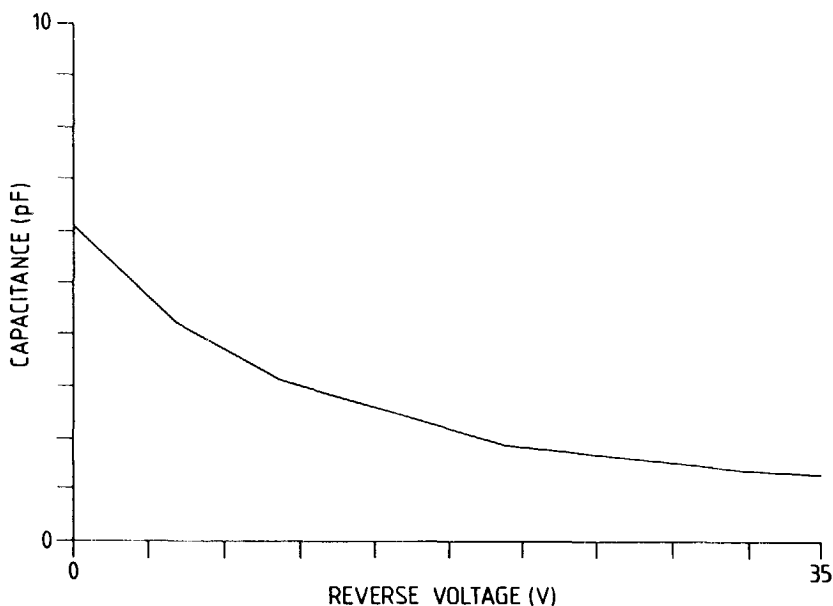
Fig. 5.10 (*a*) *Typical C–V characteristic of a resistive output from a high–purity silicon soft X–ray sensor array (IS–502).*

capacitance values obtained are in good agreement with the theoretical values predicted by one–dimensional theory due to the use of appropriate test structures. Two MOS capacitors with the same perimeters but different areas were fabricated on the same chip as the sensor array, Sect. 4.7.1.2. Upon subtraction of the *C–V* data from the two structures, the sidewall capacitance of the larger structures could be eliminated and an accurate measurement of the capacitance could be obtained.

The theoretical capacitance of the 0.03 cm² diode (total area of the three elemental diodes) at a reverse voltage of 35 V is 1.47 pF, while the measured value at this bias voltage was 1.3 pF, Fig. 5.10(a). The theoretical capacitance of the 0.03 cm² diode at a reverse voltage of 5 V is 3.9 pF, while the measured value at this bias voltage was 4.2 pF.

The log voltage versus the log capacitance curve is shown in Fig. 5.10(b). In this curve, it can be seen that the dependence of the capacitance on the bias voltage follows a relationship such that the capacitance is proportional to the bias voltage to the power (−0.47). This relationship is very similar to that associated with an asymmetric, abrupt *p–n* junction, i.e. the capacitance in the case of an abrupt junction is proportional to the bias voltage to the power (− 0.5). It can therefore be concluded that asymmetric, abrupt *p–n* junctions have been realized in this procedure and that no channelling effects from the ion implantation or diffusive effects originating from the annealing procedure have occurred, as they would have led to a linear–graded rather than an abrupt distribution.
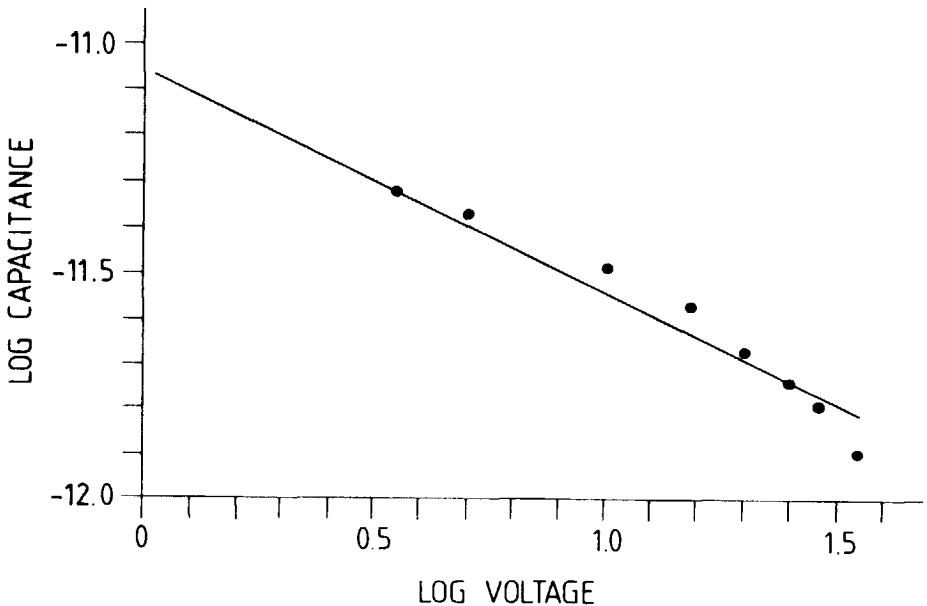
Fig. 5.10 (*b*) *Log capacitance versus log. voltage curve of a resistive output from a high–purity silicon soft X–ray sensor array (IS–502).*

5.3.1.4 Crosstalk measurements

As the size of the elemental diodes in this array were relatively large, 1 mm² in area, the crosstalk could be measured by securing a one–pinhole collimator in front of the device and exposing the device initially to a chopped white–light source and subsequently to a ^{90}Sr source, i.e. high–energetic electrons with an energy of 2 MeV. The collimator made it possible to expose only one sensing element to the radiation source at a time. All six outputs were readout. Similar results were obtained with both sources, Fig. 5.11.

The resistive–coupled relative output voltage peak from the exposed element was on the order of 9.3, while the relative output voltage peaks of the unexposed elements were on the order of 0.5, i.e. the crosstalk was less than 10 %, Fig. 5.11. Similar results were obtained from the capacitive–coupled outputs, Fig. 5.11.
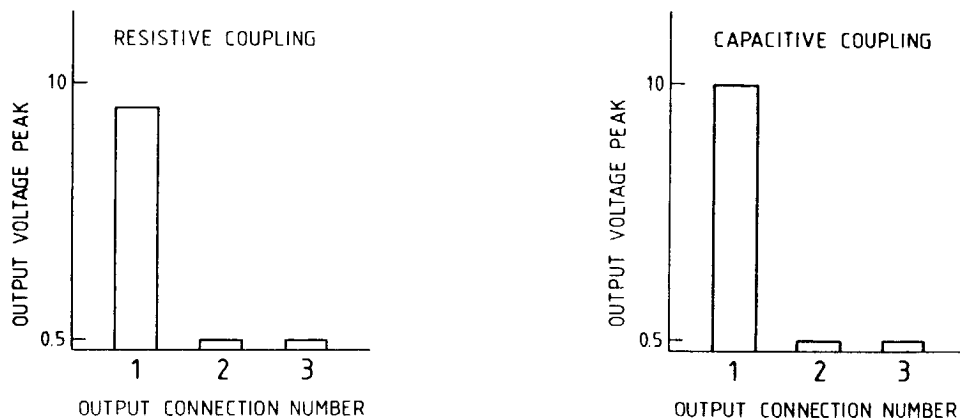
Fig. 5.11 *Relative heights of the output voltage peaks of the resistive– and the capacitive–coupled outputs from a high–purity silicon soft X–ray sensor array (IS–502).*

However, as stated in Sect. 3.1.1, one major limitation of this device design is that a large matrix of small sensing elements cannot be fabricated due to the fact that as the number of elements increases, the number of aluminum strips traversing the diodes in the horizontal direction will increase, which limits the minimum diode size in the vertical dimension. A modification of this device was therefore designed based on the same principle of resistive and capacitive coupling. However, in the modified design, the double–layer conduction scheme involves double–layer aluminum in place of heavily–doped polysilicon and aluminum conductors, Sect. 5.3.2.

5.3.2 Double–layer metalization arrays

5.3.2.1 Introduction

The measurements presented in this section were performed on four different designs (i.e. IS–531, IS–562, IS–559 and IS–560) of high–purity silicon soft X–ray sensor arrays fabricated with the process sequence depicted in Sect. 4.6.2.2. Schematics of the sensor arrays are shown in Figs. 3.1(b), (c), (d) and (e), respectively. Photographs of the arrays, fabricated up to the first level metalization, are shown in Figs. 4.9(a), (b), (c) and (d), respectively.

The design IS–531 was the first device fabricated with the improved double–layer metalization process. This prototype is composed of a 3 x 3 array of 0.25 mm² elements. Although the processing requirements included integrated–circuit fabrication techniques not commonly employed in the processing of high–purity silicon radiation sensors, the array demonstrated good detector characteristics. In addition, experimental results confirmed the ability of the array to determine the two–dimensional position of incident radiation with minimal crosstalk, see below. With this device design, large matrices of small elements can be fabricated.

Due to the success of the prototype, a 256 element array (IS–562) was fabricated with the same basic design and process sequence. As with the prototype array, this larger (16 x 16) array of smaller elements (0.0625 mm²) also demonstrated good detector characteristics and experimental results confirmed the ability of the array to determine the two–dimensional position of incident radiation with minimal crosstalk, see below.

In an effort to improve the detector characteristics, the readout electronics were altered in such a way as to make the polysilicon resistive structures unnecessary. The polysilicon resistive structures are only necessary if the preamplifiers associated with the x–addresses have low input impedances. If charge–sensitive preamplifiers are utilized with high capacitive input impedances, the polysilicon resistive structures prove unnecessary, see below. As stated in Sect. 5.1.2.1, the input impedance of the preamplifier must be compared to the capacitance value associated with the diode elements. For a charge collection deficit of less than 1 % at the x–addressed output connections, the diode capacitance must be at least 100 times less than the preamplifier input capacitance. The maximum collection of the charge generated in an array element at the charge–sensitive preamplifiers associated with the x–addresses can then be obtained without the need for the polysilicon resistive structures, which will enable a device to be realized with improved energy and position resolutions.

The original prototype design IS–531 was modified through the elimination of the polysilicon resistive structures. A modified prototype array (a 3 x 3 array of 0.25 mm² elements) was fabricated, IS–559. Due to the successful operation of the modified prototype, a 256 element array (16 x 16 array of 0.0625 mm² elements) with the same basic design as the modified prototype was fabricated, IS–560. Improved leakage current and energy resolution results were obtained from devices with the design IS–560 (without the polysilicon structures) compared to devices with the design IS–562 (with the polysilicon structures), see below.

5.3.2.2 Reverse *I–V* characteristics

Figures 5.12(a)and (b), 5.13(a)and (b), 5.14(a)and (b) and 5.15(a)and (b) show typical reverse *I–V* characteristics of the resistive–coupled outputs after (a) the first level metalizations and (b) after full fabrication from the arrays IS–531, IS–562, IS–559 and IS–560, respectively.

The leakage currents were measured after the first level metalizations and again after full fabrication of the sensor arrays in order to observe the effect(s), if any, the low–temperature deposition of silicon dioxide had on the reverse *I–V* characteristics of the sensor arrays.

In the case of the design IS–531, Figs. 5.12(a) and (b), there are practically no differences between the two curves. The PECVD technique was employed in the fabrication of this sensor array to realize the low–temperature deposition of silicon dioxide, Sect. 4.5.2, while the silox deposition method was utilized with the other three sensor array designs, i.e. IS–562, IS–559 and IS–560.

In the fabrication of the designs IS–562, IS–559 and IS–560, an aluminum alloy step was not performed after the first level metalizations, as contact between the metal layer and the diode structures was achieved directly after the metalization step. This had the effect of increasing the resistance associated with the reverse *I–V* characteristic after the first layer metalizations, Figs. 5.13(a), 5.14(a) and 5.15(a). However, as the silox depositions took place at 400 °C for 15 minutes, this appears to have effectively annealed the metal layers, as the resistive increases are not seen in the reverse *I–V* characteristics after full fabrication, Figs. 5.13(b), 5.14(b) and 5.15(b).

The difference in the magnitudes of the two leakage currents from IS–562 is insignificant.

From Figs. 5.14(a) and (b), it can be seen that the magnitude of the leakage current after the first level metalization of a high–purity silicon soft X–ray sensor array with the design IS–559 was slightly lower than that after full fabrication, i.e. −1.6 nA vs. −2.2 nA at 100 V reverse bias. This difference is slight and could be due to the temperature difference at which the measurements were taken.

The leakage current after full fabrication is slightly smaller in magnitude compared with that after the first level metalization in the high–purity silicon soft X–ray sensor array with the design IS–560. This difference may be due to a possible reduction in the electrically active interface state density at the Si/SiO_2 interface during the low–temperature process that preceded the second level metalization, which would reduce the surface component of the leakage current.

The theoretical breakdown voltage, Eqn. (4.2), is on the order of 3×10^4 V and from the figures above, the experimental breakdown voltages can be seen to be over 100 V.

A low leakage current measurement obtained from a sensor or sensor array assures that the sensor or sensor array will produce good energy resolution measurements. However, these measurements were performed in addition to the measurements of the leakage current from the resistive–coupled outputs of the high–purity silicon soft X–ray sensor arrays realized through use of the double–layer metalization technique, as well as on the diode test structures fabricated alongside each sensor array design. The FWHM of a resistive–coupled output from a high–purity silicon soft X–ray sensor array with the design IS–531 at the 59.4 keV peak of [241]AM (the use of this source is described in Sect. 1.3.1)
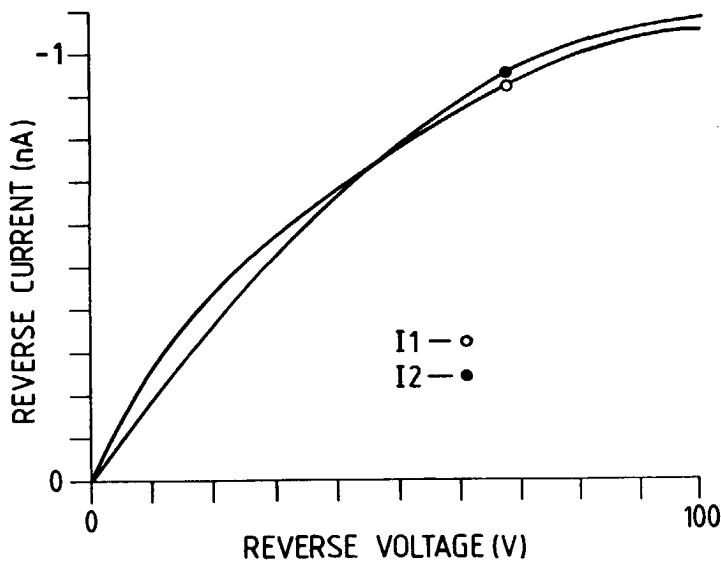
Fig. 5.12   *Typical reverse I–V characteristics of a resistive output from a high–purity silicon soft X–ray sensor array (IS–531) (a) after the first layer metalization and (b) after full fabrication.*
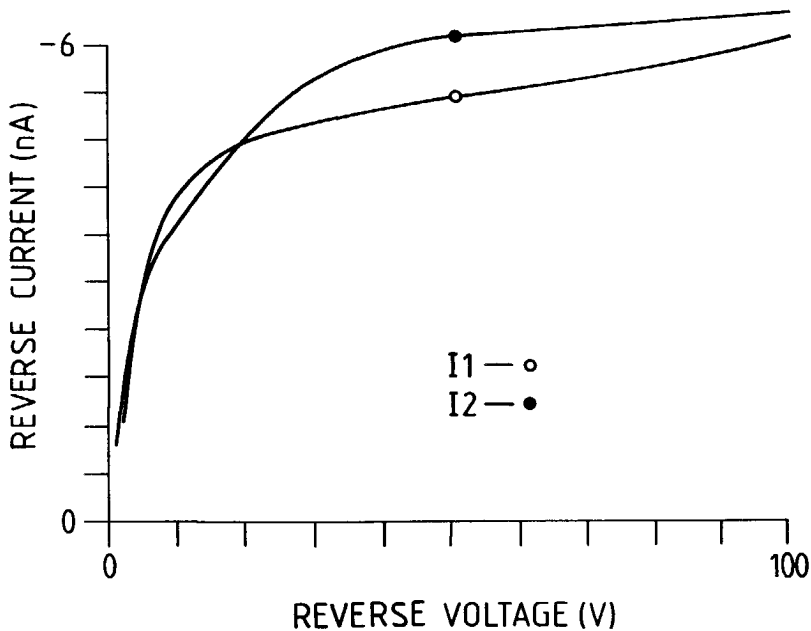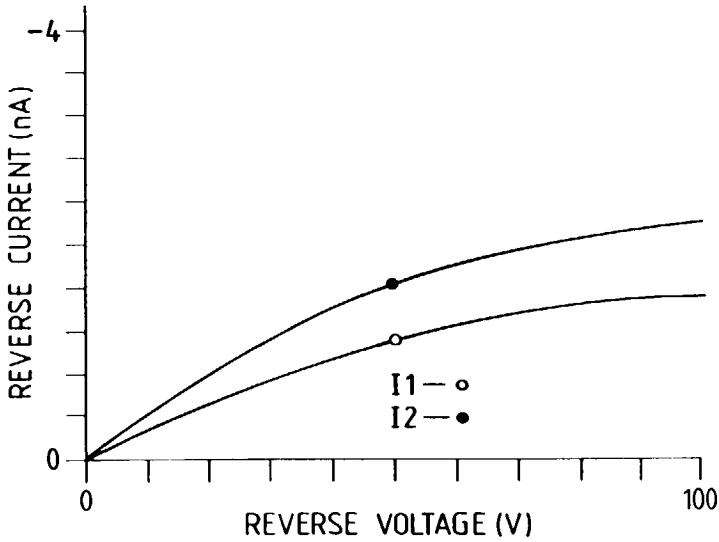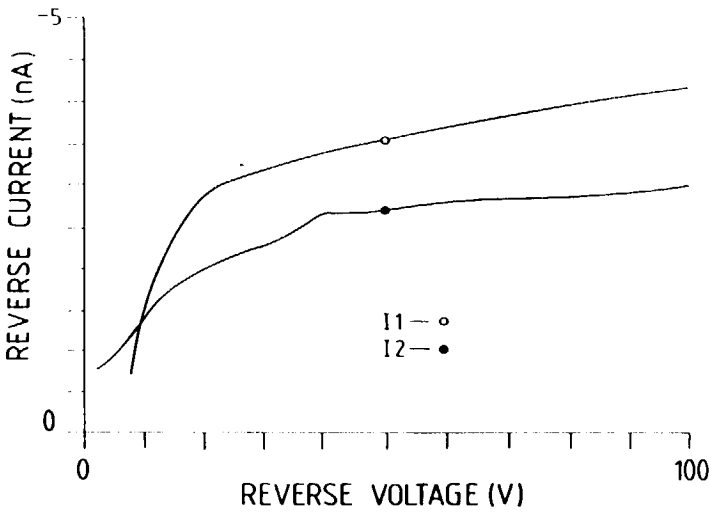
Fig. 5.13   *Typical reverse I–V characteristics of a resistive output from a high–purity silicon soft X–ray sensor array (IS–562) (a) after the first layer metalization and (b) after full fabrication.*

Fig. 5.14 *Typical reverse I–V characteristics of a resistive output from a high–purity silicon soft X–ray sensor array (IS–559) (a) after the first layer metalization and (b) after full fabrication.*

Fig. 5.15 *Typical reverse I–V characteristics of a resistive output from a high–purity silicon soft X–ray sensor array (IS–560) (a) after the first layer metalization and (b) after full fabrication.*
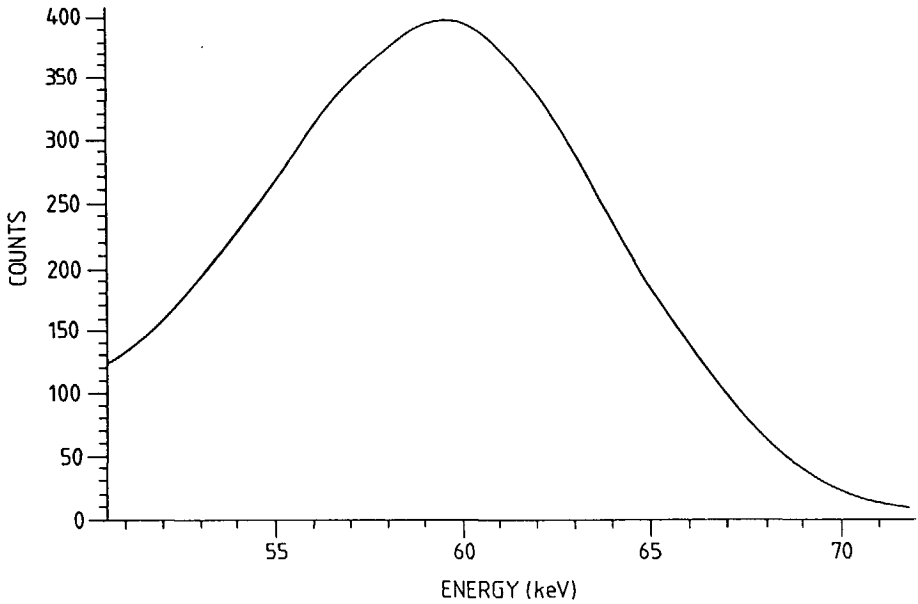
Fig. 5.16   *That part of the pulse–height spectrum of a resistive output from a high–purity silicon soft X–ray sensor array (IS–531) upon exposure to [241]Am showing the 59.4 keV peak.*

was measured to be 10 keV, Fig. 5.16. Similar results of the FWHM at the 59.4 keV peak of [241]AM were measured on the other three designs: IS–562, IS–559 and IS–560, i.e. 10 keV, 8 keV and 8 keV, respectively.

Because the sensor arrays IS–562 and IS–560 were processed simultaneously, their measurement results can be directly compared. Note that the magnitudes of the leakage currents of the 16 x 16 array without the polysilicon structures, IS–560, were approximately two times smaller than the leakage currents of the 16 x 16 array with the polysilicon resistive structures, IS–562. The energy resolution of IS–560 also proved to be better than its predecessor, IS–562. However, leakage current and energy resolution measurements of the 3 x 3 arrays cannot be directly compared, as they were not processed simultaneously.

5.3.2.3 Crosstalk measurements

In order to determine the degree of crosstalk, two outputs were measured in coincidence, as described in Sect. 3.3.4. High–energy electrons from a ^{90}Sr source were used in this investigation. Measurements performed on the sensor design IS–531 will first be described, followed by those of the designs IS–562, IS–559 and IS–560.

Figures 5.17(a) and (b) are typical measurements obtained from the middle resistive output and its neighboring resistive output (IS–531) when the coincidence condition was set on the middle output. It is important to note the different scales used in the two figures. The graphs demonstrate the reduction in counts recorded in the coincidence measurement, i.e. in the pulse–height spectrum of Fig. 5.17(b). At the threshold energy of 250 keV, the middle output records approximately 100 counts, while that of its neighbor, measured in coincidence, records approximately 5 counts. Taking the entire spectrum from 250 to 1000 keV into consideration, the crosstalk was estimated to be less than 5 %.

Figures 5.18(a) and (b) are typical measurements taken from the middle capacitive output and its neighboring capacitive output (IS–531) when the coincidence condition was set on the middle output. These graphs provide results similar to those of Figs. 5.17(a) and (b). Again the crosstalk was estimated to be less than 5 %.

The next–neighboring crosstalk was also measured for both the resistive and the capacitive outputs from a sensor array with the design IS–531. Figures 5.19(a) and (b) display the right resistive output and the left resistive output (IS–531) when the coincidence condition was set on the right output. Note the change in scales of the figures. Similar measurements were made on the capacitive–coupled next–neighboring outputs and similar results were obtained. The next–neighboring crosstalk can be seen to be equal to or less than the neighboring crosstalk.

Figures 5.20(a) and (b) are typical measurements from the sensor design IS–562 obtained from a given resistive–coupled output and its next–neighboring resistive output when the coincidence condition was set on the given output, respectively. Note the very high threshold that was set on the given output, Fig. 5.20(a), i.e. with no threshold set, the pulse–height spectrum would begin at the origin and continue through the higher energies. Again, it is important to note the different scales used in the two figures. The graphs demonstrate the reduction in counts recorded in the coincidence measurement. The crosstalk is estimated to be less than 5 %.

Figures 5.21(a) and (b) are typical measurements from the sensor design IS–562 taken from a given capacitive output and its next–neighboring capacitive output when the coincidence condition was set on the given output, respectively. These graphs provide results similar to those of Figs. 5.20(a) and (b). Again the crosstalk was estimated to be less than 5 %. Neighboring crosstalk measurements were disqualified in the case of this sensor array (IS–562), as backscatter, which occurs with high–energetic electrons and can create a pulse up to 500 μm from from the electron's point of origin, could not be distinguished from true crosstalk.

Identical measurements were then performed on the modified sensor arrays IS–559 and IS–560. Again, only the next–neighboring coincidence studies were performed on the larger sensor array (16 x 16) with the smaller elements (0.0625 mm^2), IS–560. The crosstalk measured with these arrays without polysilicon resistive structures was higher than that measured with their predecessors. However, the crosstalk remains minimal and, especially in applications where a digital detector output is sufficient, the modified sensor arrays remain useful in the imaging of soft X–rays. To avoid repetition, only those measurements obtained from IS–560 will be shown.
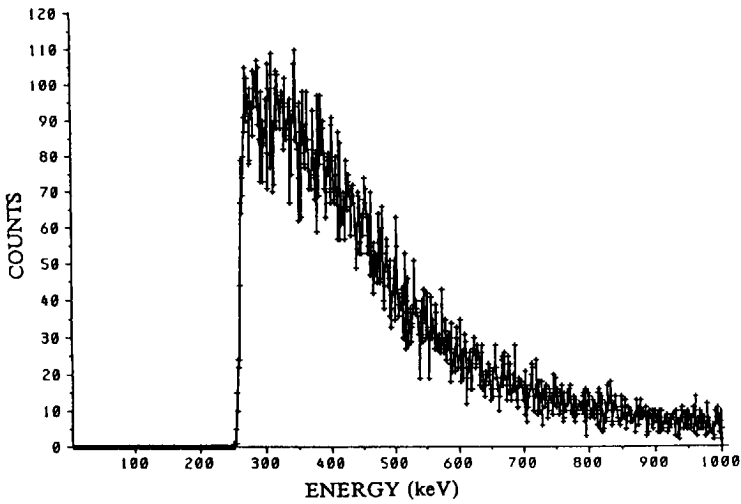
Fig. 5.17 (*a*) *Typical response from the middle resistive output (IS–531) when exposed to a* ^{90}Sr *source.*
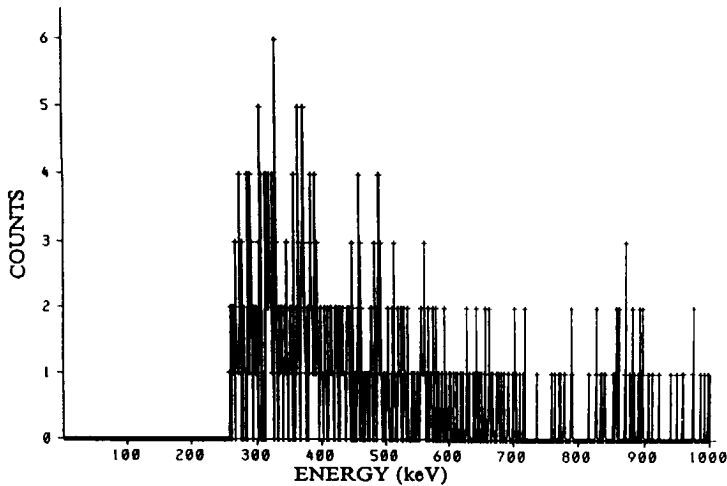
Fig. 5.17 (*b*) *Response from a neighboring resistive output (IS–531) when the coincidence condition was set on the output of Fig. 5.17(a). Note the change of scales from Fig. 5.17(a).*
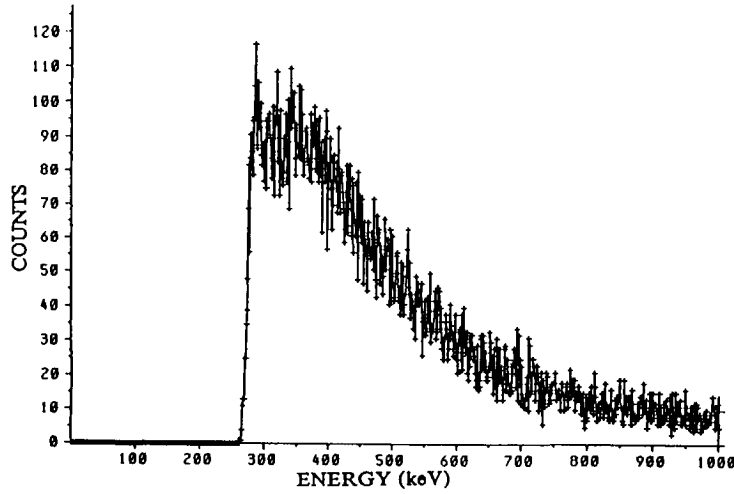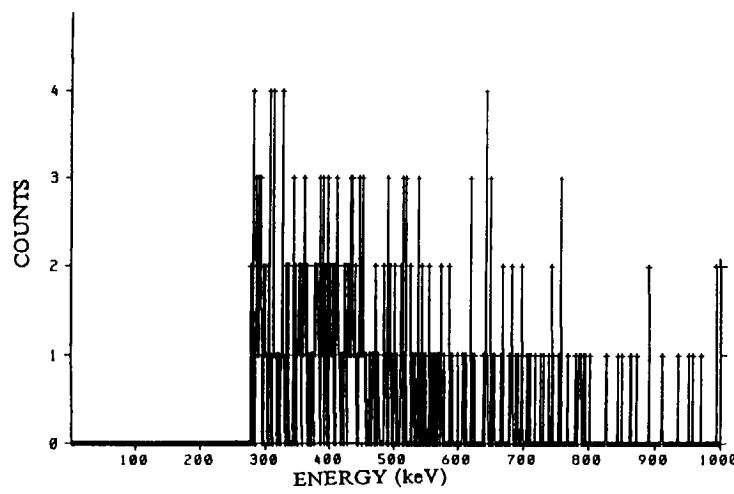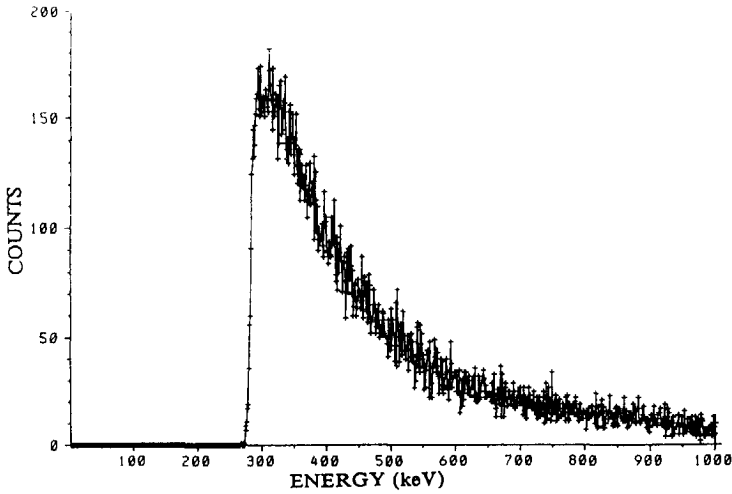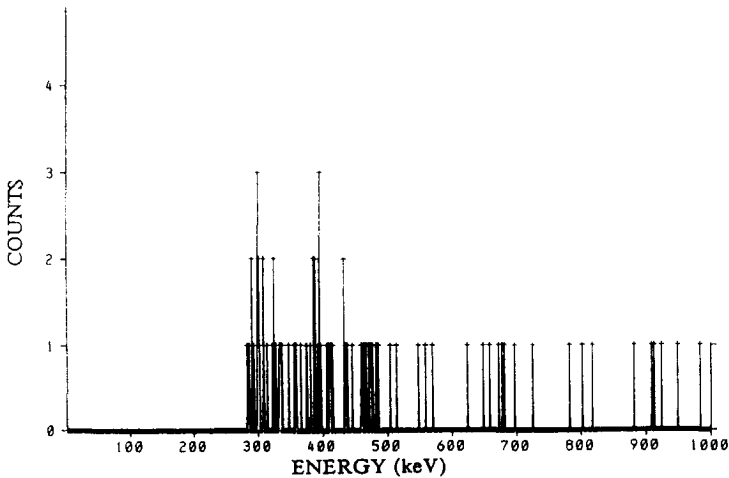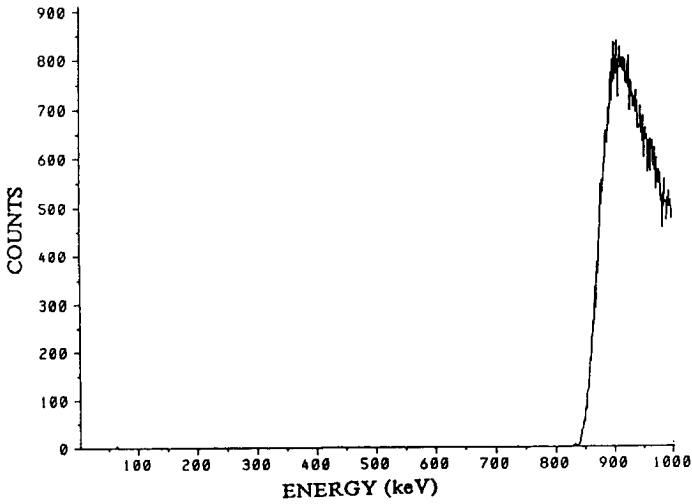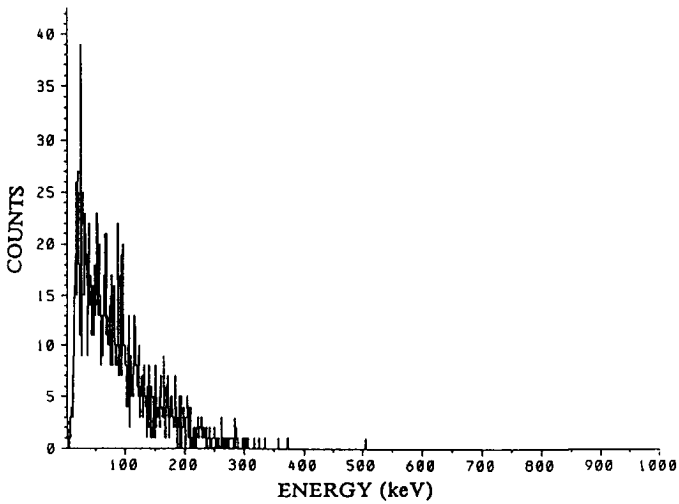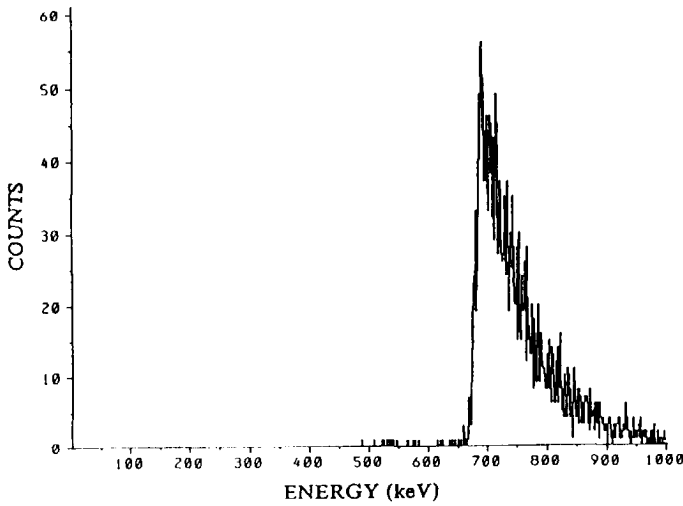
Fig. 5.18 (*a*) *Typical response from the middle capacitive output* (*IS–531*) *when exposed to a* ^{90}Sr *source.*

Fig. 5.18 (*b*) *Response from a neighboring capacitive output* (*IS–531*) *when the coincidence condition was set on the output of Fig. 5.18(a). Note the change of scales from Fig. 5.18(a).*

Fig. 5.19   (*a*) *Typical response from the right resistive output* (*IS–531*) *when exposed to a* ^{90}Sr *source.*

Fig. 5.19 (*b*) *Response from a next–neighboring resistive output* (*IS–531*) *when the coincidence condition was set on the output of Fig. 5.19(a). Note the change of scales from Fig. 5.19(a).*

Fig. 5.20 (*a*) *Typical response from a given resistive output (IS–562) when exposed to a* ^{90}Sr *source.*

Fig. 5.20 (*b*) *Response from a next–neighboring resistive output (IS–562) when the coincidence condition was set on the output of Fig. 5.20(a). Note the change of scales from Fig. 5.20(a).*

Fig. 5.21   (*a*) *Typical response from a given capacitive output* (*IS–562*) *when exposed to a* ^{90}Sr *source.*
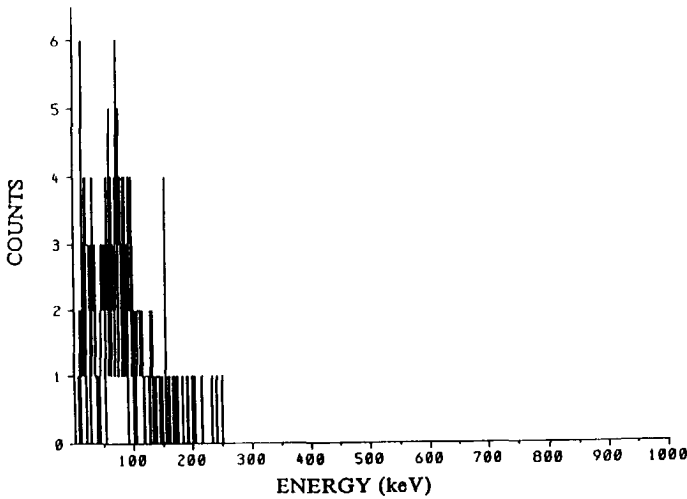
Fig. 5.21   (*b*) *Response from a next–neighboring capacitive output* (*IS–562*) *when the coincidence condition is set on the output of Fig. 5.21(a). Note the change of scales from Fig. 5.21(a)*

Figures 5.22(a) and (b) are typical measurements from the sensor design IS–560 obtained from a given resistive–coupled output and its next–neighboring resistive output when the coincidence condition was set on the given output, respectively. Note the very high threshold that was set on the given output, Fig. 5.22(a), i.e. with no threshold set, the pulse–height spectrum would begin at the origin and continue through the higher energies. Again, it is important to note the different scales used in the two figures. The graphs demonstrate the reduction in counts recorded in the coincidence measurement, i.e. in the pulse–height spectrum of Fig. 5.22(b). The crosstalk is estimated to be less than 10 %.

Figures 5.23(a) and (b) are typical measurements from the sensor design IS–560 taken from a given capacitive output and its next–neighboring capacitive output when the coincidence condition was set on the given output, respectively. These graphs provide results similar to those of Figs. 5.22(a) and (b). Again the crosstalk was estimated to be less than 10 %. Neighboring crosstalk measurements were disqualified in the case of this sensor array (IS–560), as backscatter, which occurs with high–energetic electrons and can create a pulse up to 500 μm from the electron's point of origin, could not be distinguished from true crosstalk.

5.3.2.4 Measurements on test structures

The diode, MOS capacitor and polysilicon resistive test structures, fabricated on the same chips as the sensor arrays, were measured and the results are shown below. Reverse *I–V* characteristics were measured on diode test structures, fabricated on the same chips as the high–purity silicon soft X–ray sensor arrays, after the first and after the second level metalizations. Typical results obtained on 0.25 mm^2 test diodes fabricated alongside sensor array design IS–531 are shown in Figs. 5.24(a) and (b). From the test structures, the leakage current is calculated to be 24 nA/cm^2 per 100 μm depletion depth. Diode test structures fabricated alongside the other high–purity silicon soft X–ray sensor array designs, i.e. IS–562, IS–559 and IS–560, revealed leakage current measurements after the first level metalizations and after full fabrication also on the order of $20 - 30$ nA/cm^2 per 100 μm depletion depth.

In an effort to examine the effect the highly doped polysilicon resistive structures would have on the energy resolution of the diode matrix, another study, similar to the one described in Sect. 5.2.2, was performed. This study proved to be more sensitive, as the size of the test diode was greatly reduced.

The energy resolution for the 59.4 keV peak of an ^{241}Am source of two different test structures, fabricated within the same chip as the sensor array design IS–531, were obtained. One test structure was a 0.25 mm^2 diode and the other was a 0.25 mm^2 diode with a polysilicon resistive structure (geometrically identical to those within the array) in series. The pulse–height spectrums of the two diode test structures upon exposure to ^{241}Am are shown in Figs. 5.25(a) and (b), respectively, while those parts of the pulse–height spectrums showing the 59.4 keV peaks are magnified and shown in Figs. 5.26(a) and (b), respectively.
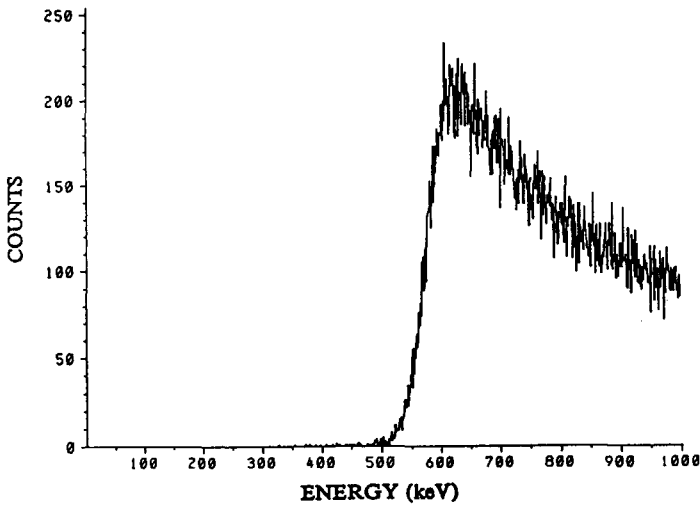
Fig. 5.22 (*a*) *Typical response from a given resistive output (IS–560) when exposed to a* ^{90}Sr *source.*
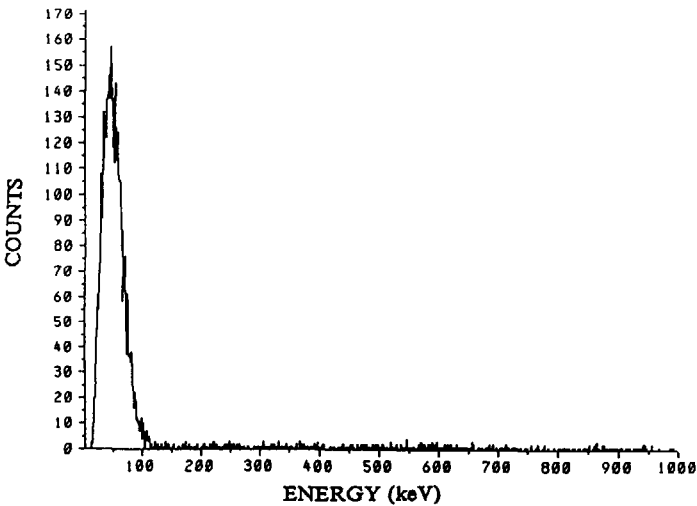
Fig. 5.22 (*b*) *Response from a next–neighboring resistive output (IS–560) when the coincidence condition was set on the output of Fig. 5.22(a). Note the change of scales from Fig. 522(a).*
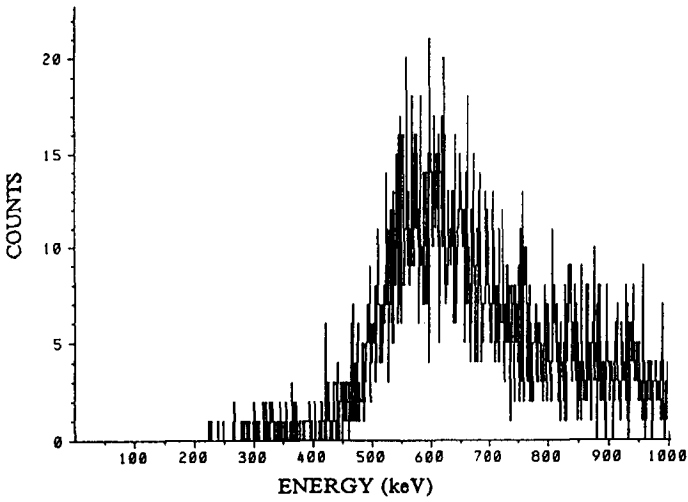
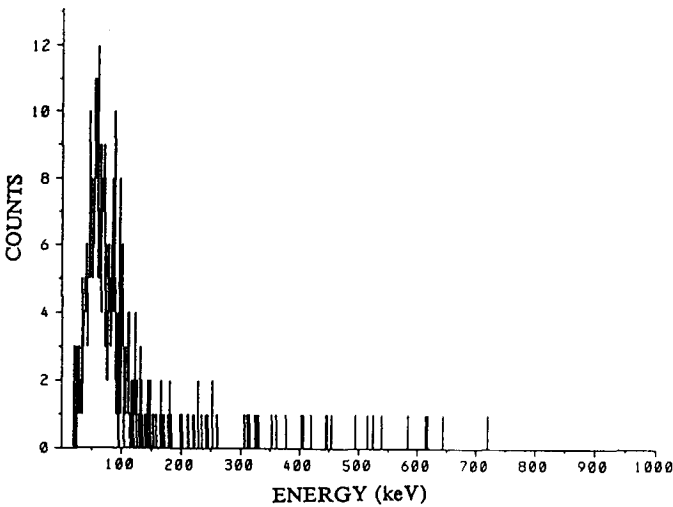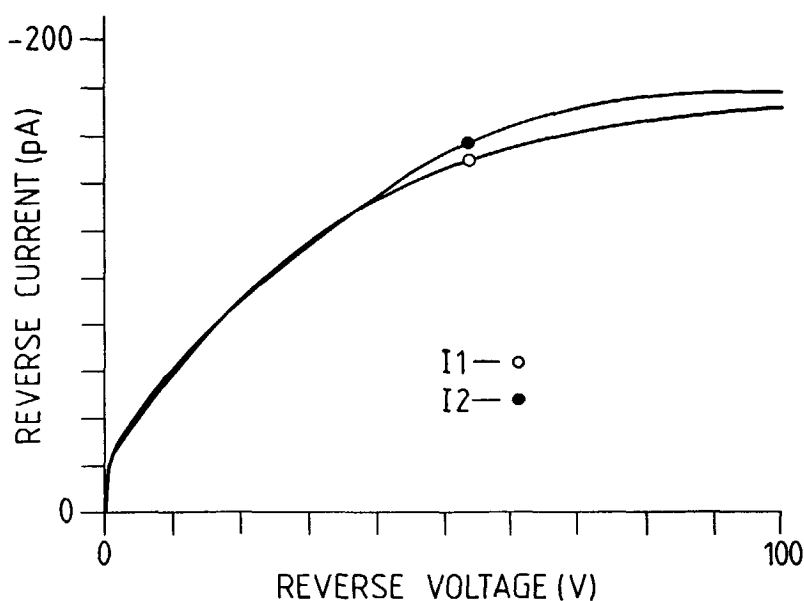Fig. 5.23 (a) *Typical response from a given capacitive output (IS–560) when exposed to a* ^{90}*Sr source.*

Fig. 5.23 (b) *Response from a next–neighboring capacitive output (IS–560) when the coincidence condition is set on the output of Fig. 5.23(a). Note the change of scales from Fig. 5.23(a).*

Fig. 5.24 *Typical reverse I–V characteristics of a test diode 0.25 mm² in area fabricated on the same chip as a high–purity silicon soft X–ray sensor array (IS–531) (a) after the first level metalization and (b) after full fabrication.*

A separation in the L X–rays can be seen in the pulse–height spectrum of the first test structure, Fig. 5.25(a), while the second test structure is not able to distinguish the two peaks. The FWHM values for the two test structures at the 59.4 keV peak were 3.7 and 5.7 keV, (Figs. 5.26(a) and (b)), respectively. The noise associated with the polysilicon structures can now be seen to be of consequence. This noise adds to the noise of the diode itself, which broadens the pulse–height spectrum and increases the FWHM value.

In order to measure the doping profiles of the substrates upon completion of the processing of the arrays, two test structures, i.e. MOS capacitors with the same perimeters but different areas, were fabricated on the same chips, Sect. 4.7.1.2. The $C–V$ data, obtained from the two devices on each chip through a $C–V$ measurement technique, were subtracted so that the sidewall capacitance of the larger structures could be eliminated. The doping profiles of the substrates were then extracted from the $C–V$ data.

The doping profiles of the substrates for the sensor arrays of designs IS–531 and IS–562 are shown in Figs. 5.27 (a) and (b), respectively. To avoid redundancy, the data for the other two sensor arrays is not displayed, however, similar results were obtained.

The doping of the substrates upon completion of the processing of the sensor arrays are comparable to that of the starting material, i.e. substrate resistivity 4 kΩ–cm; doping level on the order of $N_d = 1 \times 12$ cm^{-3}.
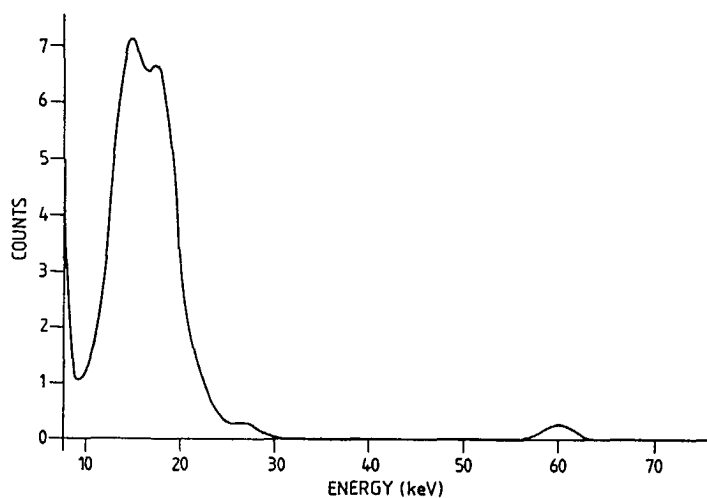
Fig. 5.25 (*a*) *Pulse–height spectrum of a test diode 0.25 mm² in area fabricated on the same chip as a high–purity silicon soft X–ray sensor array (IS–531) upon exposure to ²⁴¹Am.*
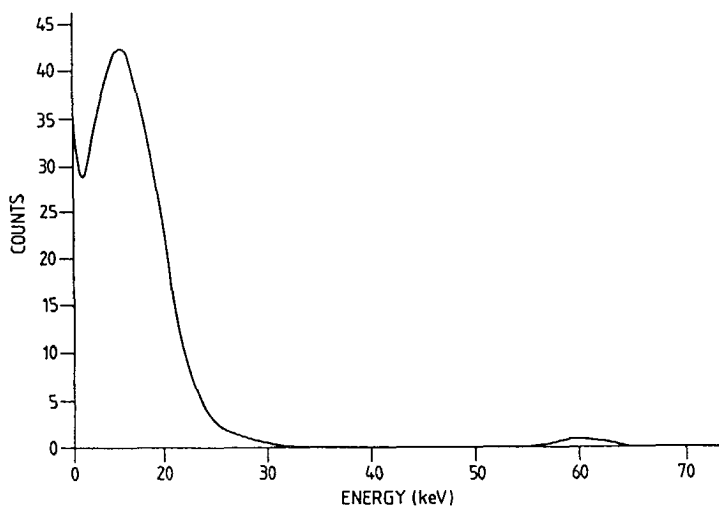

Fig. 5.25 (*b*) *Pulse–height spectrum of a test diode 0.25 mm² in area in series with a polysilicon resistive structure (geometrically identical to those within the sensor array) fabricated on the same chip as a high–purity silicon soft X–ray sensor array (IS–531) upon exposure to ²⁴¹Am.*
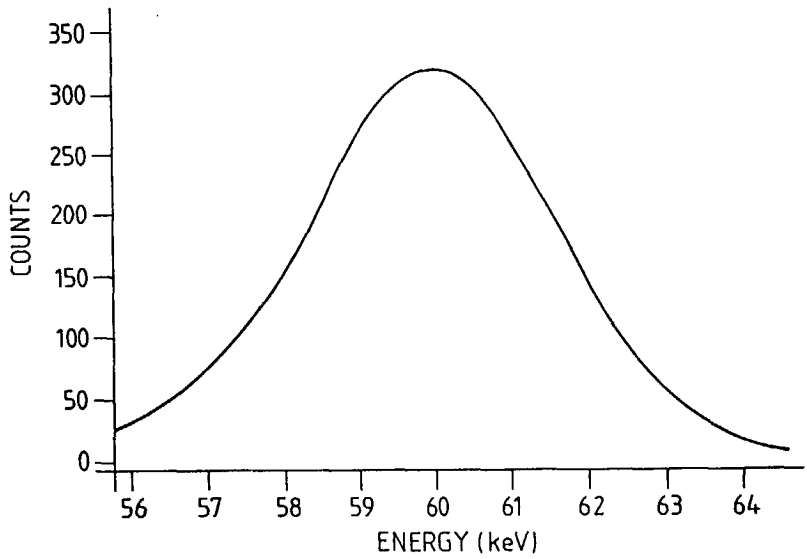
Fig. 5.26 (*a*) *That part of the pulse–height spectrum from Fig. 5.25(a) showing the 59.4 keV peak.*
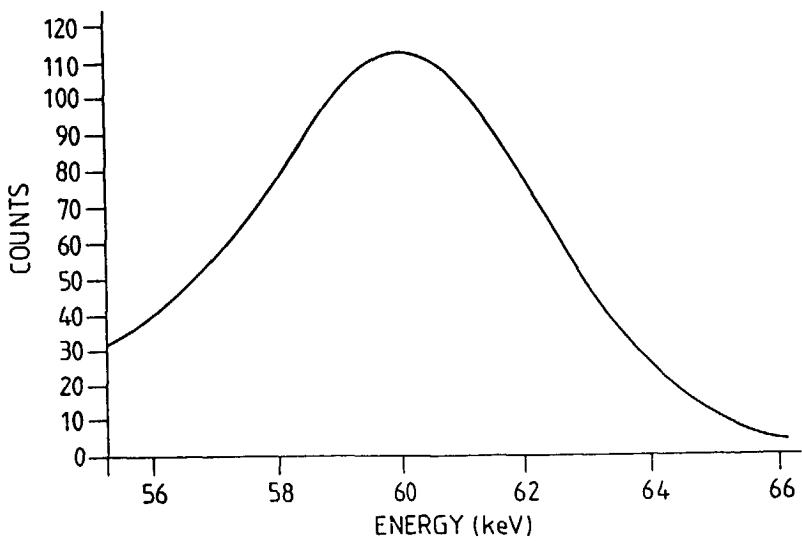
Fig. 5.26 (*b*) *That part of the pulse–height spectrum from Fig. 5.25(b) showing the 59.4 keV peak.*
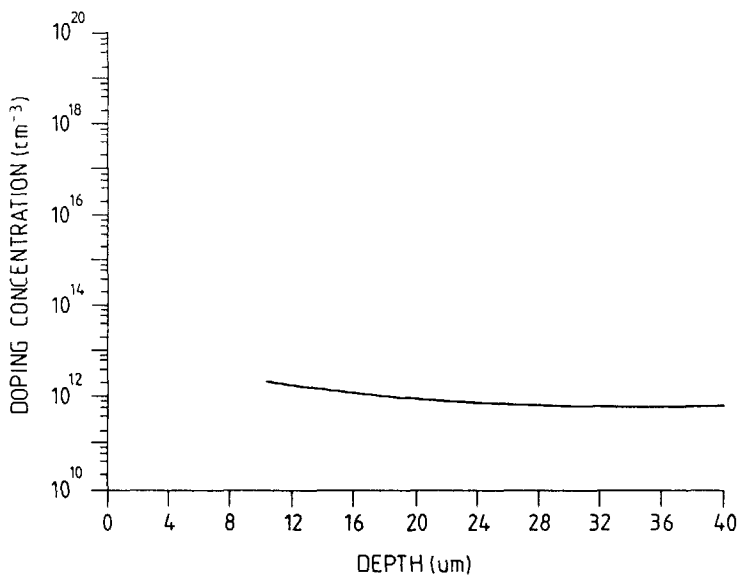
Fig. 5.27 (*a*) *The doping profile of the substrate of a high–purity silicon soft X–ray sensor array (IS–531) after full fabrication.*
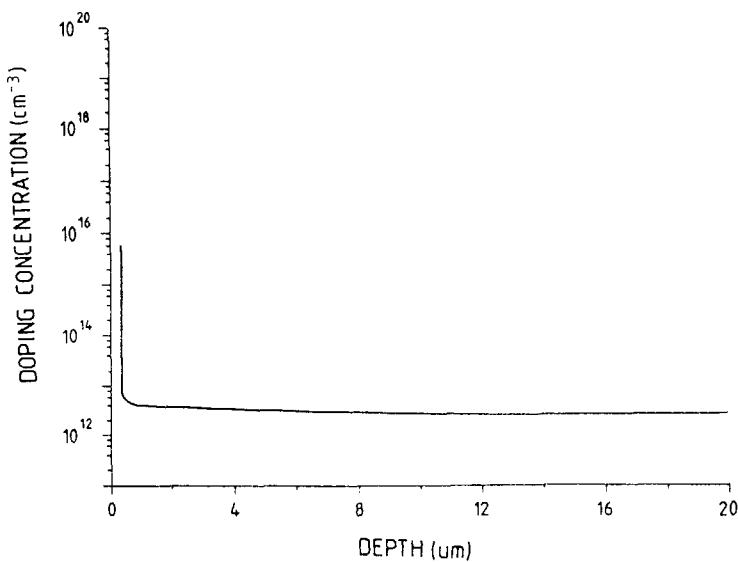
Fig. 5.27 (*b*) *The doping profile of the substrate of a high–purity silicon soft X–ray sensor array (IS–562) after full fabrication.*

From test resistors placed around the periphery of the chips with the same as well as different dimensions as those in series with the diodes the resistance values of the resistive structures within the sensor arrays of IS–531 and IS–562 could be estimated. The theoretical resistance values of the resistive structures from these two designs are calculated according to Eqn. (4.3).

The geometry of the polysilicon structures used in the two different sensor arrays of the design IS–531 were identical to those of test resistors 4 and 5, while that geometry of test resistor 4 was used in the sensor arrays of the design IS–562, Sect. 5.2.2. Resistance measurements performed on the fourteen test resistors of the designs IS–531 were similar to those average measured values presented in Table 5.1, i.e. the theoretical values were obtained ± 5 %. Only four test resistors were placed on the design IS–562, all of which had a theoretical resistance value of 195 Ω/sqr. Again, the average measured resistance values of the four test structures was the theoretical value ± 5 %.

5.4 CONCLUSIONS

The measurement system used for the detection of soft X–radiation is first described in this chapter. The magnitude of the signal obtained from a high–purity silicon soft X–ray sensor or sensor array is relatively small, due to the limited amount of charge created upon the absorption of a soft X–ray photon in the high–purity silicon bulk. As there is no gain associated with the sensor itself, preamplification of the signal is necessary. The preamplifier should provide low–noise amplification. In addition, it should be small, fast and have a low power dissipation.

A spectroscopy amplifier shapes and filters the signal, as well as amplifies the signal magnitude. After amplification, the signal is input into a multi–channel analyzer. Conventional multi–channel analyzers are equipped with level discriminators, analog–to–digital converters, coincidence capabilities and memory and display units. Multi–channel analyzers collect and store spectral data acquired from a detection system for the purposes of display and/or further analysis. A histogram of the number of counts versus the channel number or versus the elapsed time is obtained at the end of the measurement.

The experimental leakage currents obtained from the high–purity silicon soft X–ray sensors and sensor arrays were in good agreement with those values predicted by the theory. The experimental resistance values of the polysilicon resistive structures were also in good agreement with what was predicted theoretically.

Two different gettering techniques are tested: a backside arsenic implantation and a backside phosphorous diffusion. The gettering abilities of the two techniques are approximately equal.

The crosstalk is less than 10 % in the high–purity silicon soft X–ray sensor arrays based on the double–layer conduction technique, IS–502. However, this device design is limited in that large arrays of small elements cannot be realized.

The crosstalk in the high–purity silicon soft X–ray sensor arrays based on the double–layer metalization technique that employed polysilicon resistive structures in their designs, IS–531 and IS–562, is less than 5 %. The crosstalk in

those high–purity silicon soft X–ray sensor arrays based on the double–layer metalization technique that employed only the small resistance of the aluminum interconnection lines, IS–559 and IS–560, is somewhat higher (although still less than 10 %), but the energy resolutions in these arrays are superior to those of their predecessors.

A soft X–ray sensor array must be able to absorb incident soft X–rays and collect the electron–hole pairs subsequently generated within its volume in order to provide a true measure of the energy of the incident radiation and to indicate in two dimensions the radiation's position of incidence. The low leakage currents, good energy resolutions and minimal degrees of crosstalk associated with the high–purity silicon soft X–ray sensor arrays presented in this thesis establish their useful application in the imaging of soft X–rays.

Future work should concentrate on two areas: the realization of larger arrays of smaller elements and the realization of preamplification electronics on the same high–purity silicon substrate as the sensor.

Device simulation studies performed on the high–purity silicon soft X–ray sensor array design based on the double–layer metalization technique show that with this design the successful operation of a large matrix (7.6×7.6 cm^2) of small elements ($20 \times 20 \, \mu$m^2) is feasible. The fabrication of such a matrix is also feasible. An array with these specifications would involve a twenty–fold improvement in the position resolution and would be large enough to be utilized in experimental systems.

The employment of large sensor arrays in experimental systems is however often difficult due to the large number of sensor outputs. Realizing preamplification electronics on the same substrate as the sensor array would minimize the difficulty associated with the bonding of each output to a preamplifier. It would also minimize the parasitic capacitance between the two units and thereby minimize the system noise. The total power, size and wiring costs of the detection system would also be reduced [5.5]. Although a number of incompatibilities exist in the co–integration of radiation sensors and electronics on the same high–resistivity silicon substrate, the benefits such a system would provide, justify future research in this area.

REFERENCES

[5.1]   EG&G Ortec Product Information Catalog, Nuclear instruments and systems; radiation detection, measurement and analysis, Oak Ridge, TN, U.S.A., 1986/87.

[5.2]   S. Holland, An I.C.–compatible detector process, Proc. IEEE Nuclear Science Symp., Orlando, Nov. 9–11, 1988, 112–115.

[5.3]   T. Otaredian, S. Middelhoek and M.J.J. Theunissen, The theory and application of contactless microwave lifetime measurement, Materials Science and Engineering, B5 (1990) 151–156.

[5.4]   D. Lecrosnier, J. Paugam, G. Pelous, F. Richou and M. Salvi, Gold gettering in silicon by phosphorous diffusion and argon implantation: mechanisms and limitations, J. Appl. Phys., 52 (1981) 5090–5097.

[5.5]   S.A. Audet and S.E. Wouters, Monolithic integration of a nuclear radiation sensor and transistors on high–purity silicon, accepted for publication in IEEE Trans. on Nucl. Sci.

SUMMARY

The aim of the research presented in this thesis is to investigate the fundamental properties of two–dimensional position–sensitive soft X–ray sensors fabricated on high–purity silicon. Very little effort has been expended for the development of sensors for the detection of soft X–rays, i.e. electromagnetic radiation with energies between approximately 2–25 keV. In the past, there has been little need for such sensors, as there have been few sources of soft X–radiation. However, due to the recent progress made in the fundamental research and technological applications of soft X–radiation sources, e.g. synchrotron and repeatedly–pulsed plasma sources, the development of soft X–ray imaging sensor arrays has become necessary. High–purity silicon sensor arrays are ideal devices for application in those systems that utilize low–energy (soft) X–rays.

The interactions that take place when electromagnetic radiation is incident upon silicon are discussed in Chapter 2. Soft X–rays are absorbed in silicon primarily by the photoelectric effect. The number of free carriers generated upon the absorption of a photon in silicon depends on the energy of the radiation. The overall detection process not only involves the absorption of incident photons and the ensuing charge generation, but also involves the collection of the generated charge. The absolute quantum efficiency engrosses the overall process and is defined as the ratio of the number of charge carriers collected to the theoretical number that would be generated if all the incident photons emitted from the source were converted to charge carriers.

High–purity silicon soft X–ray sensors, i.e. the elemental units of the sensor arrays, are theoretically characterized in Chapter 2. Two types of sensors are examined. Both consist of $p^+-n^--n^+$ diodes realized on high–resistivity silicon. The readout of the sensors from the first type is direct, while each sensor from the second type is first connected in series with a polysilicon resistive structure before being read out. The theoretical characterization consists of analyses of the sensors' leakage currents, lifetimes, energy resolutions and noise sources. The principles of charge collection and the damage incident radiation creates within the sensors are also discussed.

The total leakage current in high–purity silicon soft X–ray sensors originates from three sources: from the surface, from thermal generation in the depletion

region and from thermal generation in the undepleted regions. In the standard mode of operation, i.e. the fully depleted mode, the greatest contribution to the total leakage current arises from thermal generation in the depletion region.

The ability of a detector to measure the energy of incident radiation is quantified by its energy resolution. The emission spectrum of a monoenergetic source should theoretically be an impulse. However, a broad pulse is typically recorded due to noise sources. Line broadening effects arise from three main sources of noise: statistical fluctuations in the number of created carriers, statistical fluctuations in the magnitudes of the diodes' reverse currents and statistical fluctuations in the currents originating from the electronic circuitry.

Electromagnetic radiation incident upon a high—purity silicon soft X—ray sensor causes damage through the generation of lattice displacement defects. However, if the energy of the incident radiation is below 130 keV, significant damage does not occur. Moreover, annealing techniques offer the possibility to reduce or eliminate the damage.

High—purity silicon soft X—ray sensor arrays are theoretically characterized in Chapter 3. Two types of sensor arrays are examined. The fabrication of one type is based on a double—layer conduction (polysilicon and aluminum) technique. This sensor array design has the limitation that large arrays of small elements cannot be realized.

This is not a limitation in the sensor array designs of the second type, which employ a double—layer metalization (aluminum, aluminum) fabrication technique. These sensor arrays are divided into two groups, the designs of which are based on the elemental sensor units described above. One group of arrays is composed of matrices of high—purity silicon soft X—ray sensor elemental units, while the elemental unit that is used to build the matrices in the second group consists of a high—purity silicon soft X—ray sensor in series with a polysilicon resistive structure.

Due to the fact that the sensor arrays are composed of sensor elemental units, many of the sensor characterization parameters apply directly to the sensor arrays. The leakage current associated with one resistive output of a sensor array is the sum total of the leakage currents of the elemental units in that column. The lifetime associated with a particular soft X—ray sensor is not dependent on the sensor design and therefore does not have to be redefined for the sensor arrays. The energy resolution and noise of a sensor array are similarly defined by the energy resolution and noise of the individual sensor elements. Parameters that do differ for the sensor arrays include spatial resolution, crosstalk and radiation damage.

Crosstalk between neighboring elements within the sensor arrays can occur when charge collected at one element induces an output at another element. Coincidence techniques can be used to determine the degree of crosstalk.

As the sensor arrays have two metalization layers and a dielectric separating them, they may not be as radiation hard as the basic sensors. Long term ionization effects due to trapped charge may affect the functioning of the dielectric. Backside illumination of the sensor arrays will reduce the possibility of this damage from occurring.

The fabrication of the high—purity silicon soft X—ray sensors and sensor arrays is detailed in Chapter 4. Fabrication of the sensors involves the formation of two junctions in high—resistivity silicon substrates through the use of ion—implantation techniques: a frontside p^+-n^- junction and a backside n^--n^+

junction. High–purity silicon is used as the substrate material for a number of reasons. It contains a relatively low impurity concentration, a low trap density and a low scattering–center density. Therefore, thermal generation in the depletion region is minimized and the depletion–region depth, the minority–carrier lifetime and the charge–carrier mobilities are maximized. In addition, a high electric field is created in the depletion region of a fully reverse–biased sensor. This electric field assures the collection of the photon–generated charge in less than 25 ns and prevents the diffusive spreading of the charge before it reaches the collecting electrode(s). Moreover, devices fabricated on high–ohmic silicon consistently have higher quantum efficiencies for soft X–rays than those fabricated on standard ohmic silicon. The resistive structures were realized through the deposition and doping of polysilicon by LPCVD and phosphorous diffusion techniques, respectively.

The process sequence developed to realize the high–purity silicon soft X–ray sensors could directly be utilized to fabricate the high–purity silicon soft X–ray sensor arrays based on the double–layer metalization technique with the addition of two steps: a low–temperature deposition of silicon dioxide and a second layer metalization.

The measurement system used for the detection of soft X–radiation is detailed in Chapter 5. The photon–generated charge must be processed after it is collected. The signal–processing units used in soft X–ray detection systems consist of preamplifiers, spectroscopy amplifiers, ADCs, coincidence units and MCAs. The successful application of high–purity silicon soft X–ray sensors and sensor arrays depends critically on the availability of small, fast, low noise amplification and signal–conditioning electronics with low power dissipations.

Experimental results are presented in Chapter 5. The leakage currents obtained from the high–purity silicon soft X–ray sensors and sensor arrays were in good agreement with those values predicted by theory. The experimental resistance values of the polysilicon resistive structures were also in good agreement with what was predicted theoretically.

The crosstalk associated with all the sensor array designs was consistently less than 10 %. The sensor arrays fabricated with the double–layer metalization technique employing polysilicon resistive structures had the lowest degree of crosstalk (less than 5 %), while those sensor arrays fabricated with the double–layer metalization technique which were not associated with polysilicon resistive structures had the best energy resolutions.

The aim of a soft X–ray sensor array is to absorb the incident radiation and to collect the electron–hole pairs subsequently generated within its volume in order to provide a true measure of the energy of the incident radiation and to indicate in two dimensions the radiation's position of incidence. The low leakage currents, good energy resolutions and minimal degrees of crosstalk associated with the high–purity silicon soft X–ray sensor arrays presented in this thesis establish their useful application in the imaging of soft X–rays.

SAMENVATTING

Het in dit proefschrift gepresenteerde onderzoek behandelt de fundamentele eigenschappen van tweedimensionale positiegevoelige sensoren voor het meten van zachte röntgenstraling. De sensoren zijn vervaardigd in hoogohmig silicium. Door de vooruitgang op het gebied van het fundamentele onderzoek naar de technische toepassingen van zachte röntgenstraling (b.v. synchrotronstraling en gepulste plasmabronnen) is de ontwikkeling van tweedimensionale positiegevoelige sensoren voor het meten van zachte röntgenstraling noodzakelijk geworden. Hoogohmige silicium sensormatrices zijn bij uitstek geschikt voor het meten van laag energetische (zachte) röntgenstraling.

De interaktiemechanismen, die de wisselwerking tussen elektromagnetische straling en silicium beschrijven, worden behandeld in Hoofdstuk 2. Zachte röntgenstraling wordt in silicium voornamelijk d.m.v. het fotoelektrisch effekt geabsorbeerd. Het aantal vrije ladingsdragers dat gegenereerd wordt door de absorbtie van een foton wordt bepaald door de energie van de invallende straling. Het komplete detektieproces hangt niet alleen af van de absorptie van de fotonen en de bijbehorende generatie van ladingsdragers, maar wordt mede bepaald door de kollektie van de gegenereerde lading. De absolute kwantumefficiency omvat het komplete proces en is gedefinieerd als de verhouding van het aantal gekollekteerde ladingsdragers en het theoretische aantal dat zou worden gegenereerd als alle invallende fotonen omgezet zouden worden in ladingsdragers.

Hoogohmige silicium sensoren voor het meten van zachte röntgenstraling, in het bijzonder de matrix–elementen van de sensormatrices, worden theoretisch gekarakteriseerd in Hoofdstuk 2. Twee soorten sensoren worden behandeld, welke beide bestaan uit p^+–n^-–n^+ diodes van hoogohmig silicium. Het uitleesmechanisme van de sensoren van het eerste type is direkt, terwijl bij de tweede soort elke sensor via een geintegreerde polysilicium weerstand wordt uitgelezen. De theoretische karakterisatie omvat de analyses van de lekstroom van de sensor, de levensduur van de ladingsdragers, de energieresolutie en de ruisbronnen. Het principe van de ladingskollektie en de schade, die de invallende straling in de sensoren veroorzaakt, wordt ook behandeld.

De totale lekstroom in hoogohmige silicium sensoren voor het meten van zachte röntgenstraling bestaat uit drie komponenten: lek via het oppervlak,

thermische generatie in de depletielaag en thermische generatie in de niet—gedepleteerde gebieden. Bij de standaardinstelling (d.w.z. dat de sensor geheel gedepleteerd is) wordt de totale lekstroom voornamelijk bepaald door de thermische generatie in de depletielaag.

De geschiktheid van een detektor om de energie te meten van invallende straling wordt weergegeven door de energieresolutie. Het energiespektrum van een monoenergetische bron is in theorie een delta—puls. Echter in de praktijk wordt een brede puls gemeten, veroorzaakt door verschillende ruisbronnen. Dit lijnverbredingseffect wordt veroorzaakt door drie ruisbronnen: statistische fluktuaties in het aantal gegenereerde ladingsdragers, statistische fluktuaties in de lekstroom en statistische fluktuaties in stromen in de elektronische circuits.

Elektromagnetische straling die binnendringt in een silicium sensor kan schade veroorzaken door de generatie van roosterfouten. Echter, zolang de energie van de invallende straling lager is dan 130 keV, blijft de stralingsschade beperkt. Bovendien biedt een temperatuurbehandeling de mogelijkheid om de schade te herstellen.

Hoogohmige silicium sensormatrices voor het meten van zachte röntgenstraling worden theoretisch gekarakteriseerd in Hoofdstuk 3. Twee soorten sensormatrices worden onderzocht. De fabrikage van de eerste soort is gebaseerd op een interkonnektiepatroon (aluminium, polysilicium). Deze methode heeft als nadeel dat grote matrices bestaande uit kleine elementen niet gemaakt kunnen worden.

Dit nadeel geldt niet voor sensormatrices van de tweede soort. Deze worden gefabriceerd volgens de dubbellaagsmetallisatietechniek (aluminium, aluminium) en worden onderverdeeld in twee groepen, beide gebaseerd op de sensorelementen zoals in de voorgaande tekst beschreven. De ene groep bestaat uit matrices van de sensorelementen, terwijl de elementen van de tweede groep bestaan uit sensoren in serie met polysilicium weerstanden.

Omdat de sensormatrices opgebouwd zijn uit sensorelementen, gelden veel van de karakteristieke parameters van de sensorelementen ook voor de elementen van de sensormatrices. De lekstroom van een resistieve uitgang van een sensormatrix is de som van de lekstromen van de sensorelementen van de kolom. De levensduur van de ladingsdragers van een bepaalde sensor hangt niet af van de geometrie van de sensor en hoeft dus niet apart gedefinieerd te worden voor sensormatrices. De energieresolutie en de ruis van een sensormatrix worden eveneens gegeven door de energieresolutie en de ruis van de individuele sensorelementen. Parameters die wel verschillend zijn voor sensormatrices zijn plaatsresolutie, overspraak en stralingsschade.

Overspraak tussen naburige elementen in een sensormatrix komt voor wanneer de lading, die door een element gekollekteerd wordt, bij een ander element een uitgangssignaal induceert. Koincidentietechnieken worden gebruikt om de mate van overspraak vast te stellen.

Omdat de sensormatrices twee metallisatielagen hebben met een dielektricum ertussen als isolatie, zijn deze matrices minder stralingsbestendig dan de sensorelementen. Ionisatie effekten veroorzaakt door ingevangen lading kunnen op den duur het funktioneren van het dielektricum nadelig beinvloeden. Wanneer de sensormatrices aan de achterkant bestraald worden, neemt de kans op dit soort stralingsschade aanzienlijk af.

De fabrikage van hoogohmige silicium sensoren en sensormatrices voor het meten van zachte röntgenstraling wordt behandeld in Hoofdstuk 4. De fabrikage

van een sensor bestaat uit het aanbrengen van twee junkties in een hoogohmig substraat d.m.v. ionenimplantatietechnieken: een p^+-n^- junktie aan de voorkant en een n^--n^+ junktie aan de achterkant. Er is een aantal redenen om hoogohmig silicium te gebruiken als substraatmateriaal. Het heeft een relatief lage verontreinigingskoncentratie, een lage dichtheid van vangcentra en een lage verstrooiingscentradichtheid. Dit heeft tot gevolg dat de thermische generatie in de depletielaag minimaal is en dat de levensduur en de mobiliteit van de minderheidsladingsdragers en de depletielaagdikte maximaal zijn. Bovendien ontstaat een sterk elektrisch veld in de depletielaag van een korrekt ingestelde sensor. Dit elektrisch veld bewerkstelligt dat de kollektie van de gegenereerde lading in minder dan 25 ns plaatsvindt en voorkomt dat de lading uitdiffundeert voordat het de elektrode(s) bereikt. Tenslotte hebben sensoren van hoogohmig silicium altijd een betere kwantumefficiency dan sensoren van standaard silicium. De geintegreerde weerstanden zijn gerealiseerd door depositie van polysilicium m.b.v. een LPCVD techniek.

De processtappen die ontwikkeld zijn om hoogohmige silicium sensoren voor het meten van zachte röntgenstraling te fabriceren kunnen direct gebruikt worden voor de fabrikage van de sensormatrices die gebaseerd zijn op de dubbellaagsmetallisatietechniek. Slechts twee stappen moeten worden toegevoegd: depositie bij lage temperatuur van siliciumdioxide en de tweede metallisatie stap.

Het meetsysteem dat gebruikt is voor de detektie van zachte röntgenstraling wordt behandeld in Hoofdstuk 5. De door een foton gegenereerde lading moet bewerkt worden nadat het is gekollekteerd. De signaalverwerkingsapparatuur die gebruikt wordt in meetsystemen voor zachte röntgenstraling bestaat uit voorversterkers, spektroskopie versterkers, A/D omzetters, koincidentiecircuits en MCAs (veelkanaals analysatoren). Het met succes toepassen van hoogohmige silicium sensoren en sensormatrices voor het meten van zachte röntgensstraling hangt zeer nauw samen met de beschikbaarheid van kleine en snelle versterkers met lage ruis en van signaalverwerkingselektronica die weinig vermogen dissipeert.

De experimentele resultaten worden gepresenteerd in Hoofdstuk 5. De gemeten waarden van de lekstromen van de sensoren en de sensormatrices zijn in overeenstemming met de door de theorie voorspelde waarden. De experimentele waarden van de geintegreerde polysilicium weerstanden zijn ook in overeenstemming met de theorie.

De overspraak van alle sensormatrices is altijd minder dan 10 %. De sensormatrices met dubbellaagsmetallisatie die gebruik maken van de geintegreerde weerstanden hebben de laagste overspraak, terwijl de sensormatrices met dubbellaagsmetallisatie die geen geintegreerde weerstanden gebruiken de beste energieresolutie hebben.

Het doel van een sensormatrix voor het meten van zachte röntgenstraling is om invallende straling te absorberen en de daarbij gegenereerde elektron–gat paren te kollekteren en zodoende een betrouwbare waarde van de energie en de positie in twee dimensies van de invallende straling te geven. De lage lekstroom, de goede energieresolutie en de kleine overspraak van de in dit proefschrift gepresenteerde hoogohmige silicium sensormatrices voor het meten van zachte röntgenstraling tonen aan dat deze sensormatrices uitermate geschikt zijn voor het meten van zachte röntgenstralingsbeelden.

LIST OF SYMBOLS

Symbol	Description	Unit
A	Area	m^2
a	Lattice constant	m
$\mathscr{B}$	Magnetic–flux density	T
B	Proportionality constant	
BV	Voltage; breakdown	V
c	Speed of light in vacuum, 2.998×10^8	m/s
C_d	Capacitance; depleted layer	F
C_{det}	Capacitance; detector	F
C_f	Capacitance; feedback	F
C_{in}	Capacitance; preamplifier input	F
C_{min}	Capacitance; inverted layer	F
C_{ox}	Capacitance; oxide layer	F
C_s	Capacitance; undepleted layer	F
D_e	Diffusion constant; electrons	m^2/s
D_{ep^+}	Diffusion constant; electrons in p^+–region	m^2/s
D_h	Diffusion constant; holes	m^2/s
D_{hn^-}	Diffusion constant; holes in n^-–region	m^2/s
D_{hn^+}	Diffusion constant; holes in n^+–region	m^2/s
$\mathscr{E}$	Electric–field strength	V/m
E	Energy	J
E_b	Binding energy of an electron to its shell	J
$\mathscr{E}_{bv}$	Maximum electric field at breakdown	V/m
E_c	Energy level; bottom of conduction band	J
E_i	Energy level; intrinsic Fermi	J
E_g	Energy; bandgap	J
E_p	Energy; photon	J
E_{qn}	Energy level; electron quasi–Fermi	J
E_{qp}	Energy level; hole quasi–Fermi	J
E_t	Energy level; trap	J
E_v	Energy level; top of valence band	J
f	Frequency	Hz
F	Fano factor	

G	Generation rate	$m^{-3}s^{-1}$
G_e	Generation rate; electrons	$m^{-3}s^{-1}$
G_h	Generation rate; holes	$m^{-3}s^{-1}$
h	Planck's constant, 6.636×10^{-34}	Js
$h\nu$	Energy; photon	J
$h\nu_q$	Energy; phonon	J
$\overline{i_f^2}$	Current; flicker noise	A
$\overline{i_{gr}^2}$	Current; generation−recombination noise	A
$\overline{i_s^2}$	Current; shot noise	A
$\overline{i_t^2}$	Current; thermal noise	A
I_e	Current; electron	A
I_h	Current; hole	A
$\mathcal{I}_0$	Initial intensity	photons/m²s
I_r	Current; average reverse	A
I_t	Current; total reverse	A
$I(t)$	Current as a function of time t	A
$\mathcal{I}(x)$	Intensity as a function of position x	photons/m²s
I_i	Reverse current contribution; region i	A
I_{ii}	Reverse current contribution; region ii	A
I_{iii}	Reverse current contribution; region iii	A
I_{iv}	Reverse current contribution; region iv	A
$I_{iii,iv}$	Reverse current contribution; region iii,iv	A
J_e	Current density; electron	A/m
J_h	Current density; hole	A/m
k	Boltzmann's constant, 1.38×10^{-23}	J/K
kT	Energy; thermal	J
l	Length	m
L_e	Diffusion length; electrons	m
L_{ep^+}	Diffusion length; electrons in p^+−region	m
L_h	Diffusion length; holes	m
L_{hn^-}	Diffusion length; holes in n^-−region	m
L_{hn^+}	Diffusion length; holes in n^+−region	m
L_{dr-e}	Drift length; electrons	m
L_{dr-h}	Drift length; holes	m
m_n^*	Effective mass; electron	kg
m_p^*	Effective mass; hole	kg
n	Concentration; electrons	m^{-3}
n_i	Concentration; intrinsic carrier	m^{-3}
n_n	Concentration; electrons in n−region	m^{-3}
n_n^-	Concentration; electrons in n^-−region	m^{-3}
n_n^+	Concentration; electrons in n^+−region	m^{-3}
n_p^+	Concentration; electrons in p^+−region	m^{-3}
$\overline{N}$	Mean number of electron−hole pairs generated	
N_a	Acceptor impurity concentration	m^{-3}
N_{ap^+}	Acceptor impurity concentration; p^+−region	m^{-3}
N_c	Density of states; conduction band	m^{-3}
N_d	Donor impurity concentration	m^{-3}
N_{dn^-}	Donor impurity concentration; n^-−region	m^{-3}

$N_{dn}{}^+$	Donor impurity concentration; n^+–region	m^{-3}
N_o	Total number of generated carriers	
N_t	Localized allowed states density	m^{-3}
N_v	Density of states; valence band	m^{-3}
p	Concentration; holes	m^{-3}
p_n	Concentration; holes in n–region	m^{-3}
$p_n{}^-$	Concentration; holes in n^-–region	m^{-3}
$p_n{}^+$	Concentration; holes in n^+–region	m^{-3}
$p_p{}^+$	Concentration; holes in p^+–region	m^{-3}
P	Pitch	m
q	Charge; magnitude of electron, 1.6 x 10^{-19}	C
Q	Charge; quantity	C
Q_e	Quantum yield; effective	
Q_i	Quantum yield; intrinsic	
Q_{ox}	Charge; oxide	C
r	Radius of diffusive cloud of charges	m
R	Recombination rate	$m^{-3}s^{-1}$
R_b	Resistance; bias resistor	Ω
R_c	Resistance; contact	Ω
R_d	Resistance; depleted layer	Ω
R_f	Resistance; feedback	Ω
R_{in}	Resistance; preamplifier input	Ω
R_p	Projected range; mean value	m
R_r	Resistance; polysilicon resistor	Ω
R_s	Resistance; undepleted layer	Ω
R_{sh}	Resistance; sheet	Ω/sqr.
s	Recombination velocity; surface	m/s
s^*	Recombination velocity; effective surface	m/s
t_e	Collection time; electron	s
t_i	Time to complete ionization process	s
t_h	Collection time; hole	s
T	Temperature; absolute	K
T_{max}	Temperature; maximum	K
v_d	Velocity; drift	m/s
v_{th}	Velocity; average thermal	m/s
V_b	Voltage; bias	V
V_{fb}	Voltage; flat–band	V
V_{ms}	Potential difference between metal and Si	V
V_{out}	Voltage; output	V
V_t	Voltage; sum of built–in and bias	V
w	Width	m
x_{bn}	Border of generation zone nearest x_n	m
x_{bp}	Border of generation zone nearest x_p	m
x_d	Total width of p^+–n^-–n^+ diode structure	m
x_{dr}	Width of the depletion region, $(x_n - x_p)$	m
x_{hl}	High–low junction depth	m
x_n	Extension; depletion region into n^-–region	m
x_p	Extension; depletion region into p^+–region	m
x_{pn}	P^+–n^- junction depth	m
Z	Atomic number	

α	Absorption coefficient	m^{-1}
α_{cs}	Absorption coeff.; compton scattering	m^{-1}
α_i	Absorption coeff.; indirect transitions	m^{-1}
α_{pe}	Absorption coeff.; photoelectric effect	m^{-1}
α_{pp}	Absorption coeff.; pair production	m^{-1}
α_t	Sum of α_{pe}, α_{cs} and α_{pp}	m^{-1}
α^*	Proportionality coefficient	
δQ	Change in induced charge on electrodes	C
Δf	Bandwidth	Hz
Δp	Change in the hole concentration	m^{-3}
ΔR_p	Projected range; standard deviation	
ϵ	Energy; average ionization	J
ϵ_0	Permittivity of free space, 8.85×10^{-12}	F/m
ϵ_{si}	Silicon's dielectric constant, 11.8	
η_a	Quantum efficiency; absolute	
η_d	Quantum efficiency; detector	
η_{dr}	Partial quantum efficiency; depletion region	
η_n	Partial quantum efficiency; n-region	
η_p	Partial quantum efficiency; p-region	
η_t	Total quantum efficiency	
λ	Wavelength; electromagnetic radiation	m
λ_{max}	Wavelength; maximum	m
μ_e	Mobility; electron	m^2/Vs
μ_h	Mobility; hole	m^2/Vs
μ_i	Mobility; impurity scattering	m^2/Vs
μ_{hall}	Mobility; Hall	m^2/Vs
μ_l	Mobility; lattice scattering	m^2/Vs
μ_t	Mobility; total	m^2/Vs
ν	Frequency; electromagnetic radiation	Hz
ρ_d	Material density	kg/m
ρ_r	Material resistivity	Ω-m
σ	Standard deviation from the mean	
σ_e	Capture cross section; electron	m^2
σ_h	Capture cross section; hole	m^2
τ	Relaxation time	s
τ_c	Lifetime; minority carrier	s
τ_e	Lifetime; electron	s
τ_{eo}	Time constant; $(v_{th}\sigma_e N_t)^{-1}$	s
τ_g	Lifetime; generation	s
τ_h	Lifetime; hole	s
τ_{ho}	Time constant; $(v_{th}\sigma_h N_t)^{-1}$	s
τ_{hn^-}	Lifetime; hole in n^--region	s
τ_{hn^+}	Lifetime; hole in n^+-region	s
τ_r	Lifetime; recombination	s
τ_t	Time; rise of the output pulse	s

ACKNOWLEDGEMENTS

LIST OF PUBLICATIONS AND PRESENTATIONS

BOOK PUBLICATIONS

[1]   S. Middelhoek and S.A. Audet, Silicon Sensors, Academic Press,
        London, 1989, 1–376.

JOURNAL PUBLICATIONS

[1]   S. Middelhoek and S.A. Audet, Silicon sensors: full of promises and
        pitfalls, J. Phys. E: Sci. Instr., 20 (1987) 1080–1086.

[2]   H.J.P. Kuykens and S.A. Audet, A 3 x 3 drift chamber array for
        application in an electronic collimator, Nucl. Instr. and Meth., A273
        (1988) 570–574.

[3]   S.A. Audet, P.J.A. Munter, P.P.L. Regtien and R.F. Wolffenbuttel,
        Sensors: materials, technology, state–of–the–art and future trends,
        United Nations Industrial Development Organization (UNIDO)
        Publication, 1989, 1–52.

[4]   S.A. Audet and W.R.Th. ten Kate, Two–dimensional silicon sensor for
        imaging radiation, Sensors and Actuators, 16 (1989) 155–165.

[5]   W.R.Th. ten Kate and S.A. Audet, Processing high–purity silicon for
        sensor applications, Sensors and Actuators, 16 (1989) 287–298.

[6]   S.A. Audet and E.M. Schooneveld, High–purity silicon radiation–sensor
        array, Nucl. Instr. and Meth., A275 (1989) 517–526.

[7]   S.A. Audet, High—purity silicon radiation—sensor array for imaging
        synchrotron radiation in digital—subtraction angiography procedures,
        Rev. of Sci. Instr., 60 (1989) 2276—2279.

[8]   S.A. Audet, Silicon sensor array for soft X—ray and IR, Sensor
        Technology, 5 (1989) 2.

[9]   S.E. Wouters, S.A. Audet, E.M. Schooneveld and M.H. Kim,
        Integrating transistors on high—ohmic silicon, Nucl. Instr. and Meth.,
        A288 (1990) 44—47.

[10]   S.A. Audet and S.E. Wouters, Monolithic integration of a nuclear
        radiation sensor and transistors on high—purity silicon, accepted for
        publication in IEEE Trans. on Nucl. Sci.

[11]   T. Otaredian and S.A. Audet, Contactless lifetime measurement in
        processed and preprocessed silicon radiation detectors, accepted for
        publication in Sensors and Actuators.

[12]   S.E. Wouters, S.A. Audet and M.H. Kim, Compatible integration of
        radiation detectors and transistors, accepted for publication in Sensors
        and Actuators.

[13]   S.A. Audet, E.M. Schooneveld, S.E. Wouters and M.H. Kim,
        High—purity silicon soft X—ray imaging sensor array, accepted for
        publication in Sensors and Actuators.

CONFERENCE PROCEEDINGS

[1]   W.R.Th. ten Kate and S.A. Audet, Silicon radiation detectors with a
        high spatial resolution, Sensor Conf., Veldhoven, April 14—15, 1987,
        79—82.

[2]   H.J.P. Kuykens and S.A. Audet, A two—dimensional silicon detector
        array for application in an electronic collimator, Sensor Conf.,
        Veldhoven, April 14—15, 1987, 83—86.

[3]   W.R.Th. ten Kate and S.A. Audet, Processing high—purity silicon for
        sensor applications, 4th Int. Conf. on Solid—State Sensors and Actuators,
        Transducers '87, Tokyo, June 2—5, 1987, 103—106.

[4]   S.A. Audet and W.R.Th. ten Kate, Two—dimensional silicon sensor for
        imaging radiation, 4th Int. Conf. on Solid—State Sensors and Actuators,
        Transducers '87, Tokyo, June 2—5, 1987, 267—270.

[5]   H.J.P. Kuykens and S.A. Audet, A 3 x 3 silicon drift chamber array,
        London Conf. on Position—Sensitive Detectors, London, Sept. 7—12,

1987, 0.20.

[6]   S.A. Audet, P.J. French, S. Middelhoek and W. Verveer,
        Two–dimensional position responsivity of a silicon radiation sensor to
        X–rays, gamma rays and beta particles, 3rd Conf. on Sensors and Their
        Applications, Eurosensors, Cambridge, Sept. 22–24, 1987, 27–28.

[7]   S.A. Audet and E.M. Schooneveld, High–purity silicon radiation–sensor
        array, Workshop on Silicon Pixel Detectors, Leuven, May 31 – June 2,
        1988, 2.

[8]   S.A. Audet, Radiation–sensor array fabricated on high–purity
        silicon with coupling impedances realized through polysilicon and
        double–layer metalization layers, Proc. Int. Electr. Dev. and Mat.
        Symp., Kaohsiung, Aug. 29–31, 1988, 212–217.

[9]   S.A. Audet, High–purity silicon radiation–sensor array for imaging
        synchrotron radiation, 3rd Int. Conf. on Synchrotron Radiation
        Instrumentation: (SRI–88), Tsukuba, Aug. 29 – Sept. 2, 1988, B043.

[10]   S.E. Wouters, S.A. Audet, M.H. Kim and E.M. Schooneveld,
        Integrating transistors on high–ohmic silicon, 5th European Symp. on
        Semiconductor Detectors, New Developments in Radiation Detectors,
        Munich, Feb. 21–23, 1989, A9.

[11]   S.A. Audet, High–purity silicon radiation–sensor array for imaging
        synchrotron radiation, Kristal en Structuuronderzoek, Utrecht,
        April 10–11, 1989.

[12]   S.A. Audet and S.E. Wouters, Making radiation detectors smart enough
        for computers, VLSI and Computer Peripherals, 3rd Annual European
        Computer Conf., Hamburg, May 8–12, 1989, 79–81.

[13]   T. Otaredian and S.A. Audet, Contactless lifetime measurement in
        processed and preprocessed silicon microstrip detectors, 5th Int. Conf.
        on Solid–State Sensors and Actuators, Transducers '89, Montreux,
        June 25–30, 1989, 180–181.

[14]   S.E. Wouters, S.A. Audet and M.H. Kim, Compatible integration of
        radiation detectors and transistors, 5th Int. Conf. on Solid–State Sensors
        and Actuators, Transducers '89, Montreux, June 25–30, 1989, 179–180.

[15]   S.A. Audet, E.M. Schooneveld, S.E. Wouters and M.H. Kim,
        High–purity silicon soft X–ray imaging sensor array, 5th Int. Conf. on
        Solid–State Sensors and Actuators, Transducers '89, Montreux,
        June 25–30, 1989, 175.

[16]   S.A. Audet, E.M. Schooneveld and S. Middelhoek, High–purity silicon
        sensor array for imaging soft X–ray and infrared radiation, IEDM 1989,
        Washington, D.C., Dec. 3–6, 1989, 177–180.

POSTER PRESENTATIONS

[1]   H.J.P Kuykens and S.A. Audet, A silicon drift chamber for application in an electronic collimator, Sensor Conf., Veldhoven, April 14–15, 1987.

[2]   S.A. Audet and W.R.Th. ten Kate, Silicon radiation detectors with a high spatial resolution, Sensor Conf., Veldhoven, April 14–15, 1987.

[3]   S.A. Audet, High—purity silicon radiation–sensor array for imaging synchrotron radiation, 3rd Int. Conf. on Synchrotron Radiation Instrumentation: (SRI–88), Tsukuba, Aug. 29 – Sept. 2, 1988.

[4]   S.A. Audet, High—purity silicon radiation–sensor array, Sensor Conf., Veldhoven, Nov. 23–24, 1988.

[5]   S.A. Audet, High—purity silicon radiation–sensor array for imaging synchrotron radiation, Kristal en Structuuronderzoek, Utrecht, April 10–11, 1989.

[6]   S.E. Wouters and S.A. Audet, MOS transistors on high—purity silicon, Sensor Conf., Veldhoven, Nov. 21–22, 1989.

COMPANY/UNIVERSITY PRESENTATIONS

[1]   S.A. Audet, Two–dimensional position–sensitive radiation sensor, Nippon Steel Corporation, Kawasaki, June 1, 1987.

[2]   S.A. Audet, Radiation sensors at Delft University of Technology, University of Pennslyvania, Center for Sensor Technologies, Philadelphia, Dec. 20, 1988.

[3]   S.A. Audet, Radiation sensors at Delft University of Technology, Lawrence Berkeley Laboratories, Berkeley, Jan. 3–4, 1989.

[4]   S.A. Audet, Radiation sensors at Delft University of Technology, I.C. Sensors, Milpitas, Jan. 5, 1989.

[5]   S.A. Audet, Radiation sensors at Delft University of Technology, Nova Sensors, Fremont, Jan. 6, 1989.

[6]   S.A. Audet, Radiation sensors at Delft University of Technology, Massachussetts Institute of Technology, Cambridge, Jan. 11, 1989.

[7]   S.A. Audet, Soft X–ray imaging sensor arrays fabricated on high–purity silicon, Syracuse University, Syracuse, Dec. 11, 1989.

[8]   S.A. Audet, Soft X–ray imaging sensor arrays fabricated on high–purity
        silicon, Cornell University, National Nanofabrication Laboratory,
        Ithaca, Dec. 18, 1989.

[9]   S.A. Audet, Soft X–ray imaging sensor arrays fabricated on high–purity
        silicon, University of Michigan, Center for Integrated Sensors and
        Circuits, Ann Arbor, Dec. 19–20, 1989.

BIOGRAPHY

Sarah Anne Steigerwald Audet was born in Syracuse, New York, U.S.A. on June 24, 1960. She received a Bachelor of Science degree in Medical Technology from the State University of New York at Upstate Medical Center in May, 1982. After working for one and one-half years at Brigham and Woman's Hospital in Boston, she returned to full time study at Boston University, where she obtained a Master of Science degree in Electrical Engineering in January, 1986. In July, 1986, she joined the Electronic Instrumentation Laboratory of the Department of Electrical Engineering at Delft University of Technology to perform research towards a Ph.D. degree in the area of soft X-ray sensor arrays.

Sarah has presented the results of her research on the subject of soft X-ray sensor arrays at numerous international conferences in Europe, the United States, Japan and Taiwan, R.O.C. and she is the author of several articles, which have been published in international scientific journals. Sarah is coauthor of a book entitled "Silicon Sensors", which was published by Academic Press in 1989.